

Monitoring, early warning and mitigation of natural and engineered slopes

Edited by

Haijun Qiu, Wen Nie and Afshin Asadi

Published in

Frontiers in Earth Science



FRONTIERS EBOOK COPYRIGHT STATEMENT

The copyright in the text of individual articles in this ebook is the property of their respective authors or their respective institutions or funders. The copyright in graphics and images within each article may be subject to copyright of other parties. In both cases this is subject to a license granted to Frontiers.

The compilation of articles constituting this ebook is the property of Frontiers.

Each article within this ebook, and the ebook itself, are published under the most recent version of the Creative Commons CC-BY licence. The version current at the date of publication of this ebook is CC-BY 4.0. If the CC-BY licence is updated, the licence granted by Frontiers is automatically updated to the new version.

When exercising any right under the CC-BY licence, Frontiers must be attributed as the original publisher of the article or ebook, as applicable.

Authors have the responsibility of ensuring that any graphics or other materials which are the property of others may be included in the CC-BY licence, but this should be checked before relying on the CC-BY licence to reproduce those materials. Any copyright notices relating to those materials must be complied with.

Copyright and source acknowledgement notices may not be removed and must be displayed in any copy, derivative work or partial copy which includes the elements in question.

All copyright, and all rights therein, are protected by national and international copyright laws. The above represents a summary only. For further information please read Frontiers' Conditions for Website Use and Copyright Statement, and the applicable CC-BY licence.

ISSN 1664-8714
ISBN 978-2-83251-477-1
DOI 10.3389/978-2-83251-477-1

About Frontiers

Frontiers is more than just an open access publisher of scholarly articles: it is a pioneering approach to the world of academia, radically improving the way scholarly research is managed. The grand vision of Frontiers is a world where all people have an equal opportunity to seek, share and generate knowledge. Frontiers provides immediate and permanent online open access to all its publications, but this alone is not enough to realize our grand goals.

Frontiers journal series

The Frontiers journal series is a multi-tier and interdisciplinary set of open-access, online journals, promising a paradigm shift from the current review, selection and dissemination processes in academic publishing. All Frontiers journals are driven by researchers for researchers; therefore, they constitute a service to the scholarly community. At the same time, the *Frontiers journal series* operates on a revolutionary invention, the tiered publishing system, initially addressing specific communities of scholars, and gradually climbing up to broader public understanding, thus serving the interests of the lay society, too.

Dedication to quality

Each Frontiers article is a landmark of the highest quality, thanks to genuinely collaborative interactions between authors and review editors, who include some of the world's best academicians. Research must be certified by peers before entering a stream of knowledge that may eventually reach the public - and shape society; therefore, Frontiers only applies the most rigorous and unbiased reviews. Frontiers revolutionizes research publishing by freely delivering the most outstanding research, evaluated with no bias from both the academic and social point of view. By applying the most advanced information technologies, Frontiers is catapulting scholarly publishing into a new generation.

What are Frontiers Research Topics?

Frontiers Research Topics are very popular trademarks of the *Frontiers journals series*: they are collections of at least ten articles, all centered on a particular subject. With their unique mix of varied contributions from Original Research to Review Articles, Frontiers Research Topics unify the most influential researchers, the latest key findings and historical advances in a hot research area.

Find out more on how to host your own Frontiers Research Topic or contribute to one as an author by contacting the Frontiers editorial office: frontiersin.org/about/contact

Monitoring, early warning and mitigation of natural and engineered slopes

Topic editors

Haijun Qiu — Northwest University, China

Wen Nie — Jiangxi University of Science and Technology, China

Afshin Asadi — Wilton Joubert Consulting Engineers, New Zealand

Citation

Qiu, H., Nie, W., Asadi, A., eds. (2023). *Monitoring, early warning and mitigation of natural and engineered slopes*. Lausanne: Frontiers Media SA.
doi: 10.3389/978-2-83251-477-1

Table of contents

- 05 **Editorial: Monitoring, early warning, and mitigation of natural and engineered slopes**
Wen Nie, Haijun Qiu and Afshin Asadi
- 08 **A Novel Method for Extracting Time Series Information of Deformation Area of a Single Landslide Based on Improved U-Net Neural Network**
Bibo Dai, Yunmin Wang, Chunyang Ye, Qihang Li, Canming Yuan, Song Lu and Yuyang Li
- 15 **Prediction and Treatment of Water Leakage Risk Caused by the Dynamic Evolution of Ground Fissures in Gully Terrain**
Dong Feng, Enke Hou, Xiaoshen Xie, Xiaoyang Che, Pengfei Hou and Tianwen Long
- 27 **A Whole Process Risk Management System for the Monitoring and Early Warning of Slope Hazards Affecting Gas and Oil Pipelines**
Yan Yan, Guanglin Xiong, Jiaojiao Zhou, Renhe Wang, Wenyao Huang, Miao Yang, Renchao Wang and Dongxian Geng
- 41 **Study on Evaluation and Prediction of the Degree of Surface Damage Caused by Coal Mining**
Xiaoshen Xie, Enke Hou, Tianwen Long, Dong Feng, Pengfei Hou, Qiming Wei, Yang Li and Jiangbin Liu
- 53 **The Impact of Geohazards on Sustainable Development of Rural Mountain Areas in the Upper Reaches of the Min River**
Yanfen He, Mingtao Ding, Kang Liu and Min Lei
- 64 **Sandstone Slope Stability Analysis Under Wetting-Drying Cycles Based on Generalized Hoek-Brown Failure Criterion**
Kai Kang, Shiyuan Huang, Wenhua Liu, Hu Cheng, Igor Fomenko and Yuxin Zhou
- 71 **Multi-Source Information Fusion Correlation Analysis of Bedrock Deterioration on Slopes Under Leaching Erosion**
Wen Zhong, Zhiqi Feng, Bo Li, Zequn Zhang, Peng Zeng, Zhongqun Guo, Kaijian Hu and Xiaojun Wang
- 84 **Experimental Study of Dynamic Characteristics of Tailings With Different Reconsolidation Degrees After Liquefaction**
Wensong Wang, Guansen Cao, Ye Li, Yuxi Zhou, Ting Lu, Ya Wang and Binbin Zheng
- 95 **Risk Evolution Study of Tailings Dam Failures Disaster Based on DEMATEL-MISM**
Binbin Zheng, Jiahe Wang, Tingting Feng, Wensong Wang, Yuxi Zhou, Guansen Cao and Yufei Wang

- 106 **Influence of Clay Content on Crack Evolution of Clay–Sand Mixture**
Xiangang Jiang, Qin Huang, Zongliang Zhang, Luis E. Vallejo, Xiaoqing Chen, Wanyu Zhao, Hongyan Deng, Xingrong Liu, Danqing Song and Zhuo Chen
- 116 **Spatial and Temporal Analysis of Quantitative Risk of Flood due to Climate Change in a China's Plateau Province**
Baolin Wu, Zhengtao Zhang, Xinrui Guo, Cheng Tan, Chengfang Huang and Jun Tao
- 128 **Impacts of Risk Perception, Disaster Knowledge, and Emotional Attachment on Tourists' Behavioral Intentions in Qinling Mountain, China**
Junqing Hao, Han Tang, Jiawei Hao, Yanting Ma and Xinxiang Jiang
- 140 **Multifractal Features of Particle-Size Distribution and Their Relationships With Soil Erosion Resistance Under Different Vegetation Types in Debris Flow Basin**
Songyang Li, Ruoyun Gao, Maowei Huang, Liusheng Yang, Hang Yu, Chenhui Yu, Xue Tian, Jian Li and Yongming Lin
- 153 **Comprehensive analysis of the stability of tailings-geotextile composite—Iron Mine Tailings Dam in Gushan, Anhui, China**
Yuxin Zhou, Jinzhi Ji, Xuelong Hu, Shengsong Hu, Xiaogang Wu, Canming Yuan and Tianqiang Zhu



OPEN ACCESS

EDITED AND REVIEWED BY
Candan Gokceoglu,
Hacettepe University, Turkey

*CORRESPONDENCE

Haijun Qiu,
haijunqiu@nwnu.edu.cn

SPECIALTY SECTION

This article was submitted to
Geohazards and Georisks,
a section of the journal
Frontiers in Earth Science

RECEIVED 10 September 2022

ACCEPTED 17 October 2022

PUBLISHED 13 January 2023

CITATION

Nie W, Qiu H and Asadi A (2023),
Editorial: Monitoring, early warning, and
mitigation of natural and
engineered slopes.
Front. Earth Sci. 10:1041180.
doi: 10.3389/feart.2022.1041180

COPYRIGHT

© 2023 Nie, Qiu and Asadi. This is an
open-access article distributed under
the terms of the [Creative Commons
Attribution License \(CC BY\)](https://creativecommons.org/licenses/by/4.0/). The use,
distribution or reproduction in other
forums is permitted, provided the
original author(s) and the copyright
owner(s) are credited and that the
original publication in this journal is
cited, in accordance with accepted
academic practice. No use, distribution
or reproduction is permitted which does
not comply with these terms.

Editorial: Monitoring, early warning, and mitigation of natural and engineered slopes

Wen Nie¹, Haijun Qiu^{2*} and Afshin Asadi³

¹Jiangxi University of Science and Technology, Ganzhou, China, ²Northwest University, Xi'an, China,
³International College of Auckland (ICA), Auckland, New Zealand

KEYWORDS

natural and engineered slopes, slope failure mechanisms, slope monitoring, risk assessment, machine learning

Editorial on the Research Topic

[Monitoring, early warning, and mitigation of natural and engineered slopes](#)

Natural and engineered slopes, including mountain slopes, highway slopes, mine slopes, and reservoir dams are widely distributed around the world (Qiu et al., 2022). Such slopes may become unstable due to natural factors or human activity, causing catastrophic loss of life and damage to infrastructure. Continuous monitoring of these slopes is required to provide early warning of disasters, enabling engineers and/or emergency services to respond accordingly. In recent years, developments in science and technology and the theory of multidisciplinary interaction have brought about new opportunities for research in this field (Liu et al., 2022; Wang L et al., 2022; Zhou et al.). However, further breakthroughs are still required in the domains of efficient monitoring, accurate early warning, reliable risk assessment, and low-cost disaster recovery. This special issue brings together 14 publications designed to present the latest research advances and methods in natural and engineered slope monitoring, early warning, disaster remediation, and risk assessment.

Slope hazard reduction technology

Five of the 14 articles in this special issue investigate improvements in landslide identification accuracy, analysis of disaster risk evolution, and quantitative prediction of hazard degree using a variety of methods, with the aim of formulating new slope hazard mitigation strategies. Zheng et al. put forward an effective and reliable method of analyzing the risk evolution of tailings pond dam breaches based on a combination of DEMATEL and MISIM, summarize 35 risk factors affecting the destruction of tailings ponds and the comprehensive impact degree of each factor, and establish an effective risk evolution model of tailings pond dam breaches. Dai et al. propose an improved U-Net fully convolutional neural network based on physical model experiments to automatically extract the deformation of a single landslide over time. Compared with mainstream superpixel methods, the improved U-Net exhibits higher recognition accuracy

and greater robustness. To explore the surface damage caused by shallow coal seam mining, [Feng et al.](#) establish a mathematical prediction model for the relationship between trench seepage volume, trench fissure width, and trench flood volume. The model is based on field measurements of ground fracture leakage on an experimental platform and also uses aerial photography *via* UAV. The authors propose a classification standard for the leak risk of mining fissures. [Xie et al.](#) examine the development characteristics of surface damage after coal seam mining. This study found that surface crack characteristics can be used to characterize the degree of surface damage. The study graded surface damage and a surface damage prediction model was established based on the GIS platform. [Yan et al.](#) used InSAR, UAV, and ground survey technology to divide pipeline slopes into different danger zones, using real-time monitoring data to simulate pipeline slope hazards, quantitatively predict the degree of hazard, and formulate rapid prevention and control measures.

Slope failure mechanisms

The other nine articles in this special issue investigate and analyze various types of disasters related to engineering projects, such as ground cracks, surface failure, slope bedrock degradation, and tailing pond failure to understand the dynamic mechanisms involved and their relationship with the project in question.

Cracks alter the structure of soil and reduce its strength and stability. In their contribution, [Jiang et al.](#) explored the crack evolution process in clay-sand mixtures under various clay content conditions. They observed almost no cracks on the surface of soil samples with clay content below 30%. In samples with a clay content greater than 50%, the formation and development of cracks can be divided into three stages. Finally, in samples with clay content greater than or equal to 30% and less than or equal to 50%, no stage characteristics were associated with the formation and development of cracks. [Kang et al.](#) studied the stages of the influence of wet-dry cycles on the stability of sandstone slopes in subsidence areas. The characteristics of strength deterioration in intact sandstone were analyzed through the application of wet-dry cycles and uniaxial compression tests. The authors found that the most serious process for the induction of sandstone slope instability occurs in the early stage of the wet-dry cycle. [Zhong et al.](#) studied the effect of leaching on the physical and mechanical properties of slope bedrock; the results showed that the mechanical properties of bedrock samples deteriorated significantly at first, then recovered significantly, and subsequently fluctuated within a narrow range. [Wang et al.](#) studied the effect of the degree of reconsolidation on the dynamic characteristics of liquefied tailings under cyclic loading. They found that the reconsolidation process undergone by tailings following liquefaction improves their liquefaction resistance. In another study, [Li et al.](#) explore the differences between multiple types of vegetation in terms of soil erosion resistance and multifractal parameters. They found that soil erosion resistance was significantly correlated with multifractal parameters and that multifractal parameters could predict soil erosion

resistance. [Wu et al.](#) explored how quantitative flood risk and emission reduction contribute to risk mitigation by constructing a loss rate curve and quantitatively characterizing the spatiotemporal variation characteristics of flood loss rate. The results show that the curve representing flood loss rates from 2020 to 2060 exhibits a trend of “rising in the early stage, stabilizing in the middle stage, and declining in the late stage” in low- and medium-emission scenarios and an upward fluctuation trend in a high-emission scenario. [Zhou W et al. \(2022\)](#) used a seepage field numerical simulation method to analyze the permeability and physical properties of composite materials. They found that the permeability coefficient of these materials increases with increasing backfill tension in the initial stage of composite stacking, while permeability decreases gradually in the later stage to become stable. Taking the Qinling mountain disaster as a case study, [Hao et al.](#) used a questionnaire-based method to analyze the impact of the disaster on tourists’ behavioral intentions. The results show that perception of risk exerts a negative impact on tourists’ behavioral intentions, while knowledge of the disaster exerts a positive effect. Finally, through analysis of geological hazard data, settlement data, and cultivated land data, the study by [He et al.](#) identified a coupling mechanism between geological hazards, rural settlements, and cultivated land in mountainous areas of the upper Min River.

Perspectives

This special issue is dedicated to the use of modern technologies, data-based approaches, and techniques, grounded in multiple disciplines for monitoring natural and engineered slopes and for early warning and mitigation of the associated risks. However, in the context of extreme weather and the execution of large-scale construction projects, slope failure requires further research. On this basis, this set of articles provides reference points for the following aspects of damage mitigation: 1) multiscale and multidisciplinary integration for analyses of the physical mechanisms and dynamic processes inside slopes; 2) early warning and analysis of slope instability based on big data and field-refined detection systems; and 3) innovative green, efficient, and sustainable post-disaster slope restoration projects.

Author contributions

Three authors co-organized the album, with NW on Slope Hazard Reduction Technology, QH on hazard risk assessment, and AA on Failure mechanism of slope.

Conflict of interest

The authors declare that the research was conducted in the absence of any commercial or financial relationships that could be construed as a potential conflict of interest.

Publisher's note

All claims expressed in this article are solely those of the authors and do not necessarily represent those of their affiliated

organizations, or those of the publisher, the editors and the reviewers. Any product that may be evaluated in this article, or claim that may be made by its manufacturer, is not guaranteed or endorsed by the publisher.

References

Liu, Z., Qiu, H., Zhu, Y., Liu, Y., Yang, D., Ma, S., et al. (2022). Efficient identification and monitoring of landslides by time-series InSAR combining single- and multi-look phases. *Remote Sens.* 14, 1026. doi:10.3390/rs14041026

Qiu, H., Zhu, Y., Zhou, W., Sun, H., He, J., and Liu, Z. (2022). Influence of DEM resolution on landslide simulation performance based on the Scoops3D model. *Geomatics, Nat. Hazards Risk* 13 (1), 1663–1681. doi:10.1080/19475705.2022.2097451

Wang, L., Qiu, H., Zhou, W., Zhu, Y., Liu, Z., Ma, S., et al. (2022). The post-failure spatiotemporal deformation of certain translational landslides may follow the pre-failure pattern. *Remote Sens.* 14, 2333. doi:10.3390/rs14102333

Zhou, W., Qiu, H., Wang, L., Pei, Y., Tang, B., Ma, S., et al. (2022). Combining rainfall-induced shallow landslides and subsequent debris flows for hazard chain prediction. *CATENA* 213, 106199. doi:10.1016/j.catena.2022.106199



A Novel Method for Extracting Time Series Information of Deformation Area of a Single Landslide Based on Improved U-Net Neural Network

Bibo Dai^{1,2,5}, Yunmin Wang^{3,5}, Chunyang Ye³, Qihang Li³, Canming Yuan³, Song Lu^{4,6*} and Yuyang Li³

¹School of Resources and Civil Engineering, Northeastern University, Shenyang, China, ²Geomechanics Research Center, Northeastern University, Shenyang, China, ³School of Resources and Environmental Engineering, Jiangxi University of Science and Technology, Ganzhou, China, ⁴Quanzhou Institute of Equipment Manufacturing, Haixi Institutes, Chinese Academy of Sciences, Quanzhou, China, ⁵State Key Laboratory of Safety and Health for Metal Mines, Maanshan, China, ⁶Zhejiang Zhipu Engineering Technology Corporation Limited, Huzhou, China

OPEN ACCESS

Edited by:

Wen Nie,
Jiangxi University of Science and
Technology, China

Reviewed by:

Pooya Saffari,
Qingdao Technological University
Qindao College, China
Chunyang Zhang,
Wuhan University of Technology,
China
Guangzhe Zhang,
Technical University Bergakademie
Freiberg, Germany

*Correspondence:

Song Lu
lusong@outlook.jp

Specialty section:

This article was submitted to
Geohazards and Georisks,
a section of the journal
Frontiers in Earth Science

Received: 29 September 2021

Accepted: 08 November 2021

Published: 03 December 2021

Citation:

Dai B, Wang Y, Ye C, Li Q, Yuan C, Lu S
and Li Y (2021) A Novel Method for
Extracting Time Series Information of
Deformation Area of a Single Landslide
Based on Improved U-Net
Neural Network.
Front. Earth Sci. 9:785476.
doi: 10.3389/feart.2021.785476

This paper proposed an improved U-Net fully convolutional neural network to automatically extract a single landslide deformation information under time series based on the physical model experiments. This method extracts time series information for three different landslide deformation ranges. Compared to U-Net and mainstream superpixel method, evaluation indicators of DSC, VOE and RVD verify the high recognition accuracy and strong robustness of our method.

Keywords: landslide, U-Net neural network, superpixel method, point cloud, evaluation indicators

INTRODUCTION

Landslides usually cause a large number of casualties and property losses (Lee et al., 2006; Shahabi et al., 2013; Shirzadi et al., 2017), so it is very important to obtain characteristic information when landslides occur (Guzzetti et al., 1994; Malamud et al., 2004; Lee et al., 2018). Some scholars have done a lot of research on it from different angles (Kurtz et al., 2014; Tang et al., 2014; Zhang et al., 2016; Zhang et al., 2020; Li et al., 2021a; Li et al., 2021b). Computer vision technology such as image transformation algorithms improved the application of image recognition in landslide mapping (Ardizzone et al., 2007; Cheng et al., 2013; Mwaniki et al., 2017; Bui et al., 2020; Shi et al., 2020). While the image recognition of landslide deformation area in specific time deformation area of a single landslide is few considered.

In the mainstream automatic recognition of Superpixel segmentation, Xie et al., proposed a method of super pixel generation for SAR images based on significant differences and spatial distance (Xie et al., 2019). Zhu et al., proposed a region merging method (Zhu et al., 2016). Hashiba et al., uses the superpixel SLICO method to check the appropriate area size to extract the landslide area with high accuracy (Hashiba and Sonobe, 2020). Yang et al., used superpixel algorithm to realize the automatic extraction of landslide deformation information (Yang et al., 2019). But these methods are lacking in accuracy and recognition speed. Some scholars use u-net neural network to extract landslide deformation information (Ghorbanzadeh et al., 2021). Sanghoon Lee et al., used U-Net to quantitative spatial analysis on whole slide images (Lee et al., 2020). Chen Yu et al., developed a U-net like model suitable for mapping post-earthquake landslide susceptibility (Chen et al., 2020). Unfortunately, these methods cannot achieve both high accuracy and strong robustness for recognition of landslide deformation area.

TABLE 1 | Architectural details of the improved U-Net.

Layers		Image size	Operation	Kernel size	Stride	Dilation
S1	L1	(512,512,3)	The improved ResNet block	(33,64)	1	2
	L2	(512,512,64)	Double Conv + BN + ReLU	(33,64)	1	1
	L3	(512,512,64)	MaxPool	(2,2)	2	-
S2	L4	(256,256,64)	The improved ResNet block	(33,64)	1	2
	L5	-25,62,56,128	Double Conv + BN + ReLU	(33,128)	1	1
	L6	-25,62,56,128	MaxPool	(2,2)	2	-
S3	L7	-12,81,28,128	The improved ResNet block	(33,128)	1	2
	L8	-12,81,28,256	Double Conv + BN + ReLU	(33,256)	1	1
	L9	-12,81,28,256	MaxPool	(2,2)	2	-
S4	L10	(64,64,256)	The improved ResNet block	(33,256)	1	2
	L11	(64,64,512)	Double Conv + BN + ReLU	(33,512)	1	1
	L12	(64,64,512)	MaxPool	(2,2)	2	-
S5	L13	(32,32,512)	The improved ResNet block	(33,512)	1	2
	L14	(32,32,1024)	Double Conv + BN + ReLU	(33,1024)	1	1
	L15	(32,32,1024)	ConvTrans	(22,1024)	2	1
S6	L16	(64,64,512)	Cat(L11,L15)	-	-	-
	L17	(64,64,1024)	The improved ResNet block	(33,1024)	1	2
	L18	(64,64,512)	Double Conv + BN + ReLU	(33,512)	1	1
	L19	(64,64,512)	ConvTrans	(22,512)	2	1
S7	L20	-12,81,28,256	Cat(L8,L20)	-	-	-
	L21	-12,81,28,512	The improved ResNet block	(33,512)	1	2
	L22	-12,81,28,256	Double Conv + BN + ReLU	(33,256)	1	1
	L23	-12,81,28,256	ConvTrans	(22,256)	2	1
S8	L24	-25,62,56,128	Cat(L5,L24)	-	-	-
	L25	-25,62,56,256	The improved ResNet block	(33,256)	1	2
	L26	-25,62,56,128	Double Conv + BN + ReLU	(33,128)	1	1
	L27	-25,62,56,128	ConvTrans	(22,128)	2	1
S9	L28	(512,512,64)	Cat(L2,L28)	-	-	-
	L29	-51,25,12,128	The improved ResNet block	(33,128)	1	2
	L30	(512,512,64)	Double Conv + BN + ReLU	(33,64)	1	1
	L31	(512,512,64)	Conv + Softmax	(11,64)	1	1
	OUT	(512,512,1)				

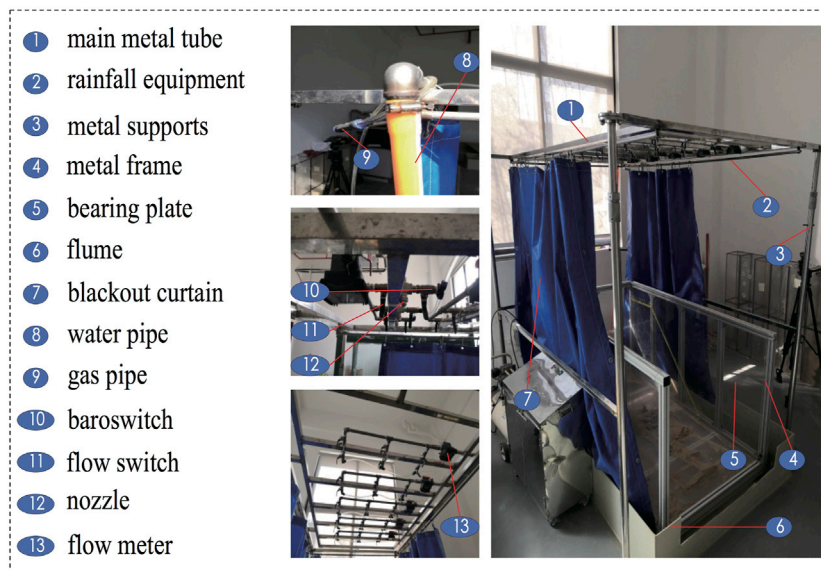


FIGURE 1 | Rainfall device model.

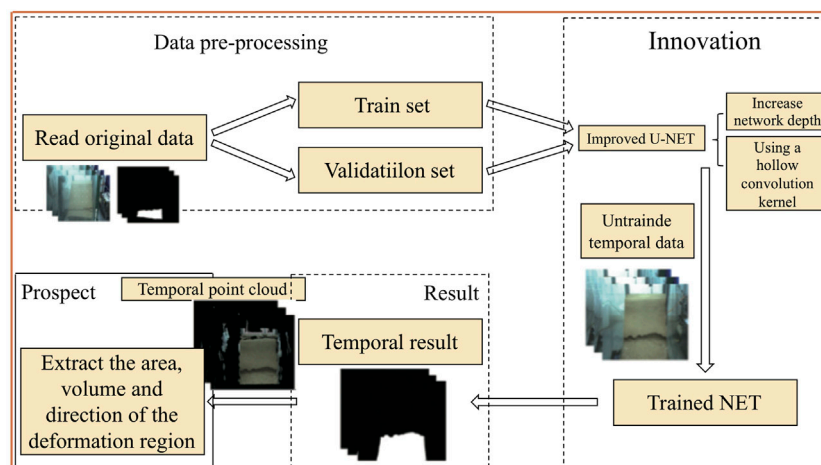


FIGURE 2 | The flow chart of time sequence information extraction of landslide deformation area.

In this study, we propose an automatic recognition method for landslide deformation characteristics based on improved U-Net neural network. Compared with U-Net neural network and mainstream superpixel methods, it has higher accuracy and robustness in identifying landslide deformation features under time series. Physical simulated landslide experiments verify the reliability of our method.

METHODS

The U-Net network was first proposed by Olaf et al. to segment images of biological cells. It is well known for its small training set. U-Net consists of two parts: a contraction path and an expansion

path. The contraction path includes downsampling, ReLU, and pooling; the expansion path includes upsampling and ReLU (Ronneberger et al., 2015). This study improves the U-Net network by: 1) that increasing the depth of the network is conducive to extracting deeper features of the image (He et al., 2015); 2) that replacing part of the traditional convolution kernel using a hollow convolution kernel increase the receptive field to preserve more local details of the picture (Wang et al., 2016). **Table 1** lists the specific operations of each layer of the improved U-Net network. The improved U-Net contains 9 improved residual modules, each of which is composed of two hole convolutions, two BNs and two ReLU functions; 19 convolutional layers, four pooling layers and four transposed convolutional layers.

Data Set and Experimental Environment

The data used in this study was from indoor rainfall-induced landslides experiments. The physical model device is mainly composed of a rainfall simulation equipment and a set of monitoring sensors. The rainfall simulation system includes a metal frame, a metal support, 15 nozzles, and 5 flowmeters (water velocity was 25–250 ml/min for each flowmeter). The length, width, and height of the metal frame are 1.6, 0.8, and 0.8 m respectively (Figure 1). The main landslide monitoring sensor in our study is a trinocular camera (type: Point Gray Bumblebee X3, resolution: 1,280 × 960), which saves the captured images every 5 s. There are five groups of experimental models in the experiment, named S1, S2, S3, S4, and S5. The five groups of physical model experiment materials are all ionic rare earths, and each group of tests rains for 5 h, and the total rainfall is 260 mm. In addition, the back-peak rainfall method uses decreasing rainfall intensity, which are 140 mm/h, 70 mm/h, 40 mm/h, 20 mm/h, and 10 mm/h respectively. On the other hand, the front-peak rainfall method uses incremental rainfall intensity, which are 10 mm/h, 20 mm/h, 40 mm/h, 70 mm/h and 140 mm/h respectively (Li et al., 2020). In these five sets of experiments, due to the different physical model building methods and rainfall methods, the forms of slope landslide damage are also different. These experiments provide more data support for later method validation.

Test Procedure

In this part, we use an improved U-Net method to extract landslide deformation information (Figure 2), and use currently popular evaluation indicators to evaluate the experimental segmentation results. Since there is no public dataset of continuous deformation images of landslides, we used LabelMe software to make the training set labels in the experiment. This experiment uses a neural network framework based on PyTorch to implement U-Net full convolutional networks. The data in the experiment consists of two parts consisting of 500 pieces of training set and 100 pieces of test set. Each group of tests extracts an average of 100 training sets (30 small-scale damage images, 40 medium-scale damage images, and 30 large-scale damage images) and 20 test sets (6 small-scale damage images, 8 medium-scale damage images and 6 large-scale damage images). In order to better utilize the characteristic of U-Net full convolutional network, this paper keeps the size of each image in the experiment 512 × 512. In the experiment we used i7-6,700 (CPU), NVIDIA RTX 2060s (GPU) in the Windows 10 environment, and the computer's RAM is 16G. This paper uses the following parameters to set up the U-Net network: learning rate = 1e-4, batch size = 1 and training epoch = 100.

Evaluation Index

Currently, most of the image evaluation methods are widely used in the fields of medicine and computer vision, and have the characteristics of high accuracy (Huang et al., 2018; Sudan et al., 2019; Kromp et al., 2021). This paper uses DSC, VOE and RVD evaluation indicators to evaluate the segmentation effect of the model (Dash et al., 2019; Liu et al., 2019). DSC is used to evaluate the consistency between the segmentation results and the real results, and is defined as follows:

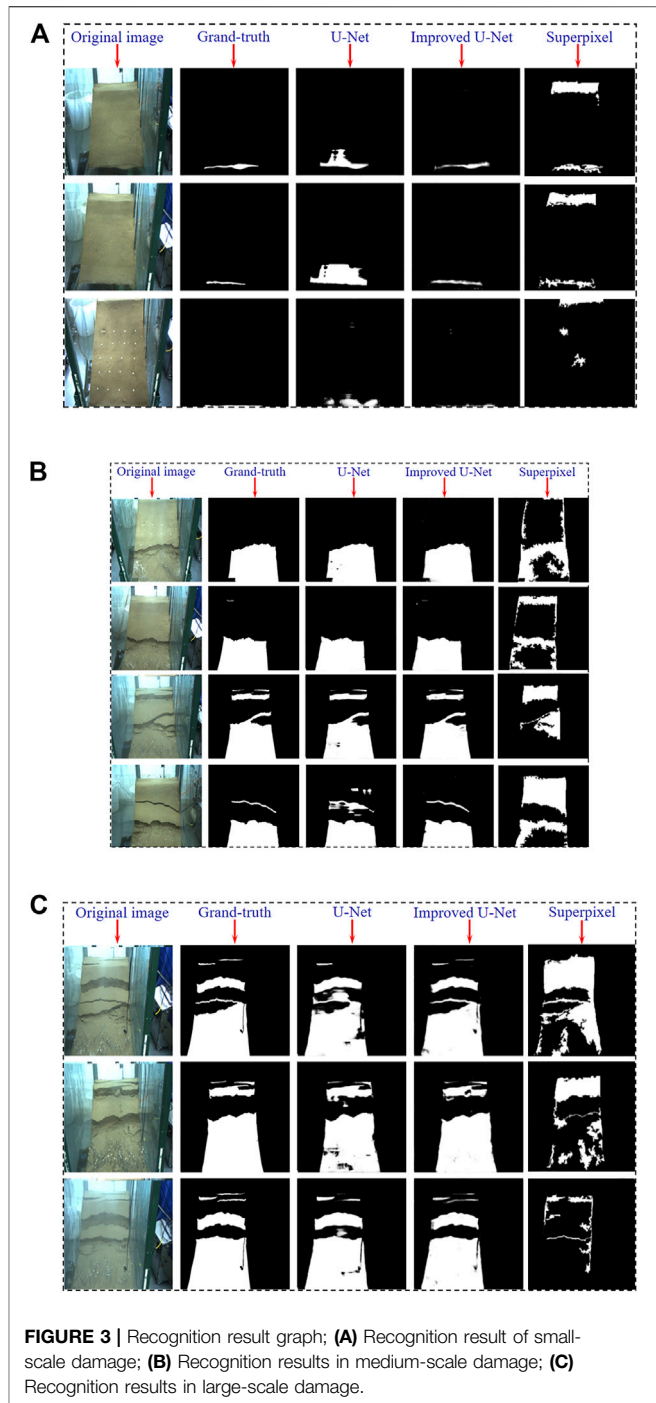


FIGURE 3 | Recognition result graph; (A) Recognition result of small-scale damage; (B) Recognition results in medium-scale damage; (C) Recognition results in large-scale damage.

$$DSC(G, P) = \frac{2|G \cap P|}{|G| + |P|} \quad (3-1)$$

The VOE calculation method is as follows:

$$VOE(G, P) = 1 - \frac{|G \cap P|}{|G \cup P|} \quad (3-2)$$

The RVD is defined as follows:

$$RVD(G, P) = \frac{|P| - |G|}{|G|} \quad (3-3)$$

Among them, *DSC* represents the Dice Similarity Coefficient, *VOE* represents the Volumetric Overlap Error, *RVD* represents the Relative Volume Difference, *G* represents the real result and *P* represents the algorithm segmentation result. The closer *DSC* is 1, the better the segmentation result. The closer *VOE* and *RVD* is 0, the better the segmentation result.

RESULTS

To verify the effectiveness of the proposed method, the proposed method is compared with the original U-Net network and the mainstream landslide deformation region segmentation superpixel algorithm, and the evaluation coefficients *DSC*, *VOE*, and *RVD* mentioned above are used to evaluate the segmentation results.

In this study, three small-scale landslide damage images, four medium-scale landslide damage images, and three large-scale landslide damage images at different times during training are randomly selected. The results of the three algorithms in the task of identifying small-scale landslide damage are shown in **Figure 3A**. It can be found that the performance of the improved U-Net model is better than that of the original U-Net and superpixel algorithm; The original U-Net model misidentifies the large non-destructive area as the destructive area, while the superpixel algorithm fails to distinguish the deformation area of landslide well. **Figure 3B** shows the results of the three algorithms in the identification of mesoscale landslide damage areas. Both the U-Net and the improved U-Net algorithms can well identify the damaged area in the landslide. However, the original U-Net method is easy to lose information in some subtle places, and it is easy to cause misrecognition at the edge of the damaged area. The superpixel algorithm can hardly identify the landslide deformation area. To comprehensively analyze and compare the performance of the three algorithms, this paper adds a landslide with a larger damage area to test the algorithm. **Figure 3C** shows that the U-Net model has obvious misrecognition and missed recognition in the identification of large-scale landslide damage areas, and the improved U-Net model still has a good performance. The traditional landslide deformation area recognition algorithm still does not perform well. The specific data is described below.

When small-scale deformation of the landslide occurs, the *DSC* evaluation indexes of U-Net, Superpixel and Improved U-Net are respectively: 0.953, 0.335, 0.978; *VOE* evaluation indexes are: 0.088, 0.775, 0.043; *RVD* evaluation indexes are: 0.066, 0.495, 0.032. When a medium-scale deformation of a landslide occurs, the *DSC* evaluation indexes of U-Net, Superpixel and Improved U-Net are respectively: 0.871, 0.433, 0.893; *VOE* evaluation indexes are: 0.084, 0.435, 0.076; *RVD* evaluation indexes are: 0.089, 0.376, 0.081. When large-scale deformation of the landslide occurs, the *DSC* evaluation indicators of U-Net, Superpixel and Improved U-Net are respectively: 0.933, 0.335, 0.958; *VOE* evaluation indicators are: 0.031, 0.775, 0.021; *RVD* evaluation indicators are: 0.032, 0.495, 0.020.

DISCUSSION

Highlights of Improved U-Net Model

The improved U-Net model is better than the original U-Net and superpixel algorithm. The reason why the superpixel algorithm performs poorly in the large, medium and small-scale destruction is that the algorithm cannot adapt to images with complex backgrounds, and this is the advantage of the deep learning algorithm. In the *DSC* evaluation index, both U-Net and the improved U-Net model have high indicators. This method uses a large sample training set to automatically and continuously identify and extract deformation features in time series from different deformation scales, the recognition accuracy is high and the robustness is strong under complex environmental conditions.

Limitations and Outlook

In our study, we automatically identify the landslide physical model with relatively simple material particle size in the time series. For some landslide scenarios with complicated background and disordered particle size (such as mine excavation, tailings dam etc.) identification has not been studied yet. In the future, automatic identification of landslide deformation areas in complex environments will be a major trend.

CONCLUSION

The improved U-Net fully convolutional neural network is used to automatically identify and extract the deformation characteristics of the landslide time series. Some conclusions have been drawn:

- 1) The increase in depth of the neural network and the introduction of the spatial convolution kernel can effectively extract deep deformation features and retain more local deformation details.
- 2) In a large-capacity training set, the improved U-Net method has a good batch recognition processing effect.
- 3) Under the situation of multi-scale landslide damage, three different evaluation indicators verify that the improved U-Net method has higher recognition accuracy and stronger robustness than the U-Net method and the superpixel method.

DATA AVAILABILITY STATEMENT

The raw data supporting the conclusion of this article will be made available by the authors, without undue reservation.

AUTHOR CONTRIBUTIONS

Drafting of article: BD and SL; planning and supervision of the research: YW; analysis and interpretation of data: CY and QL; acquisition of data: CY; Model construction: YL.

FUNDING

The work was supported by the National Natural Science Foundation of China (No.51874268), Major science and technology projects of

Anhui Province (No.202003a0702002), Fujian Transportation Science and Technology Project (No. 201911) and South Taihu Elite Plan Innovation Team Project of Huzhou city.

ACKNOWLEDGMENTS

We gratefully acknowledge the funding provided by the National Natural Science Foundation of China

REFERENCES

- Ardizzone, F., Cardinali, M., Galli, M., Guzzetti, F., and Reichenbach, P. (2007). Identification and Mapping of Recent Rainfall-Induced Landslides Using Elevation Data Collected by Airborne Lidar. *Nat. Hazards Earth Syst. Sci.* 7 (6), 637–650. doi:10.5194/nhess-7-637-2007
- Bui, T. A., Lee, P. J., Lum, K. Y., Loh, C., and Tan, A. K. (2020). Deep Learning for Landslide Recognition in Satellite Architecture. *IEEE Access* 8, 143665–143678. doi:10.1109/ACCESS.2020.3014305
- Chen, Yu., Wei, Y., Wang, Q., Chen, F., Lu, C., and Lei, S. (2020). Mapping Post-Earthquake Landslide Susceptibility: A U-Net like Approach. *Remote Sensing* 12 (17), 2767. doi:10.3390/rs12172767
- Cheng, G., Guo, L., Zhao, T., Han, J., Li, H., and Fang, J. (2013). Automatic Landslide Detection from Remote-Sensing Imagery Using a Scene Classification Method Based on boVW and pLSA. *Int. J. Remote Sensing* 34 (1), 45–59. doi:10.1080/01431161.2012.705443
- Dash, M., Londhe, N. D., Ghosh, S., Semwal, A., and Sonawane, R. S. (2019). PsLSNet: Automated Psoriasis Skin Lesion Segmentation Using Modified U-Net-Based Fully Convolutional Network. *Biomed. Signal Process. Control.* 52, 226–237. doi:10.1016/j.bspc.2019.04.002
- Ghorbanzadeh, O., Alessandro, C., Pedram, G., Hejar, S., and Blaschke, T. (2021). A Comprehensive Transferability Evaluation of U-Net and ResU-Net for Landslide Detection from Sentinel-2 Data (Case Study Areas from Taiwan, China, and Japan). *Scientific Rep.* 11 (1), 14629. doi:10.1038/S41598-021-94190-9
- Guzzetti, F., Cardinali, M., and Reichenbach, P. (1994). The AVI Project: A Bibliographical and Archive Inventory of Landslides and Floods in Italy. *Environ. Manage.* 18 (4), 623–633. doi:10.1007/BF02400865
- Hashiba, H., and Sonobe, M. (2020). Extraction of Scattered Small-Scale Landslides Distribution by Object-Based Classification Using Optical High-Resolution Satellite Images. *Int. Arch. Photogramm. Remote Sens. Spat. Inf. Sci.* XLIII-B3, 1213–1218. doi:10.5194/isprs-archives-XLIII-B3-2020-1213-2020
- He, K., Zhang, X., Ren, S., and Sun, J. (2015). “Deep Residual Learning for Image Recognition,” in 2016 IEEE Conference on Computer Vision and Pattern Recognition (CVPR), Las Vegas, NV, June 27–30, 2016, 770–778. doi:10.1109/CVPR.2016.90
- Huang, Q., Sun, J. F., Ding, H., Wang, X. D., and Wang, G. Z. (2018). Robust Liver Vessel Extraction Using 3D U-Net with Variant Dice Loss Function. *Comp. Biol. Med.* 101, 153–162. doi:10.1016/j.compbiomed.2018.08.018
- Kromp, F., Fischer, L., Bozsaky, E., Ambros, I. M., Dorr, W., Beiske, K., et al. (2021). Evaluation of Deep Learning Architectures for Complex Immunofluorescence Nuclear Image Segmentation. *IEEE Trans. Med. Imaging* 40, 1934. doi:10.1109/TMI.2021.3069558
- Kurtz, C., Stumpf, A., Malet, J. P., and Gancarski, P. (2014). Hierarchical Extraction of Landslides from Multiresolution Remotely Sensed Optical Images. *ISPRS J. Photogramm. Remote Sens.* 87, 122–136. doi:10.1016/j.isprsjprs.2013.11.003
- Lee, C. F., Huang, W. K., Chang, Y. L., and Chi, S. Y. (2018). Regional Landslide Susceptibility Assessment Using Multi-Stage Remote Sensing Data along the Coastal Range Highway in Northeastern Taiwan. *Geomorphology* 300, 113–127. doi:10.1016/j.geomorph.2017.10.019
- Lee, S., Ryu, J. H., Lee, M. J., and Won, J. S. (2006). The Application of Artificial Neural Networks to Landslide Susceptibility Mapping at Janghung, Korea. *Math. Geol.* 38 (2), 199–220. doi:10.1007/s11004-005-9012-x
- Lee, S., Zhao, Y., Mohamed, M., and Belkasim, S. (2020). Quantitative Spatial Analysis on Whole Slide Images Using U-Net. *Comput. Biol. Bioinformatics* 8 (2), 90–96. doi:10.11648/J.CBB.20200802.18
- (No.51874268), Major science and technology projects of Anhui Province (No.202003a0702002), Fujian Transportation Science and Technology Project (No. 201911) and South Taihu Elite Plan Innovation Team Project of Huzhou city. We also thank CY and QL for their assistance in the test. Finally, we would like to thank the handling editor and reviewers whose valuable and constructive comments greatly improved this article.
- Li, C., Zhong, W., Luo, J., Xiao, C. B., Song, S. L., and Wang, J. (2020). Test Study on Rainfall Infiltration Law and Failure. *Model. Waste Rare Earth Tailings* 529, 66–74. doi:10.19614/j.cnki.jsks.202007010
- Li, X., Peng, K., Peng, J., and Hou, D. (2021a). Experimental Investigation of Cyclic Wetting-Drying Effect on Mechanical Behavior of a Medium-Grained sandstone. *Eng. Geol.* 293, 106335. doi:10.1016/j.enggeo.2021.106335
- Li, X. S., Peng, K., Peng, J., and Hou, D. (2021b). Effect of thermal Damage on Mechanical Behavior of a fine-grained sandstone. *Arabian J. Geosci.* 14, 1212. doi:10.1007/s12517-021-07607-0
- Liu, Z., Song, Y. Q., Sheng, V. S., Wang, L., Jiang, R., Zhang, X., et al. (2019). Liver CT Sequence Segmentation Based with Improved U-Net and Graph Cut. *Expert Syst. Appl.* 126 (JUL), 54–63. doi:10.1016/j.eswa.2019.01.055
- Malamud, B. D., Turcotte, D. L., Guzzetti, F., and Reichenbach, P. (2004). Landslide Inventories and Their Statistical Properties. *Earth Surf. Process. Landforms* 29 (6), 687–711. doi:10.1002/esp.1064
- Mwaniki, M. W., Kuria, D. N., Boitt, M. K., and Ngigi, T. G. (2017). Image Enhancements of Landsat 8 (OLI) and SAR Data for Preliminary Landslide Identification and Mapping Applied to the central Region of Kenya. *Geomorphology* 282, 162–175. doi:10.1016/j.geomorph.2017.01.015
- Ronneberger, O., Fischer, P., and Brox, T. (2015). U-net: Convolutional Networks for Biomedical Image Segmentation. *Int. Conf. Med. Image Comput. Comput. Assisted Intervention* 9351, 234–241. doi:10.1007/978-3-319-24574-4_28
- Shahabi, H., Ahmad, B. B., and Khezri, S. (2013). Evaluation and Comparison of Bivariate and Multivariate Statistical Methods for Landslide Susceptibility Mapping (Case Study: Zab basin). *Arabian J. Geosci.* 6 (10), 3885–3907. doi:10.1007/s12517-012-0650-2
- Shi, W. Z., Zhang, M., Ke, H. F., Fang, X., Zhan, Z., and Chen, S. X. (2020). Landslide Recognition by Deep Convolutional Neural Network and Change Detection. *IEEE Trans. Geosci. Remote Sensing* 59, 1–19. doi:10.1109/TGRS.2020.3015826
- Shirzadi, A., Shahabi, H., and Chapi, K. (2017). A Comparative Study between Popular Statistical and Machine Learning Methods for Simulating Volume of Landslides. *Catena* 157, 213–226. doi:10.1016/j.catena.2017.05.016
- Sudan, J., Son, L. H., Kumar, R., and Priyadarshini, I. (2019). Neutrosophic Image Segmentation with Dice Coefficients. *Measurement* 134, 762–772. doi:10.1016/j.measurement.2018.11.006
- Tang, H. M., Crosta, G. B., and Wang, F. W. (2014). Special Issue on “advances in Engineering Geology for Landslides and Slope Stability Problems: Part I. *Eng. Geol.* 182, 1–2. doi:10.1016/j.enggeo.2014.10.014
- Wang, Y. J., Hu, S. Y., Wang, G. D., Chen, C. L. Z., and Pan, Z. K. (2016). Multi-scale Dilated Convolution of Convolutional Neural Network for Crowd Counting. *Multimedia Tool Appl.* 79 (1-2), 1057–1073. doi:10.1007/s11042-019-08208-6
- Xie, T., Huang, J. J., Shi, Q. Z., Wang, Q., and Yuan, N. (2019). PSDSD-A Superpixel Generating Method Based on Pixel Saliency Difference and Spatial Distance for SAR Images. *Sensors (Basel)* 19 (2), 304. doi:10.3390/s19020304
- Yang, Y., Song, S. L., Yue, F. C., He, W., Shao, W., and Zhao, K. (2019). Superpixel-based Automatic Image Recognition for Landslide Deformation Areas. *Eng. Geol.* 259, 105166. doi:10.1016/j.enggeo.2019.105166
- Zhang, C. Y., Wang, Y. X., and Jiang, T. T. (2020). The Propagation Mechanism of an Oblique Straight Crack in a Rock Sample and the Effect of Osmotic Pressure under In-Plane Biaxial Compression. *Arabian J. Geosci.* 13 (15), 736. doi:10.1007/s12517-020-05682-3
- Zhang, Q. G., Huang, R. Q., Liu, Y. X., Su, X. P., Li, G. Q., and Nie, W. (2016). A Physically-Based Geometry Model for Transport Distance Estimation of

Rainfall-Eroded Soil Sediment. *Appl. Sci. (Switzerland)* 6 (2), 34. doi:10.3390/app6020034

Zhu, S., Cao, D., Wu, Y., and Shixiong, J. (2016). Improved Accuracy of Superpixel Segmentation by Region Merging Method. *Front. Optoelectron.* 9 (4), 633–639. doi:10.1007/s12200-015-0482-2

Conflict of Interest: Author SL was employed by the company Zhejiang Zhipu Engineering Technology Corporation Limited.

The remaining authors declare that the research was conducted in the absence of any commercial or financial relationships that could be construed as a potential conflict of interest.

Publisher's Note: All claims expressed in this article are solely those of the authors and do not necessarily represent those of their affiliated organizations, or those of the publisher, the editors, and the reviewers. Any product that may be evaluated in this article, or claim that may be made by its manufacturer, is not guaranteed or endorsed by the publisher.

Copyright © 2021 Dai, Wang, Ye, Li, Yuan, Lu and Li. This is an open-access article distributed under the terms of the Creative Commons Attribution License (CC BY). The use, distribution or reproduction in other forums is permitted, provided the original author(s) and the copyright owner(s) are credited and that the original publication in this journal is cited, in accordance with accepted academic practice. No use, distribution or reproduction is permitted which does not comply with these terms.



Prediction and Treatment of Water Leakage Risk Caused by the Dynamic Evolution of Ground Fissures in Gully Terrain

Dong Feng^{1,2*}, Enke Hou^{1,2*}, Xiaoshen Xie^{1,2}, Xiaoyang Che^{1,2}, Pengfei Hou^{1,2} and Tianwen Long^{1,2}

¹College of Geology and Environment, Xi'an University of Science and Technology, Xi'an, China, ²Shaanxi Provincial Key Laboratory of Geological Support for Coal Green Exploitation, Xi'an, China

OPEN ACCESS

Edited by:

Wen Nie,
Jiangxi University of Science and
Technology, China

Reviewed by:

Baoqin Lian,
Northwest University, China
Li Xinyan,
East China University of Technology,
China
Jian Cao,
Inner Mongolia University of Science
and Technology, China

*Correspondence:

Dong Feng
zyfd20180619@163.com
Enke Hou
houek@xust.edu.cn

Specialty section:

This article was submitted to
Geohazards and Georisks,
a section of the journal
Frontiers in Earth Science

Received: 28 October 2021

Accepted: 01 December 2021

Published: 03 January 2022

Citation:

Feng D, Hou E, Xie X, Che X, Hou P
and Long T (2022) Prediction and
Treatment of Water Leakage Risk
Caused by the Dynamic Evolution of
Ground Fissures in Gully Terrain.
Front. Earth Sci. 9:803721.
doi: 10.3389/feart.2021.803721

Groundwater leakage in the loess gully terrain is one of the main hazards of coal seam mining at shallow burial depth. The burial depth of the 5⁻² coal seam is less than 50 m from the ground in the gully of the study site. The fissures that expand upward after mining can easily penetrate the ground to form a water-conducting channels. During rainy periods, there is a potential risk of groundwater leakage. In order to reveal the characteristics of plane development and the dynamic evolution of gully ground fissures, the typical U-shaped gully in the northern Shaanxi coal mine was studied using the field measurement methods of “On-site measurement” and UAV aerial photography. Based on the experimental platform of ground fissure leakage developed and designed by the team, an indoor test model corresponding to the actual situation was established. In addition, the mathematical models of actual flood inrush, fissure width, and flood flow in the channel were established. The actual mine water flow and the mine drainage capacity were compared and analyzed, thus proposing criteria for classifying gully mining ground fissure collapsed water hazards. These criteria can provide theoretical references for predicting fissure leakage hazard zones in the ground gully of shallow buried coal seams. According to the development height of the water-conducting fissure zone (WCFZ), the treatment methods of ground fissures in gullies under different security conditions were designed, which was applied in the field with good results. The results showed that the treatment methods in this paper could effectively prevent the leakage of groundwater in the gullies along the ground fissures.

Keywords: gully leakage, leakage experiment, surface fissure management, water leakage risk, gully terrain

INTRODUCTION

Coal resources are the main resource of China. Coal production in western China accounts for about 65% of the total production in China (Zhuo et al., 2018). In recent years, China has vigorously promoted the construction of large coal bases in the west. Effective development of coal resources in the west is an important guarantee for the energy needs of China. The land subsidence caused by coal mining leads to environmental damage and affects the normal land application (Chen et al., 2020).

Coal resources of the Jurassic coal fields in northern Shaanxi are characterized by shallow burial and thin overlying bedrock (Huang, 2005; Huang 2009). Under geological conditions of the loess gully (Zhang et al., 2019; Lian et al., 2020; Duan et al., 2021), after the coal seam is retrieved, the top cover generally collapses as a whole due to the relatively simple structure of the overlying bedrock, making the WCFZ directly reach the ground (Liu et al., 2017; Prakash et al., 2018). Subsequently, the zone becomes a channel and pathway for groundwater to flow into the mining area (Wang et al., 2016; Zhang et al., 2015). After coal seam retrieval, the terrain of loess gully above the shallow buried coal seam can cause groundwater in the gully to leak downhole when mining the coal below and to the side, resulting in a severe threat of water leakage (Zhang et al., 2010; Ju and Xu, 2015; Hou et al., 2019; Yang et al., 2019). Therefore, mine water hazard control is still an important task in coal mine safety.

Xie et al. (2021) studied the formation mechanism and development height of hydraulic conductivity fissure zone in coal seam mining by field measurement. Yang et al. (2012) mastered the relationship between ground fissures and the progress of pushing mining and measured the amount of ground subsidence by establishing ground observation stations. Li et al. (2017) revealed that the ground fissures in the wind-deposited sand area had “M” type dynamic development characteristics with the self-healing characteristics of rapid closure. Some scholars predicted the development height of the WCFZ in coal seam retrieval by numerical simulation. In addition, scholars predicted the risk of groundwater leakage in the mining area by comparing the development height of the “two zones” with the burial depth of the coal seam roof (Zhang et al., 2012; Zhu et al., 2014). In recent years, the mining-induced fissures in coal seams and their water leakage problems have been studied from different perspectives (Ma et al., 2013; Xu et al., 2019; Hu and Zhao, 2021). However, only few quantitative analyses have been conducted to study the water leakage caused by mining ground fissures in shallow buried coal seam gullies and the risk of water hazards caused by leakage.

In order to solve the hazard of ground water leakage caused by shallow buried coal seam mining in western China, the dangerous degree of ground water leakage from shallow buried coal seams was calculated by the self-developed and designed water leakage test platform and based on the characteristics of ground fissure development in the field investigation. Through this study, some theoretical references can be provided for preventing and controlling water hazards from gully leakage in shallow buried coal seam overburden mining.

BACKGROUND

The study site is located in Fugu County, Yulin City, in the northeast corner of the Shenfu mining area of the Jurassic coalfield in northern Shaanxi Province. The study site is cut gully erosion, and the gullies are developed in different directions, showing a loess gully landscape. The study site is located in the

interior of western China. The rainfall is mainly concentrated in July to September, accounting for 64% of the total annual rainfall, especially the most in July, with an average of 128.48 mm, accounting for 25.56% of the total annual rainfall. The high frequency of heavy rainfall is likely to cause floods and other geological hazards.

Figure 1 shows the specific location of working faces 125203, 125205, and 125207 in the study site. The above working faces are located in the west-central part of the mine, diagonally crossing the gully, at an angle of orientation approximately 45° to the direction of the gully. The gully is seasonally flowing, and the bedrock is exposed in the lower part of the gully. The bedrock is mainly covered by the Neoproterozoic laterite and Quaternary loess above the bedrock. The average mining height of the above working faces is 2.31 m, and the comprehensive mechanized coal mining process is used for recovery. In the bottom area of the gully, the burial depth of the 5⁻² coal seam is about 20–35 m. **Figure 2** shows the over-gully profile of the working face in the study site.

METHODS AND MATERIALS

A hazard zoning prediction of gully leakage in shallow buried coal seam was proposed using the experimental platform of ground gully fissure leakage independently developed and designed by the team. The specific process of the proposed prediction method is shown in **Figure 3** and is divided into five steps.

First step: UAV remote sensing technology was used to largely map the ground fissure characteristics of the typical working face retrieved in the study site, so as to grasp the characteristics of ground fissure development in the gully. Through on-site measurement, its plane spreading pattern and dynamic full development process are mastered.

Second step: The flood flow of the main channel in the study site was obtained through the field measurement of the overwater cross-section, the height of the flood level scour line, the channel development characteristics, and the formula calculation method.

Third step: The relationship between gully flood leakage, gully fissure width, and gully flood flow was simulated by converting the similar ratio between indoor experiments and actual geological conditions in the study site using the above-mentioned platform. The amount of gully flood leakage can be determined by observing water leakage at different flow rates and fissure widths.

Fourth step: After establishing the criteria for classifying gully flooding hazards, the prediction results of different gully water leakage hazards were obtained by comparing the current situation of mine water gushing and the drainage capacity of the mine drainage system.

Fifth step: Based on the prediction of gully leakage hazard, bubble fissure safety zoning, and ground land type, different treatment methods of ground gully fissures were proposed.

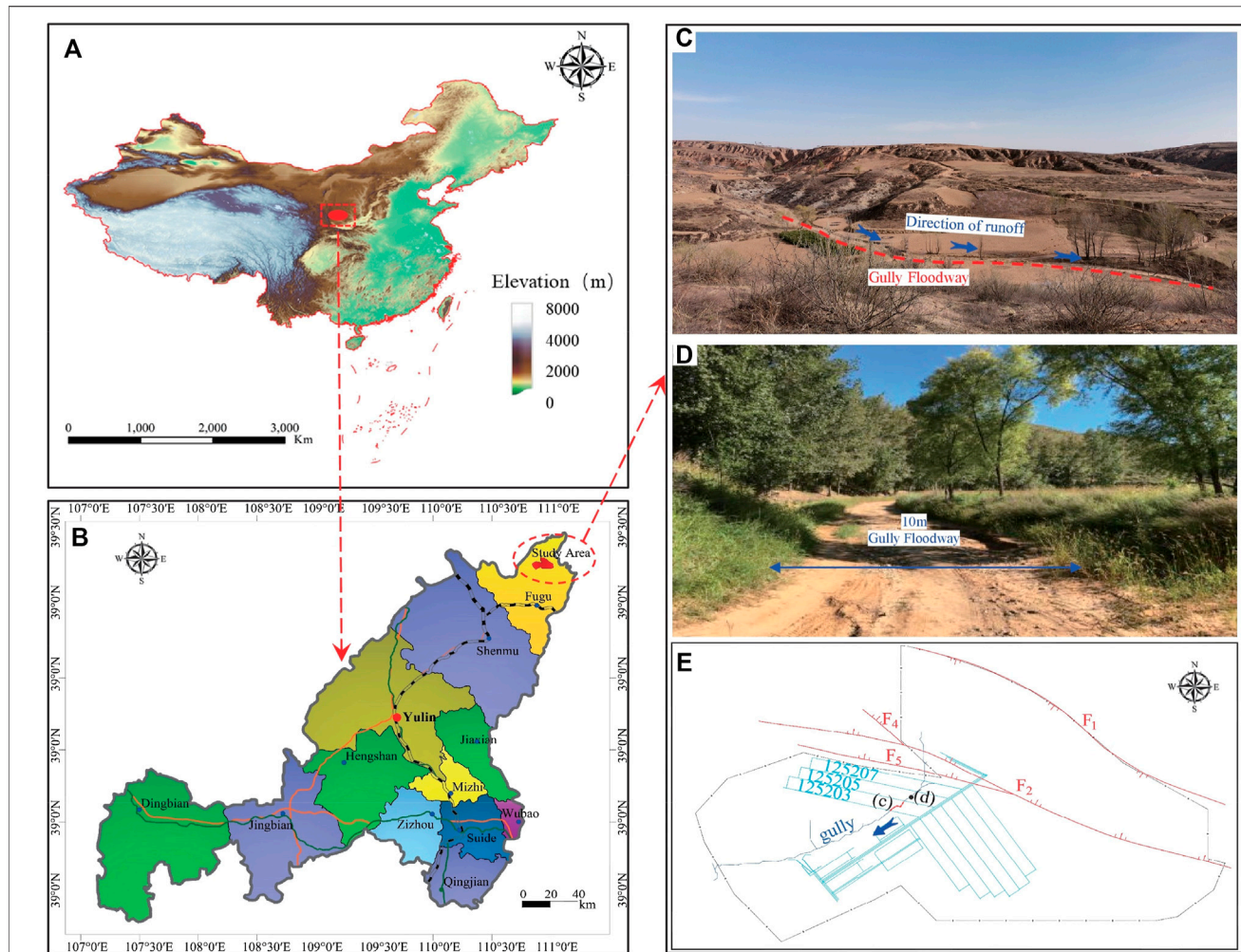


FIGURE 1 | Location and topography of the working face in the study site. **(A)** Location of study area in China; **(B)** Location of study area in Yulin, China; **(C)** Site map of gully morphology; **(D)** Site map of gully floodway.

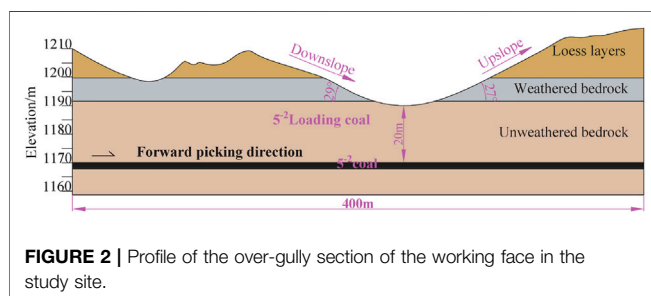


FIGURE 2 | Profile of the over-gully section of the working face in the study site.

CHARACTERISTICS OF GROUND FISSURE DEVELOPMENT

According to the actual production plan of the mine, the scope of the field investigation is the gully section of 125203 working face retrieval. By applying UAV remote sensing technology and actual on-site measurements, the dynamic development

pattern of ground fissures and the development characteristics of the ground fissure plane, including the development number, location, and the development width of ground fissures, are shown.

Development Characteristics of the Ground Fissure

The dynamic development of the fissures at the bottom of the gully in the study site from the initial appearance to the stable development stage was measured in the field. **Figure 4** shows the whole process of the dynamic changes of 10 typical ground fissures in the gully area of the 125203 working face. The ground fissures cannot be completely closed during the whole stage of “initial appearance → maximum development width → stable.” The whole development cycle is about 5 days.

By fitting the maximum width to the stable width, the linear positive correlation function is satisfied. The fitted curve equation is shown in **Figure 5**. The specific fitted linear

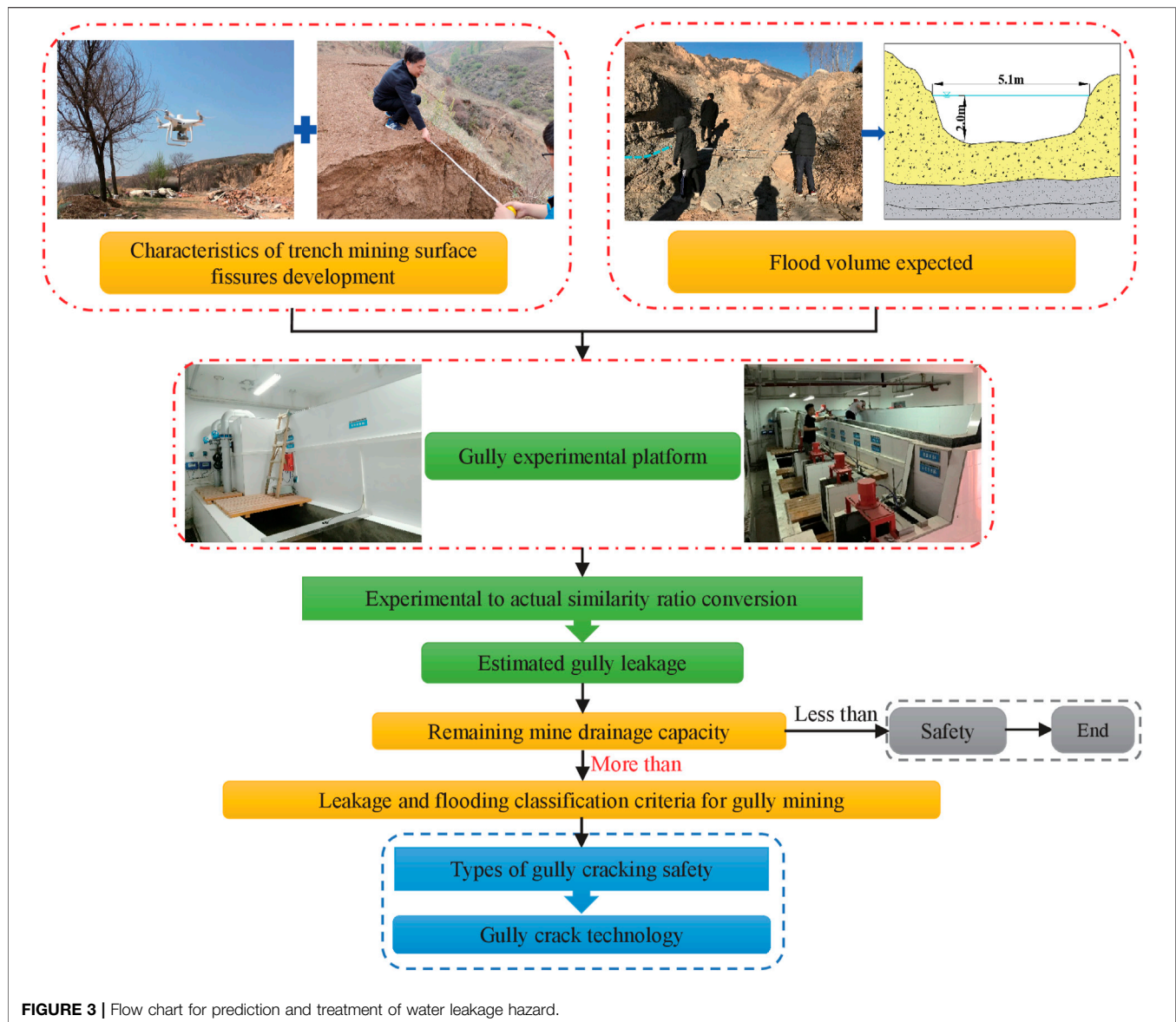


FIGURE 3 | Flow chart for prediction and treatment of water leakage hazard.

regression model equation is $Width_{stab} = 0.57816 \times Width_{max} - 0.3441$, $R^2 = 0.9809$.

The ground fissures in the gully cannot be completely closed during the whole stage of “initial appearance → maximum width of development → stability.” According to the development characteristics of ground fissures, the treatment of ground fissures must be conducted at the end of the gully in the working face to avoid the potential risk of water leakage in the mine gully.

Dynamic Evolutionary Characteristics of Ground Fissures

After completing over-gully retrieval of 125203 working faces and the dynamic evolution of ground fissures, the stable width of ground fissures in parallel open-off cut at the bottom of the gully in the study site was measured again on May 8, 2020. A total of 50 ground fissures

were investigated. Among these fissures, 3 of them have a width less than 5 cm, accounting for 64%; 10 of them have the width of 5–10 cm, accounting for 20%; 5 of them are 10–20 cm in width, accounting for 10%; 3 have a width greater than 20 cm, accounting for 6% (**Figure 6**).

Prediction of Ground Fissures in the Area to be Mined

The geological conditions of working faces 12503, 125205, and 125207 in the study site are the same through field exploration near the working faces and drilling exploration in the vicinity of the study site. The development of ground fissures in the gully when the over-gully section of 125203 working face was retrieved from the site showed that about 100 ground fissures were generated in the over-gully section after 125203 working face was retrieved (**Figure 4A**), and the length of the over-gully section reached about 450 m within

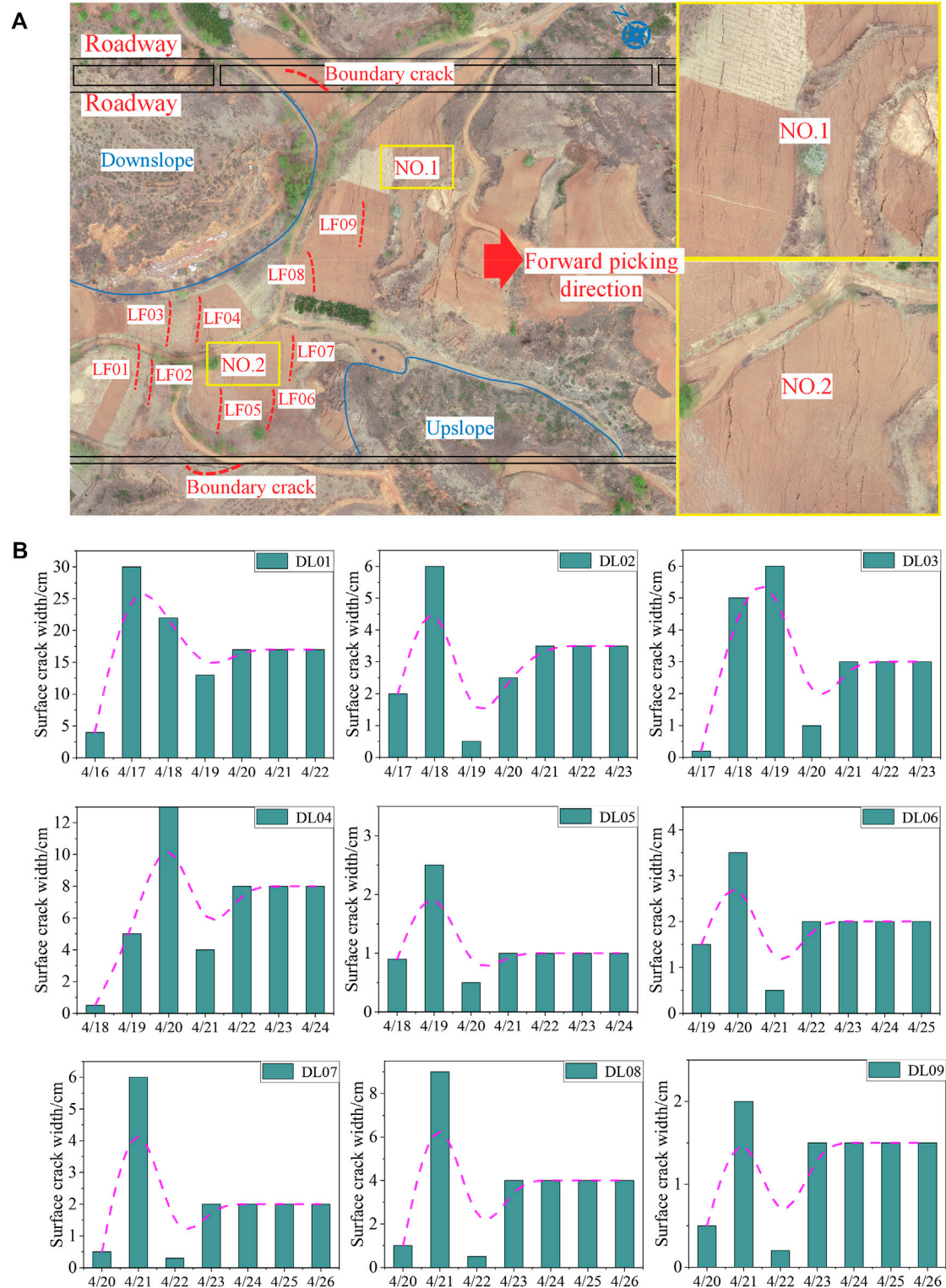
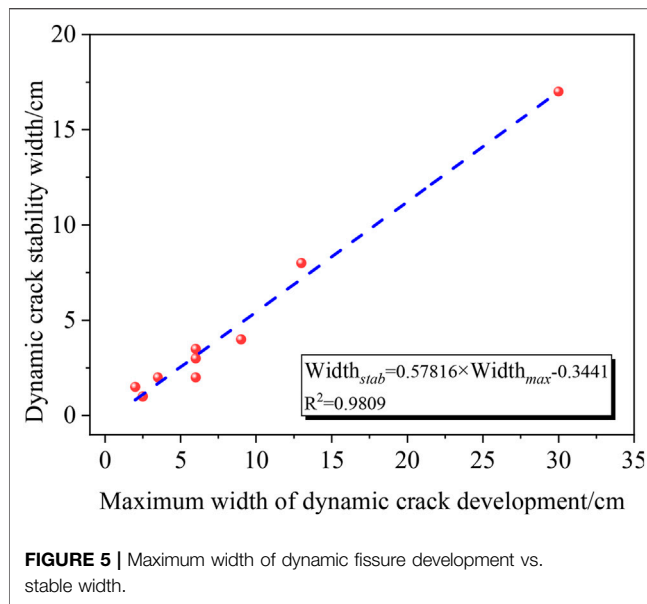


FIGURE 4 | Aerial photography and actual measurement of ground fissures on site: **(A)** Aerial photograph of ground fissures after retrieval; **(B)** Dynamic development characteristics of ground fissures in the gully.



the 125203 working face. The ground fissures after gulying in the 125205 and 125207 working faces were compared and analogously analyzed. The length of the gulying section in the 125205 working face was about 400 m, and the length of the gulying section in the 125207 working faces was about 300 m. The analogous analysis of ground fissure number in different widths in the 125203 working face showed that about 90 ground fissures were generated after the over-gulying in working face 125205, and 68 ground fissures were generated after the over-gulying in working face 125207.

THE HAZARD PREDICTION OF GULLY WATER LEAKAGE

Whether the groundwater of the gully during the rainy season causes water hazards in the mine requires the following three conditions:

TABLE 1 | Results of gully flood flow calculation.

Region	Watershed area (km ²)	Q _{B5%} (m ³ /s)
125203 working face	4.02	10.48
125205 working face	3.05	8.54
125207 working face	2.59	7.56

- 1) Whether there is a river on the ground, or whether there will be rainfall when the surface cracks occur.
- 2) Whether groundwater routing channels can be formed after the coal seam is retrieved.
- 3) Whether the amount of groundwater flowing from the gully into the underground mining area during rainfall (Q_{re-dr}) is greater than the remaining drainage capacity of the mine drainage system (B_q —the difference between the mine drainage capacity and the normal mine surge).

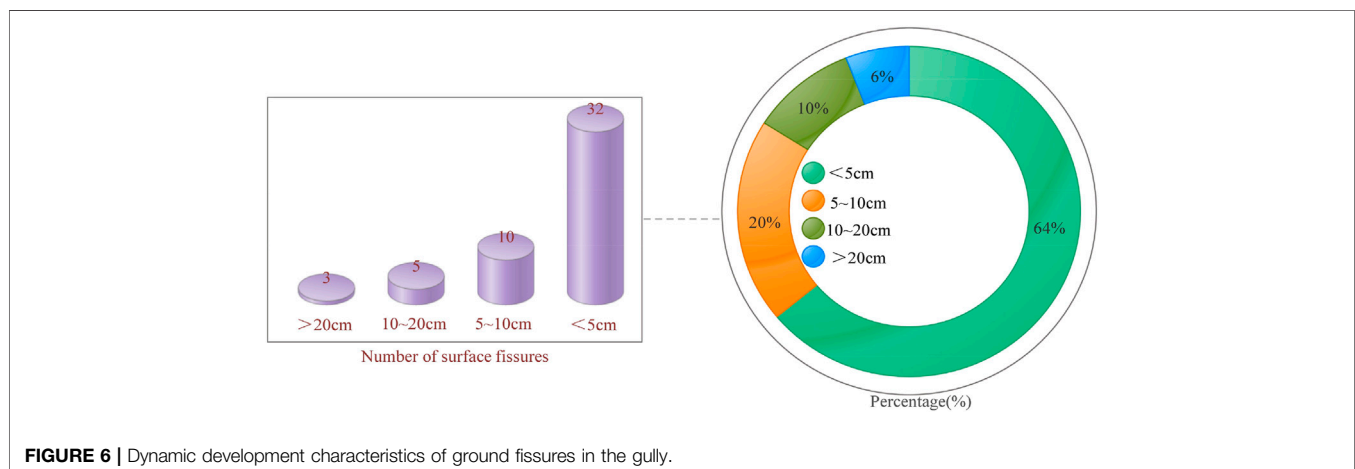
The Main Control Factors of Groundwater Leakage and the Identification Method Gully Flood Volume Estimation

Combining the rainfall characteristics of the study site, the 5-year flood flows for the study site watersheds were calculated using the formula for flood flows in small watersheds applicable to the study site:

$$Q_{5\%} = 0.009F^{0.742}J^{0.324}H_{6P}^{1.301} \quad (1)$$

where $Q_{5\%}$ represents the 5-year flood flow (m³/s); F represents the designed watershed area (km²); J represents the average specific drop in the main channel (‰), $J = 11.49\text{‰}$ (measured on topographic and geological maps); H_{6P} represents the duration of rainstorms with a design frequency of 6 h (mm), based on *Yulin Hydrology Manual*, $H_{6P} = 56$ mm.

The results of the 5-year flood flow calculation for each working face in the study site are shown in **Table 1**.



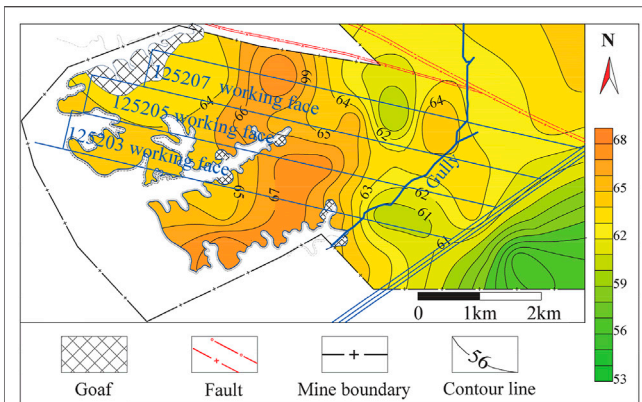


FIGURE 7 | The contour map of 5^{-2} WCFZ development.

Routing Channel Discrimination of Ground Gully

In the vertical direction, whether the ground fissure in the study site becomes a channel of water collapse affecting mine safety production can be determined by comparing the difference in the burial depth of coal seam (D_m) and the development height of the WCFZ (H_{WCFZ}) after coal seam retrieval. If $D_m - H_{WCFZ} < 0$, the ground fissure will penetrate the surface and become a channel and path for groundwater to flow into the mining area.

Based on the statistical results of the development height of the “three zones” in the shallow buried coal seam in Yushen mining area, Wang et al. (2020) suggested that the development range of the upstream fissure zone should be selected according to the fissure mining ratio of 18–28 times.

According to the geological conditions of the study site and many previous studies (Fan et al., 2019), the guide height of the comprehensive mining working face is generally 21–30 times the mining height, about 26 times on average. The riser height is generally 2.12–6.97 times the mining height, about 5 times on average.

Based on the statistical results of the development height of the “three zones” in the shallow buried coal seam in the Yushen mining area (Fan et al., 2019; Wang et al., 2020), the height of WCFZ is generally 21–30 times of the mining height, about 26.5 times on average, and the height of FZ is generally 2.12–6.97 times of the mining height, about 5 times on average.

In this study, WCFZ of the comprehensive mining working face is selected 26.5 times the mining height, and FZ of the comprehensive mining working face is selected 5 times the mining height.

$$H_{FZ} = 5H_m \quad (2)$$

where H_m is the coal seam mining height and H_{FZ} is the height of the FZ.

$$H_{WCFZ} = 26.5H_m \quad (3)$$

where H_m is the coal seam mining height and H_{WCFZ} is the height of WCFZ.

Figure 7 shows the contour map of the development height of the WCFZ of 5^{-2} coal seam.

Gully Fissure Leakage Experiment

According to the site survey, the actual width of the bottom of the gully is 10 m, and the bottom of the leakage gully in the experiment is 0.4 m. Therefore, the determined model ratio with the corresponding geometric ratio is 25:1.

In order to improve the safety of conversion according to the proportional model, the ground fissure width developed in each interval section was calculated according to the maximum width of the fissure in that section when calculating the gully leakage. Due to the limited experimental conditions, ground fissures with a width less than 20 cm were calculated using 50 cm as the maximum limit value to obtain the gully fissure width values required for the experiment (**Table 2**).

By simulation experiments, the leakage amounts with ground fissure width of 0.2, 0.4, 0.8, and 2.0 cm and the leakage amount of gully with different flood flows and different experimental widths were obtained (**Table 3**).

The experimental data on gully leakage of ground fissures of different widths and water flows were compiled and analyzed. In this way, the relationship between the total water volume of a single ground fissure that is not of the same width and the amount of gully leakage was obtained. The regression relationship is shown in **Figure 8**.

The above relationship shows that the overall positive correlation trend between gully leakage and total gully water. The geometric model ratio of $\lambda_L = 25:1$ was obtained according to the ratio of the actual width of the river channel to the width of the experimental model channel.

The indoor leakage experimental platform was designed according to the gravity similarity criterion. The corresponding ratios are: the corresponding total water flow ratio is $\lambda_Q = \lambda_L^{2.5} = 25^{2.5} = 3125:1$; the flow velocity ratio is $\lambda_V = \lambda_L^{0.5} = 25^{0.5} = 5$. Since the initial velocity of both the experimental platform and the actual gully water flow is 0, the corresponding leakage ratio is consistent with the geometric ratio of $\lambda_L = 25:1$ (Wei et al., 2019).

Converting the geometric and flow ratios of the above experimental model to the actual model, and based on the

TABLE 2 | Summary of experimental fissure widths.

Actual width of the gully/m	Experimental width/m	Model geometric scale	Actual width of ground fissures/cm	Experimental width of ground fissures/cm
10.0	0.4	25:1	<5 cm	0.20
			5–10 cm	0.40
			10–20 cm	0.80
			>20 cm	2.00

TABLE 3 | Experimental gully leakage under different flood volumes and seam widths.

Experimental width of ground fissures							
0.2 cm		0.4 cm		0.8 cm		2.0 cm	
Flood amount (m ³ /h)	Leakage amount (m ³ /h)	Flood amount (m ³ /h)	Leakage amount (m ³ /h)	Flood amount (m ³ /h)	Leakage amount (m ³ /h)	Flood amount (m ³ /h)	Leakage amount (m ³ /h)
13.750	2.388	19.449	3.513	19.388	4.587	16.122	8.338
23.310	2.812	30.890	3.561	20.217	4.852	17.731	9.306
41.967	2.925	32.327	3.891	25.068	6.295	31.431	14.567
48.100	3.026	46.563	4.382	36.631	6.505	34.595	16.426
61.109	3.840	58.427	4.986	48.802	7.097	58.513	19.471
62.929	3.891	77.200	5.286	60.905	7.636	80.295	21.928
87.632	4.027	79.334	5.513	68.950	8.124	86.820	22.783
95.286	4.185	97.116	5.809	83.199	8.802	101.408	23.722
95.732	4.220	112.712	6.638	88.315	8.868	122.012	26.144
126.616	4.603	125.754	6.898	96.904	9.680	128.510	26.904
133.184	4.773	142.534	7.385	118.619	10.594	144.940	27.875
169.616	5.388	159.531	7.892	156.717	11.845	184.331	32.717
207.025	5.766	186.294	8.636	190.486	13.340	224.369	36.720
238.350	6.945	246.034	9.565	221.651	13.935	282.609	40.617
267.687	7.686	285.108	10.398	245.404	14.560	308.901	44.107
312.818	7.892	313.552	11.694	247.271	15.305	—	—

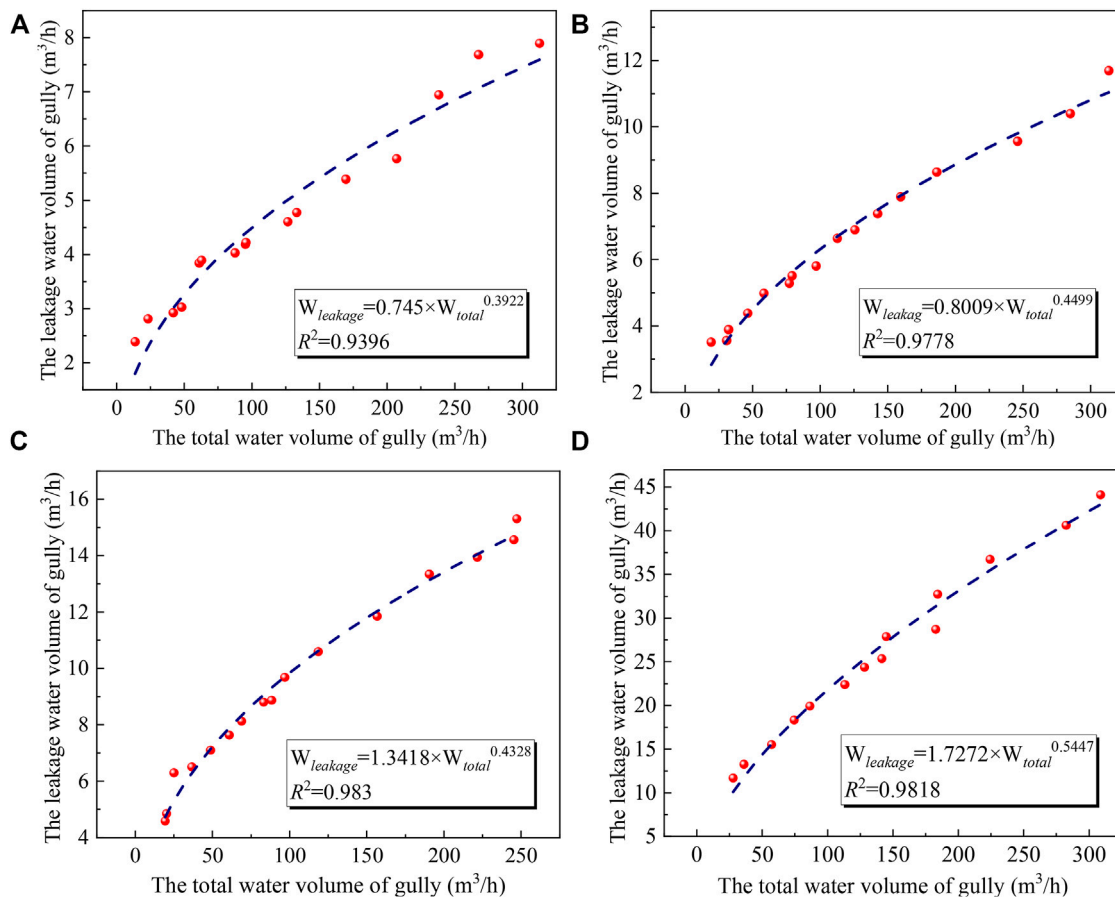
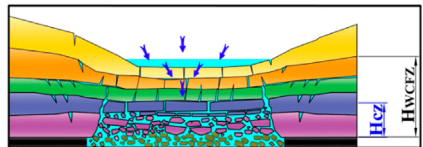
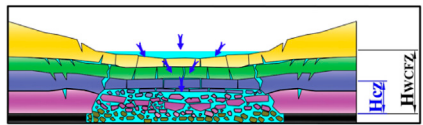
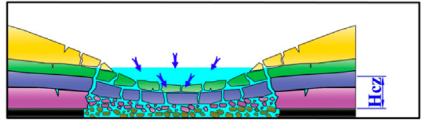
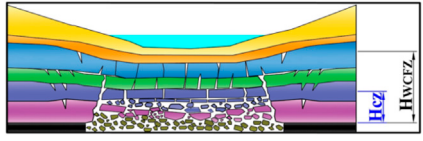
**FIGURE 8** | Leakage for different experimental fissure widths: (A) 0.20 cm; (B) 0.40 cm; (C) 0.80 cm; (D) 2.00 cm.

TABLE 4 | The amount of water leakage and the risk degree.

Working face	Confluence area (km ²)	Flood volume (m ³ /h)	Different fissure width leakage (m ³ /h)				B_q (m ³ /h)	Q_a (m ³ /h)	Dangerousness
			< 5 cm	5–10 cm	10–20 cm	> 20 cm			
125207	2.59	27216	13.05	15.09	25.67	44.02	1140.01	313	danger
125205	3.05	30744	13.69	16.80	27.06	47.04	1575.73		danger
125203	4.02	37728	14.84	18.42	29.57	51.75	1765.63		danger

TABLE 5 | Classification of gully ground fissures for treatment.

Classification standard	Classification of difficulty types of ground fissure treatment	Classification diagram
$\frac{H_{WCFZ}}{2} < M \leq H_{WCFZ}$	Type "I"	
$H_{FZ} < M \leq \frac{H_{WCFZ}}{2}$	Type "II"	
$M \leq H_{CZ}$	Type "III"	
$M > H_{WCFZ}$	Type "IV"	

leakage reduction coefficients of the study site with similar geological conditions by the study (Hou et al., 2020), the leakage volume between different flood volumes and seam widths in the gully under actual conditions in the region is obtained by the following equations:

- 1) When the actual seam width of the gully is <5 cm:

$$q = 0.745 \times a \times \lambda_L \times \left(\frac{Q_f}{\lambda_Q} \right)^{0.3922} \quad (4)$$

- 2) When the actual seam width of the gully is 5–10 cm:

$$q = 0.8009 \times a \times \lambda_L \times \left(\frac{Q_f}{\lambda_Q} \right)^{0.4499} \quad (5)$$

- 3) When the actual seam width of the gully is 10–20 cm:

$$q = 1.3418 \times a \times \lambda_L \times \left(\frac{Q_f}{\lambda_Q} \right)^{0.4328} \quad (6)$$

- 4) When the actual seam width of the gully is >20 cm:

$$q = 1.8056 \times a \times \lambda_L \times \left(\frac{Q_f}{\lambda_Q} \right)^{0.5447} \quad (7)$$

where q is represents single fissure leakage (m³/h); $a = 0.3$ is the leakage discount factor [9]; Q_f represents actual flood volume in the gully (m³/h); λ_L is the geometric ratio between the experiment and the practical situation; λ_Q is the flow ratio between the experiment and the practical situation.

Evaluation of the Risk Degree of Water Hazard From Gully Breaching

The Current Situation of Mine Water Output

The average water output of the mine in 2018 in the study site was 27.5 m³/h, and the maximum water output was 46.4 m³/h. In 2019, the average water output of the mine was 30.27 m³/h, and the maximum water output was 38.5 m³/h. In 2020, the average water output of the mine was 40.81 m³/h, and the maximum water output was 45 m³/h.

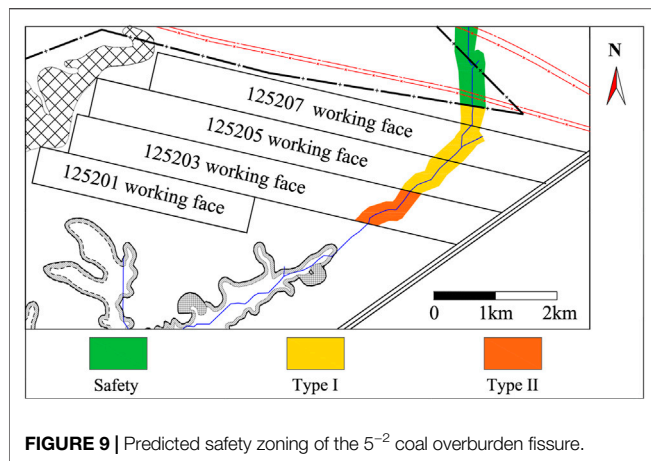


FIGURE 9 | Predicted safety zoning of the 5⁻² coal overburden fissure.

Calculation of Mine Drainage Capacity

The water flow in the underground production process and the configuration of the drainage system show that the maximum drainage capacity (Q_{dr-max}) of the mine drainage system is 360 m³/h.

The remaining drainage capacity (Q_{re-dr}) of the mine can be obtained by subtracting the maximum daily drainage amount by the actual drainage capacity of the drainage system (Q_{m-max}).

$$Q_{re-dr} = Q_{dr-max} - Q_{m-max} \quad (8)$$

By applying the characteristics of ground fissure development in the study site obtained in the previous paper, the amount of gully

outburst water (B_q) of different working faces was calculated for comparing the amount of gully outburst water with the remaining drainage capacity. In this way, the risk degree of water hazard from gully outburst water in the study site could be determined. If $Q_{re-dr} > B_q$, the risk is low; if $Q_{re-dr} < B_q$, the risk is high. The specific results are shown in Table 4.

CLASSIFICATION OF GULLY GROUND FISSURES FOR TREATMENT

According to the evaluation of the degree of risk of water hazard from gully collapse, the ground fissures should be treated after the end of over-gully retrieval in the working face of the study site to avoid potential water hazards from gully collapse in the mine.

A ground fissure treatment grade based on the correspondence between the development height of H_{WCFZ} and D_m is created according to *Dynamic Evolutionary Characteristics of Ground Fissures*, as shown in Table 5. This treatment grade provides a scientific basis for the accurate and efficient treatment of different types of ground fissures.

The relationship between the burial depth of the 5⁻² coal seam in the study site and the development height of the hydraulic conductivity fissure zone after mining the coal seam is analyzed. The type of fissure in the gully section of the study site is predicted by the classification criteria of fissure safety in the mining gully. The predicted results of the safety zoning of fissure in the overlying rock layer of the 5⁻² coal in the gully of the study site are given in Figure 9.

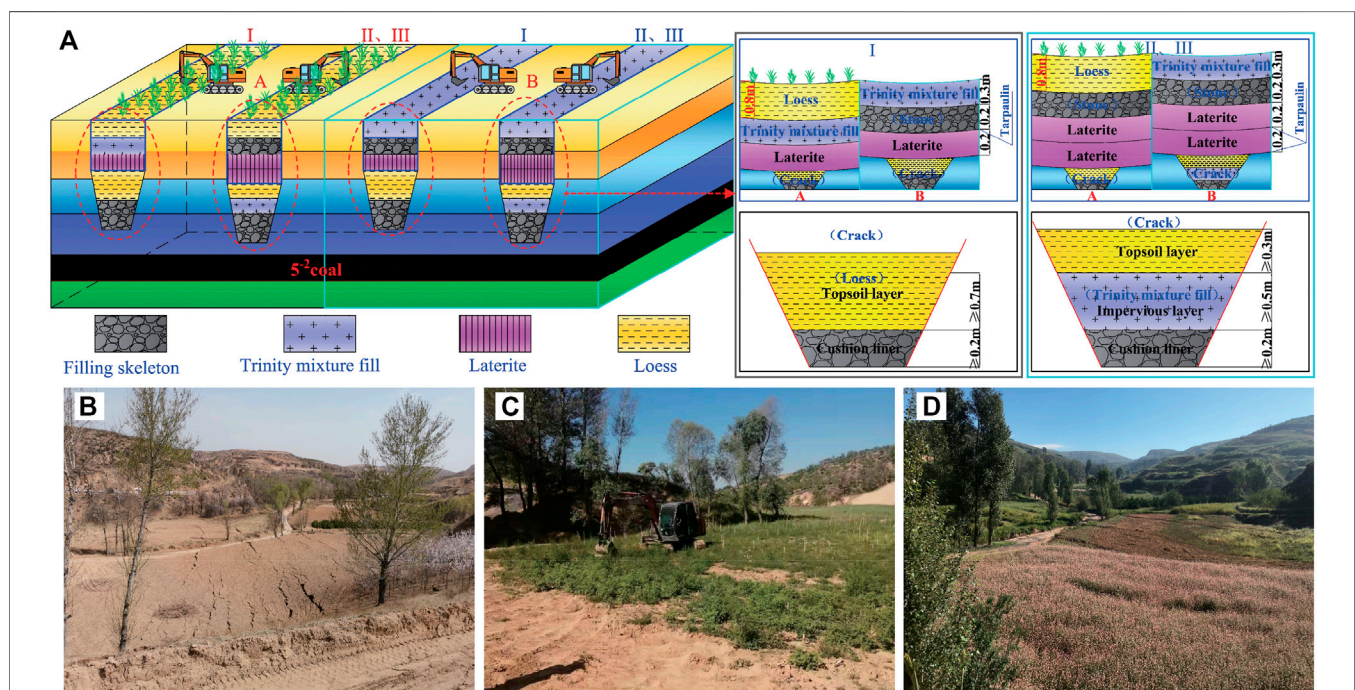


FIGURE 10 | Diagram of ecological restoration and treatment effects: (A) treatment repair schematic; (B) before treatment; (C) during treatment; (D) after treatment.

According to the ground fissure development characteristics of the gully after the 5⁻² coal seam retrieval and the water collapse level map of different gully sections in the study site, if the retrieval location 125203, 125205, and 125207 working faces pass through the gully before the onset of the rainy season from July to September, the water catchment area at the bottom of the gully will easily collapse into the well along the ground fissure, posing a certain threat of water collapse and water hazards to the safe retrieval of the working faces.

DISCUSSION

The results of the field measurements show that the ground fissures are stable after 5 days. In order to avoid the secondary fracture of ground fissures to destroy the treatment effect, 1 week after the working face is completely mined over the gully, the ground fissures in the gully should be treated in time and completed before the rainy season comes. The main factor affecting the amount of water leakage from the working face is the width of the surface cracks. The indoor leakage experimental platform obtained the amount of leakage from ground fissures of different widths in gullies, and found the overall positive correlation trend between gully leakage and total gully water.

Converting the geometric and flow scales of the above experimental model to the actual model, and the actual water leakage hazards on different working faces are obtained. The results of water leakage experiments show that if the working face is not treated after mining, there is a certain threat of water leakage risk in the mine.

A ground fissure treatment grade based on the correspondence between the development height of H_{WCFZ} and D_m , the grades of different working faces in the study site are Type “I” and Type “II.” Based on the above, in order to reduce the treatment cost and shorten the period, different grades of treatment methods are proposed. In the following, the 125203 working face is taken as an example to discuss the treatment of ground fissures.

Firstly, the ground was excavated as a whole. Secondly, “I” type was backfilled according to “cushion liner” and “topsoil layer.” “II and III” types were backfilled according to “cushion liner,” “impervious layer,” and “topsoil layer.” Finally, the excavated river was treated from bottom to top with red clay, gravel, interlayer tarpaulin, trinity mixture fill, or loess. The specific number and thickness of backfill layers are shown in **Figure 10**. If the treatment area is farmland (area A), the thickness of the topsoil layer after excavation and backfilling needs to reach 0.8 m, and the filling material is loose loess to ensure normal cultivation after treatment. After excavation and backfilling in area B, the thickness of the topsoil layer needs to be greater than 0.3 m, and the filling material is trinity mixture fill. When the safety of fissure is “IV,” it is safe. After the workings are retrieved, the water-conducting fissured zone will not penetrate the ground. There is no threat of water leakage or water hazard in the mine, so there is no need for treatment. After ground treatment, the original slope of the terrain will be maintained and not affect the normal flooding.

CONCLUSION

In this study, the quantitative calculation and risk prediction of water leakage caused by surface cracks in gully terrain are carried out, on the basis of which the corresponding treatment methods are put forward. The research results were applied in the field treatment of Anshan coal mine in Shaanxi, which proved the practicality and reliability of the method. The main conclusions are drawn as follows:

- 1) In this study, we have used the self-developed and designed water leakage test platform, and the mathematical prediction model between the amount of gully flood leakage and the width of gully fissures and gully flood flow was obtained. The prediction model shows that the overall positive correlation trend between gully leakage and total gully water is changing.
- 2) Given the water hazard in mines caused by frequent flowing water in the gully and flooding along with the mining fissures during heavy rainfall seasons, the criteria for classifying the risk of water leakage from the mining fissures in the gully were proposed. Besides, a method for predicting the amount of water leakage from the mining fissures in the gully was proposed, and the safety of bubbling fissures was evaluated.
- 3) The zoning of the risk of water leakage was divided according to the remaining drainage capacity of the mine. The dynamic development of mining ground fissures is about 5 days. Therefore, the treatment of ground fissures in the gully should be started 1 week after the shallow buried coal seam is completely retrieved over the gully and mined back, which can better ensure the treatment effect. The field application results show that the treatment method can effectively prevent water hazards by mining ground fissures in the gully, which is of significance to prevent gully collapse accidents and improve coal mine safety production.

DATA AVAILABILITY STATEMENT

The original contributions presented in the study are included in the article/supplementary material. Further inquiries can be directed to the corresponding authors.

AUTHOR CONTRIBUTIONS

DF and EH designed the study; DF, XX, and PH investigated the ground fissures; DF, XC, and TL completed the water leakage experiment process; DF analyzed the information obtained from the experiment; DF and EH improved the manuscript draft. All authors have read and agreed to the published version of the manuscript.

FUNDING

This research was supported by the National Natural Science Foundation of China (No. 42177174), the Basic Research Program of Natural Science of Shaanxi Province (2020ZY-JC-03), and the Shaanxi Province Joint Fund Project (2021JLM-09).

REFERENCES

- Chen, Q., Li, J., and Hou, E. (2020). Dynamic Simulation for the Process of Mining Subsidence Based on Cellular Automata Model. *Open Geosciences* 12, 832–839. doi:10.1515/geo-2020-0172
- Duan, Z., Yan, X., Sun, Q., Tan, X., and Dong, C. (2021). Effects of Water Content and Salt Content on Electrical Resistivity of Loess. *Environ. Earth Sci.* 80, 1–15. doi:10.1007/s12665-021-09769-2
- Fan, L. M., Ma, X. D., Jiang, Z. Q., Sun, K., and Ji, R. J. (2019). Review and Thirty Years prospect of Research on Water-Preserved Coal Mining(in Chinese). *Coal Sci. Tech.* 47, 1–30. doi:10.13199/j.cnki.cst.2019.07.001
- Hou, E. K., Che, X. Y., Feng, J., Duan, Z. H., Gao, L. J., and Li, J. (2019). Abundance of Aquifers in Yushenfu Coal Field and the Measures for Water-Preserved Coal Mining(in Chinese). *J. China Coal Soc.* 44, 813820. doi:10.13225/j.cnki.jccs.2018.6046
- Hou, E. K., Che, X. Y., Long, T. W., Ye, Z. N., and Wen, Q. (2020). Prediction Method of Water Inrush from Ground Cracks in Shallow Buried Seams(in Chinese). *J. China Coal Soc.* 45, 4154–4162. doi:10.13225/j.cnki.jccs.2020
- Hu, W., and Zhao, C. (2021). Evolution of Water Hazard Control Technology in China's Coal Mines. *Mine Water Environ.* 40, 334–344. doi:10.1007/s10230-020-00744-0
- Huang, Q. X. (2005). Study on Loading Distribution Law on Key Roof and its Structure upon Mining Face under Thick sandy Layer(in Chinese). *J. China Univ. Mining Tech.* 34, 289–293. CNKI:SUN:ZGKD.0.2005-03-0 06.
- Huang, Q. X. (2009). Simulation of clay Aquifuge Stability of Water Conservation Mining in Shallow-Buried Coal Seam(in Chinese). *Chin. J. Rock Mech. Eng.* 28, 987–992. CNKI:SUN:YSLX.0.2009-05-019.
- Ju, J., and Xu, J. (2015). Surface Stepped Subsidence Related to Top-Coal Caving Longwall Mining of Extremely Thick Coal Seam under Shallow Cover. *Int. J. Rock Mech. Mining Sci.* 78, 27–35. doi:10.1016/j.ijrmms.2015.05.003
- Li, L., Wu, K., Hu, Z. Q., Xu, Y. K., and Zhou, D. W. (2017). Analysis of Developmental Features and Causes of the Ground Cracks Induced by Oversized Working Face Mining in an Aeolian Sand Area. *Environ. Earth Sci.* 76, 1–12. doi:10.1007/s12665-017-6452-9
- Lian, B., Peng, J., Zhan, H., Huang, Q., Wang, X., and Hu, S. (2020). Formation Mechanism Analysis of Irrigation-Induced Retrogressive Loess Landslides. *Catena* 195, 1–13. doi:10.1016/j.catena.2019.104441
- Liu, H., Deng, K., Lei, S., Bian, Z. F., and Chen, D. Y. (2017). Dynamic Developing Law and Governance Standard of Ground Fissures Caused by Underground Mining(in Chinese). *J. Min. Saf. Eng.* 34, 884–890. doi:10.13545/j.cnki.jmse.2017.05.009
- Ma, L. Q., Du, X., Wang, F., and Liang, J. M. (2013). Water-Preserved Mining Technology for Shallow Buried Coal Seam in Ecologically-Vulnerable Coal Field: A Case Study in the Shendong Coal Field of China. *Disaster Adv.* 6, 268–278.
- Prakash, A., Kumar, N., Kumbhakar, D., Singh, A. K., and Paul, A. (2018). A Safe Depillaring Design for Shallow Depth of Cover with Influence of Surface Ground Movements: a Study in Jharia Coalfield. *Arabian J. Geosci.* 11, 1–8. doi:10.1007/s12517-018-3508-410
- Wang, F., Tu, S., Zhang, C., Zhang, Y., and Bai, Q. (2016). Evolution Mechanism of Water-Flowing Zones and Control Technology for Longwall Mining in Shallow Coal Seams beneath Gully Topography. *Environ. Earth Sci.* 75, 1–16. doi:10.1007/s12665-016-6121-4
- Wang, S. M., Shen, Y. J., Sun, Q., and Hou, E. K. (2020). Scientific Issues of Coal Detraction Mining Geological Assurance and Their Technology Expectations in Ecologically Fragile Mining Areas of Western China(in Chinese). *J. Mining Strata Control. Eng.* 2, 5–19. doi:10.13532/j.jmsce.cn10-1638/td.20200817.001
- Wei, B. Q., Huang, L., Yuan, H. S., Li, L. B., and Jin, H. X. (2019). Hydraulic Characteristics and Optimization of Fishway Combined with Vertical Slot and Nature-like Section(in Chinese). *Hydro-Sci. Eng.* 4, 9–16. doi:10.16198/j.cnki.1009-640x.2019.04.002
- Xie, X., Hou, E., Wang, S., Sun, X., Hou, P., Wang, S., et al. (2021). Formation Mechanism and the Height of the Water-Conducting Fractured Zone Induced by Middle Deep Coal Seam Mining in a Sandy Region: A Case Study from the Xiaobaodang Coal Mine. *Adv. Civil Eng.* 2021, 1–11. doi:10.1155/2021/6684202
- Xu, Y., Wu, K., Li, L., Zhou, D., and Hu, Z. (2019). Ground Cracks Development and Characteristics of Strata Movement under Fast Excavation: a Case Study at Bulianta Coal Mine, China. *Bull. Eng. Geol. Environ.* 78, 325–340. doi:10.1007/s10064-017-1047-y
- Yang, Y. K., Kang, T. H., Hao, X. L., Zheng, T. B., and Wang, A. (2012). Research on In-Situ Purification Technique of Mine Water in Shendong Mining Area. *Energ. Educ. Sci. Technol.* 29, 209–216.
- Yang, X., Wen, G., Dai, L., Sun, H., and Li, X. (2019). Ground Subsidence and Surface Cracks Evolution from Shallow-Buried Close-Distance Multi-Seam Mining: A Case Study in Bulianta Coal Mine. *Rock Mech. Rock Eng.* 52, 2835–2852. doi:10.1007/s00603-018-1726-4
- Zhang, D., Fan, G., Liu, Y., and Ma, L. (2010). Field Trials of Aquifer protection in Longwall Mining of Shallow Coal Seams in China. *Int. J. Rock Mech. Mining Sci.* 47, 908–914. doi:10.1016/j.ijrmms.2010.06.018
- Zhang, S. F., Hu, R. L., and Wu, X. (2012). Dynamic Prediction of Ground Deformation and Drainage Design for Shallow Thick Coal Seam Mining(in Chinese). *J. China Coal Soc.* 37, 301–306. doi:10.13225/j.cnki.jccs.2012.s2.035
- Zhang, C., Tu, S., Bai, Q., Yang, G., and Zhang, L. (2015). Evaluating Pressure-Relief Mining Performances Based on Surface Gas Venthole Extraction Data in Longwall Coal Mines. *J. Nat. Gas Sci. Eng.* 24, 431–440. doi:10.1016/j.jngse.2015.04.01210
- Zhang, F., Yan, B., Feng, X., Lan, H., Kang, C., Lin, X., et al. (2019). A Rapid Loess Mudflow Triggered by the Check Dam Failure in a Bulldoze Mountain Area, Lanzhou, China. *Landslides* 16, 1981–1992. doi:10.1007/s10346-019-01219-2
- Zhu, G., Wh, X., Li, P. H., Qi, R. J., Mu, W. P., and Fu, R. Z. (2014). Coalmine Surface Water Prevention and Drainage in Loess Area(in Chinese). *J. China Coal Soc.* 39, 1354–1360. doi:10.13225/j.cnki.jccs.2012.s2.035
- Zhuo, H., Qin, B., Shi, Q., and Li, L. (2018). Development Law of Air Leakage Fractures in Shallow Coal Seams: a Case Study in the Shendong Coalfield of China. *Environ. Earth Sci.* 77, 1–11. doi:10.1007/s12665-018-7961-x

Conflict of Interest: The authors declare that the research was conducted in the absence of any commercial or financial relationships that could be construed as a potential conflict of interest.

Publisher's Note: All claims expressed in this article are solely those of the authors and do not necessarily represent those of their affiliated organizations, or those of the publisher, the editors and the reviewers. Any product that may be evaluated in this article, or claim that may be made by its manufacturer, is not guaranteed or endorsed by the publisher.

Copyright © 2022 Feng, Hou, Xie, Che, Hou and Long. This is an open-access article distributed under the terms of the Creative Commons Attribution License (CC BY). The use, distribution or reproduction in other forums is permitted, provided the original author(s) and the copyright owner(s) are credited and that the original publication in this journal is cited, in accordance with accepted academic practice. No use, distribution or reproduction is permitted which does not comply with these terms.



A Whole Process Risk Management System for the Monitoring and Early Warning of Slope Hazards Affecting Gas and Oil Pipelines

Yan Yan¹, Guanglin Xiong¹, Jiaojiao Zhou¹, Renhe Wang¹, Wenyao Huang², Miao Yang², Renchao Wang³ and Dongxian Geng^{4*}

¹Key Laboratory of High-Speed Railway Engineering, MOE/School of Civil Engineering, Southwest Jiaotong University, Chengdu, China, ²Guangdong Dapeng LNG Company Ltd, Shenzhen, China, ³School of Computer Science and Engineering, University of Electronic Science and Technology of China, Chengdu, China, ⁴Analysis and Test Center of Sichuan Province, Chengdu, China

OPEN ACCESS

Edited by:

Haijun Qiu,
Northwest University, China

Reviewed by:

Chao Kang,
University of Northern British Columbia
Canada, Canada
Haowen Xu,
Oak Ridge National Laboratory (DOE),
United States

*Correspondence:

Dongxian Geng
geng0909@126.com

Specialty section:

This article was submitted to
Geohazards and Georisks,
a section of the journal
Frontiers in Earth Science

Received: 10 November 2021

Accepted: 13 December 2021

Published: 12 January 2022

Citation:

Yan Y, Xiong G, Zhou J, Wang R,
Huang W, Yang M, Wang R and
Geng D (2022) A Whole Process Risk
Management System for the
Monitoring and Early Warning of Slope
Hazards Affecting Gas and
Oil Pipelines.
Front. Earth Sci. 9:812527.
doi: 10.3389/feart.2021.812527

Pipelines are important methods of oil and gas transportation and are fundamental to many country's economies. Pipeline safety is a critical issue; over 96% of pipeline accidents due to ground movement are caused by slope hazards and these can lead to serious personnel and property losses. Therefore, effective pipeline slope hazard monitoring and early warning is crucial, but there are many limitations to existing measures. The recent advance in remote sensing technologies enables the collection of slope hazards information that maps the spatial distribution of landslide. But this approach cannot provide real-time monitoring and early warning as there is a time lag due to image processing. Also, pipelines are considered separately from the slope hazard, with only slope event occurrence assessed rather than quantification of the impact of the hazard on the pipeline. Here, we report on a whole process risk management system for the pipeline slope hazard, incorporating monitoring and early warning of pipeline slope hazards. Three sites at risk of slope hazard on the Guangdong Dapeng Liquefied Natural Gas (LNG) Company pipeline in Guangdong, South China - Zhangmutou, Huoshaogang and Dapeng New District - were selected for research and implementation of the whole process risk management, monitoring and early warning system. The system is shown to operate well and, overall, we found that the three sites are relatively stable at present. This research provides widely applicable guidance for the prevention, control, and early warning of pipeline slope hazards.

Keywords: pipeline slope hazards, monitoring and early warning, whole process risk, refined hierarchical management system, Guangdong Dapeng LNG

1 INTRODUCTION

As important methods of oil and gas transportation, oil and gas pipelines are fundamental to the economy of many countries, and pipeline safety is a critical issue. The total length of global oil and gas pipelines is expected to increase from 1.89 million km in 2020 to 2.03 million km in 2024 (GlobalData, 2020). As of the end of 2020, there were 144,000 km of long-distance oil and gas pipelines in China, with many under planning and construction (Gao et al., 2021). Long-distance transportation pipelines inevitably traverse complex geological areas (Hall et al., 2003) and face many

natural hazards (Zhao et al., 2006). The EGIG report on failure data (EGIG, 2020) showed that 96.55% of pipeline accidents due to ground movement in 2010–2019 were caused by slope hazards, and these can lead to serious personnel and property losses (Honegger et al., 2010; Liu et al., 2010; Zheng et al., 2012). For example, in July 2016, a landslide along the Sichuan-East Gas Pipeline, China, caused two deaths, nine injuries, direct economic losses of nearly 30 million yuan and indirect economic losses of over 23 million yuan (Zhou, 2018). In March 2019, a landslide induced by heavy rainfall caused a natural gas pipeline in Iran to rupture and explode, interrupting the gas supply to over 12,000 users (Vasseghi et al., 2021). Prevention and control of pipeline slope hazards is needed to reduce the losses associated with pipeline slope accidents, and this requires effective monitoring and early warning. Two main approaches to slope hazard monitoring are remote sensing and ground monitoring.

Improvements in the technology for remote sensing of slope hazards means that information on the spatial distribution of landslide kinematics can be obtained rapidly (Delacourt et al., 2007; Wasowski and Bovenga, 2014). Optical remote sensing methods have been successfully used in semi-autonomous mapping of landslide morphometrics (Martha et al., 2010; Lahousse et al., 2011), but interpretation efficiency is low. With increasing launches of radar satellites and improvements in processing technology, Interferometric Synthetic Aperture Radar (InSAR) has also been used in landslide monitoring (Strozzi et al., 2005; Carla et al., 2019; Zhang et al., 2020). However, vegetation coverage, atmospheric effects and deformation gradients all complicate interpretation of the surface deformation signal so that landslide identification is not sufficiently accurate for early warning (Li et al., 2021). In recent years, remote sensing based on uncrewed aerial vehicles (UAVs) has been increasingly used to obtain spatially distributed data for landslide monitoring (Marek et al., 2015; Turner et al., 2015; Balek and Blahůt, 2016; Peppia et al., 2017; Peternel et al., 2017; Rossi et al., 2018), and hazard mapping, monitoring and analysis (Giordan et al., 2018). However, remote sensing approaches are based on comparative analysis of multiple phases of images, and this processing takes time, so they cannot achieve real-time monitoring and early warning.

Ground monitoring broadly covers three aspects, rainfall, ground displacement and soil hydrological properties (Luo et al., 2008; Yin et al., 2010; Bittelli et al., 2012). Data obtained from multiple monitoring instruments can be combined to assess the risk level of landslides (Macciotta et al., 2015) and establish warning standards (Yin et al., 2010). However, hazard locations need to be identified in advance of installing the monitoring/warning network; the sudden and destructive nature of the hazard means that installation and operation of instruments is difficult (Vaziri et al., 2010). Also, there is also a certain amount of physical contact with the monitored object, which may influence the results.

In recent years, studies have applied the developments in remote sensing and ground monitoring technology to pipeline geological hazard monitoring and early warning (Leynes et al., 2005; Li et al., 2009; Marinos et al., 2019; Yan et al., 2021). Long-

term monitoring allows pipeline geological hazards to be effectively identified and mitigated to ensure safe operation of the pipeline (Vasconez et al., 2010). The safety of pipelines under the action of landslides can be evaluated using strength theory based on monitoring surface displacement and strain of the pipeline slope (Feng and Huang, 2009; Liu et al., 2010; Marinos et al., 2019). To deal with the particularity and complexity of pipeline landslides, Yan et al. (2019) developed a multi-parameter comprehensive monitoring system that could be applied to pipeline evaluation using a mechanical model of failure probability (Alvarado-Franco et al., 2017). However, most monitoring approaches separate the pipeline from the slope hazard and only assess hazard occurrence; the impact of the hazard on the pipeline, and the vulnerability of the pipeline, needs further research.

In this study, we develop a procedure for whole process risk management, monitoring and early warning to prevent and control pipeline slope hazards. The whole process of slope hazards: formation process, evolution process, and disaster process. First, InSAR, UAV and ground survey are used to divide the pipeline into different hazard risk areas/sections. Then, monitoring and early warning measures are implemented for the risky areas – those with high hazard probability and high potential for pipeline damage. The real-time monitoring data is used to numerically simulate pipeline slope hazards, quantitatively predict the hazards, and formulate rapid prevention and control measures. The procedure developed in this research provides widely applicable guidance for the prevention, control, and early warning of pipeline slope hazards.

2 STUDY AREA

2.1 Introduction to Dapeng Pipeline

The main gas pipeline of Guangdong Dapeng LNG Co., Ltd. is c. 442.35 km in length, with a design pressure is 9.2 MPa, and includes one main line, three branch lines and ten user dedicated lines. As the pipeline construction schedule was restricted by the government's land use plan, the dangers of natural and artificial geological hazards and water damage during the pipeline operation period were not fully documented. Sections of the pipeline traverse water networks, around 190 km of pipeline pass through mountains, with steep slopes and high landslide potential, and the nearby coastline is prone to typhoon that generate heavy rainfall. Risk zoning of the pipeline route (**Figure 1**) identifies sections of high, medium, and low risk. We selected three sites representing typical pipeline unstable slope hazards in high-risk sites for our monitoring and early warning research: Zhangmutou, Dongguan; Huoshaogang landfill in Panyu; and Shenzhen Dapeng New District.

2.2 Characteristics of Pipeline Slope Hazard Monitoring and Early Warning Study Sites

The first monitoring site is at Zhangmutou in Huangjiang Town, in the south of Dongguan City (22°54'5.4" N, 114°2'9" E). Surface stratum is dominated by silty clay or gravel clay, and the sub-



FIGURE 1 | Geological hazard risk zoning map of the Dapeng Pipeline, Guangdong, China. The main hazards relate to the mountainous setting of part of the pipeline, combined with the effects of heavy rainfall and typhoons.

surface comprises strongly weathered granite or shale. Zhangmutou is a forest site with low mountain and hill topography that is relatively prone to landslides. The landslides are generally small and medium-sized, and mainly occur in the rainy season, from April to October. Lithology exposed in the pipeline trench comprises heavily weathered and fragmented quartz sandstone and the surface of the slope is strongly or completely weathered. In the trench, the fully weathered layer is about 0.5–1.0 m thick, with an unknown thickness of the strongly weathered layer below. The fragmented lithology in this section is susceptible to formation of shallow landslides, especially within the fully weathered layer, which endangers the safety of the pipeline.

The second monitoring site is at Huoshagang landfill, Guangzhou (22°59'8" N, 113°21'46" E). The topography of the area comprises plains and hills, with a few low mountains, and surface stratum mainly comprises silty soil or clay. The landfill site is now full, with accumulation of waste extending to the upper hillside; a retaining wall has been constructed and the pipeline is locally less than 10 m from the toe of the slope. On-site investigations show the pipeline was constructed before the storage yard, and the complicated hydrogeological conditions of the accumulated waste have led to drainage of water at the foot of the slope to form a swampy depression. The soil in the pipeline trench is plastic to soft plastic. The existing protection and reinforcement work, which include engineering measures such as stacking forms and retaining walls, are not sufficient to prevent seepage of surface water into the spoil yard. If the waste heap deformed, it would seriously threaten pipeline safety.

The third monitoring site is in Dapeng New District in Shenzhen, Guangdong (22°34'10" N, 114°28'35" E). The regional topography comprises low mountains and hills, with stratum of strongly and moderately weathered granite, conglomerate, and gravel-bearing sandstone. The surface is covered by gravelly soil, with silty clay and gravel in valley bottoms. The pipeline is laid along a shoulder of flat land halfway up the mountainside. The surrounding terrain is

steep, with highly weathered rock formations and boulders outcropping locally on the surface. Excavation during pipeline construction has affected slope stability to some extent, but the steep slope is in any case prone to landsliding with heavy rain. The pipeline is about 5 m from the toe of the slope, which has low retaining walls, and the pipeline is within the range of the landslide hazard area, which threatens its safe operation.

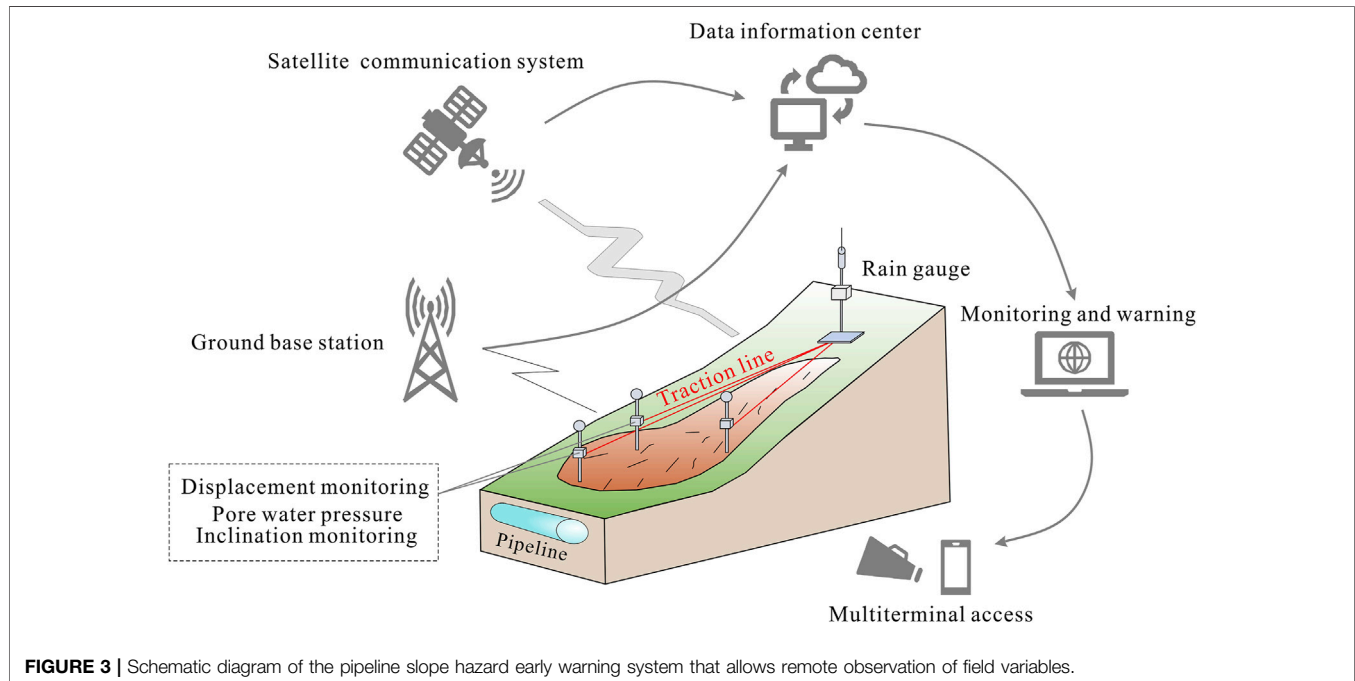
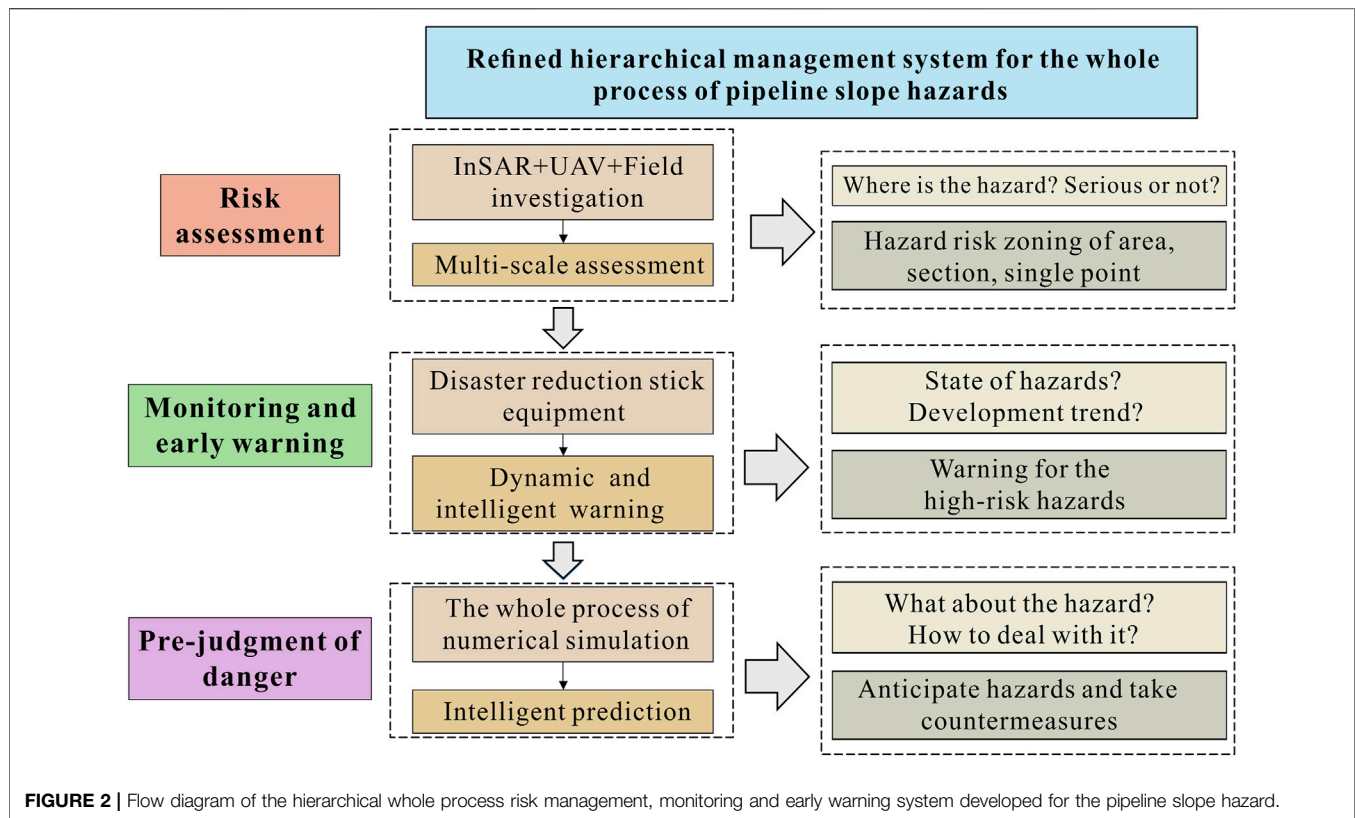
3 METHODOLOGY

3.1 Refined Whole Process Hierarchical Management System for the Pipeline Slope Hazard

The procedure we developed for whole process risk management, monitoring and early warning of pipeline slope hazards, which incorporates pre-hazard risk assessment-hazard monitoring and early warning-real-time calculation of hazard risk, is in the form of a hierarchical management system (Figure 2). The whole process of management we propose includes risk assessment before hazards, monitoring and early warning when hazards are about to occur, and pre-judgment of danger for downstream risks after hazards occur. Preliminary hazard risk assessment, using InSAR and UAV technology to facilitate multi-scale assessment, quantitatively assesses hazard risk and severity at three levels (areas, sections, and single points along the pipeline). Based on the hazard risk assessment, monitoring and early warning is established for areas, sections and points deemed high risk, comprising real-time monitoring of the status and trend of pipeline hazards. Numerical simulation is used to analyze the real-time monitoring data and predict forthcoming hazards, which allows emergency plans to be made.

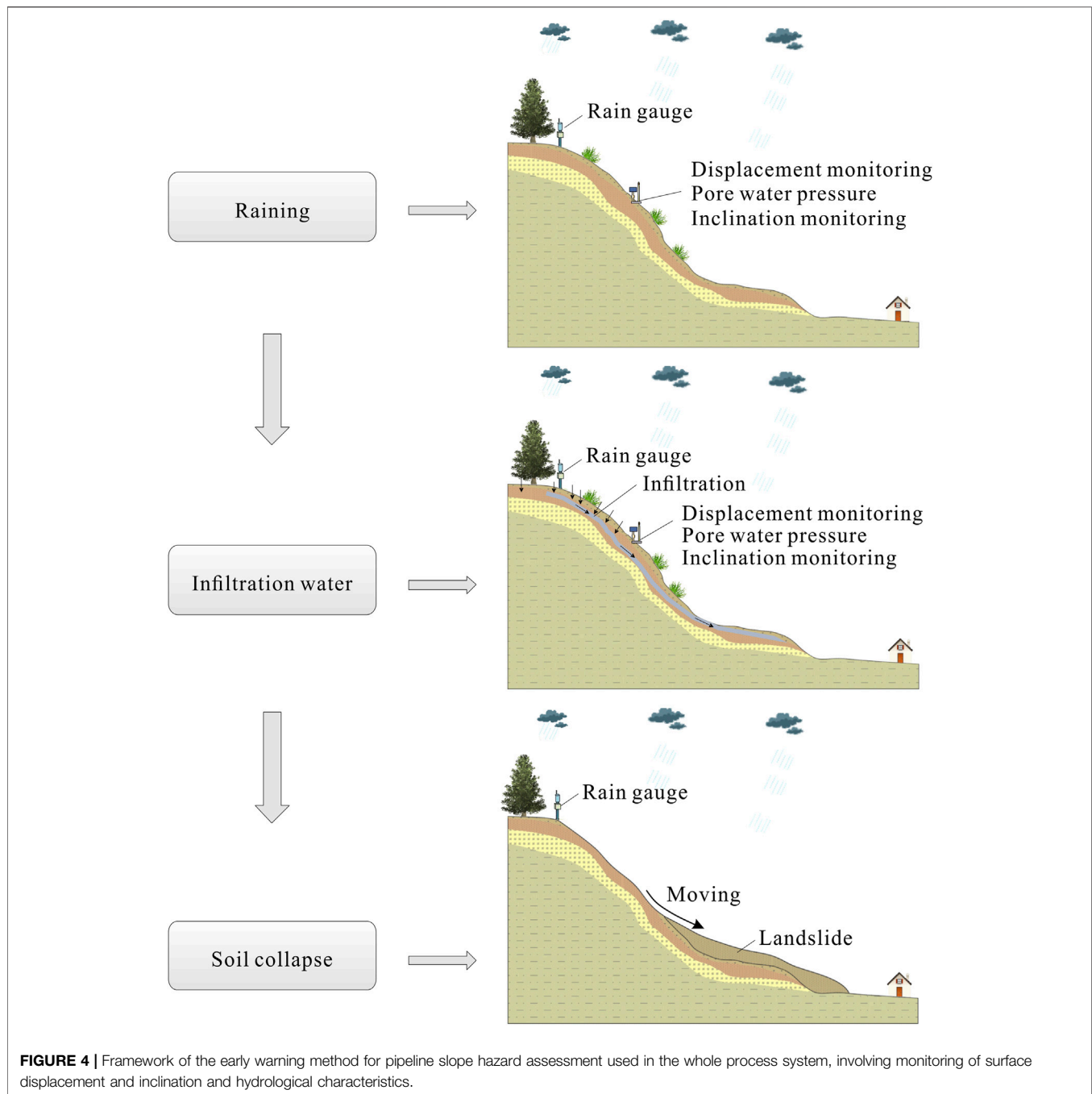
3.2 Monitoring and Early Warning

To analyze the deformation trend of the unstable slope and judge the stability and danger of the pipeline project's operating state we



needed to monitor the driving factors of the pipeline slope hazards in the study area. We identified the key monitoring parameters as: 1) rainfall conditions, specifically, hourly, and daily totals; 2) pore water pressure in the shallow surface soil; 3)

angular displacement and tilting deformation of unstable slopes; 4) horizontal displacement of the unstable slope to obtain cumulative deformation and the deformation rate. We used our self-developed pipeline slope hazard monitoring stick



equipment system (Yan et al., 2019) to measure these parameters. The system includes multiple sensors and a network data platform so that sensor parameters can be directly uploaded to the network system, and data can be directly observed and retrieved through the web client (**Figure 3**). The stick equipment was installed at the three pipeline monitoring sites in January 2020. The system automatically collects monitoring data and transmits it to the server in real time to allow background analysis of the real-time deformation of unstable slopes. The inherent data collection frequency of the monitoring equipment is once every 5 min, but it can be adjusted as needed.

At the study sites, data collection frequency was varied according to conditions: 1) under normal climatic conditions and when the slope is stable, data is collected every hour; 2) during floods, rainy season, forecast period, and control project construction period monitoring frequency is increased to every 5, 10, 15 or 30 min, according to needs.

The early warning framework is based on likelihood of slope hazard occurrence (**Figure 4**), with four warning levels (Levels I–IV). When rainfall reaches the warning rainfall threshold, the warning level is determined with reference to changes in parameters such as surface displacement, deep tilt and pore

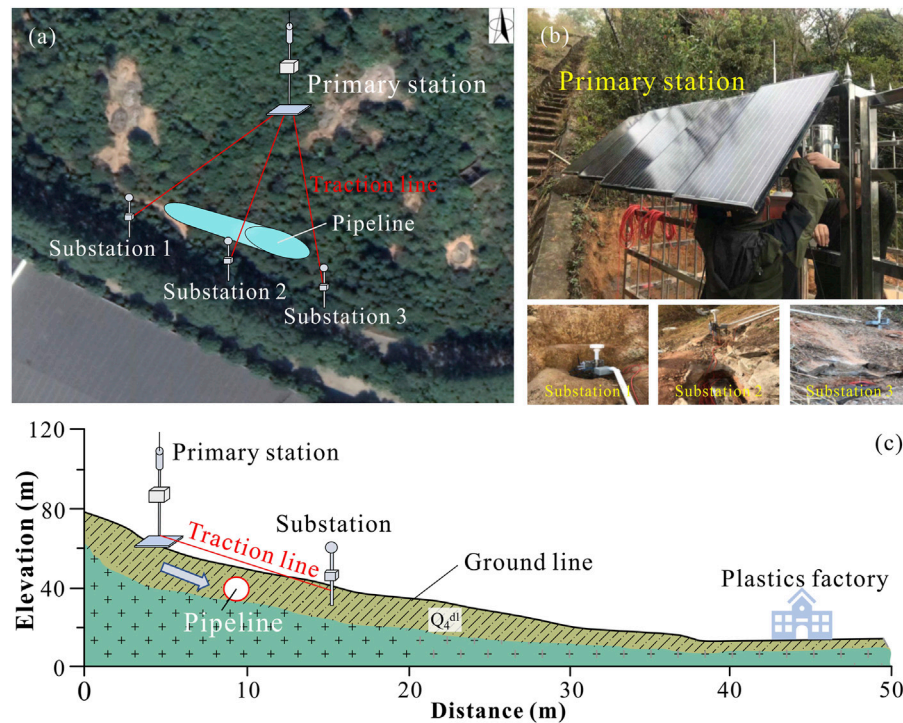


FIGURE 5 | Layout of slope hazard monitoring equipment at Zhangmutou. **(A)** Aerial view of the monitoring configuration; **(B)** Detail of monitoring set-up at each station; **(C)** Elevation-distance plot showing location of the pipeline and monitoring equipment.

water pressure. Level I (Attention level) is the initial deformation stage where the possibility of damage within a year is unlikely. Level II (Warning level) is where uniform deformation is detected and the probability of damage in a few months to a year is relatively high. Level III (Alert level) is in the initial acceleration and deformation stage, with certain macro-precursor characteristics, and the probability of damage in a few days or weeks is high. Level IV (Alarm level) is in the critical deformation stage, where short-term pre-sliding signs are marked, and the probability of damage in a few hours or weeks is very high.

4 RESULTS AND ANALYSIS

4.1 Construction of Monitoring and Early Warning Systems at the Study Sites

The monitoring set-up at each site involved a primary station and three substations. The primary station was positioned on the slope above the pipeline, and the substations below the pipeline. The equipment configurations at Zhangmutou, Huoshaogang and Dapeng New District are shown in **Figures 5–7**, respectively. According to the pipeline design specifications, all the Dapeng LNG pipelines are designed to be buried at a depth of 1.2 m from the top of the pipeline to the earth's surface. Therefore, the buried depth of the substation we designed in this study is 1.5 m, which can effectively monitor the displacement and inclination of the soil around the pipeline.

The distance between the primary station and the substations varied at each site, depending on ground conditions, etc. At

Zhangmutou, substations 1, 2 and 3 were placed at distances of 13, 10 and 14 m from the primary station. At Huoshaogang landfill, substations 1, 2 and 3 were placed at 10, 8 and 10 m from the primary station. At Dapeng New District, substations 1, 2 and 3 were placed 10, 12 and 11 m from the primary station. According to on-site investigations, we install the primary station on the bedrock outside the landslide body, or drive deep concrete piles, so that the primary station basically does not follow the landslide body movement. The substations are installed on the landslide body.

4.2 Analysis of Monitoring Data

Rainfall is the most important trigger for landslide hazards in the region. Monitoring equipment at each of the three study sites recorded higher annual and rainy season (April 1 to August 31) rainfall totals in 2021 compared with 2020. For example, at Zhangmutou annual rainfall of 1215.5 mm was recorded in 2020, of which 578.7 mm was in the rainy season. In 2021, annual rainfall was 1809.1 mm, of which 1685.6 mm was in the rainy season. We selected the rainy season of 2021 as the test data set for our risk management and early warning procedure due to its higher rainfall total.

4.2.1 Zhangmutou Unstable Slope

Cumulative rainy season rainfall for 2021 was 1685.6 mm (**Figure 8**). Two rainfall peaks are evident in early June and

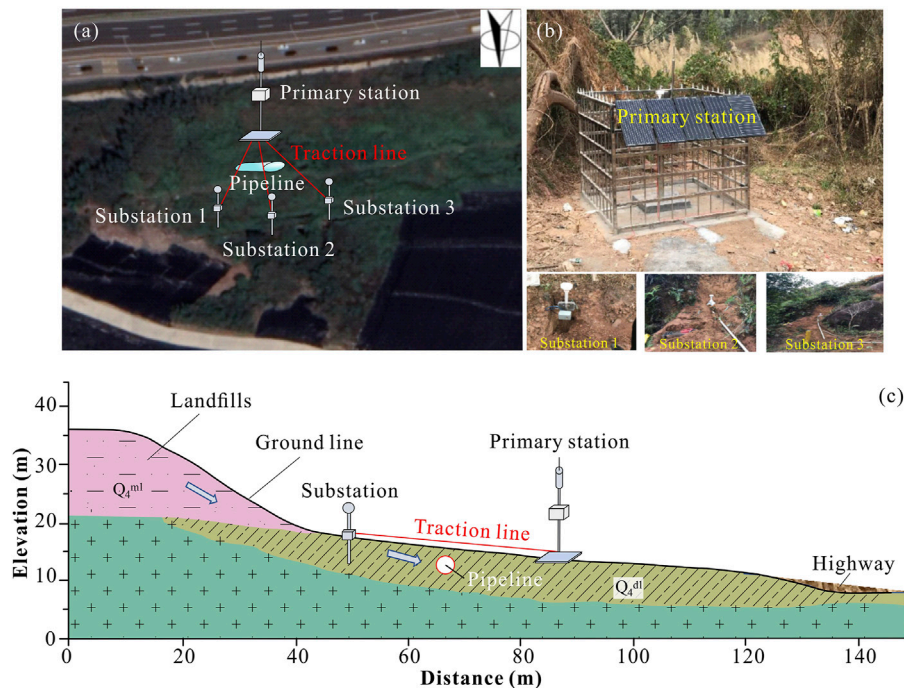


FIGURE 6 | Layout of slope hazard monitoring equipment at Huoshaogang. **(A)** Aerial view of the monitoring configuration; **(B)** Detail of monitoring set-up at each station; **(C)** Elevation-distance plot showing location of the pipeline and monitoring equipment.

early August, with daily totals of over 75 mm on June 4 and August 9. The maximum daily total of 84.3 mm was during a heavy rainstorm on August 9. However, hourly rainfall, single-day rainfall and 3-day maximum rainfall days did not reach the warning threshold, so the pipeline was deemed to be in a safe state and no alert was needed.

Pore water and displacement monitoring data from the three substations show relatively stability over the 2021 rainy season. Maximum pore water pressure at substation 1 was 101.2 KPa, the maximum pore water pressure difference was 2.5 KPa, the maximum dip angle deviation was 0.08° and the maximum horizontal displacement was 5.3 mm. The trend at substation 2 is similar. Substation 2 recorded maximum pore water pressure of 101.3 KPa, maximum pore water pressure difference of 2.6 KPa, maximum dip angle deviation of 0.097° , and maximum horizontal displacement of 3 mm. However, substation 3 recorded larger fluctuations in pore water pressure and dip angle deviation; maximum pore water pressure was 106.3 KPa, maximum pore water pressure difference was 7.6 KPa, maximum dip angle deviation was 0.179° and maximum horizontal displacement 2.64 mm. Due to the greater variability in monitoring data that is more useful for testing purposes, we focused our pipeline risk analysis on substation 3.

The maximum pore water pressure of 106.3 KPa at substation 3 was recorded on August 10 and the minimum of 98.7 KPa on August 4 (**Figure 9A**). The rate of water pressure change (0.67 KPa/d) and the pore water pressure values are within the normal tolerable range, so there was no danger to the pipeline. The maximum tilt angle and horizontal deviation at substation 3

were also all within the safe range (**Figures 9B,C**); maximum tilt of 0.149° in the x direction and 0.179° in the y direction, maximum rate of change $0.014^\circ/\text{d}$, and maximum horizontal displacement 2.64 mm. Thus, no pipeline warning was triggered.

4.2.2 Huoshaogang Landfill Unstable Slope

The monitoring data shows that rainy season rainfall at this site in 2021 was relatively evenly distributed (**Figure 10**), with a cumulative total of 1201.4 mm. The overall trend shows generally low magnitude rainfall across the season, with episodic high magnitude events. Heavy rain, classed as daily rainfall over 70 mm, was recorded on May 2, June 1 and August 25, with a maximum single-day rainfall of 97.8 mm on June 1. None of the rainfall events reached the warning threshold, and the pipeline was considered as within a safe range.

Pore water and displacement monitoring results for Huoshaogang landfill site show greater fluctuations at substation 1 compared to substations 2 and 3. Substation 1 recorded maximum pore water pressure of 107.8 KPa, maximum pore water pressure difference of 8.4 KPa and maximum displacement in the horizontal direction is 8.94 mm. At substation 2, maximum pore water pressure was 101.5 KPa, maximum pore water pressure difference was 2.4 KPa and maximum horizontal displacement was 4.94 mm. Substation 3 recorded maximum pore water pressure of 100.6 KPa, maximum pore water pressure difference of 2.4 KPa and maximum horizontal displacement of 5.2 mm. Due to the larger data fluctuations that are more useful for testing purposes, substation 1 was chosen for further analysis.

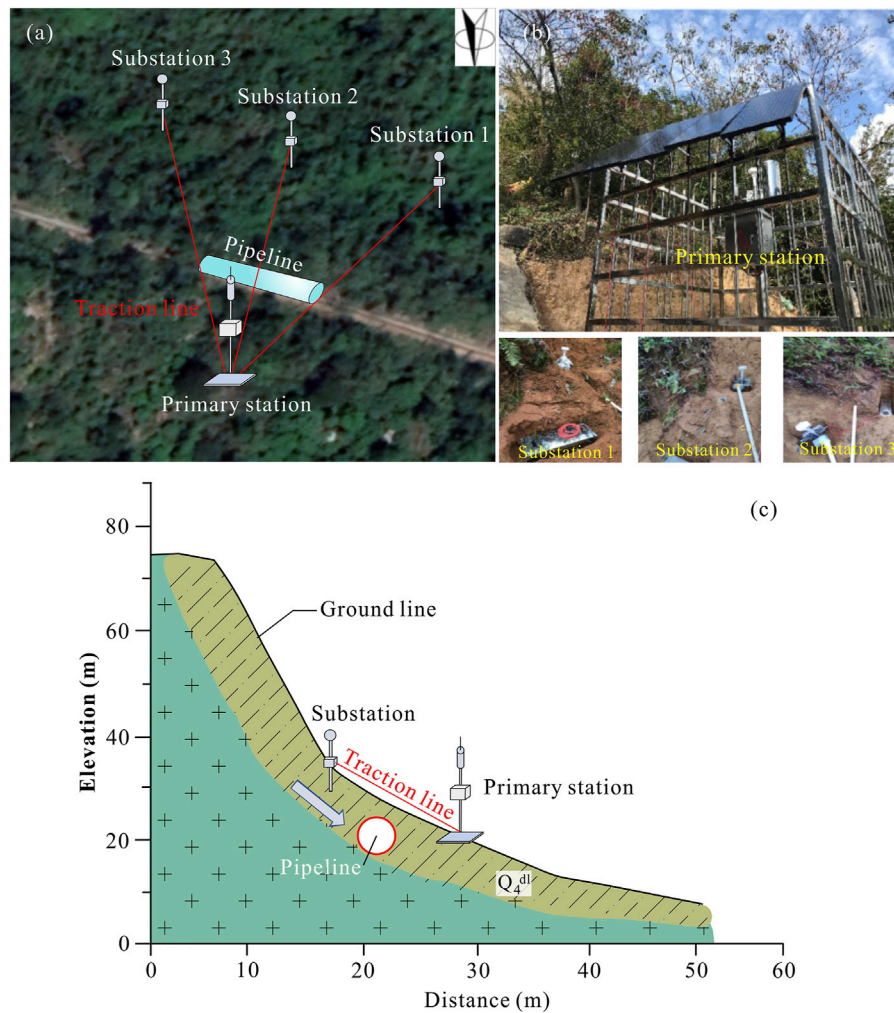


FIGURE 7 | Layout of slope hazard monitoring equipment at Dapeng New District. **(A)** Aerial view of the monitoring configuration; **(B)** Detail of monitoring set-up at each station; **(C)** Elevation-distance plot showing location of the pipeline and monitoring equipment.

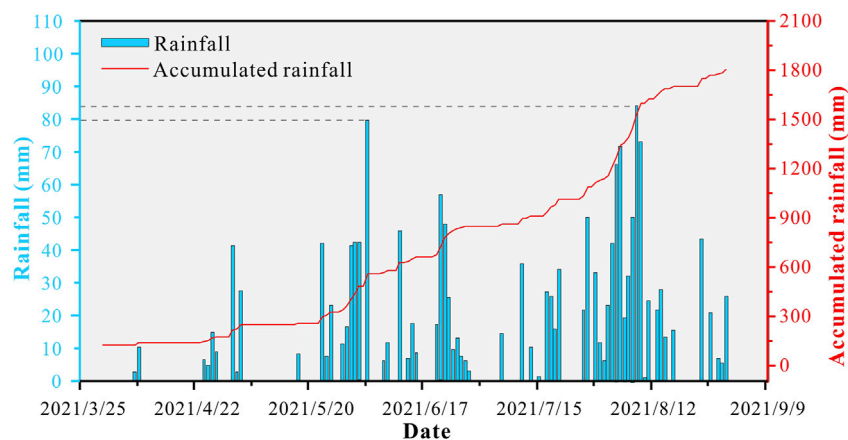


FIGURE 8 | Daily and accumulated rainy season rainfall at Zhangmutou site, April 1 to August 31, 2021.

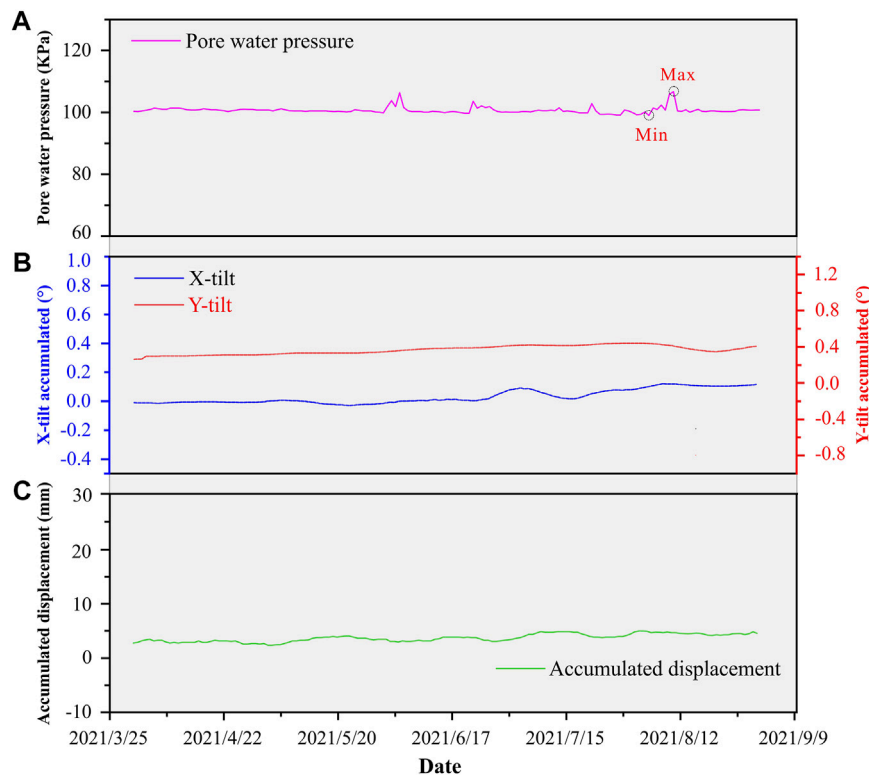


FIGURE 9 | Slope monitoring data recorded at Zhangmutou substation 3, April 1 to August 31, 2021. **(A)** Daily pore water pressure; **(B)** Accumulated offset in the x and y directions; **(C)** Accumulated horizontal displacement.

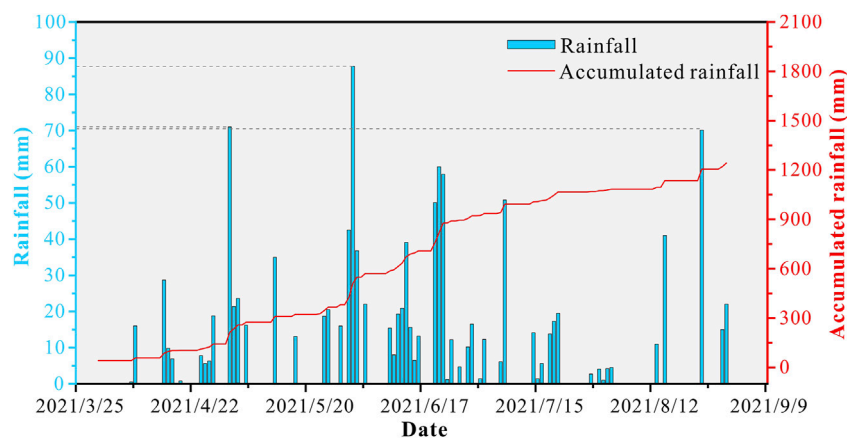


FIGURE 10 | Daily and accumulated rainfall at Huoshaogang landfill site, April 1 to August 31, 2021.

Pore water pressure at substation 1 increased significantly with daily rainfall peaks, with maximum water pressure corresponding with the large rainfall event on June 1 (**Figure 11A**). The minimum pore water pressure of 99.4 KPa was on August 4, with a maximum pore pressure change rate of 0.78 KPa/d. All the pore water pressure data recorded at substation 1 is within the allowable variation range. In terms of ground deformation, the

maximum x direction inclination angle deviation was 0.096° , with a maximum rate of change of $0.008^\circ/\text{d}$; in the y direction, the maximum deviation was 0.368° and the maximum rate of change $0.019^\circ/\text{d}$ (**Figure 11B**). The maximum horizontal displacement was 8.94 mm (**Figure 11C**). All displacement indicators are within the safe range, so the pipeline was considered in a safe state.

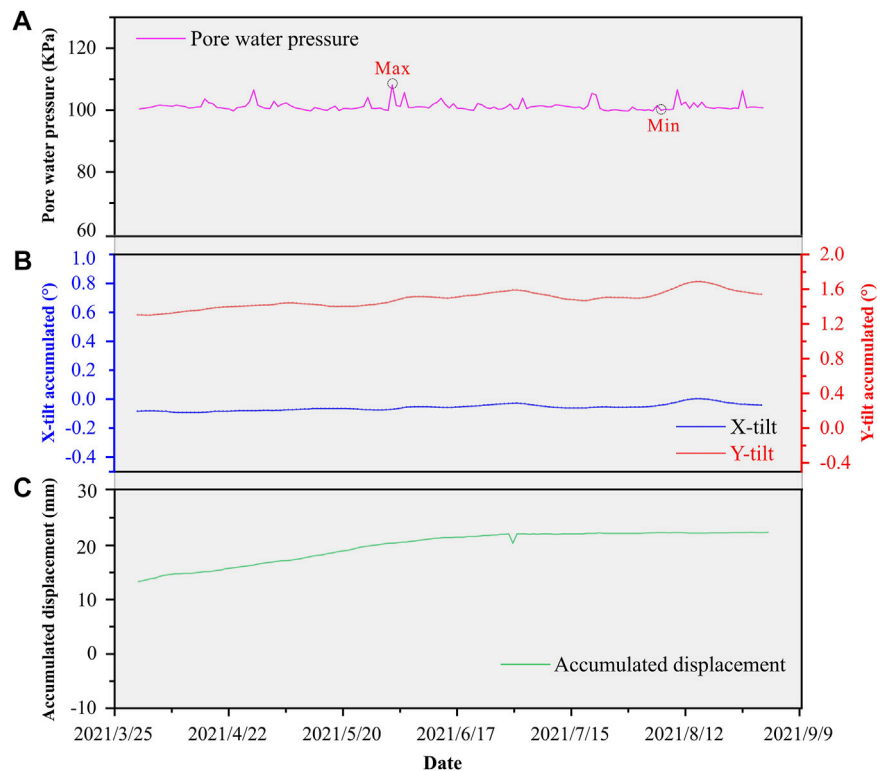


FIGURE 11 | Slope monitoring data recorded at Huoshaogang substation 1, April 1 to August 31, 2021. **(A)** Daily pore water pressure; **(B)** Accumulated offset in the x and y directions; **(C)** Accumulated horizontal displacement.

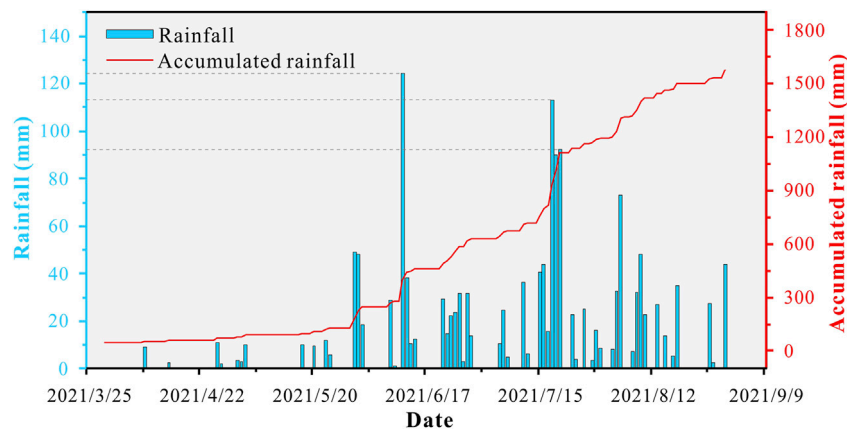


FIGURE 12 | Daily and accumulated rainfall at Dapeng New District site, April 1 to August 31, 2021.

4.2.3 Dapeng New District Unstable Slope

Rainfall monitoring data for Dapeng New District (**Figure 12**) shows cumulative rainy season rainfall in 2021 of 1528.9 mm, with the highest daily totals concentrated around mid-June and late July. Daily rainfall exceeding 90 mm, classed as a heavy rainstorm, was recorded on June 24 (124.3 mm) and over a 3-day period on July 19–21. None of the short-term heavy rainfall events reached the rainfall threshold. Thus, no danger of landslide

hazards was triggered, and the pipeline was considered in a safe state.

Pore water data from the three substations are quite similar, but the displacement results are more varied. Maximum pore water pressure recorded at substation 1 was 100.4 KPa, minimum pore water pressure value was 98 KPa and maximum inclination deviation was 0.754°. At substation 2, maximum and minimum pore water pressure was 100.5 KPa

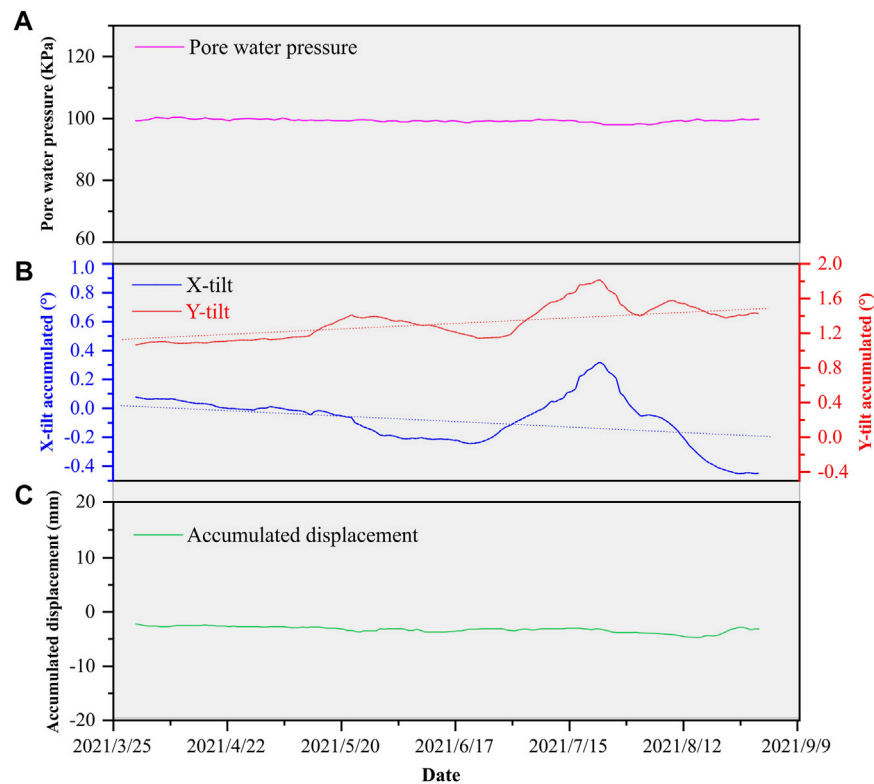


FIGURE 13 | Slope monitoring data recorded at Dapeng New District substation 1, April 1 to August 31, 2021. **(A)** Daily pore water pressure; **(B)** Accumulated offset in the x and y directions; **(C)** Accumulated horizontal displacement.

and 98.2 KPa, respectively, with maximum inclination deviation of 0.063° . At substation 3, maximum and minimum pore water pressure was 99.8 KPa and 97.7 KPa, with a maximum inclination angle deviation of 0.085° . The maximum inclination offset monitored by substation 1 is much larger than that of the other two substations. The positions monitored by substation 2 and substation 3 are dangerous, so substation 1 was selected for further analysis.

The maximum pore water pressure of 100.4 KPa at substation 1 was recorded on April 11, and the minimum pore water pressure of 98 KPa was recorded on several days (**Figure 13A**). The maximum pore water pressure difference was 2.4 KPa and maximum rate of change was 0.15 KPa/d. The pore water pressure data is all within the normal tolerable range, so the pipeline was not considered to be in danger. In terms of ground deformation, the maximum deviation of the inclination angle was 0.771° in the x direction, with a maximum change rate of $0.102^\circ/\text{d}$, and the maximum deviation in the y direction was 0.754° , with a maximum change rate of $0.108^\circ/\text{d}$ (**Figure 13B**). The maximum inclination angle deviation and deviation rate are slightly elevated but are both within the controllable range. The maximum horizontal displacement was only 2.52 mm (**Figure 13C**). Based on these results, the pipeline in the monitoring area was considered in a safe state.

4.3 Trend Estimation and Recommendations

According to the risk assessment, three high-risk hazard points were selected to monitor the formation process, evolution process, and disaster process. For real-time monitoring data, we use a sliding window-based method to detect anomalous points in the rainfall, pore water pressure, displacement, and inclination data to conduct preliminary detection of hazard events. We have established an early warning system driven by both the physical model and the data model. Within the framework of the traditional physical early warning model, the early warning threshold is continuously adjusted and optimized through the multiobjective evolutionary optimization method (Yan et al., 2020). Once the occurrence of hazards is forewarned, numerical simulation scenarios and data mining methods are used to quickly make recommendations for downstream risks.

Since the installation of the three slope hazard monitoring and early warning demonstration sites in January 2020, we have been focusing our research on the development of pipeline slope hazards. The annual rainy season at the sites is concentrated between April and September, and is characterized by abundant heavy rainfall events, but these are scattered throughout the period. The warning thresholds for rainfall intensity (75 mm in 1 h), and hourly, daily and 3-days maximum totals were not reached in our monitoring period. Likewise, the maximum

recorded slope deformation rate is relatively small, and no characteristic features such as collapses and landslides have been observed on site, so the early warning threshold was not reached, and no warning was issued. Therefore, it was not possible to enact real-time simulation and pipeline hazard assessment. Our monitoring data shows that the three hazard sites are in a relatively stable state at present. In the future, now that the monitoring system is established, implementation of the proposed pipeline slope hazard risk management, monitoring and early warning system should ensure that there is effective early warning of pipeline danger.

5 DISCUSSION

This study proposes a whole process risk management, monitoring and early warning system for pipeline slope hazards. A real-time simulation/calculation system, based on monitoring data transmitted from on-site equipment, gives timely hazard risk assessment that early warning of hazard risk using a hierarchical approach. Traditional early warning systems for the pipeline slope hazard use a black box model based on the critical rainfall threshold, which has limitations and often lead to false alarms. Also, existing monitoring methods usually separate the pipeline from the slope hazard and can only determine hazard occurrence; they cannot quantify the impact of the hazard on the pipeline. Based on the event process chain of pipeline slope hazards (i.e., rainfall–water infiltration–slope collapse), this study proposes a four-level early warning method that effectively overcomes the shortcomings of traditional monitoring and early warning methods. We use real-time monitoring data to numerically simulate pipeline slope hazards, focusing on areas where hazards are most likely to occur, and the risk of pipeline damage is high. The hazard risk is quantitatively estimated, and rapid prevention and control measures are then formulated. The procedure allows monitoring and early warning measures to be more targeted, reducing the incidence of false alarms, and guides the implementation of prevention and control measures.

Three sites of high slope instability risk along the Guangdong Dapeng LNG Company pipeline were selected for demonstration of the approach, located at Zhangmutou, Huoshaogang and Dapeng New District, and the whole process risk management, monitoring and early warning system of pipeline slope hazards was implemented. The system operated well; overall, the three hazard sites were shown to be in a state of relative stability at present. In future research, we will further develop the rapid numerical simulation of pipeline slope hazards based on real-time monitoring data to predict the danger of pipeline slope hazards and allow timely formulation of emergency plans.

In fact, this research also has some limitations that could be addressed in the future. The substation used in this study only

measures within 10 m in space, which is only suitable for shallow slope hazards. Before the construction of oil and gas pipelines, large-scale hazards have been avoided, and only some shallow slope hazards will exist around the pipeline. In view of this situation, we generally install three substations on the landslide body to meet the measurement requirements. After the installation is completed, the sensor transmits data to the early warning system through the ad-hoc network. We use rainfall to judge the triggering effect of external stimulating factors on hazards; pore water pressure is only used to judge whether the soil has an abnormal precursor after rainfall infiltration; and the inclination and displacement can reflect the precursors of landslide sliding. Data transmission relies on 5G and China Beidou satellite transmission technology. The emergence of extreme weather will affect 5G signals, and China Beidou satellite transmission technology will play a good role in emergency communications. In future research, we will study low-cost open-source technologies to create and deploy your sensors. At the same time, we will use more physical models and data models to establish early warning systems to make our early warning methods more accurate.

6 CONCLUSION

In this study, we develop a procedure for whole process risk management, monitoring and early warning to prevent and control pipeline slope hazards. Three sites at risk of slope hazard on the Guangdong Dapeng Liquefied Natural Gas (LNG) Company pipeline in Guangdong, South China - Zhangmutou, Huoshaogang and Dapeng New District - were selected for research and implementation of the whole process risk management, monitoring and early warning system. The three hazard sites were shown to be in a state of relative stability at present. This research provides widely applicable guidance for the prevention, control, and early warning of pipeline slope hazards.

DATA AVAILABILITY STATEMENT

The original contributions presented in the study are included in the article/Supplementary Material, further inquiries can be directed to the corresponding author.

AUTHOR CONTRIBUTIONS

YY is the first author, is responsible for most of the work and paper writing in this research. GX is the second author and is responsible for the processing and verification of the article data. JZ is the third author and is responsible for the production

of the article figures. RW is the fourth author and is responsible for checking the overall logical structure of the article. WH and MY are responsible for the measurement of field data. RW is the seventh author and is responsible for drawing the Instrument layout figures. DG is the corresponding author and is responsible for construction of monitoring and early warning system.

REFERENCES

- Alvarado-Franco, J. P., Castro, D., Estrada, N., Caicedo, B., Sánchez-Silva, M., Camacho, L. A., et al. (2017). Quantitative-mechanistic Model for Assessing Landslide Probability and Pipeline Failure Probability Due to Landslides. *Eng. Geology*. 222, 212–224. doi:10.1016/j.enggeo.2017.04.005
- Balek, J., and Blahút, J. (2016). A Critical Evaluation of the Use of an Inexpensive Camera Mounted on a Recreational Unmanned Aerial Vehicle as a Tool for Landslide Research. *Landslides* 14 (3), 1217–1224. doi:10.1007/s10346-016-0782-7
- Bittelli, M., Valentino, R., Salvatorelli, F., and Rossi Pisa, P. (2012). Monitoring Soil-Water and Displacement Conditions Leading to Landslide Occurrence in Partially Saturated Clays. *Geomorphology* 173–174, 161–173. doi:10.1016/j.geomorph.2012.06.006
- Carla, T., Intrieri, E., Raspini, F., Bardi, F., Farina, P., Ferretti, A., et al. (2019). Perspectives on the Prediction of Catastrophic Slope Failures from Satellite InSAR. *Sci. Rep.* 9 (1), 14137. doi:10.1038/s41598-019-50792-y
- Delacourt, C., Allemand, P., Berthier, E., Raucoules, D., Casson, B., Grandjean, P., et al. (2007). Remote-sensing Techniques for Analysing Landslide Kinematics: a Review. *Bull. de la Société Géologique de France* 178 (2), 89–100. doi:10.2113/gssgfbull.178.2.89
- EGIG (2020). “11th Report of the European Gas Pipeline Incident Data Group, 1970–2019,”. Available at: <https://www.egig.eu/>.
- Feng, W., and Huang, J. Z. (2009). Influence of Landslide Deformation on Safety of Gas Pipeline. *Chin. J. Geol. Hazard. Control*. 20 (1), 51–54. (In Chinese).
- Gao, P., Gao, Z. Y., and Liu, G. R. (2021). New Progress in China's Oil and Gas Pipeline Construction in 2020. *Int. Petrol. Econ.* 29, 53–60.
- Giordan, D., Hayakawa, Y., Nex, F., Remondino, F., and Tarolli, P. (2018). Review Article: The Use of Remotely Piloted Aircraft Systems (RPASs) for Natural Hazards Monitoring and Management. *Nat. Hazards Earth Syst. Sci.* 18 (4), 1079–1096. doi:10.5194/nhess-18-1079-2018
- GlobalData (2020). Global Length and Capital Expenditure Outlook for Oil and Gas Pipelines, 2020–2024: Asia Leads Global Pipeline Growth. Available at: <https://store.globaldata.com/report/global-length-and-capital-expenditure-outlook-for-oil-and-gas-pipelines-2020%e2%88%922024-asia-leads-global-pipeline-growth/>
- Hall, W., Nyman, D., Johnson, E., and Norton, J. (2003). “Performance of the Trans-Alaska Pipeline in the November 3, 2002 Denali Fault Earthquake,” in Sixth U.S. Conference and Workshop on Lifeline Earthquake Engineering (TCLEE) 2003, Long Beach, California, United States, August 10–13, 2003. doi:10.1061/40687(2003)54
- Honegger, D. G., Hart, J. D., Phillips, R., Popelar, C., and Gailing, R. W. (2010). Recent PRCI Guidelines for Pipelines Exposed to Landslide and Ground Subsidence Hazards. *8th Int. Pipeline Conf.* Vol. 2, 71–80. doi:10.1115/ipc2010-31311
- Lahousse, T., Chang, K. T., and Lin, Y. H. (2011). Landslide Mapping with Multi-Scale Object-Based Image Analysis - a Case Study in the Baichi Watershed, Taiwan. *Nat. Hazards Earth Syst. Sci.* 11 (10), 2715–2726. doi:10.5194/nhess-11-2715-2011
- Leynes, R. D., Pioquinto, W. P. C., and Caranto, J. A. (2005). Landslide hazard Assessment and Mitigation Measures in Philippine Geothermal fields. *Geothermics* 34 (2), 205–217. doi:10.1016/j.geothermics.2004.08.002
- Li, C., Huiming, T., Liangqing, W., and Jing, H. (2009). “Hazard Evaluation Method Study on Pipeline of Underground Crossing Landslide Area,” in International Conference on Pipelines and Trenchless Technology (ICPTT) 2009, Shanghai, China, October 18–21, 2009, 1081–1092. doi:10.1061/41073(361)115
- Li, G., Hu, B., Li, H., Lu, F., and Maruccio, G. (2021). Early Identifying and Monitoring Landslides in Guizhou Province with InSAR and Optical Remote Sensing. *J. Sensors* 2021, 1–19. doi:10.1155/2021/6616745
- Liu, P. F., Zheng, J. Y., Zhang, B. J., and Shi, P. (2010). Failure Analysis of Natural Gas Buried X65 Steel Pipeline under Deflection Load Using Finite Element Method. *Mater. Des.* 31 (3), 1384–1391. doi:10.1016/j.matdes.2009.08.045
- Luo, X., Wang, F., Zhang, Z., and Che, A. (2008). Establishing a Monitoring Network for an Impoundment-Induced Landslide in Three Gorges Reservoir Area, China. *Landslides* 6 (1), 27–37. doi:10.1007/s10346-008-0140-5
- Macciotta, R., Hendry, M., and Martin, C. D. (2015). Developing an Early Warning System for a Very Slow Landslide Based on Displacement Monitoring. *Nat. Hazards* 81 (2), 887–907. doi:10.1007/s11069-015-2110-2
- Marek, L., Mirijovsky, J., and Tuček, P. (2015). Monitoring of the Shallow Landslide Using UAV Photogrammetry and Geodetic Measurements. *Eng. Geology. Soc. Territory* 2, 113–116. doi:10.1007/978-3-319-09057-3_8
- Marinos, V., Stoumpos, G., and Papazachos, C. (2019). Landslide Hazard and Risk Assessment for a Natural Gas Pipeline Project: The Case of the Trans Adriatic Pipeline, Albania Section. *Geosciences* 9 (2), 61. doi:10.3390/geosciences9020061
- Martha, T. R., Kerle, N., Jetten, V., van Westen, C. J., and Kumar, K. V. (2010). Characterising Spectral, Spatial and Morphometric Properties of Landslides for Semi-automatic Detection Using Object-Oriented Methods. *Geomorphology* 116 (1–2), 24–36. doi:10.1016/j.geomorph.2009.10.004
- Peppas, M. V., Mills, J. P., Moore, P., Miller, P. E., and Chambers, J. E. (2017). Brief Communication: Landslide Motion from Cross Correlation of UAV-Derived Morphological Attributes. *Nat. Hazards Earth Syst. Sci.* 17 (12), 2143–2150. doi:10.5194/nhess-17-2143-2017
- Peternel, T., Kumelj, Š., Oštir, K., and Komac, M. (2017). Monitoring the Potoška Planina Landslide (NW Slovenia) Using UAV Photogrammetry and Tachymetric Measurements. *Landslides* 14 (1), 395–406. doi:10.1007/s10346-016-0759-6
- Rossi, G., Tanteri, L., Tofani, V., Vannocci, P., Moretti, S., and Casagli, N. (2018). Multitemporal UAV Surveys for Landslide Mapping and Characterization. *Landslides* 15 (5), 1045–1052. doi:10.1007/s10346-018-0978-0
- Strozzi, T., Farina, P., Corsini, A., Ambrosi, C., Thüring, M., Zilger, J., et al. (2005). Survey and Monitoring of Landslide Displacements by Means of L-Band Satellite SAR Interferometry. *Landslides* 2 (3), 193–201. doi:10.1007/s10346-005-0003-2
- Turner, D., Lucieer, A., and de Jong, S. (2015). Time Series Analysis of Landslide Dynamics Using an Unmanned Aerial Vehicle (UAV). *Remote Sensing* 7 (2), 1736–1757. doi:10.3390/rs70201736
- Vasconez, F., Estrella, M., Velastegui, A., Nunez, J., Ponce, H., and Riofrio, P. (2010). Landslide Hazard Assessment, Monitoring, and Stabilization: Villano Oil Pipeline System, Ecuador. in SPE Annual Technical Conference and Exhibition, Florence, Italy, September 2010. doi:10.2118/135504-ms
- Vasseggh, A., Haghshenas, E., Soroushian, A., and Rakhshandeh, M. (2021). Failure Analysis of a Natural Gas Pipeline Subjected to Landslide. *Eng. Fail. Anal.* 119, 105009. doi:10.1016/j.engfailanal.2020.105009
- Vaziri, A., Moore, L., and Ali, H. (2010). Monitoring Systems for Warning Impending Failures in Slopes and Open Pit Mines. *Nat. Hazards* 55 (2), 501–512. doi:10.1007/s11069-010-9542-5
- Wasowski, J., and Bovenga, F. (2014). Investigating Landslides and Unstable Slopes with Satellite Multi Temporal Interferometry: Current Issues and Future Perspectives. *Eng. Geology*. 174, 103–138. doi:10.1016/j.enggeo.2014.03.003

FUNDING

This study was financially supported by the National Natural Science Foundation of China (No. 42120104002 and No. 41901008), the Fundamental Research Funds for the Project of Science and Technology Department of Sichuan Province (No. 2020YFH0085).

- Yan, Y., Ma, S., Yin, S., Hu, S., Long, Y., Xie, C., et al. (2021). Detection and Numerical Simulation of Potential Hazard in Oil Pipeline Areas Based on UAV Surveys. *Front. Earth Sci.* 9. doi:10.3389/feart.2021.665478
- Yan, Y., Yang, D.-s., Geng, D.-x., Hu, S., Wang, Z.-a., Hu, W., et al. (2019). Disaster Reduction Stick Equipment: A Method for Monitoring and Early Warning of Pipeline-Landslide Hazards. *J. Mt. Sci.* 16 (12), 2687–2700. doi:10.1007/s11629-019-5613-6
- Yan, Y., Zhang, Y., Hu, W., Guo, X.-j., Ma, C., Wang, Z.-a., et al. (2020). A Multiobjective Evolutionary Optimization Method Based Critical Rainfall Thresholds for Debris Flows Initiation. *J. Mt. Sci.* 17 (8), 1860–1873. doi:10.1007/s11629-019-5812-1
- Yin, Y., Wang, H., Gao, Y., and Li, X. (2010). Real-time Monitoring and Early Warning of Landslides at Relocated Wushan Town, the Three Gorges Reservoir, China. *Landslides* 7 (3), 339–349. doi:10.1007/s10346-010-0220-1
- Zhang, Y., Meng, X. M., Dijkstra, T. A., Jordan, C. J., Chen, G., Zeng, R. Q., et al. (2020). Forecasting the Magnitude of Potential Landslides Based on InSAR Techniques. *Remote Sensing Environ.* 241, 111738. doi:10.1016/j.rse.2020.111738
- Zhao, Z. G., Yao, A. L., and Zhao, X. F. (2006). Types of Geologic Disasters for Long Distance Transmission Pipelines as Well as Prevention Control Measures and Prediction Techniques. *Pet. Eng. Constr.* 32, 7–12. doi:10.3969/j.issn.1001-2206.20
- Zheng, J. Y., Zhang, B. J., Liu, P. F., and Wu, L. L. (2012). Failure Analysis and Safety Evaluation of Buried Pipeline Due to Deflection of Landslide Process. *Eng. Fail. Anal.* 25, 156–168. doi:10.1016/j.engfailanal.2012.05.011
- Zhou, X. J. (2018). Analysis of 10 Third Party Damage Accidents of High Pressure and above Gas Pipeline from 2009 to 2017. *Technology Market* 25, 59–61+64.
- Conflict of Interest:** Author WH, MY are employed by Guangdong Dapeng LNG Company Ltd. Author DG is employed by Analysis and Test Center of Sichuan Province.
- The remaining authors declare that the research was conducted in the absence of any commercial or financial relationships that could be construed as a potential conflict of interest.
- Publisher's Note:** All claims expressed in this article are solely those of the authors and do not necessarily represent those of their affiliated organizations, or those of the publisher, the editors and the reviewers. Any product that may be evaluated in this article, or claim that may be made by its manufacturer, is not guaranteed or endorsed by the publisher.

Copyright © 2022 Yan, Xiong, Zhou, Wang, Huang, Yang, Wang and Geng. This is an open-access article distributed under the terms of the Creative Commons Attribution License (CC BY). The use, distribution or reproduction in other forums is permitted, provided the original author(s) and the copyright owner(s) are credited and that the original publication in this journal is cited, in accordance with accepted academic practice. No use, distribution or reproduction is permitted which does not comply with these terms.



Study on Evaluation and Prediction of the Degree of Surface Damage Caused by Coal Mining

Xiaoshen Xie^{1,2*}, Enke Hou^{1,2*}, Tianwen Long^{1,2}, Dong Feng^{1,2}, Pengfei Hou^{1,2}, Qiming Wei³, Yang Li⁴ and Jiangbin Liu⁴

¹College of Geology and Environment, Xi'an University of Science and Technology, Xi'an, China, ²Shaanxi Provincial Key Laboratory of Geological Support for Coal Green Exploitation, Xi'an, China, ³Shicaocun Coal Mine of Ningxia Coal Industry Co., Ltd. of National Energy Group, Lingwu, China, ⁴Yangchangwan Coal Mine of Ningxia Coal Industry Co., Ltd. of National Energy Group, Lingwu, China

OPEN ACCESS

Edited by:

Wen Nie,
Jiangxi University of Science and
Technology, China

Reviewed by:

Zhen Huang,
Jiangxi University of Science and
Technology, China
Yanxu Zhang,
China University of Mining and
Technology, China
Weiqiang Zhang,
China University of Mining and
Technology, China

*Correspondence:

Xiaoshen Xie
xxswpp0816@163.com
Enke Hou
houek@xust.edu.cn

Specialty section:

This article was submitted to
Geohazards and Georisks,
a section of the journal
Frontiers in Earth Science

Received: 30 October 2021

Accepted: 29 November 2021

Published: 21 January 2022

Citation:

Xie X, Hou E, Long T, Feng D, Hou P,
Wei Q, Li Y and Liu J (2022) Study on
Evaluation and Prediction of the
Degree of Surface Damage Caused by
Coal Mining.
Front. Earth Sci. 9:805248.
doi: 10.3389/feart.2021.805248

Surface damage caused by coal mining is one of the problems perplexing ecological environment restorations in coal mining areas. Accurately evaluating and predicting the degree of surface damage induced by coal mining with reasonable and correct indexes are of great significance to the restoration and treatment of the ecological environment. In this paper, these methods including the unmanned aerial vehicle aerial photography and manual measurement were used to investigate the development characteristics of surface damage caused by 2[#] coal seam mining in Yangchangwan Coal Mine. The results showed that with the change of mining conditions, the characteristics of surface cracks change obviously, which can be adopted to indicate the degree of surface damage. Thus, based on the results of the investigation, the classification standard of surface damage degree was established based on the evaluation indexes including density of crack, drop height of surface crack, crack width, maximum surface subsidence, and geological disaster caused by cracks and the damage characteristics of buildings. The evaluation method and process of surface damage degree also were given. Based on the ratio of the buried depth to the thickness of the coal seam (H/M), ratio of the thickness of overlying bedrock to the thickness of the coal seam, the thickness of loose layers (Ms), geomorphology, distance to faults, and distance to folds, the prediction model of surface damage degree was built on the GIS platform. The weight coefficient of each prediction index was obtained by the analytic hierarchy process (AHP) method. The surface damage degree map of 2[#] coal seam in Yangchangwan Coal Mine was divided into four classes: very minor, minor, moderate, and serious, which provides a relatively applicable method for the prediction of surface damage degree in Yangchangwan Coal Mine and its adjacent mining areas.

Keywords: ground collapse, surface damage, coal mining, GIS, AHP, Yangchangwan coal mine

INTRODUCTION

At present, the proportion of coal consumption to total primary energy consumption began to decline after implementation of the coal industry rationalization action by the Chinese government (Wang et al., 2020; Yan et al., 2018; Xie et al., 2021). But coal still plays an important role in the development of regional economy, especially the western China economy (Yan et al., 2021; Zhu et al., 2018). Undoubtedly, exploitation of coal resources will do harm to the environment of the ground

surface, such as exhaustion of groundwater resources, death of vegetation, cracking of the land, and damage to surface structures, such as railroad tracks, roads, and buildings. Moreover, with the increase of scale and intensity of coal resources, the environmental problems caused by mining will be more serious (Zeng et al., 2020; Xu Y. et al., 2019; Fan et al., 2017; Fan et al., 2015; Huang et al., 2013; Bell et al., 2000). Thus, clearly grasping the distribution of ground subsidence and accurately evaluating the susceptibility of ground subsidence is the prerequisite for ensuring the safety of the workers and restoration and treatment of the environment.

Evaluation is a description and characterization of objects that have emerged (Djamaluddin et al., 2011; Si et al., 2010). Some indicators including water (Guo, et al., 2019; Xiao et al., 2020; Zeng et al., 2020), landform (Hu Z. et al., 2014a), landscape (Xu J. et al., 2019; Quanyuan et al., 2009), geological disaster (Shao, 2019), and building damage (Djamaluddin, et al., 2011; Malinowska and Hejmanowski, 2010) have been used to evaluate the degree of ground collapse. In addition, Yu et al. divided the land subsidence damage into four grades using the surface subsidence (Yu, et al., 2008). Youfeng Zou et al. divided the land damage into six grades according to the stable ground slope, the relationship between surface inclination deformation, and soil erosion (Zou, et al., 2003). Xiaojing Li et al. used the surface crack, surface subsidence and collapse crater, and additional gradient to classify the degree of land damage caused by coal mining (Li, et al., 2012). Zishao Zhang et al. determined the evaluation criteria for the degree of geological environment induced by coal mining using the horizontal deformation, the deformation of slope, and curvature (Zhang and Sui, 2017).

The above results have laid the foundation for the in-depth study of the evaluation of the degree of surface damage. However, it was impractical to use the horizontal movement deformation and tilt deformation as an index to evaluate the degree of surface damage because not all working faces have these two values that need to be measured for a long time, and the cost is relatively high to obtain these two parameters. In addition, for the workers in the coal mine, the evaluation standard established in the above research is too complex to be applied in practical work. For these reasons, selecting intuitive, convenient, and easy to obtain parameters as the index to evaluate the degree of surface damage caused by working in face mining is one of the problems to be solved in the paper.

Generally, surface damage can be decreased to a certain extent by predicting the degree of surface damage. In recent years, several models including the analytic hierarchy process (AHP) (Rezaei, et al., 2020; Zhang, et al., 2011), artificial neural network (ANN) (Lee, et al., 2012; Kim, et al., 2009), rough set (RS) (Feng and Luo, 2016), and other methods in tandem with GIS were adopted to evaluate the ground subsidence susceptibility caused by coal mining by some experts. But there are two shortcomings. One is that the above research methods or models were used to predict the ground subsidence susceptibility rather than the degree of surface damage, the other was that the indicators used for prediction were not consistent with parameters of coal mining such as mining thickness of coal seam, depth of

coal seam, bedrock thickness, thickness of soil layer, and so on. Therefore, using the reasonable prediction model to predict the degree of surface damage caused by coal mining with appropriate factors is another problem to be solved in this paper.

In order to complete the research content, Yangchangwan Coal Mine was taken as the study area and the UAV remote sensing and field investigation were applied to investigate the ground collapse caused by working face mining. According to the survey results, the evaluation factors of surface damage were determined, and then the surface damage level was divided. Combined with the coal mining information and geological information of the working face, the prediction model of surface damage could be established with the appropriate index of surface damage under the GIS platform.

GENERAL SITUATION OF THE STUDY AREA AND INVESTIGATION METHOD

General Situation of the Study Area

Yangchangwan Coal Mine chosen as the study area is located in Ningxia Province, China, within latitudes 37°54'49" N to 38° 02' 27" N, and longitudes 106°33'46" E to 106°39'49" E (Figure 1). The study area belongs to Ningxia Coal Industry Group, which is an important mining area in the coal base located in the east of Ningxia. The coal mine's length is about 12.8 km from north to south, and its width is approximately 9.8 km, the overall area is about 58.21 km². Land types in the study area are mainly grass, bare land, and residential areas. The altitude ranges from 1,320.25 m to 1,497.69 m and increases from north to south. The surface is mainly covered by the loess and wind aeolian loose layer, and bedrock appears sporadically.

As can be seen from Figure 2, the strata, from old to new, in the coal mine are mainly Triassic, Jurassic, Cretaceous, and Quaternary. The Yanan formation of Jurassic is the main coal bearing strata in the area, with an average thickness of 91.47 m, which contains 32 layers of coal seam. Among these coal seams, the stable 2[#] coal seam with dip angle ranges from 5° to 28° is being mined. The occurrence thickness of 2[#] coal seam ranges from 4.73 to 10.66 m (7.80 m averagely), and the mining depth ranges from 50 to 1,300 m and decreases from north to south. The thickness of the surface loose layer ranges from 1.65 to 36.95 m, and the average thickness is 10.17 m. There are about 23 faults in the study area, of which 15 faults are normal and eight faults are reverse. In addition, there are nine folds in the region.

Methods for Investigation of Surface Damage

Ground collapse, which includes surface crack, surface subsidence, collapse, and landslide caused by coal mining, is the main form of surface damage and also is the object of this investigation. In order to accurately obtain the surface damage date of each working face, UAV and manual monitoring were carried out (Figure 3), and the indexes of UAV are shown in Table 1.

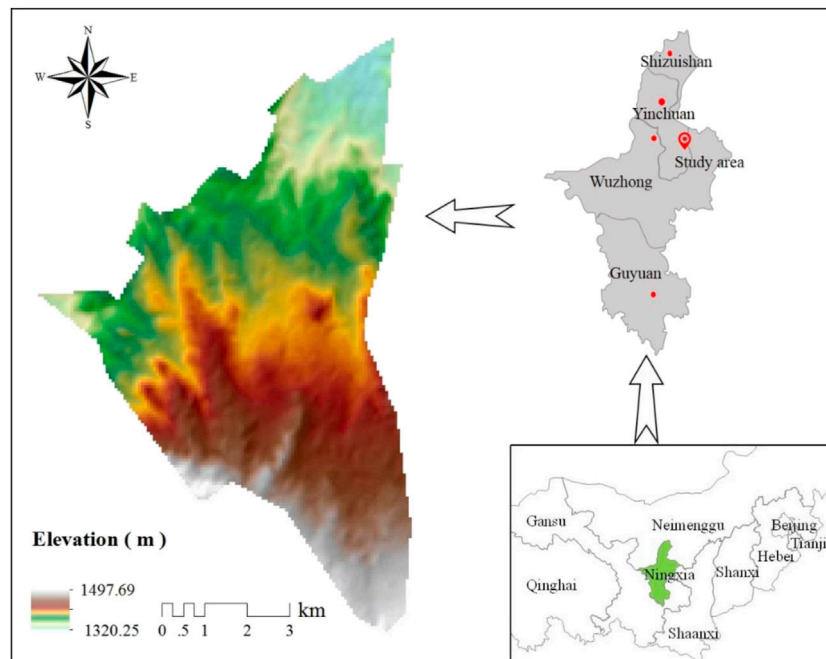


FIGURE 1 | Study area location.

EVALUATION OF SURFACE DAMAGE DEGREE

Results of Investigation on Surface Damage

A total of 10 working faces were investigated in the study area (**Figure 4**). The surface damage caused by 120,211 and 120,209 working face mining had been repaired. Thus, there is a lack of data on surface damage induced by 120,211 and 120,209 working face. The investigation results of the remaining working faces are shown in **Table 2**.

The surface damage caused by 110,207 working face located in the north of the study area was serious. The density of surface cracks was 181 l/km² (l/km² indicates the number of cracks in the 1 km² area), the maximum width and the maximum drop height of surface cracks were 150 and 160 cm, respectively. A collapse groove with a width of 4.0 m was developed on the surface above the working face. Since the surface subsidence had not been measured in the mining process of the working face, there is no way to obtain the maximum surface subsidence. In addition, the number of associated disasters caused by the working face was zero, and there were no roads and buildings above the working face.

The density of surface cracks, the maximum width, and the maximum drop height caused by 110,201 working face were 280 l/km², 76 cm, and 45 cm, respectively. There was no collapse groove, associated disasters, roads and buildings above the working face, and the surface subsidence was not measured in the mining process.

The density of surface cracks, the maximum width, and the maximum drop height caused by 120,215 working face were

206 l/km², 34 cm, and 10 cm, respectively. There was no collapse groove, associated disasters, or roads and buildings above the working face. The maximum subsidence was not obtained.

In 120,210 working face, the surface damage characteristics are more obviously caused by coal mining. The density of surface cracks is 145 l/km², the width is generally less than 30 cm, and the maximum drop height was 18 cm. There was no measured data on surface subsidence and buildings. However, a road in the working face was cracked by coal mining.

The 130,204 working face was located in the south of the mine field. The surface damage caused by 130,204 working face was minor, the density of surface cracks is 41 l/km², and the maximum drop height and width of surface cracks were 8 and 15 cm. There was no collapse groove development in the working face. In addition, there are no roads and buildings in the working face.

According to the survey results, the density of the surface cracks was 104 l/km², the maximum drop height and width of the surface cracks caused by 160,203 working face were 11 and 30 cm, respectively. After mining, there were no collapse groove and associated disasters on the surface.

The density of surface cracks caused by 120,212 working face was 65 l/km² and all surface cracks have no drop height, the maximum width was 5 cm. Furthermore, the road in the working face was intact.

As similar to 120,212 working face, the surface damage induced by 160,202 working face was very minor. The surface crack was the only form of surface damage. The density of surface cracks was 61 l/km², the maximum drop height and width were 5 and 21 cm, respectively.

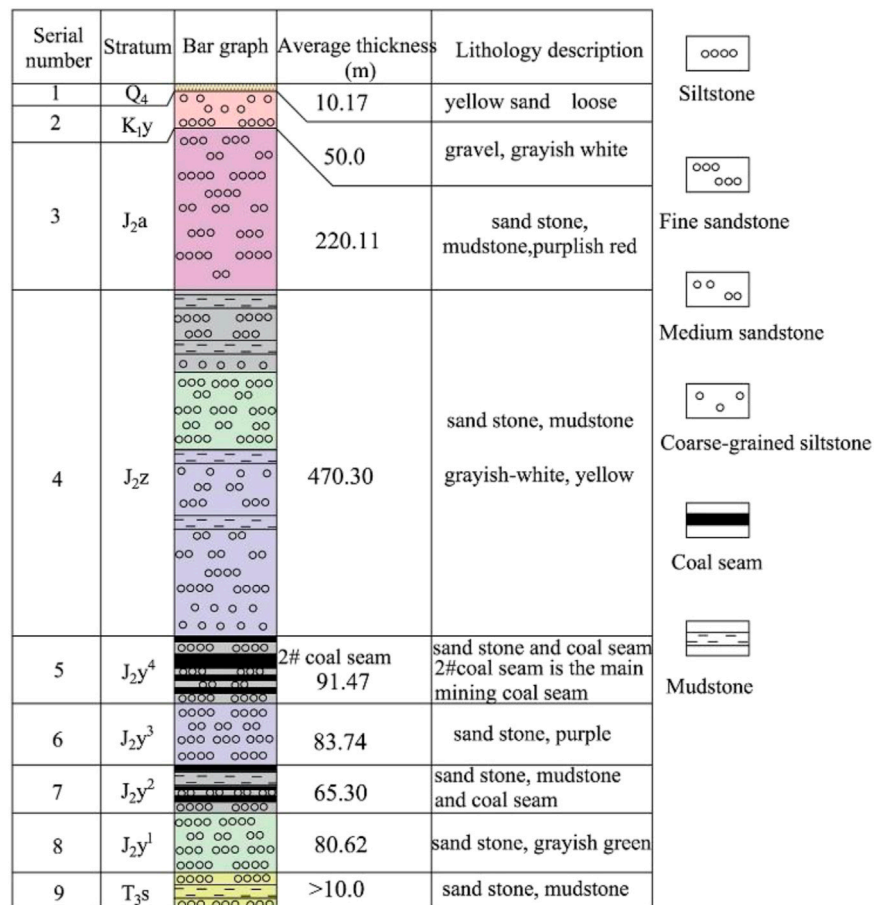


FIGURE 2 | The overburden strata histogram of the 2[#] coal seam.

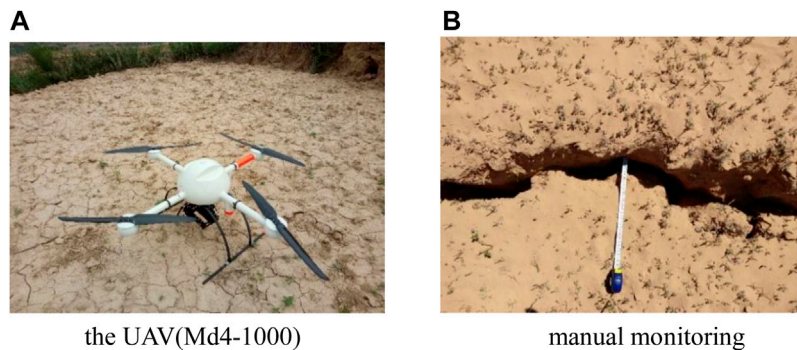


FIGURE 3 | Methods for investigation of surface damage. **(A)** The UAV(Md4-1,000). **(B)** Manual monitoring.

CLASSIFICATION OF SURFACE DAMAGE DEGREE OF WORKING FACE

According to the investigation results of surface damage caused by working face, the surface crack was the most intuitive and convenient parameter to characterize the surface damage degree. Based on the

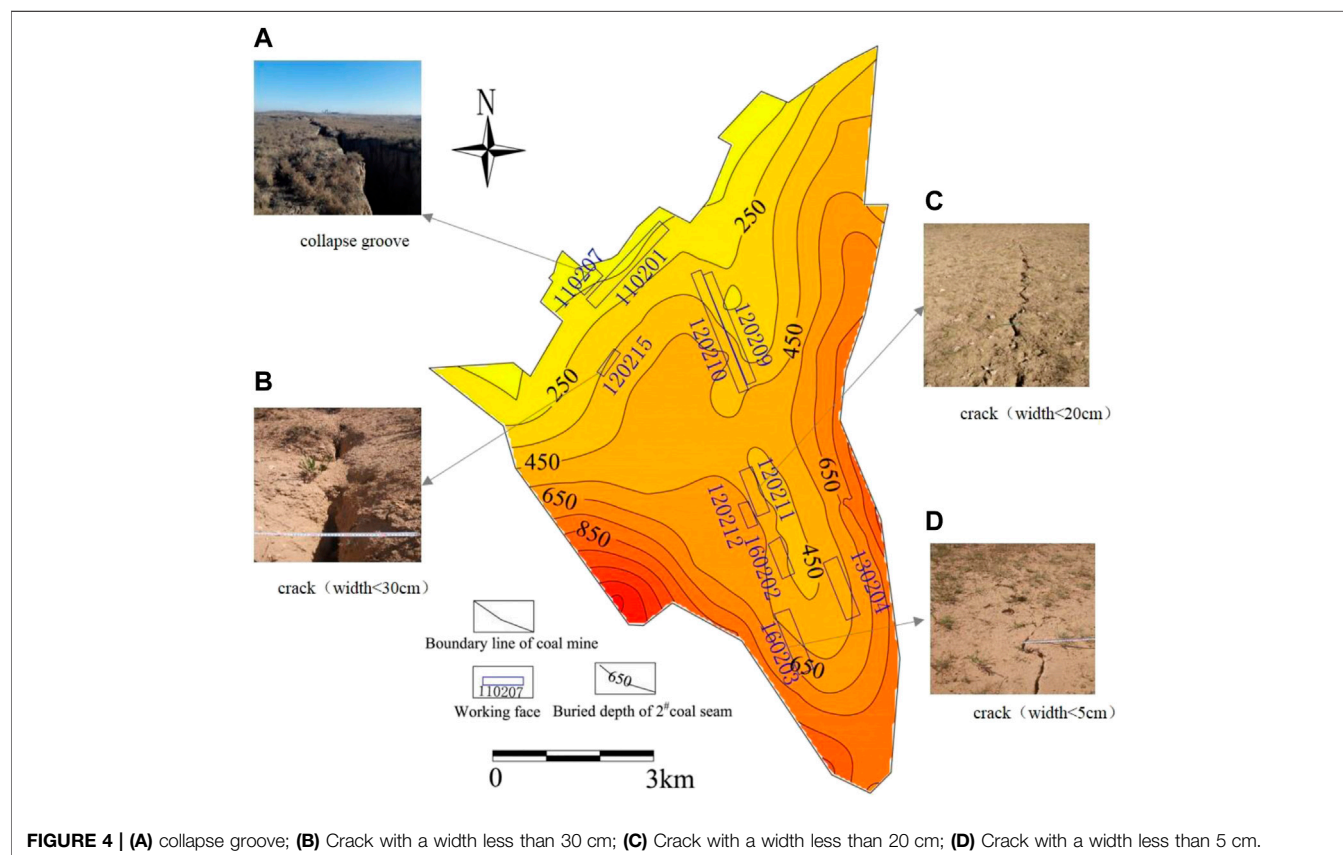
combination of actual management experience and the investigation results, the crack density, maximum drop height, maximum width, maximum subsidence, associated disasters, and other features were taken as the classification standard of the surface damage degree, and the degree of surface damage was divided into four grades, which were serious, moderate, minor, and very minor (**Table 3**).

TABLE 1 | The indexes of UAV.**Performance of UAV (Md4-1,000)**

Climbing rate	7.5 m/s	Cruising speed	15.0 m/s
Maximum power	1,000 w	Weight of the UAV	2,650 g
Flight time	< 50 min	Load	2000 g
Flight radius	5,000 m	Flight altitude	1,000 m
Remote control distance	5,000 m	Wind resistance	<12 m/s

EVALUATION RESULT OF SURFACE DAMAGE DEGREE OF WORKING FACE

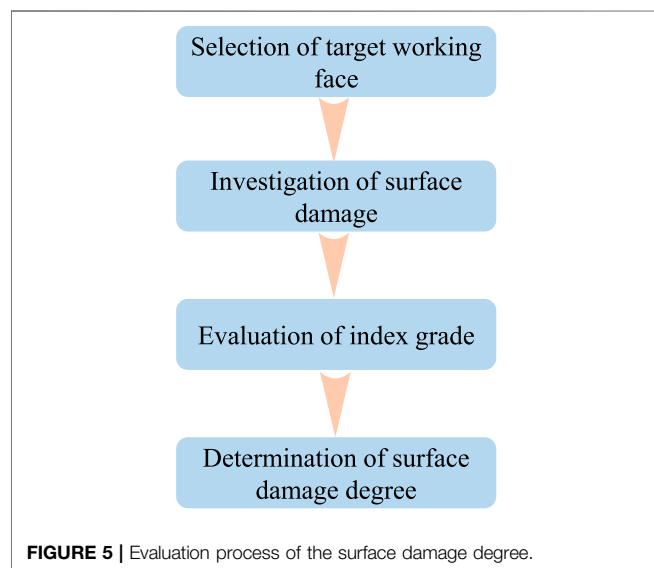
The evaluation process of the surface damage degree is shown in **Figure 5**. The first step was selection of target working face. The second step was to investigate the surface damage characteristics of the target face. The third step was to evaluate the index grade according to **Table 3**. The last step was to take the highest grade of the index as the grade of the

**TABLE 2 |** Results of surface damage.

Name	Surface crack			Collapse	Maximum subsidence (m)	Number of associated disasters	Other features	
	Crack density (/km ²)	Maximum drop (cm)	Maximum width (cm)				Roads	Buildings
110,207	181	160	150	400	No data	0	No roads	No buildings
110,201	280	45	76	0	No data	0	No roads	No buildings
120,215	206	10	34	0	No data	0	No roads	No buildings
120,210	145	18	30	0	No data	0	Cracked	No buildings
130,204	41	8	15	0	No data	0	No roads	No buildings
160,203	104	11	30	0	No data	0	No roads	No buildings
120,212	65	0	5	0	No data	0	Intact	Cracked
160,202	61	5	21	0	No data	0	No roads	No buildings

TABLE 3 | The degree of surface damage.

Surface damage degree	Crack density (l/km ²)	Maximum drop (cm)	Maximum width (cm)	Maximum subsidence (m)	Associated disasters	Other features	
						Roads	Buildings
Very minor	< 20	0	< 1.0	< 0.1	0	Intact	Intact
Minor	20 ~ 100	< 5.0	1.0 ~ 30	0.1 ~ 1.0	< 10	Deformed	Deformed
Moderate	100 ~ 300	5.0 ~ 30	1.0 ~ 50	1.0 ~ 3.0	10 ~ 50	Cracked	Cracked
Serious	>300	>30	>50	>3.0	>50	Severely cracked	Severely cracked

**TABLE 4** | The degree of surface damage of the working face in the study area.

The name of the working face	The degree of surface damage
110,207	Serious
110,201	Serious
120,215	Moderate
120,210	Moderate
130,204	Moderate
160,203	Moderate
120,212	Minor
160,202	Moderate

surface damage degree of the working face according to the evaluation results of the index.

According to the above evaluation process and combined with the formulated level of the surface damage degree, the evaluation of the surface damage degree of 8 working faces in the study area was completed, and the results were as follows: the degree of surface damage caused by 110,207 working face and 110,201 working face were serious, the degree of surface damage induced by 120,215, 120,210, 130,204, 160,203, and 160,202 working face mining were moderate, and that induced by 120,212 the degree of surface damage was minor (Table 4).

PREDICTION OF SURFACE DAMAGE

Factors of the Surface Damage Degree

According to previous literature and surface damage of the study area, 6 conditioning factors were selected, including the ratio of the buried depth to the thickness of the coal seam (H/M), ratio of the thickness of overlying bedrock to the thickness of the coal seam, the thickness of the loose layer (Ms), geomorphology, distance to faults, and distance to folds in the study. All above factor maps were converted into raster format with a spatial resolution of 20 × 20 m.

The actual mining thickness of the coal seam is generally less than or equal to the thickness of the coal seam, which is positively correlated with the degree of surface damage induced by coal mining. In general, the working face with large mining thickness has a large goaf after mining, which provides sufficient activity space for the overlying strata, which leads to the stronger disturbance to the surface. The buried depth of the coal seam is negatively correlated with the degree of surface damage. Generally, the greater the buried depth of the coal seam, the longer the time for the disturbance caused by mining to be transmitted to the surface, the more attenuation of the disturbance, and the more minor the surface damage. Therefore, in the study the ratio of the buried depth to the thickness of the coal seam (H/M) was taken as a factor to predict the degree of surface damage caused by coal mining. The ratio (H/M) was reclassified into four classes (Figure 6A).

As a parameter negatively related to the degree of surface damage caused by coal mining, the thickness of overlying bedrock can prolong the time for the deformation to extend to the surface, which reduces the degree of surface damage induced by coal mining. Thus, in the present study, the ratio of the thickness of overlying bedrock to the thickness of the coal seam (Hj/M) was reclassified into four categories: < 45, 45–70, 70–95, >95 (Figure 6B).

The loose layer refers to the sedimentary strata in Quaternary and Neogene, which has great influence on the characteristics of surface movement, especially horizontal movement and horizontal deformation. Commonly, the greater the thickness of the loose layer, the more uniform the surface deformation and the smaller the less developed the surface cracks. The thickness of the loose layer (Ms) of the study area ranged from 0 to 56 m and was divided into four classes (Figure 6C).

Geomorphology is also an important factor affecting the degree of surface damage caused by coal mining. Generally, the surface damage induced by coal mining under the loess

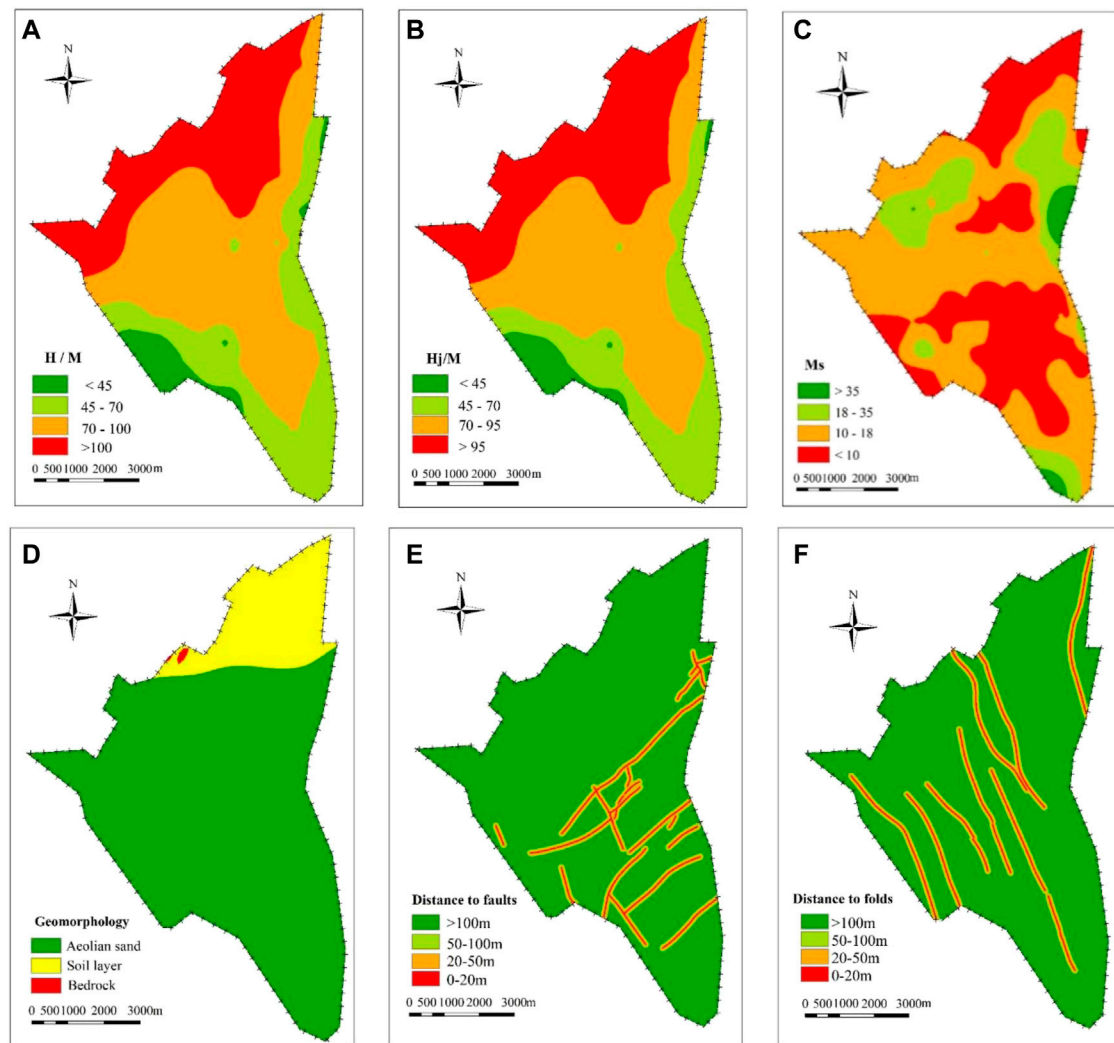


FIGURE 6 | Study area thematic area: **(A)** H/M, **(B)** H/M, **(C)** Ms, **(D)** geomorphology, **(E)** distance to faults, and **(F)** distance to folds.

gully landform is more serious than that under the sandy region. In this study, the geomorphology was reclassified into three categories: aeolian sand, soil layer, and bedrock (**Figure 6D**). Generally, the degree of surface damage caused by coal mining under bedrock was greatest, and the degree of surface damage was least under aeolian sand.

As an independent index, the fault restricts the surface damage by means of affecting the mechanical property of the bedrock and the slip of faults along the cross-section. In general, the surface damage caused by mining of the working face near the geological fault is relatively serious because the surrounding rock strength decreases, and fault slip due to tectonic break. In this study, the fault buffers were reclassified into four categories to produce the map of distance to the faults (**Figure 6E**).

In general, mining leads to the superposition of overlying rock and surface movement caused by folds, and it is easy to appear as discontinuous movement and deformation and increase the amount of subsidence on the axis of folds. Thus, the surface

damage caused by coal mining in the geological fold areas is more serious. Like distance to faults, fourfold buffers were created (**Figure 6F**).

METHODOLOGY OF AHP

In order to accurately predict the degree of surface damage by coal mining, the analytic hierarchy process (AHP) method, which is a multi-criteria decision making (MCDM) and was put forward by Saaty (1980), and was applied in the essay and was divided into four steps (Saaty, 1980; Durmuşoğlu, 2018; Gnanavelbabu and Arunagiri, 2018).

In the current study, building an AHP model is the first step. In this study, occurrence conditions of the coal seam are subdivided into the ratio of the buried depth to the thickness of coal seam (H/M) and the ratio of the thickness of overlying bedrock to the thickness of the coal seam (Hj/M). The geological

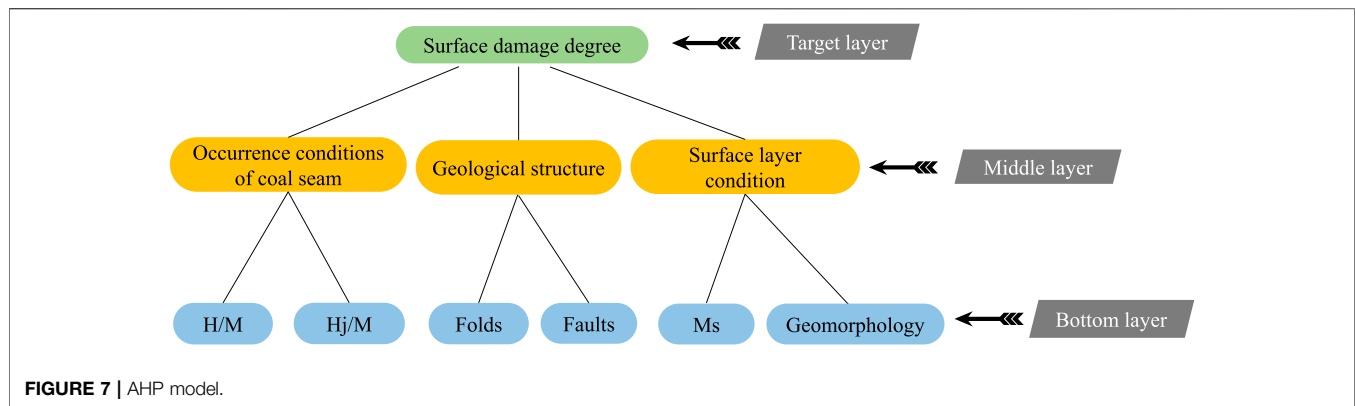


TABLE 5 | Weights of factors for prediction of the degree of surface damage.

Factors	Conditions of the coal seam		Geological structure		Surface layer condition	
	H/M	Hj/M	Distance to faults	Distance to folds	Geomorphology	Ms
Weights	0.271	0.453	0.052	0.031	0.072	0.121

structure condition is based on the fault and the fold. The surface layer condition is subdivided into two indexes such as thickness of loose layer (Ms) and geomorphology. The AHP model which was built in the previous step was divided into three layers, the degree of surface damage is the target layer (A layer). Occurrence conditions of the coal seam, the geological structure condition, and the surface layer condition belong to the middle layer (B layer). The bottom layer (C layer) consists of six factors derived from occurrence conditions of the coal seam, the geological structure condition, and the surface layer condition (Figure 7).

The second step was to construct a judgment matrix for the degree of surface damage caused by coal mining, which was used to verify the AHP model constructed in the first step by comparing the consistency parameters. The judgment matrix for the degree of surface damage is as follows:

$$A = \begin{bmatrix} C_{11} & C_{12} & C_{13} & C_{14} & C_{15} & C_{16} \\ C_{21} & C_{22} & C_{23} & C_{24} & C_{25} & C_{26} \\ \vdots & \vdots & \vdots & \vdots & \vdots & \vdots \\ C_{61} & C_{62} & C_{63} & C_{64} & C_{65} & C_{66} \end{bmatrix}$$

As the next step, sub-criteria under each main criterion are compared two by two by three experts by using Mesh cade software, and then the weight coefficient of each index was calculated. Table 5 indicates the weights for all factors, the sum of factor weights was 1, and the most important factor for the degree of surface damage is “ratio of the thickness of overlying bedrock to the thickness of the coal seam (Hj/M)” which weight was 0.465. The least important factor was folds which weight was 0.051. Finally, the key of the AHP method is the consistency test, which was adopted to examine the rationality of the judgment that was constructed in the previous step. As shown in Table 5, the consistency index of the judgment matrix (C_R) is

0.063 < 0.1, which indicated that the judgment matrix was reasonable.

$$C_R = 0.0623$$

Prediction Model of the Degree of Surface Damage

Based on the above analysis and the weight of each factor, the prediction model of the degree of surface damage was established, as follows:

$$W = \sum_{i=1}^n W_i \times f_i(x, y) = 0.271 \times f_1(x, y) + 0.453 \times f_2(x, y) + 0.052 \times f_3(x, y) + 0.031 \times f_4(x, y) + 0.048 \times f_5(x, y) + 0.145 \times f_6(x, y)$$

where W is the value indicating the degree of surface damage by coal mining, higher values indicate serious surface damage. w_i is the weight value of the i factor and $f_i(x, y)$ is the normalized value of the i.

RESULTS OF THE DEGREE OF SURFACE DAMAGE

First, the above factors of surface damage were normalized. The positive factors were normalized by Eq. 1, and the negative factors were normalized by Eq. 2. However, the geomorphology that cannot be normalized by the formula was normalized by the reassignment method. The aeolian sand area was assigned as 0.4, the soil area was assigned as 0.6, and 1.0 was assigned to the bedrock area.

Equation 1:

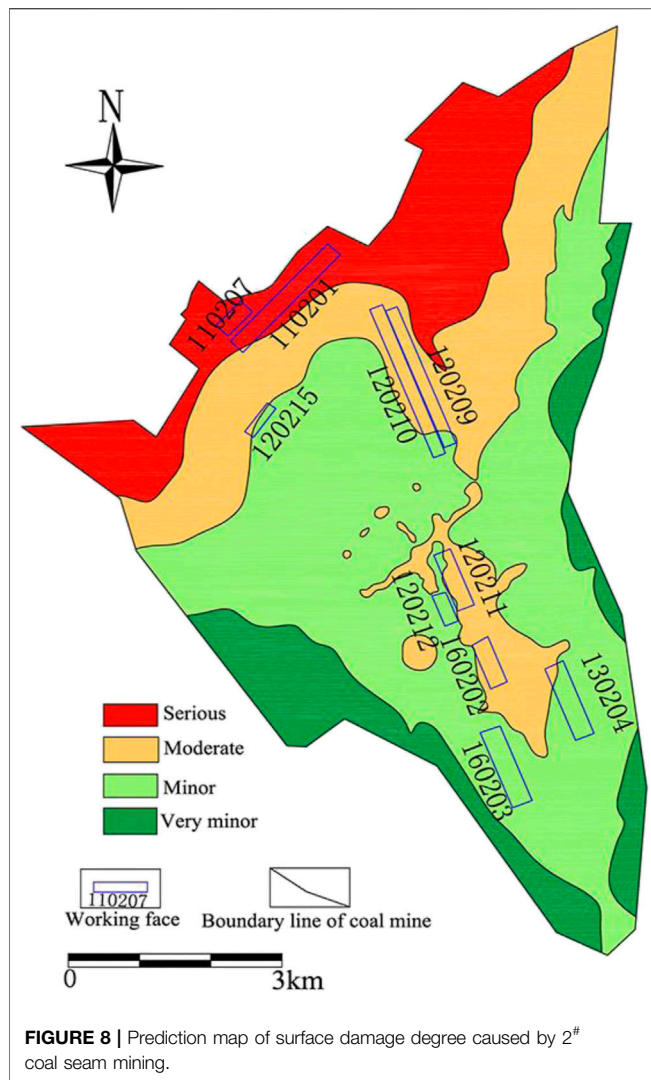


FIGURE 8 | Prediction map of surface damage degree caused by 2[#] coal seam mining.

$$x'_i = \frac{x_i - \min x_i}{\max x_i - \min x_i} \quad (1)$$

Equation 2:

$$x'_i = \frac{\max x_i - x_i}{\max x_i - \min x_i} \quad (2)$$

where the X'_i was the dimensionless value, X_i was the actual value of the i factor, $\min X_i$ was the minimum value in the index value, and $\max X_i$ was the maximum value in the index value.

Furthermore, the value of the degree of surface damage (W) was calculated using the prediction model. The calculated W values are in the range 0.1–0.9. After that, all W values were converted into ArcGIS 10.2 to produce the map of the degree of surface damage by 2[#] coal seam mining (Figure 8). Finally, the map was reclassified by the natural discontinuity method into four classes such as serious ($W > 0.7$), moderate ($0.50 < W < 0.7$), minor ($0.0.3 < W < 0.5$), and very minor ($0.10 < W < 0.3$). The area within 9.53 km² of the northern boundary of the Yangchanwan Coal Mine was severe. The 14.41 km² area in

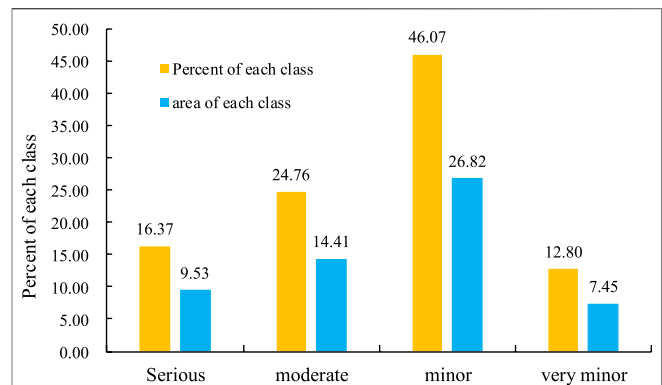


FIGURE 9 | Percentage of each class of the degree of surface damage.

TABLE 6 | Comparison of the degree of surface damage.

Names of working face	Evaluation degree	Predicted degree
110,207	Serious	Serious
110,201	Serious	Serious
120,215	Moderate	Moderate
120,210	Moderate	Moderate
130,204	Moderate	Moderate
160,203	Moderate	Minor
120,212	Minor	Minor
160,202	Minor	Moderate

the north and the middle was a moderately damaged area of surface damage. Meanwhile, due to the influence of folds and faults, some of the middle areas were striped and slightly scattered. The remaining parts were the minor area and very minor area. The area percentages of each class are shown in Figure 9. The minor class has the largest area (46.07%), followed by moderate (24.76%), serious (16.37%), and very minor (12.80%).

Validation of Prediction Results

The 8 usable working faces investigated in this study were added to the map of the degree of surface damage caused by 2[#] coal seam mining by using the back substitution method. In the 8 working faces, the degree of surface damage obtained by the prediction was basically consistent with the level of the evaluation, and the accuracy was 87.5% (Table 6), indicating that this method can be used for the prediction of the degree of surface damage induced by coal mining.

DISCUSSION

As an important part of the whole ecological environment in the coal mine, the surface ecological environment is bound to undergo negative changes due to coal mining. Especially in Northwest China, the impact of coal mining on the surface ecological environment is more serious. According to the

statistics, the total surface collapse area has exceeded 1,189 ha (Shang, 2013) in Lingwu mining area caused by large-scale coal mining, resulting in a continuous decline in the quality of the surface ecological environment. Thus, it is necessary to accurately evaluate the impact of coal mining on the surface environment based on determining the form and degree of surface damage. In this study, the surface damage degree and the classification standard were established. However, this evaluation system is only aimed at surface damage and is the basis of surface ecological environment assessment. Therefore, the evaluation system of vegetation and surface water resources needs to be constructed in the follow-up research, and then improve the evaluation system of the impact of coal mining on the surface ecological environment.

Several reports have shown that the surface damage caused by coal mining is a complex process, which can be summarized as two stages: rock collapse and topsoil deformation (Chen and Hu., 2018). In the stage of rock collapse, the overlying rock mass will subside and collapse under the action of gravity. In the stage of topsoil deformation, the movement and deformation of topsoil will damage the integrity of the surface. Surface damage mainly includes surface collapse, surface cracks, surface subsidence, and associated disasters, among which, surface cracks are the most common type of surface damage in the coal mine area. Different from the previous research results in using surface deformation parameters (Yu, et al., 2008; Zou, et al., 2003) to evaluate the degree of surface damage caused by coal mining, we selected surface cracks, associated disasters, and buildings as the basis for dividing the degree of surface damage, which reduces the difficulty of obtaining the characteristic data of the evaluation index.

There are many factors affecting the degree of surface damage caused by coal mining, which can be divided into three categories: coal mining, geology, and geomorphology (Hu, et al., 2014b). Therefore, the prediction of mining surface damage degree is a multi-disciplinary and complex research field, which needs to be combined with different data sources to predict the degree of surface damage. In this study, six conditioning factors were selected as prediction factors, and the prediction model of surface damage degree is constructed by the AHP method. Through superposition analysis, the prediction map of surface damage degree of 2[#] coal seam in the Yangchangwan Coal Mine was obtained. The minor class has the largest area (46.07%), followed by moderate (24.76%), serious (16.37%), and very minor (12.80%), and the overall accuracy is 87.5% (Table 6). However, in addition to the influencing factors discussed in this paper, the surface damage induced by coal mining is also related to the coal mining process, mining speed, working face layout, the nature of overlying bedrock, rainfall, and topography, and the control effect of each factor on the surface damage needs to be further studied. In addition, the prediction model of the surface damage degree constructed in this paper is relatively simple and does not involve more predictive factors such as multi-coal seam mining conditions, topography, lithology, and so on. The treatment method for structural geological conditions is relatively simple, so it is necessary to construct a complex prediction model covering multiple factors in future research.

CONCLUSION

- (1) Based on the results of the surface damage investigation, the degree and the classification standard were established with these factors including the crack density, maximum drop of crack, maximum width, maximum subsidence, the associated disasters, and other features. The degree was divided into four grades such as serious, moderate, minor, and very minor. Meanwhile, the evaluation method and process of surface damage degree by mining of the working face were given.
- (2) In this research, the AHP model was systematically analyzed for application in the prediction of surface damage caused by coal mining. Six factors were extracted for the study including ratio of the buried depth to the thickness of the coal seam (H/M), ratio of the thickness of overlying bedrock to the thickness of the coal seam (Hj/M), thickness of the loose layer (Ms), geomorphology, distance to faults, and distance to folds, and the weights for these factors were calculated, which were 0.271, 0.453, 0.121, 0.072, 0.052, and 0.031.
- (3) According to the predicted result of the degree of surface damage by 2[#] coal seam mining, four groups such as serious, moderate, minor, and very minor were reclassified by the natural discontinuity method, and the minor class has the largest area, followed by moderate, serious, and very minor. The verification result of the back-substitution method shows that the AHP model has an accuracy rate of 0.875. Finally, these study results may be useful for protection of the ecology.

DATA AVAILABILITY STATEMENT

The original contributions presented in the study are included in the article/Supplementary Material, further inquiries can be directed to the corresponding authors.

AUTHOR CONTRIBUTIONS

XX and EH provided all the basic data of this manuscript, determined the research ideas and methods, discussed the related research progress, and wrote this manuscript. TL collected data on surface cracks by UAV aerial photography. XX, DF, and PH completed the calculation based on AHP. QW, YL, and JL provided the basic maps and borehole data of the study area.

FUNDING

This research was supported by the National Natural Science Foundation of China (No. 42177174), the Basic Research Program of Natural Science of Shaanxi Province (2020ZY-JC-03), and the Shannxi Province Joint Fund Project (2021JLM-09), major projects supported by Shaanxi Coal Chemical Group Co., Ltd. (2018SMHKJ-A-J-03).

REFERENCES

- Bell, F. G., Stacey, T. R., and Genske, D. D. (2000). Mining Subsidence and its Effect on the Environment: Some Differing Examples. *Environ. Geology*. 40 (1), 135–152. doi:10.1007/s002540000140
- Chen, C., and Hu, Z. Q. (2018). Research Advances in Formation Mechanism of Ground Crack Due to Coal Mining Subsidence in China. *J. China Coal Soc.* 43 (3), 810–823. doi:10.13225/j.cnki.jccs.2017.0942
- Djmaluddin, I., Mitani, Y., and Esaki, T. (2011). Evaluation of Ground Movement and Damage to Structures from Chinese Coal Mining Using a New GIS Coupling Model. *Int. J. Rock Mech. Mining Sci.* 48 (3), 380–393. doi:10.1016/j.ijrmms.2011.01.004
- Durmuşoğlu, Z. D. U. (2018). Assessment of Techno-Entrepreneurship Projects by Using Analytical Hierarchy Process (AHP). *Tech. Soc.* 54, 41–46. doi:10.1016/j.techsoc.2018.02.001
- Fan, L. M., Ma, X. D., Li, Y. H., Li, C., Yao, C. W., Xiang, M. X., et al. (2017). Geological Disasters and Control Technology in High Intensity Mining Area of Western China (In Chinese). *J. China Coal Soc.* 42 (2), 276–285. doi:10.13225/j.cnki.jccs.2016.6002
- Fan, L. M., Zhang, X. T., Xiang, M. X., Zhang, H. Q., Shen, T., and Lin, P. X. (2015). Characteristics of Ground Fissure Development in High Intensity Mining Area of Shallow Seam in Yushenfu Coal Field (In Chinese). *J. China Coal Soc.* 40 (6), 1442–1447. doi:10.13225/j.cnki.jccs.2014.1707
- Feng, Y. L., and Luo, Q. W. (2016). The Risk Evaluation for Goaf Surface Subsidence Based on Rough Set (In Chinese). *J. Henan Polytechnic Univ. (Natural Science)* 35 (6), 759–764.
- Gnanavelbabu, A., and Arunagiri, P. (2018). Ranking of MUDA Using AHP and Fuzzy AHP Algorithm. *Mater. Today Proc.* 5 (5), 13406–13412. doi:10.1016/j.matpr.2018.02.334
- Guo, W. B., Guo, M. J., Tan, Y., Bai, E. H., and Zhao, G. B. (2019). Sustainable Development of Resources and the Environment: Mining-Induced Ecological Environmental Damage and Mitigation Measures-A Case Study in the Henan Coal Mining Area, China. *Sustainability* 11 (16), 4366. doi:10.3390/su11164366
- Hu, Z. Q., Wang, X. J., and He, A. M. (2014b). Distribution Characteristic and Development Rules of Ground Fissures Due to Coal Mining in Windy and sandy Region (In Chinese). *J. China Coal Soc.* 39 (1), 11–18. doi:10.13225/j.cnki.jccs.2013.1289
- Hu, Z., Yang, G., Xiao, W., Li, J., Yang, Y., and Yu, Y. (2014a). Farmland Damage and its Impact on the Overlapped Areas of Cropland and Coal Resources in the Eastern plains of China. *Resour. Conservation Recycling* 86, 1–8. doi:10.1016/j.resconrec.2014.01.002
- Huang, F., Zhu, H., Xu, Q., Cai, Y., and Zhuang, X. (2013). The Effect of Weak Interlayer on the Failure Pattern of Rock Mass Around Tunnel - Scaled Model Tests and Numerical Analysis. *Tunnelling Underground Space Tech.* 35, 207–218. doi:10.1016/j.tust.2012.06.014
- Kim, K.-D., Lee, S., and Oh, H.-J. (2009). Prediction of Ground Subsidence in Samcheok City, Korea Using Artificial Neural Networks and GIS. *Environ. Geol.* 58 (1), 61–70. doi:10.1007/s00254-008-1492-9
- Lee, S., Park, I., and Choi, J.-K. (2012). Spatial Prediction of Ground Subsidence Susceptibility Using an Artificial Neural Network. *Environ. Manag.* 49 (2), 347–358. doi:10.1007/s00267-011-9766-5
- Li, X. J., Shao, F., Li, J., and Liu, X. (2012). Evaluation to Damage Situation of Coal Mining Subsidence Land in Mountainous Area Based on MSPS and GIS. *Amr* 518–523, 5692–5696. doi:10.4028/www.scientific.net/AMR.518-523.5692
- Malinowska, A., and Hejmanowski, R. (2010). Building Damage Risk Assessment on Mining Terrains in Poland with GIS Application. *Int. J. Rock Mech. Mining Sci.* 47 (2), 238–245. doi:10.1016/j.ijrmms.2009.09.009
- Quanyuan, W., Jiewu, P., Shanzhong, Q., Yiping, L., Congcong, H., Tingxiang, L., et al. (2009). Impacts of Coal Mining Subsidence on the Surface Landscape in Longkou City, Shandong Province of China. *Environ. Earth Sci.* 59 (4), 783–791. doi:10.1007/s12665-009-0074-9
- Rezaei, M., Yazdani Noori, Z., and Dashti Barmaki, M. (2020). Land Subsidence Susceptibility Mapping Using Analytical Hierarchy Process (AHP) and Certain Factor (CF) Models at Neyshabur plain, Iran. *Geocarto Int.* 2020, 1–17. doi:10.1080/10106049.2020.1768596
- Saaty, T. L. (1980). *The Analytical Hierarchy Process*. New York: McGraw Hill.
- Shang, H. (2013). *Assessment and Dynamic Monitoring of Mining Geo-Environment in Ningxia*. Beilin: Chang'an University.
- Shao, L. (2019). Geological Disaster Prevention and Control and Resource protection in mineral Resource Exploitation Region. *Int. J. Low-Carbon Tech.* 14 (2), 142–146. doi:10.1093/ijlct/ctz003
- Si, H., Bi, H., Li, X., and Yang, C. (2010). Environmental Evaluation for Sustainable Development of Coal Mining in Qijiang, Western China. *Int. J. Coal Geology*. 81, 163–168. doi:10.1016/j.coal.2009.11.004
- Wang, S. M., Sun, Q., Qiao J. W., and Wang, S. Q. (2020). Geological Guarantee of Coal green Mining. *J. China Coal Soc.* 45 (1), 8–15. doi:10.13225/j.cnki.jccsYG191758
- Xiao, W., Lv, X., Zhao, Y., Sun, H., and Li, J. (2020). Ecological Resilience Assessment of an Arid Coal Mining Area Using index of Entropy and Linear Weighted Analysis: A Case Study of Shendong Coalfield, China. *Ecol. Indicators* 109, 105843. doi:10.1016/j.ecolind.2019.105843
- Xie, X., Hou, E., Wang, S., Sun, X., Hou, P., Wang, S., et al. (2021). Formation Mechanism and the Height of the Water-Conducting Fractured Zone Induced by Middle Deep Coal Seam Mining in a Sandy Region: A Case Study from the Xiaobaodang Coal Mine. *Adv. Civil Eng.* 2021, 1–11. doi:10.1155/2021/6684202
- Xu, J., Zhao, H., Yin, P., Wu, L., and Li, G. (2019b). Landscape Ecological Quality Assessment and its Dynamic Change in Coal Mining Area: A Case Study of Peixian. *Environ. Earth Sci.* 78 (24), 1–13. doi:10.1007/s12665-019-8747-5
- Xu, Y., Wu, K., Li, L., Zhou, D., and Hu, Z. (2019a). Ground Cracks Development and Characteristics of Strata Movement under Fast Excavation: a Case Study at Bulianta Coal Mine, China. *Bull. Eng. Geol. Environ.* 78 (1), 325–340. doi:10.1007/s10064-017-1047-y
- Yan, W., Dai, H., and Chen, J. (2018). Surface Crack and Sand Inrush Disaster Induced by High-Strength Mining: Example from the Shendong Coal Field, China. *Geosci. J.* 22 (2), 347–357. doi:10.1007/s12303-017-0031-7
- Yan, Y., Yan, W., Dai, H., and Guo, J. (2021). Distribution Characteristics and Formation Mechanism of Surface Crack Induced by Extrathick Near Horizontal Seam Mining: An Example from the Datong Coal Field, China. *Adv. Civil Eng.* 2021, 1–10. doi:10.1155/2021/5545128
- Yu, X. Y., Li, B. B., Li, R. B., Duan, W. S., and Liu, P. L. (2008). Analysis of Mining Damage in Huge Thick Collapsible Loess of Western China (In Chinese). *J. China Univ. Mining Tech.* 37 (1), 43–47.
- Zeng, W., Huang, Z., Wu, Y., Li, S., Zhang, R., and Zhao, K. (2020). Experimental Investigation on Mining-Induced Strain and Failure Characteristics of Rock Masses of Mine Floor. *Geomatics, Nat. Hazards Risk* 11 (1), 491–509. doi:10.1080/19475705.2020.1734102
- Zhang, J., Zhang, Q., Zhao, C., and Qu, F. (2011). “The Sensitivity Evaluation of Ground Fissures in Yuncheng, Shanxi, China with GIS and AHP Method,” in 2011 19th International Conference on GeoInformatics, Shanghai, China, June 24–26, 2011 (IEEE), 1–6. doi:10.1109/geoinformatics.2011.5981011
- Zhang, Z. S., and Sui, W. H. (2017). An Evaluation Model for Geological Environmental Impact of Coal Mines in Xinjiang (In Chinese). *J. China Coal Soc.* 42 (2), 344–352. doi:10.13225/j.cnki.jccs.2016.6011
- Zhu, H., He, F., and Fan, Y. (2018). Development Mechanism of Mining-Induced Ground Fissure for Shallow Burial Coal Seam in the Mountains Area of Southwestern China: a Case Study. *Acta GeodynGeomater* 15 (4), 349–362. doi:10.13168/AGG.2018.0026
- Zou, Y. F., Deng, K. Z., and Ma, W. M. (2003). *Mining Engineering Mining Subsidence Engineering*. Xuzhou: China University of Mining and Technology press.

Conflict of Interest: Authors QW, YL, JL were employed by the company Ningxia Coal Industry Co., Ltd.

The remaining authors declare that the research was conducted in the absence of any commercial or financial relationships that could be construed as a potential conflict of interest.

The authors declare that this study received funding from Shaanxi Coal Chemical Group Co., Ltd. The funder was not involved in the study design, collection, analysis, interpretation of data, the writing of this article or the decision to submit it for publication.

Publisher's Note: All claims expressed in this article are solely those of the authors and do not necessarily represent those of their affiliated organizations, or those of

the publisher, the editors and the reviewers. Any product that may be evaluated in this article, or claim that may be made by its manufacturer, is not guaranteed or endorsed by the publisher.

Copyright © 2022 Xie, Hou, Long, Feng, Hou, Wei, Li and Liu. This is an open-access article distributed under the terms of the Creative Commons Attribution License (CC BY). The use, distribution or reproduction in other forums is permitted, provided the original author(s) and the copyright owner(s) are credited and that the original publication in this journal is cited, in accordance with accepted academic practice. No use, distribution or reproduction is permitted which does not comply with these terms.



The Impact of Geohazards on Sustainable Development of Rural Mountain Areas in the Upper Reaches of the Min River

Yanfen He^{1,2}, Mingtao Ding^{3*}, Kang Liu¹ and Min Lei¹

¹College of Urban and Environmental Sciences, Northwest University, Xi'an, China, ²Yellow River Institute of Shaanxi Province, Northwest University, Xi'an, China, ³Faculty of Geosciences and Environmental Engineering, Southwest University, Chengdu, China

OPEN ACCESS

Edited by:

Haijun Qiu,
Northwest University, China

Reviewed by:

Xuefeng Yuan,
Chang'an University, China
Shujun Tian,
Southwest University of Science and
Technology, China

*Correspondence:

Mingtao Ding
mingtaodding@163.com

Specialty section:

This article was submitted to
Geohazards and Georisks,
a section of the journal
Frontiers in Earth Science

Received: 26 January 2022

Accepted: 25 February 2022

Published: 23 March 2022

Citation:

He Y, Ding M, Liu K and Lei M (2022)
The Impact of Geohazards on
Sustainable Development of Rural
Mountain Areas in the Upper Reaches
of the Min River.
Front. Earth Sci. 10:862544.
doi: 10.3389/feart.2022.862544

There is a coupling mechanism among geohazards, rural settlements, and cultivated land in mountainous areas in the upper reaches of the Min River by analyzing geohazards data, settlements data and cultivated land data. Geohazards change the landform and provide material basis and space for the occurrence and development of cultivated land and settlements. However, human production and life are not only stressed by geohazards, but also one of the main factors inducing geohazards. The Settlements in the upper reaches of the Min River can be categorized into production-stressed settlements and life-stressed settlements. With the transformation of the social economy and society's attention to the ecological function of the region, geohazards risk management of life-stressed settlements is of more importance. The "two-wheel-drive" strategy of new urbanization and rural revitalization provides opportunities for rural development in mountainous areas and also changes the role of land in human-land relationships. To fully consider natural capital in the sustainable livelihoods of farmers, it is necessary to evaluate the risk degree of geohazards in settlements at the small catchment scale and improving the external connectivity of the settlements, which is the key for promoting the optimization of natural environmental assets in these mountain settlements.

Keywords: rural settlements, geohazards, mountains, transition period, the upper reaches of Min river, natural resources, spatial scale, sustainable development

INTRODUCTION

Disaster reduction is an integral component of sustainable development, to reduce social, economic, and environmental losses due to natural hazards and related technological and environmental disasters (Twigg, 1999; Armstrong, 2000; Paton et al., 2000; Klein et al., 2004; United Nations Office for Disaster Risk Reduction, 2005). Community-based disaster risk management (CBDRM) is a common approach to international disaster prevention and reduction, which was first established in the UK in the late 1980s and has since been widely applied by international, national, and local organizations (Mimaki et al., 2009; Tiwari, 2015). The main idea of CBDRM is to rely on community organizations to mobilize residents to participate in the construction of community disaster prevention and reduction with the support of governments and non-government groups (Ikeda et al., 2008; Sha and Liu, 2010; Hossain, 2013). Current research of CBDRM focuses on the construction of disaster prevention and reduction systems (Chen and Cui, 2013), comparisons of the

reconstruction modes (Liu et al., 2017), architecture and planning design strategy of post-disaster temporary settlement (Huang and Long, 2015), innovations in management mechanisms (Gao, 2013; Xu et al., 2020), capacity-building for disaster prevention and reduction (Yin et al., 2009; Xia, 2010; Zhou et al., 2010; Fei, 2015), disaster prevention awareness (Liu, 2010), risk perception to environmental hazards (Peng et al., 2018; Ahmed et al., 2019), disaster risk and adaption of settlement (Utami et al., 2014), disaster prevention behaviors of rural households (Long and Zhuang, 2009; Zhang, 2013; Wu, 2015), vulnerability assessment for debris flows (Ding et al., 2016), and factors influencing flood impacts in settlements (Dalu et al., 2018). However, few studies have attempted to comprehend the change of the impact of geohazards on sustainable development from the macro perspective when society and economy transformed.

The interactions between human society and geohazards are dynamic. With the transformation of the social economy, the intensity and mode of human utilization of natural resources have changed. Especially with urbanization, the national economic development strategy has been transformed into ecological civilization construction (Pan, 2016), which promotes sustainable development of green development, and urban-rural integrated development (Li, 2011). Rural spaces and resources therein are being developed to meet the urban demand for rural areas (Holmes, 2006), changing uses of rural land to supporting secondary products, leisure, and entertainment, affecting the livelihood of farmers in mountainous areas (Liu et al., 2018). The impact of these changes will affect the composition of farmers' livelihood assets (or capital), and the focus of community-based disaster risk management will also change.

The village, a basic type of settlement, is a place-based community with the totality of individuals and social structures within a specific geographical location. Rural settlements in mountainous areas are the product of human adaptation to the environment (Jin, 1988). Located in the mountainous areas with fragile environments and frequent geohazards (such as collapse, unstable slope, landslides and debris flow), and the beautiful natural landscape and unique folk culture, the socio-economic development of a village is a balance of coping with various adverse conditions with the development of rural tourism (Liu et al., 2018). With China entering the middle stages of industrialization, the environment in mountainous areas has increasingly become a part of livelihood capital, which is an important barrier for farmers to resist various risk shocks (Yang and Zhao, 2009), especially in ethnic minority areas, consisting of both the material and immaterial contents (Li et al., 2019). The development of the tourist industry, based on resources such as the natural landscape and folk culture (Xu et al., 2020), has reduced the stress of natural disasters on livelihood. The ability to absorb the effects of pressure sources through resilience or adaptation has become one of the main capabilities of some communities (Twigg, 1999).

This paper analyzes the coupling relationship and mechanisms between the spatial distribution of mountain settlements and geohazards in the upper reaches of the Min

River on a regional scale. This provides a basis for the sustainable development of mountain villages in the transition period, in which the society transforms from the subsistence agricultural society to service-oriented industrial and commercial society (Lu, 1997).

MATERIALS AND METHODS

Study Area

The upper reaches of the Min River refers to the reaches above Dujiangyan, bounded by the latitudes 30°45'–33°09' N and the longitudes 102°35'–103°56' E, covering an area of about 22,000 km² in the southeast margin of Qinghai-Tibet Plateau. Features include complex geological structures and fault developments (Figure 1). Areas covered by the tributaries include Wenchuan County, Li County, Heishui County and the major part of Songpan County and Mao County, which are all in the Aba Tibetan Autonomous Prefecture, and a small part of Dujiangyan City (the five counties listed are the focus of this paper). The terrain in the area is high in the west and low in the east; the elevation range is 734–6,153 m (Figure 2).

The study area, with an azonal arid valley climate, is characterized by a dry and windy climate, cold in winter and cool in summer, with large temperature differences between day and night, regions, and altitudes. Because of the control of westerly circulation and the monsoon warm current, the climate transitions from the subtropics to a warm temperate zone and then to a cold temperate zone; it demonstrates a climate distribution form of echelonment (Ding et al., 2014). The annual mean temperature of the area is 5.7–13.5°C, and annual precipitation is 400–800 mm for which 80% is concentrated in the period from May to October (Ding et al., 2014). Due to the foehn effect caused by a deep valley and large relative elevation difference, the warm and humid airflow in the southeast and southwest is separated by the mountains, which is not conducive to the formation of precipitation in the valley. Precipitation is relatively abundant in the high mountain areas. The multi-year average precipitation in the northwest of Heishui County is ~1,200 mm, and coupled with Mao County is the precipitation center, which gradually increases to the southeast and northwest (Ding et al., 2014).

Geohazard Data

The China Geological Survey from May 2008 to April 2017 was used to classify types of geohazards (Table 1; Figure 3). By 2017, 824 collapses were documented in five counties in the upper reaches of the Min River, with a maximum scale of 300 × 104 m³ and a minimum scale <1 m³. Among them, small collapses account for 79.3%, whereas giant collapses, large-scale collapses, and medium-scale collapses account for 0.24, 2.42, and 17.96%, respectively.

There were 579 unstable slopes, and the maximum number of people threatened is 800. The unstable slopes in this area are divided into three grades: small, medium, and large. The percentages of medium-scale and small-scale unstable slopes were 48.8 and 45.3% respectively, and large-scale accounted for 5.9%.

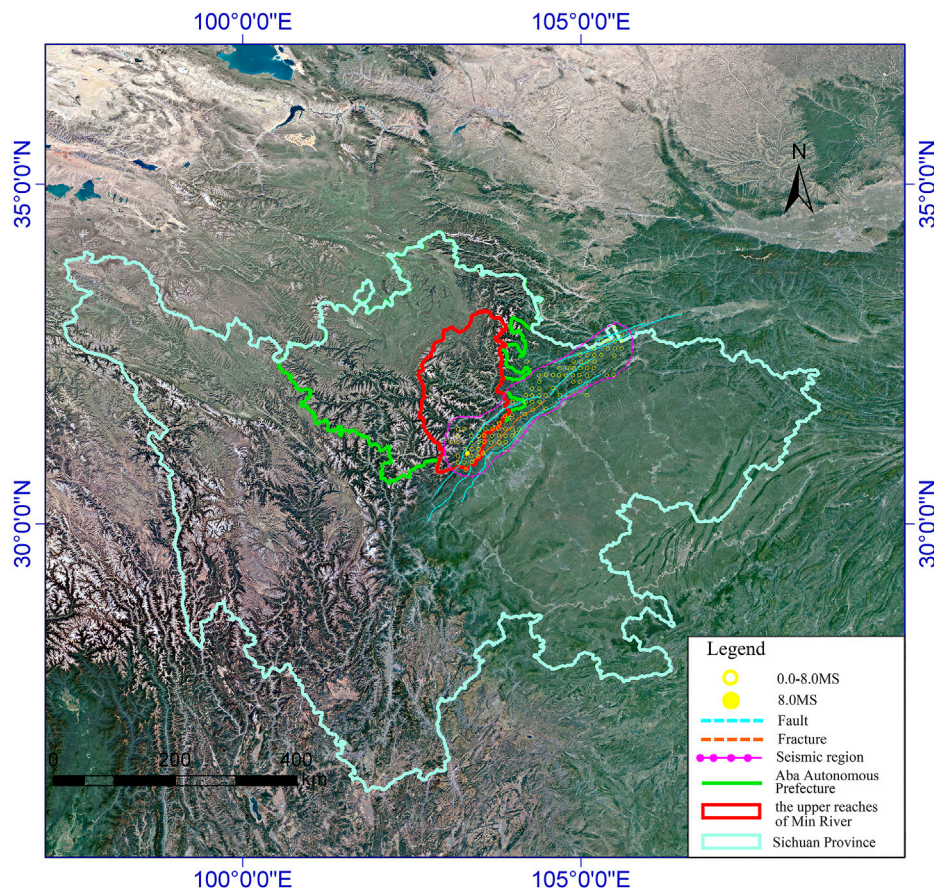


FIGURE 1 | Location of the upper reaches of Min River (according to Cui, 2011).

There were 921 landslides, with a maximum scale of $540 \times 104 \text{ m}^3$ and a minimum scale $<1 \text{ m}^3$. Small-scale landslides accounted for the majority (83.3%) of the total number of collapses; large- and medium-scale collapses accounted for 14.7 and 2%.

There were 841 debris flows, with a maximum scale of $200 \times 104 \text{ m}^3$ and a minimum scale of 0.01 m^3 . Small-scale debris flows accounted for the vast majority (54.2%) of the total number; medium-scale, large-scale and giant-scale debris flows accounted for 38.6, 5, and 2.1%, respectively.

The grading standard here is slightly modified according to Zhang et al. (2002) in which the unstable slope is graded according to the number of people threatened.

Settlement and Cultivated Land

People belong to Tibetan, Qiang, Hui, and Han ethnicities, and the area has a diversified economy and many cultures (Wu et al., 2003). According to the data of the sixth census, there were more than 320,000 people in the five counties in 2010. Because of the high mountains and valleys, people build settlements along the river valley, with the distribution affected by natural and geographical conditions. The settlement locations vary in altitude, forming mountain villages or mountain market towns with a hyper-normal vertical distribution of rural settlements

(Ding et al., 2014). The size of villages is small, mainly because of the undulating mountainous terrain, the flat land is confined, and topographic conditions are challenging for building large villages. The residential buildings in this area are mostly stone or Earth rock, with attractive appearances in form and structure and with unique landscape values. The bottom of the valley of the river also is the location of agricultural activity (Ding and Hu, 2020). Affected by the terrain and limited water and soil resources, there is less flat cultivated land, and terracing is common.

The distribution data of point settlements were manually extracted from 91 satellite map software. The location of settlements was represented by the administrative village committee in the local area (Figure 4). The cultivated land data was 1:10,000 in vector form from the land management department.

Methods

Frequency–Elevation Relations

Each geological hazard, village, and cultivated land were labeled. Using ArcGIS software and high-precision DEM data, the joint distribution of settlement, geohazard and cultivated land area with elevation were obtained. We calculated the number of geohazards, settlements and cultivated land area according to the elevation range of 200 m.

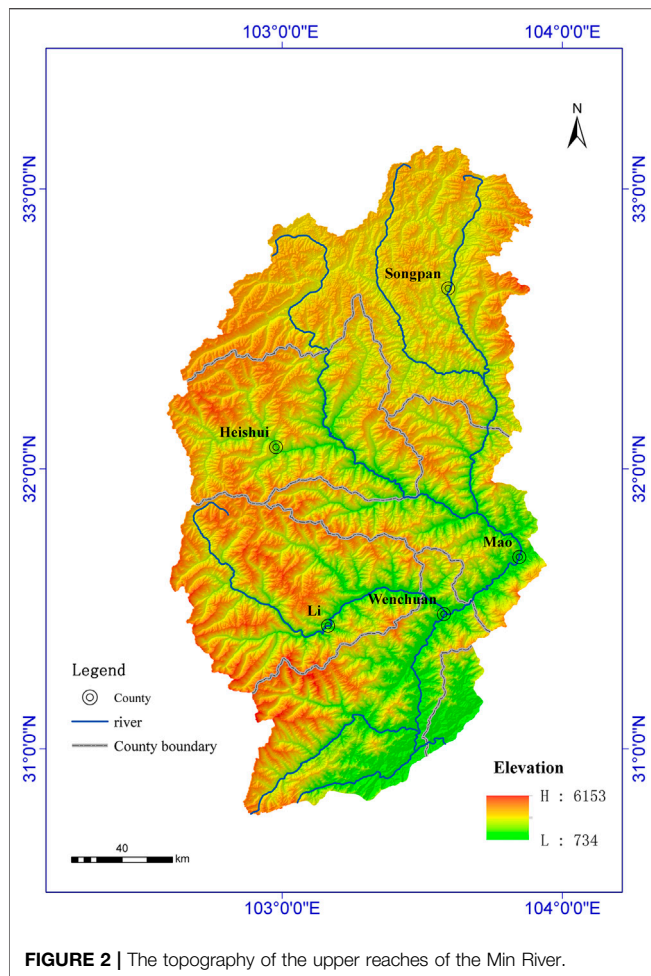


FIGURE 2 | The topography of the upper reaches of the Min River.

Correlation Analysis

With the joint distribution of settlement, geohazard and cultivated land area with elevation obtained above, the Pearson correlation coefficient r between the number of settlements and cultivated land area and between the number of settlements and each type of geohazards were calculated, with professional statistical software SPSS. The specific formula is:

$$r = \frac{\sum_{i=1}^n (x_i - \bar{x})(y_i - \bar{y})}{\sqrt{(\sum_{i=1}^n (x_i - \bar{x})^2)(\sum_{i=1}^n (y_i - \bar{y})^2)}}$$

$$\bar{x} = \frac{1}{n} \sum_{i=1}^n x_i, \bar{y} = \frac{1}{n} \sum_{i=1}^n y_i$$

where x_i , y_i refers to the frequency of geohazards and settlements within the i th elevation range or the settlement frequency and cultivated land area within the i th elevation range.

RESULTS

A total of 559 settlements were distributed from 870 to 3,900 m in 2020 (**Figure 5**). There were 91 settlements distributed in 2,800–3,000 m (16.279% of the total number); settlements distributed 2,200–3,200 m account for 58.497%. **Table 2** shows the number of settlements and cultivated land area distribution at different elevations. There was high correlation between the number of settlements and cultivated land area ($r = 0.814$, $p = 0.000$).

Figure 6 shows the spatial distribution of geohazards of collapses, unstable slopes, landslides, debris flows, and settlements in the upper reaches of the Min River. At the regional scale, the distribution of geohazards and settlements has substantial overlap. Settlements and geohazards are mainly distributed along the river valley.

Figure 7 show the distribution of collapses, landslides, unstable slopes, debris flows, and settlements by elevation. The elevation range of settlements was 870–3,900 m. The elevation range of geohazards was 850–3,850 m, with collapses 890–3,300 m, landslides 870–3,510 m, unstable slopes 880–3,330 m, and debris flow 850–3,840 m. The highest frequency of settlements was at 2,800–3,000 m; whereas collapse, landslide, unstable slope, and debris flow elevation had the highest frequency at 1,600–1,800 m, and the unstable slope variable has a second maximum at 2,000–2,200 m. In general, settlements are found more frequently at higher elevations and disasters at lower elevations (**Figure 7**).

Correlation analysis showed that there was a weak correlation between the number of settlements and collapses ($r = 0.278$, $p = 0.297$), an apparent correlation between the number of settlements and landslides ($r = 0.604$, $p = 0.013$), a moderate correlation between unstable slopes and settlements ($r = 0.442$, $p = 0.086$), and an apparent correlation between debris flows and settlements ($r = 0.663$, $p = 0.005$).

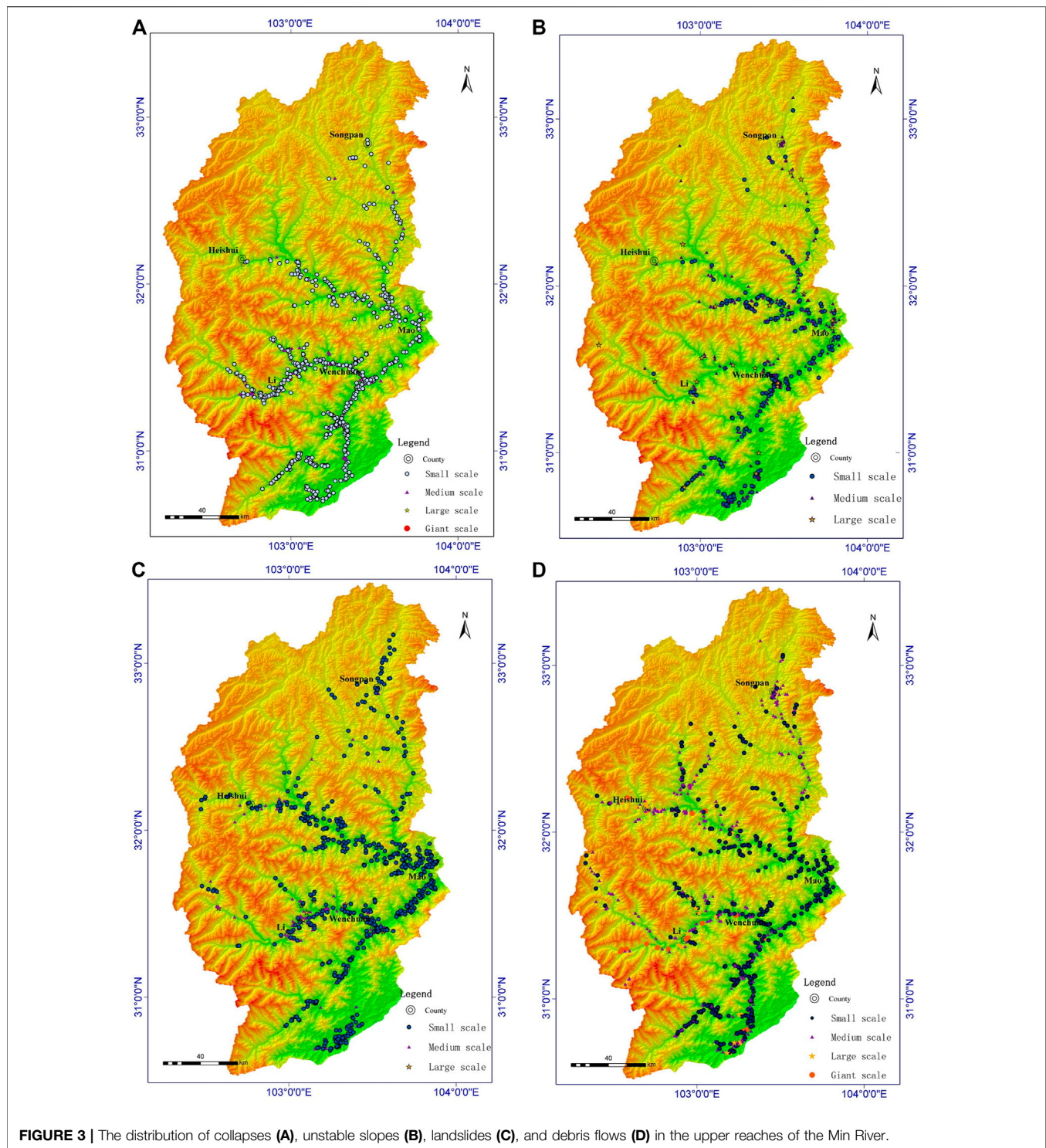
DISCUSSION

Material Basis and Space for Cultivated Land and Settlements

Valley settlement is the most important settlement form in the upper reaches of the Min River (Ding et al., 2018). Deep “V”-shaped erosion

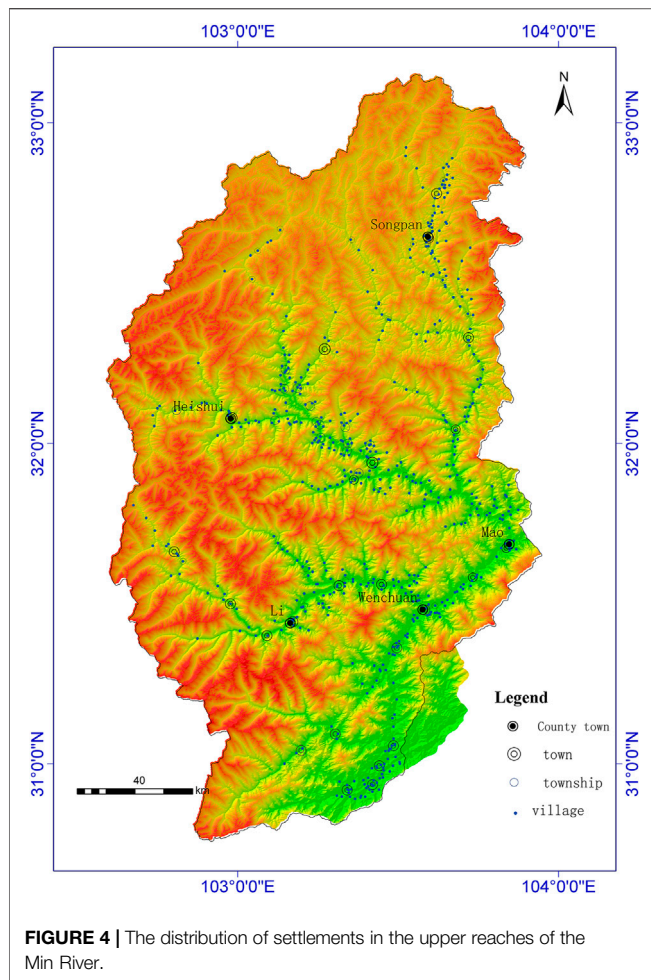
TABLE 1 | The scale and classification standard of landslides, collapses, unstable slopes, and debris flow.

Grade	Landslide (104 m ³)	Collapse (104 m ³)	Unstable slope (persons)	Debris flow (104 m ³)
Giant-scale	≥1,000	≥100	≥1,000	≥50
Large-scale	100–1,000	10–100	100–1,000	20–50
Medium-scale	10–100	1–10	10–100	2–20
Small-scale	<10	<1	<10	<2



small catchments are well developed in this area (Ding et al., 2014). Unstable slopes, collapses, and landslides change landforms, especially topographic slope, which provides relatively flat space for agricultural production and settlements. The rock and soil on a slope may lose stability, breaking away from the parent body under the action of gravity, collapses, and rolls. They accumulate at the foot

of the slope (or valley), or the rock and soil slide downward along the slope caused by natural factors such as rainfall, river scouring, earthquakes, snow melting, and rainstorms. The flood flow with a large number of solid substances (such as mud, sand, and stones), brought by water sources such as ice/snow meltwater or dam releases, forms a relatively deep soil layer attractive for cultivation (Cui, 2011).



In the past, under a small-scale peasant economy in the period of traditional agricultural society, people were self-sufficient, and the land was the most basic and important resource (Zhou et al., 2020), and agricultural production mainly depended on cultivated land in mountainous areas, and the scale of settlements is closely related to the quality and quantity of arable land (Ding et al., 2014).

To facilitate farming and basic life activities, settlements were distributed according to intercepted water and soil flow (Ding et al., 2014). The contact zone between a mountain and plain, or the contact zone between a hillside and alluvial fan, often supported rural settlements. To minimize the occupation of cultivated land, the site selection of Tibetan and Qiang settlements was along the mountain. Houses were built close to small and medium-sized streams with good water quality or with convenient places for water intake (Zhou et al., 2020). Many rural settlements often chose relatively stable diluvial, colluvial, or alluvial fans, and relatively wide and slow ice erosion valley areas, which increases the potential risk from geohazards.

Human Production and Well-Being Affected and Caused by Geohazards

Human production and life are threatened by geohazards. When a settlement is located in a collapse area, the front edge of the landslide with the passing area and accumulation area of debris flow will lead to casualties and damage to buildings (Ding and Hu, 2020). Roads and bridges are vulnerable to collapses, landslides, and debris flow, resulting in road obstruction and damage; arable land also will be damaged.

Unreasonable human activities are one of the main factors inducing geohazards (Ding and Hu, 2020). The reconstruction of the slope in the mountainous area of the upper reaches of the Min

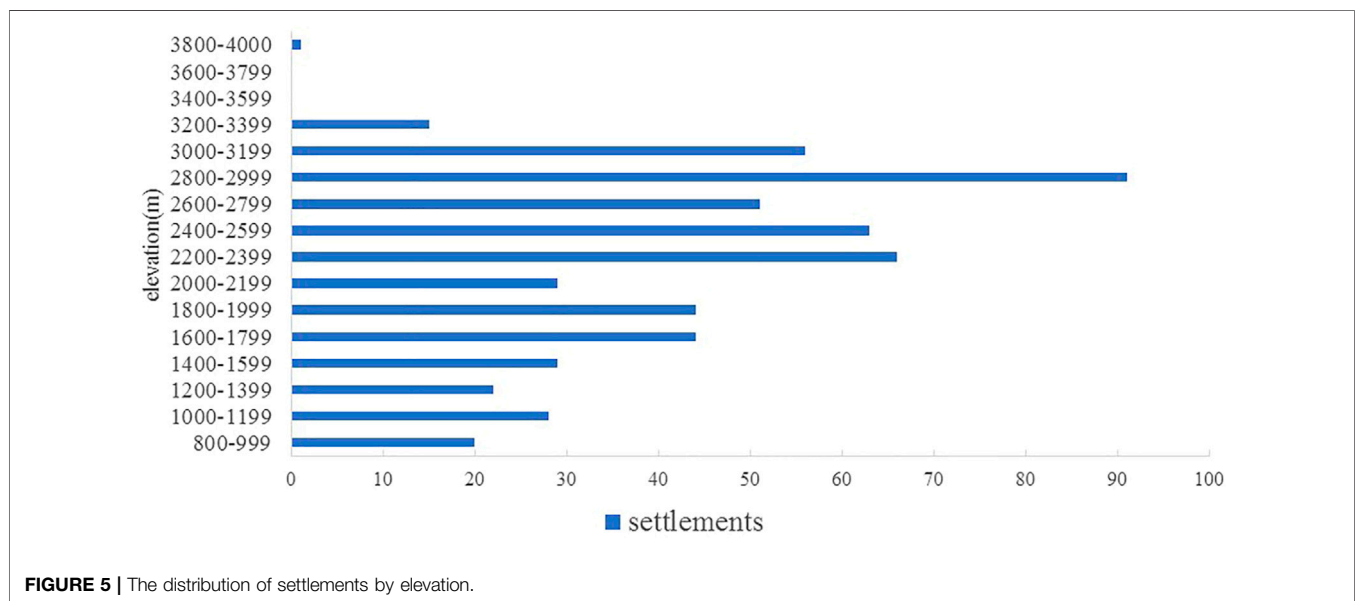
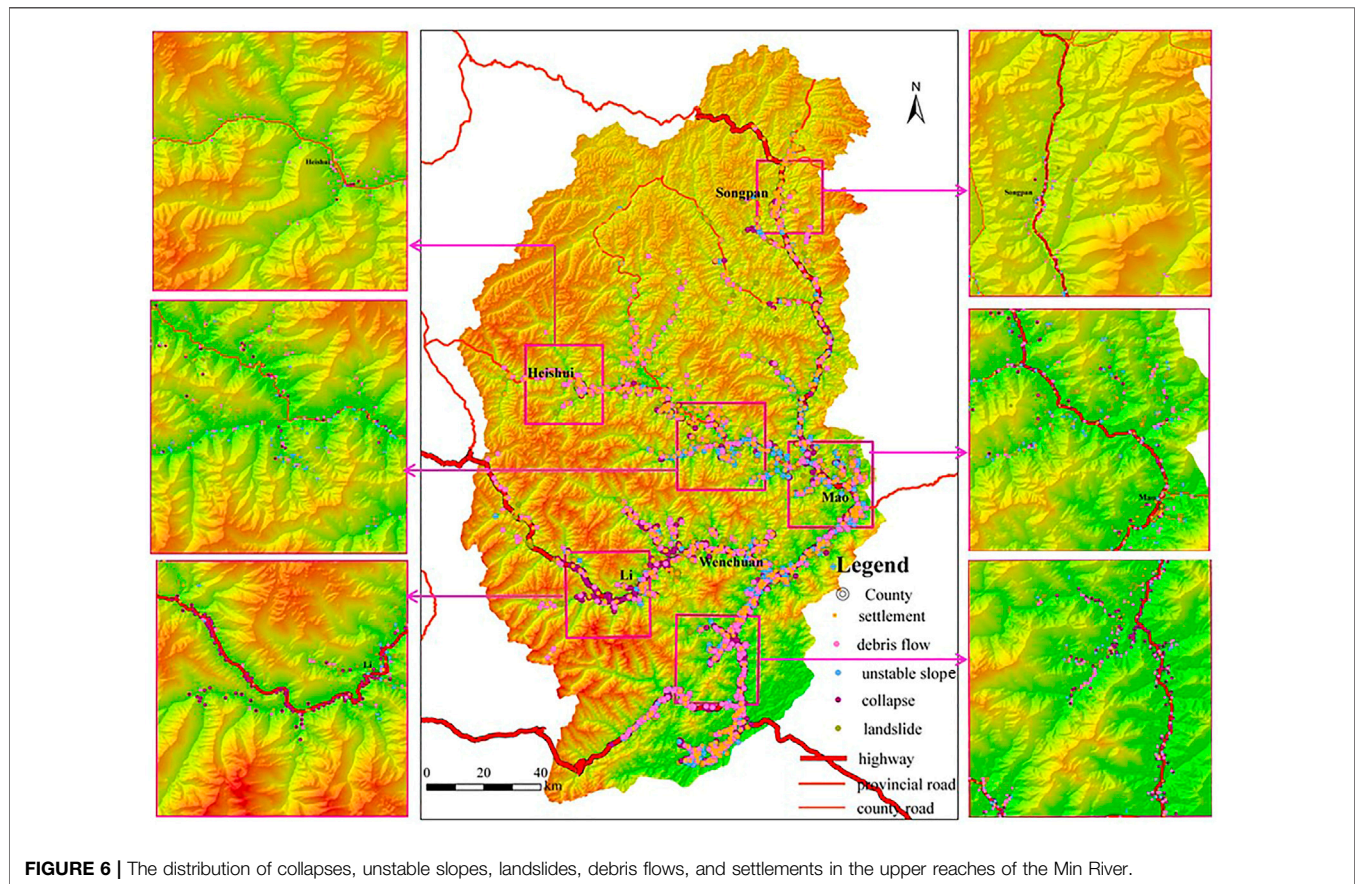


TABLE 2 | Distribution of settlement numbers and cultivated land area with elevation in the upper reaches of the Min river.

Elevation range/m	Number	Percent/%	Cultivated land area/hm ²	Percent/%	Elevation range/m	Number	Percent/%	Cultivated land area/hm ²	Percent/%
800–999	20	3.578	449.479	1.015	1,000–1,199	28	5.009	1090.214	2.462
1,200–1,399	22	3.936	837.113	1.891	1,400–1,599	29	5.188	923.394	2.085
1,600–1,799	44	7.871	2141.193	4.836	1800–1999	44	7.871	2607.553	5.889
2000–2,199	29	5.188	4198.986	9.483	2,200–2,399	66	11.807	3879.125	8.761
2,400–2,599	63	11.270	3790.922	8.561	2,600–2,799	51	9.123	5341.747	12.064
2,800–2,999	91	16.279	7147.622	16.142	3,000–3,199	56	10.018	7872.610	17.780
3,200–3,399	15	2.683	3572.284	8.068	3,400–3,599	0	0.000	408.926	0.924
3,600–3,799	0	0.000	10.458	0.024	3,800–3,999	1	0.179	6.533	0.015
4,000–4,199	0	0.000	0.825	0.002					

**FIGURE 6 |** The distribution of collapses, unstable slopes, landslides, debris flows, and settlements in the upper reaches of the Min River.

River by excavating ore resources, and building roads, houses, and other engineering projects have rendered the slope unstable and the environment is damaged. Even if measures, such as artificial tree planting, are taken to restore the environment, the control of rock and soil stability is low and water and soil loss continue (Ding and Hu, 2020). Further, human activities such as reservoir water storage, channel leakage, stacking of waste, slag filling, and strong mechanical vibrations will lead to slope instability and rock and soil movement. This can result in the destruction of cultivated land and houses, as well as casualties, furthermore, landslides and rock collapses produce loose materials, which become the source of rock debris in the

affected areas (Cui et al., 2011). The material in the river valley is easily washed away and transformed into debris flow during a rainstorm. Therefore, the relationship among geohazards, settlements and cultivated land is “hazards appear with human being”.

However, different types of geohazards have different effects on people’s production and life. Collapse occurs suddenly, and can pose a fatal threat to life and property, and the accumulation formed by large slope is poor sorting, which is difficult to cultivate. The formation of landslide is slow, with the rock and soil movement being an integrity, which does not destroy

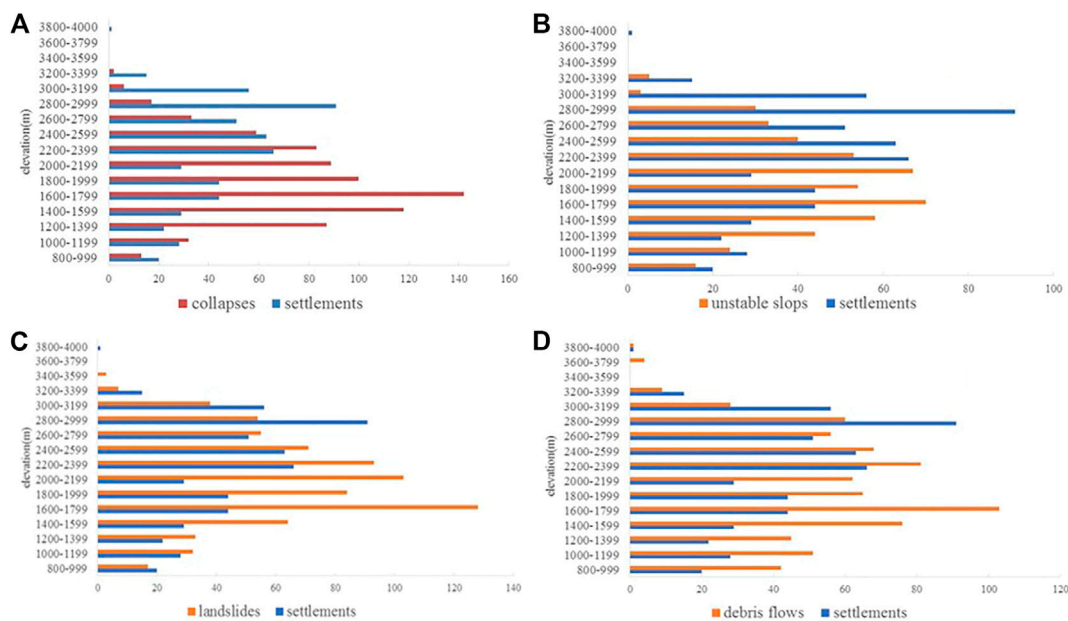


FIGURE 7 | The distribution of collapses (A), unstable slopes (B), landslides (C) and debris flows (D) with settlements by elevation in the upper reaches of the Min River.

the basic soil structure, and even can effectively slow down the slope, which can increase the farming area. Debris flow mainly occurs at the bottom of river channels or gullies, with relatively concentrated scope and little impact on farming areas, which mainly affects human settlements built along rivers or gullies. However, the debris flow is relatively easier to warn than disasters caused by collapse. Unstable slope is mainly due to its unpredictability, which increases the utilization risk.

The Settlement Types Based on Coupling Mechanisms

The coupling mechanism of geohazards, settlements, and cultivated land is shown in **Figure 8**. Geohazards change local landforms, provide materials, and open space for the development of cultivated land and settlements. In the traditional self-sufficient subsistence agriculture stage, there is an interdependent relationship between production space and living space. Yet, human activities, such as reservoir creation, irrigation, deforestation, and slope planting, as well as building houses, roads, and bridges, induce geohazards.

The main function of settlements is supporting life activities, whereas the main function of cultivated land is production. According to the different nature of geohazards, settlements can be categorized into production-stressed settlements and life-stressed settlements. A production-stressed settlement means that the cultivated land maintaining the production function of the settlement is damaged or has the potential risk of damage by geohazards. A life-stressed settlement means that the settlement itself is (or can be) affected by geohazards.

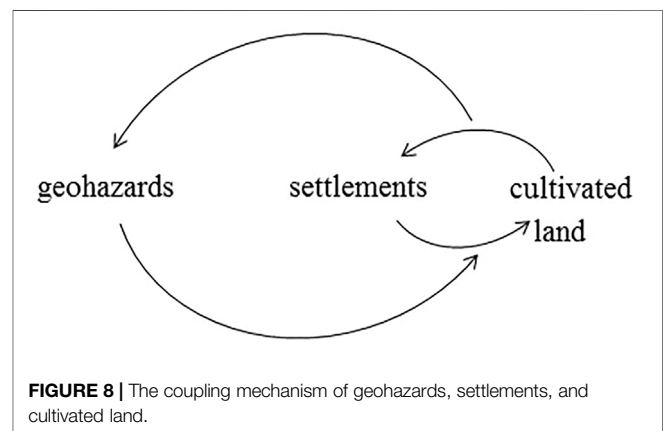


FIGURE 8 | The coupling mechanism of geohazards, settlements, and cultivated land.

Impacts of Geohazards on Sustainable Development of Mountainous Villages

The Wenchuan earthquake on 12 May 2008, destroyed the stability of mountains in the fault zone and triggered collapses, landslides, barrier lakes ("earthquake lakes"), debris flow, and unstable slopes (Cui et al., 2011); The Wenchuan earthquake on 12 May 2008, had similar effects and further affected the weathering of regional rock mass via faults and folds in subsequent aftershocks. The earthquakes exacerbated the instability of the slope (Cui et al., 2011; Ding and Hu, 2020), and landslides and rock collapses produce loose materials which are sources of rock debris of debris flow in the affected areas (Cui et al., 2011). The chain effects of geohazards made the stresses on local settlements long-lasting (Cui et al., 2011; Zhang et al., 2011).

China has entered the middle stage of industrialization. The impacts on rural areas have been exacerbated by impacts of urbanization and industrialization, and the social and economic structure has been transformed. China has transformed from a rural society to an industrial and urban society, from a closed and semi-closed society to an open society, and from a single homogeneous society to a diversified society (Lu, 1997). The economy has changed from self-sufficient livelihoods to a market-oriented commodity economy (Liu, 2007). With the development of China's economy, lifestyles are increasingly urbanized, and there is more demand for unaltered environments. Rural areas are no longer just described as remote, backward places in urgent need of modernization (Woods, 2019). Many functions and values possessed by rural areas can relieve excessive pressure on urban systems.

The upper reaches of the Min River are in the historical ethnic corridor and the channel connecting Qiang and Tibet between Han and Tibet. It is a transitional area of Han, Qiang, and Tibetan culture (Wu et al., 2003). With urbanization, the number and scale of cities and towns in this region have increased rapidly, and the relationship between man and land is symbiotic and fed each other in many directions. Under the background of the construction of ecological civilization (Pan, 2016) and the promotion to building beautiful countryside, the priority development of agriculture and rural areas is not only to make up for the rural shortcomings of building a well-off society in an all-round way but also a major task to realize the great rejuvenation of the Chinese nation (Pan, 2016), and the development of mountain society is the top priority of rural revitalization, facing the opportunity of transformation and development.

With the implementation of the two-wheel-drive strategy of new-type urbanization and rural revitalization, the change of the human social and economic systems will cause changes in the human-land relationship in the upper reaches of the Min River. New-type Urbanization Plan (2014–2020) was put forward by China's National Development and Reform Commission to refine the existing mode of urbanization and promote the citizenization of transferring agricultural residents (Wang et al., 2015), which means more and more peasants will engage in non-agricultural industries. Rural revitalization strategy aimed to achieve high standards for living, rural civilization, clean and tidy villages, and democratic management (Wang and Zhuo, 2018), which pays more attention to the sustainable development of rural areas and the improvement of farmers' living standards. Settlement is the spatial form of human survival and residence in mountainous areas, which is the most closely connected space-time unit between human beings and the mountainous environment (Ding et al., 2014). The settlements in the upper reaches of the Min River are the product of local people's long-term adaption to the mountainous environment and have unique cultural value. With the rapid development of transportation, the economy and society of mountain settlements are undergoing development driven by a series of external factors (Zhou et al., 2013). The unique culture and

beautiful mountain scenery have attracted many tourists and promoted the development of mountain tourism. With the increasing development of mountain tourism, the protection of cultural resources has received more attention (Chen et al., 2011). In this context, the effect of geohazards on the transformation and development of settlements is vital to understand. Biodiversity, the sensitivity of ecological environments, the human and environment relationship, and the security and livability of settlements should be considered in the urbanization process.

CONCLUSION

- 1) There is a coupling mechanism among geohazards, settlements, and cultivated land. According to the nature of geohazards, settlements can be categorized into production-stressed and life-stressed.
- 2) The impact of geohazards on settlements is lasting and the safety for life-stressed settlements is of great importance.
- 3) The “two-wheel-drive” strategy of new urbanization and rural revitalization provides opportunities for rural development in mountainous areas and also changes the role of land in human-land relationships, which promotes the change in the focus of community-based disaster risk management.
- 4) The basis of community-based disaster risk management is to evaluate the risk degree of geohazards to the settlements and to promote optimal utilization of natural environment assets.

DATA AVAILABILITY STATEMENT

The datasets presented in this article are not readily available due to privacy restrictions. Requests to access the datasets should be directed to yanfen_lily@163.com.

AUTHOR CONTRIBUTIONS

MD provide the general idea of the paper, YH Wrote this article, KL analysis the relationship among settlements, cultivated land and ML made correlation analysis.

FUNDING

This work was funded by the National Natural Science Foundation of China (Grant No. 41871174). The Second Tibetan Plateau Scientific Expedition and Research Program (STEP) (Grant No. 2019QZKK0902).

ACKNOWLEDGMENTS

We thank the reviewer and editor, whose constructive comments substantially improved this manuscript.

REFERENCES

- Ahmed, B., Sammonds, P., Saville, N. M., Le Masson, V., Suri, K., Bhat, G. M., et al. (2019). Indigenous Mountain People's Risk Perception to Environmental Hazards in Border Conflict Areas. *Int. J. Disaster Risk Reduction* 35, 101063. doi:10.1016/j.ijdrr.2019.01.002
- Armstrong, M. J. (2000). Back to the Future: Charting the Course for Project Impact. *Nat. Hazards Rev.* 1, 138–144. doi:10.1061/(asce)1527-6988(2000)1:3(138)
- Chen, R., and Cui, P. (2013). Current Situation and prospect of Community-Based Disaster Risk Management (In Chinese). *J. Catastrophol.* 28, 133–138.
- Chen, W., Zhang, P., Zhang, X., Deng, W., Yang, Z., Xue, J., et al. (2011). The Research Progress on Typical Areas in China. *Prog. Geogr.* 30 (12), 1538–1547. (in Chinese). doi:10.11820/dlkxjz.2011.12.011
- Cui, P., Chen, X.-Q., Zhu, Y.-Y., Su, F.-H., Wei, F.-Q., Han, Y.-S., et al. (2011). The Wenchuan Earthquake (May 12, 2008), Sichuan Province, China, and Resulting Geohazards. *Nat. Hazards* 56, 19–36. doi:10.1007/s11069-009-9392-1
- Cui, P. (2011). *Formation Mechanism and Risk Control of Mountain Disasters Caused by Wenchuan Earthquake*. Beijing: Science Press.
- Dalu, M. T. B., Shackleton, C. M., and Dalu, T. (2018). Influence of Land Cover, Proximity to Streams and Household Topographical Location on Flooding Impact in Informal Settlements in the Eastern Cape, South Africa. *Int. J. Disaster Risk Reduction* 28, 481–490. doi:10.1016/j.ijdrr.2017.12.009
- Ding, M.-t., Cheng, Z.-l., and Wang, Q. (2014). Coupling Mechanism of Rural Settlements and Mountain Disasters in the Upper Reaches of Min River. *J. Mt. Sci.* 11 (1), 66–72. doi:10.1007/s11629-012-2366-x
- Ding, M., Heiser, M., Hübli, J., and Fuchs, S. (2016). Regional Vulnerability Assessment for Debris Flows in China—a CWS Approach. *Landslides* 13 (3), 537–550. doi:10.1007/s10346-015-0578-1
- Ding, M., and Hu, K. (2020). *Debris Flow hazard Risk Analysis and Settlement Disaster Reduction – a Case Study of the Upper Reaches of Min River*. Beijing: Science Press. (In Chinese).
- Ding, M., Miao, C., and Huang, T. (2018). On Characteristics and Evolution Analysis of valley Settlement in the Upper Reaches of Min River. *J. Southwest China Normal Univ. (Natural Sci. Edition)* 43 (08), 37–43. (in Chinese). doi:10.13718/j.cnki.xsxb.2018.08.008
- Fei, X. (2015). *Community-based Waterlogging Disaster Risk Analysis and Management—A Case Study of Jingqiao Town, Jiading District of Shanghai, Master*. Shanghai, China: Shanghai Normal University. (In Chinese).
- Gao, Y. (2013). *Community Based Disaster Risk Management— a Case Study of Dijiatai Community, Baiyin City, Gansu Province, Master*. Lanzhou, Gansu, China: Lanzhou University. (In Chinese).
- Holmes, J. (2006). Impulses towards a Multifunctional Transition in Rural Australia: Gaps in the Research Agenda. *J. Rural Stud.* 22 (2), 142–160. doi:10.1016/j.jrurstud.2005.08.006
- Hossain, M. A. (2013). Community Participation in Disaster Management: Role of Social Work to Enhance Participation. *J. Anthropol.* 9, 159–171.
- Huang, L., and Long, E. (2015). Architecture and Planning Design Strategy of Post-disaster Temporary Settlement with High Building Density—Analysis Based on the Questionnaire in Dujiangyan after Wenchuan Earthquake. *Proced. Eng.* 121, 101–106. doi:10.1016/j.proeng.2015.08.1028
- Ikedo, S., Sato, T., and Fukuzono, T. (2008). Towards an Integrated Management Framework for Emerging Disaster Risks in Japan. *Nat. Hazards* 44, 267–280. doi:10.1007/s11069-007-9124-3
- Jin, Q. (1988). *Rural Settlement Geography*. Beijing: Science Press. (in Chinese).
- Klein, R. J. T., Nicholls, R. J., and Thomalla, F. (2004/2003). Resilience to Natural Hazards: How Useful Is This Concept. *Environ. Hazards* 5, 35–45. doi:10.1016/j.hazards.2004.02.001
- Li, Y. (2011). Urban-rural Interaction in China: Historic Scenario and Assessment. *China Agric. Econ. Rev.* 3 (3), 335–349. doi:10.1108/17561371111165770
- Li, Y., Westlund, H., and Liu, Y. (2019). Why Some Rural Areas Decline while Some Others Not: An Overview of Rural Evolution in the World. *J. Rural Stud.* 68, 135–143. doi:10.1016/j.jrurstud.2019.03.003
- Liu, H., Zhang, D., Wei, Q., and Guo, Z. (2017). Comparison Study on Two post-earthquake Rehabilitation and Reconstruction Modes in China. *Int. J. Disaster Risk Reduction* 23, 109–118. doi:10.1016/j.ijdrr.2017.04.016
- Liu, Y. (2007). Rural Transformation Development and New Countryside Construction in Eastern Coastal Area of China. *Acta Geographica Sinica* 62 (06), 563–570. doi:10.11821/xb200706001
- Liu, Y., Wang, Q., Liao, Y., and Du, J. (2018). Ecotourism Development Model in the Upper Reaches of Min River from the Sustainable Livelihood Standpoint View. *Tourism Res.* 10 (2), 37–49. doi:10.3969/j.issn.1674-5841.2018.02.004
- Liu, Z. (2010). *The Research on Prevention and Mitigation System for Normality Disaster in Ethnic Minority Region*. Master Changsha, Hunan, China: Central South University. (In Chinese). doi:10.13885/j.issn.1000-2804.2010.02.009
- Long, Y., and Zhuang, T. (2009). Status Analysis of Villagers' Autonomous Organization Participating in Reconstruction after Earthquake—A Case of Sichuan Disastrous Area. *J. Hebei Agric. Sci.* 13129–132. (In Chinese), 129–132.
- Lu, X. (1997). *Social Structural Transition*. Beijing: China Social Sciences Press. (In Chinese).
- Mimaki, J., Takeuchi, Y., and Shaw, R. (2009). The Role of Community-Based Organization in the Promotion of Disaster Preparedness at the Community Level: a Case Study of a Coastal Town in the Kochi Prefecture of the Shikoku Region, Japan. *J. Coast Conserv.* 13, 207–215. doi:10.1007/s11852-009-0065-8
- Pan, J. (2016). *China's Environmental Governing and Ecological Civilization*. Beijing: China Social Sciences Press and Springer-Verlag GmbH. doi:10.1007/978-3-662-47429-7
- Paton, D., Smith, L., and Violanti, J. (2000). Disaster Response: Risk, Vulnerability and Resilience. *Disaster Prev. Manag.* 9, 173–180. doi:10.1108/09653560010335068
- Peng, Y., Zhu, X., Zhang, F., Huang, L., Xue, J., and Xu, Y. (2018). Farmers' Risk Perception of Concentrated Rural Settlement Development after the 5.12 Sichuan Earthquake. *Habitat Int.* 71, 169–176. doi:10.1016/j.habitatint.2017.11.008
- Sha, Y., and Liu, H. (2010). US Disaster Relief Community Construction and its Effect on Chinese Emergency Management. *J. Lanzhou Univ.* 38, 72–79. (In Chinese). doi:10.13885/j.issn.1000-2804.2010.02.009
- Tiwari, A. (2015). “From Capability Trap to Effective Disaster Risk Management Capacity: what Can Governments, Communities, and Donors Do,” in *The Capacity Crisis in Disaster Risk Management*. Editor A. Tiwari (Cham: Environmental Hazards Springer International Publishing Switzerland), 201–207. doi:10.1007/978-3-319-09405-2_8
- Twigg, J. (1999). The Age of Accountability?: Future Community Involvement in Disaster Reduction. *Aust. J. Emerg. Manag.* 14, 51–58.
- United Nations Office for Disaster Risk Reduction (2005). Hyogo Framework for Action 2005–2015: Building the Resilience of Nations and Communities to Disasters. Available at: <http://www.unisdr.org/2005/wcdr/intergover/official-doc/L-docs/>.
- Utami, S., and Bisri, M. Soemarno; Surjono (2014). Disaster Risk and Adaptation of Settlement along the River Brantas in the Context of Sustainable Development, Malang, Indonesia. *Proced. Environ. Sci.* 20, 602–611. doi:10.1016/j.proenv.2014.03.073
- Wang, H., and Zhuo, Y. (2018). The Necessary Way for the Development of China's Rural Areas in the new era-rural Revitalization Strategy. *Open Journal of Social Sciences* 06, 97–106. doi:10.4236/jss.2018.66010
- Wang, X.-R., Hui, E. C.-M., Choguill, C., and Jia, S.-H. (2015). The New Urbanization Policy in China: Which Way Forward? *Habitat Int.* 47, 279–284. doi:10.1016/j.habitatint.2015.02.001
- Woods, M. (2019). *Rural*. Beijing: Commercial Press. (in Chinese).
- Wu, N., Yan, Z., Luo, P., and Liu, J. (2003). Acculturation and Diversity of Ethnic Cultures on the Upper Minjiang River. *J. Mountain Sci.* Z1 (01), 16–23. (in Chinese). doi:10.16089/j.cnki.1008-2786.2003.01.003
- Wu, Y. (2015). *Coping Capacities of in Ethnic Minority Communities in Anthropology* (Beijing, China: MinZu University of China). Ph.D.thesis(in Chinese).
- Xia, J. (2010). *A Study on Evaluation System of Community Disaster Risk* (Shanghai, China: Fudan University). Shanghai, M.S. Thesis(In Chinese).
- Xu, Y., Qiu, X., Yang, X., Lu, X., and Chen, G. (2020). Disaster Risk Management Models for Rural Relocation Communities of Mountainous Southwestern China under the Stress of Geological Disasters. *Int. J. Disaster Risk Reduction* 50, 101697. doi:10.1016/j.ijdrr.2020.101697
- Yang, Y., and Zhao, F. (2009). A Survey of Farmers' Livelihood Capital in the Framework of the Sustainable Livelihood Approach: A Case Study of the

- Reservoir Zone of the South-To-North Water Transfer (Middle Line) Project. *Issues Agric. Economy* (3), 58–65. doi:10.13246/j.cnki.iae.2009.03.010
- Yin, J., Yi, Z., Wang, J., Xu, S., and Chen, Z. (2009). GIS-based Disaster Risk Assessment of the Urban Community Rainstorm Waterlogging. *Geogr. Geo. Inf. Sci.* 25, 92–95. (In Chinese).
- Zhang, J. (2013). *A Study of Disaster Management in Rural Community of Minority Regions with Multiple Subjects' Participation-Based on the Investigation in South West Region, Master*. Yaan, Sichuan, China: Sichuan Agricultural University. (In Chinese).
- Zhang, L., Zhang, Y., and Gaon, X. (2002). *Geological hazard Economics*. Shijiazhuang: Hebei Peoples Publishing House. (In Chinese).
- Zhang, T., Zhou, A., Feng, X., and Tian, F. (2011). "Analysis on the Law of Geological Disaster Chain of "5 · 12" Wenchuan Earthquake —Taking an County as an Example," in Proceedings of 2011 National Academic Conference on Engineering Geology (Beijing: Science Press). (In Chinese).
- Zhou, G., He, Y., Tang, C., Yu, T., Xiao, G., and Zhong, T. (2013). Dynamic Mechanism and Present Situation of Rural Settlement Evolution in China. *J. Geographical Sci.* 23 (03), 513–524. doi:10.1007/s11442-013-1025-7
- Zhou, L., Huang, X., and Zhang, L. (2020). Geography, Settlement and Space: Environment Perception and Landscape Adaptation of the Qiang Ethnic Group in Northwest Sichuan. *J. Aba Teach. Univ.* 37 (04), 12–19. (In Chinese).
- Zhou, M., Fan, Y., Yang, S., Chen, S., and Wang, X. (2010). *Natural Disaster Risk Management and Early Warning System*. Beijing, China: Science Press. (In Chinese).

Conflict of Interest: The authors declare that the research was conducted in the absence of any commercial or financial relationships that could be construed as a potential conflict of interest.

Publisher's Note: All claims expressed in this article are solely those of the authors and do not necessarily represent those of their affiliated organizations, or those of the publisher, the editors and the reviewers. Any product that may be evaluated in this article, or claim that may be made by its manufacturer, is not guaranteed or endorsed by the publisher.

Copyright © 2022 He, Ding, Liu and Lei. This is an open-access article distributed under the terms of the Creative Commons Attribution License (CC BY). The use, distribution or reproduction in other forums is permitted, provided the original author(s) and the copyright owner(s) are credited and that the original publication in this journal is cited, in accordance with accepted academic practice. No use, distribution or reproduction is permitted which does not comply with these terms.



Sandstone Slope Stability Analysis Under Wetting-Drying Cycles Based on Generalized Hoek-Brown Failure Criterion

Kai Kang^{1*}, Shiyuan Huang², Wenhua Liu¹, Hu Cheng¹, Igor Fomenko³ and Yuxin Zhou⁴

¹School of Environment and Civil Engineering, Jiangnan University, Wuxi, China, ²Engineering Research Center of Diagnosis Technology and Instruments of Hydro-Construction, Chongqing Jiaotong University, Chongqing, China, ³Faculty of Hydrogeology, Russian State Geological Prospecting University, Moscow, Russia, ⁴State Key Laboratory of Safety and Health for Metal Mines, Maanshan, China

OPEN ACCESS

Edited by:

Wen Nie,
Jiangxi University of Science and
Technology, China

Reviewed by:

Shengrong Zhang,
Northeast Forestry University, China
Weiwei Zhan,
Tufts University, United States
Yanjun Lu,
Yanshan University, China

*Correspondence:

Kai Kang
kevinkang8@mail.ru

Specialty section:

This article was submitted to
Geohazards and Georisks,
a section of the journal
Frontiers in Earth Science

Received: 18 December 2021

Accepted: 15 February 2022

Published: 23 March 2022

Citation:

Kang K, Huang S, Liu W, Cheng H,
Fomenko I and Zhou Y (2022)
Sandstone Slope Stability Analysis
Under Wetting-Drying Cycles Based
on Generalized Hoek-Brown
Failure Criterion.
Front. Earth Sci. 10:838862.
doi: 10.3389/feart.2022.838862

The deterioration of rock strength due to cyclic fluctuations in the groundwater level in drawdown regions influences bank slope stability. Based on wetting–drying cycling and uniaxial compression tests of sandstone specimens, the intact rock strength deterioration characteristics were analyzed. Considering different types of rock mass discontinuities, the rock mass strength deterioration features were shown. The results of rock mass strength deterioration characteristics were then applied in sandstone slope stability analysis. Using the finite element method, the safety factors of the slope under different wetting–drying cycles were computed based on the generalized Hoek–Brown failure criterion. Meanwhile, statistical distribution features of strength parameters were considered, and safety factor distribution of studied slopes was obtained with Monte Carlo simulation. The results show that rock mass deformation modulus decreased during wetting–drying cycling. The mean safety factors of the slope with any type of discontinuities were reduced by wetting–drying cycling in probabilistic analyses. Wetting–drying cycling plays an important role in damaging slope stability at initial stages since the degree of rock mass strength deterioration is remarkable during initial wetting–drying cycles. However, the rock mass strength and safety factor of the slope are reduced gently after 10 wetting–drying cycles. This research presents the phases of the effect of wetting–drying cycles on sandstone slope stability in drawdown regions.

Keywords: wetting–drying cycles, slope stability, Hoek–Brown criterion, Monte Carlo simulation, safety factor

INTRODUCTION

Bank slopes in drawdown regions are prone to be damaged by wetting–drying effects due to cyclic fluctuations in the groundwater level. Wetting–drying cycling would soften the geologic materials on the banks, decrease their shear strength, and in turn affect the stability of bank slopes (Sun et al., 2015; Liao et al., 2020).

Most studies focused on the multiple-layer landslides, whose failure mostly depends on existing sliding zone or soil-bedrock interlayer (Tang et al., 2016; Zhang et al., 2020; Li et al., 2021). Such landslides usually have relatively obvious sliding surfaces, and the slope failure occurred due to structurally controlled surfaces. However, few studies particularly assessed the stability of jointed

rock slopes only defined by intersecting discontinuity systems, whose type of slope failure does not depend on structurally controlled surfaces. This sort of slope can be considered homogeneous and isotropic when discontinuity sets are sufficiently closely spaced relative to the size of the structure (Hoek and Brown, 2019). The steep homogeneous-like sandstone slopes, which spread widely in Three Gorges Reservoir bank, are the focus of this research.

Regarding quantitative approaches, the deterministic analysis is a common method adopted for assessing slope stability. However, due to the randomness and uncertainty of the parameters affecting slope stability, it is more reasonable to use probabilistic analysis (Miao et al., 2016; Guo et al., 2020; Kang et al., 2021). Therefore, the dispersion of sandstone strength properties will be considered in current quantitative assessment of slope stability.

In the present study, a typical rock slope composed of sandstone on the bank of Three Gorges Reservoir was selected. Based on the strength deterioration law of intact sandstone, the strength characteristics of rock masses due to wetting-drying cycles were explored. Meanwhile, statistical distribution features of strength parameters were considered with Monte Carlo simulation. Accordingly, with the help of the RS2 program (Rocscience, 2021), finite element analysis (FEM) based on the generalized Hoek-Brown failure criterion was conducted to investigate the changing rule of safety factors of sandstone banks.

METHODS

Cyclic Wetting-Drying Tests of Intact Sandstone

The sandstone specimens in the Chongqing Reservoir area were selected for strength tests under wetting-drying cycles (Huang et al., 2018). A uniaxial compression test in the laboratory was carried out to observe the effects of cyclic wetting-drying on uniaxial compressive strength (UCS) and deformation modulus (E_i) of intact rocks. Before the test, sandstone specimens were subjected to 1–30 wetting and drying cycles. Meanwhile, 3 untreated sandstone specimens were also tested to determine the initial mechanical properties of the specimens without wetting-drying cycles. The material's damage due to wetting-drying cycling can be defined as a value of "Degradation Degree (DD)". DD indicates the change of the material strength, which refers to UCS and E_i in this study. Degradation Degree was calculated as

$$DD_{UCS} = (1 - UCS_N/UCS_0) \times 100\% \quad (1)$$

$$DD_{E_i} = (1 - E_{iN}/E_{i0}) \times 100\% \quad (2)$$

where DD_{UCS} and DD_{E_i} are the total degradation degree of UCS and E_i , respectively; UCS_N and E_{iN} are the compressive strength and deformation modulus of specimens after N wetting-drying cycles, and UCS_0 and E_{i0} are the uniaxial compressive strength without wetting-drying cycling.

The change of the Degradation Degree represents that sandstone had a different amount of degradation with

increasing number (N) of wetting-drying cycles. The relationships between DD_{UCS} and DD_{E_i} of intact sandstone and "N + 1" could be fitted by a logarithmic curve as follows (Huang et al., 2018):

$$DD_{UCS} = 15.548 \ln(N + 1) + 6.198 \quad (3)$$

$$DD_{E_i} = 14.872 \ln(N + 1) + 0.186 \quad (4)$$

Regarding the limitation of specimen selection location, the rock strength without wetting-drying cycles in the above tests could not be representative enough. To solve that, the more presentative UCS and E_i of sandstone were adopted in following calculation. The strength deterioration relationships obtained above were then applied to compute UCS and E_i with different wetting-drying cycles.

Generalized Hoek-Brown Criterion

The generalized Hoek-Brown criterion reported by Hoek et al. (2002) was developed as a means to estimate rock mass strength. The Hoek-Brown criterion is based on the assumption of isotropic behavior, which is considered reasonable for rock masses composed of blocks of intact rock separated by intersecting discontinuities. It integrates the intact rock properties from laboratory tests and geological characteristics from the field observations. Based on rock mass quality, the intact rock strength is quantitatively downgraded in order to estimate the strength of rock mass. The generalized Hoek-Brown criterion is expressed as

$$\sigma_1 = \sigma_3 + \sigma_{ci} \left(m_b \frac{\sigma_3}{\sigma_{ci}} + s \right)^a \quad (5)$$

where σ_1 and σ_3 are Major and Minor principal stress, respectively; σ_{ci} is uniaxial compressive strength (UCS) of the intact rock; and s , a , and m_b are Hoek-Brown material constants determined by a constant m_i , geological strength index (GSI), and disturbance factor D :

$$m_b = m_i \exp \left(\frac{GSI - 100}{28 - 14D} \right) \quad (6)$$

$$s = \exp \left(\frac{GSI - 100}{9 - 3D} \right) \quad (7)$$

$$a = \frac{1}{2} + \frac{1}{6} (e^{GSI/15} - e^{20/3}) \quad (8)$$

Rock mass deformation modulus E_m could be estimated by the following equation (Hoek and Diederichs, 2006):

$$E_m = E_i \left(0.02 + \frac{1 - D/2}{1 + e^{(60+15D-GSI)/11}} \right) \quad (9)$$

where E_i is the intact rock deformation modulus (MPa).

Through the field observations, the value of GSI can be obtained via the basic GSI chart (Hoek and Marinos, 2000). The selection of GSI value depends on structure and surface conditions of the discontinuities. Note that assigning a range of values to GSI is more realistic than a precise value.

The geotechnical software RS2 (Rocscience, 2021) for slope stability analysis allows the nonlinear generalized Hoek-Brown

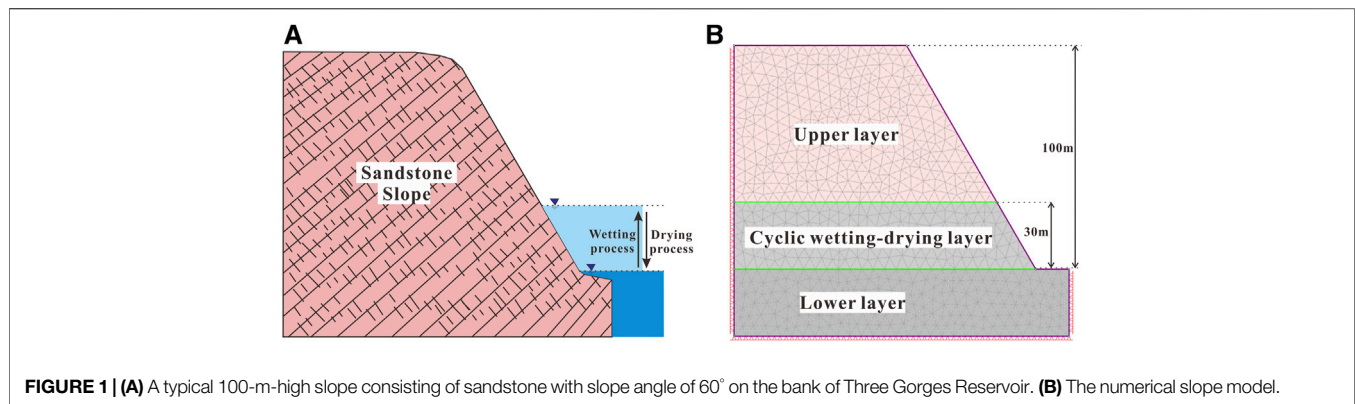


FIGURE 1 | (A) A typical 100-m-high slope consisting of sandstone with slope angle of 60° on the bank of Three Gorges Reservoir. **(B)** The numerical slope model.

TABLE 1 | Values of mechanical parameters of the intact rock and the rock masses.

Number of wetting-drying cycles	UCS (MPa)				Ei (GPa)				Em (GPa)		
	Degradation degree, D_{UCS}	Range	Mean	COV	Degradation degree, D_{Ei}	Range	Mean	COV	GSI =	GSI =	GSI =
									25–35	40–50	60–70
0	0%	50–100	75.0	0.11	0%	14.0–16.0	15.0	0.02	0.80–1.80	2.20–4.90	7.30–11.70
1	17%	42–83	62.3		10%	12.7–14.3	13.5		0.76–1.60	2.00–4.30	6.60–10.50
5	34%	33–66	49.5		27%	10.3–11.7	11.0		0.60–1.30	1.60–3.60	5.40–8.50
10	43%	29–57	42.8		36%	9.0–10.2	9.6		0.54–1.10	1.40–3.10	4.70–7.30
15	49%	26–51	38.3		41%	8.4–9.4	8.9		0.50–1.07	1.34–2.90	4.40–6.90
20	54%	23–46	34.5		45%	7.8–8.8	8.3		0.47–1.00	1.25–2.70	4.10–6.50
25	57%	22–43	32.3		49%	7.2–8.2	7.7		0.43–0.93	1.15–2.50	3.70–6.00
30	60%	20–40	30.0		51%	6.9–7.8	7.4		0.42–0.89	1.12–2.40	3.64–5.80

criterion to be used directly, rather than equivalent linear Mohr-Coulomb criterion to be obtained firstly. Therefore, the RS2 program was used to assess the slope stability in this research.

Finite Element Modeling With Strength Reduction Analysis

A typical 100-m-high rock slope composed of sandstone on the bank of Three Gorges Reservoir was selected, shown in **Figure 1A**. The numerical model of slope stability was set up using the FEM software RS2 (Rocscience, 2021). In this model, the total height of the slope is 100 m, and slope angle is 60° (see **Figure 1B**). Considering that the reservoir water level rises and falls between 145 and 175 m (Huang et al., 2020), the middle part of sandstone slope with a height of 30 m is regarded as a cyclic wetting-drying layer, the mechanical properties of which were the focus of this research, presented in **Table 1**. The material properties of the upper layer and the lower layer are regarded natural and saturated, respectively. The input parameters for slope stability analysis included unit weight (γ), Poisson's ratio (μ), E_i , UCS, GSI, m_i , and D . The values of the following parameters were set to be constant: $\gamma = 24 \text{ kN/m}^3$; $\mu = 0.3$; $m_i = 17$; and $D = 0$. The other parameters were set to be variables, which will be presented in the following content.

Only the effect of gravity was considered in this slope model. The model was meshed with six-noded triangles with 1,369 elements. In terms of boundary conditions, the lateral sides

and the bottom were totally restrained, while free boundary condition was applied to ground surface.

Note that the study slope was without dominant sliding zone or structural surface. The rock mass could be considered homogeneous and isotropic, whose failure pattern is sliding and rotation, according to the generalize Hoek-Brown criterion.

Strength reduction analysis does not require any assumptions about the shape or location of the failure surface. The critical strength reduction factor is regarded as the safety factor of a slope. The strength reduction method will automatically determine the most critical failure mode and the corresponding safety factor.

Monte Carlo Method

Monte Carlo simulation is one of the most popular probabilistic methods developed to incorporate uncertainties in slope stability (Griffiths and Fenton, 2004). In this study, the Monte Carlo method is employed to the probabilistic slope stability analysis. Fundamental to the Monte Carlo method are the randomly generated input parameters that are fed into a deterministic model. This needs to be done using a random number generation function. The random numbers generated from the function are uniformly distributed with values between 0 and 1. The generated random number is then used to get a new parameter value for the sampling function. In this study, the normal distribution function is selected as the sampling function, depending on mean value and coefficient of variation (COV).

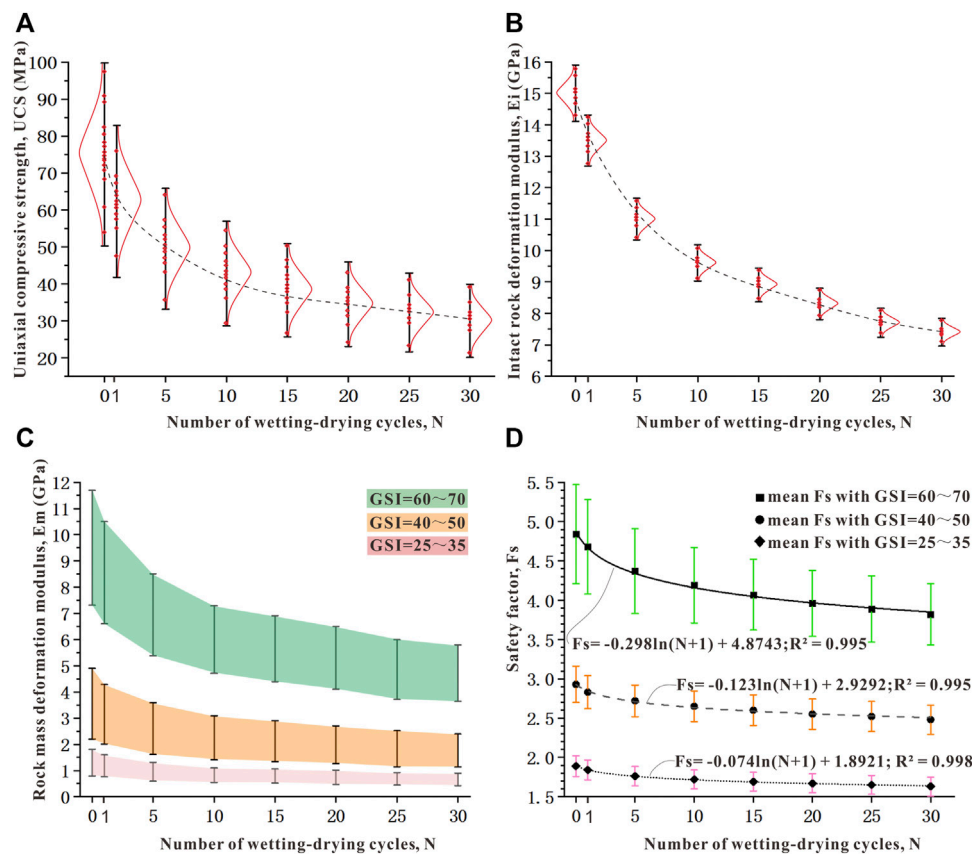


FIGURE 2 | (A) Uniaxial compressive strength range and **(B)** deformation modulus range of intact sandstone exposed to 1, 5, 10, 15, 20, 25, and 30 wetting–drying cycles incorporating normal distribution. **(C)** Rock mass deformation modulus changing trend at different stages of wetting–drying cycling. **(D)** Relationships between the number of wetting–drying cycles and the safety factor of the slope.

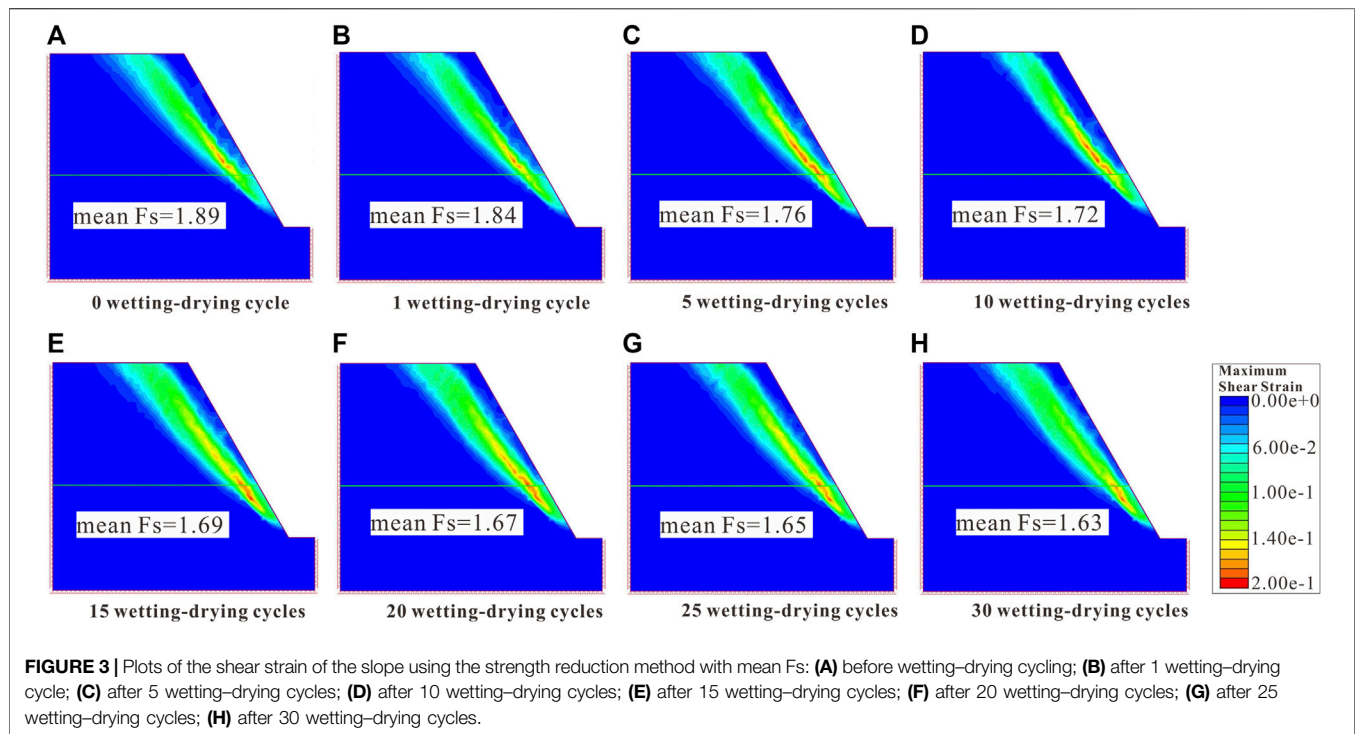
As previously mentioned, assigning a range of values to GSI is more realistic than a precise value. The GSI could be seen as an uncertain parameter. Meanwhile, UCS can vary from point to point in one rock slope. UCS can also be assigned to a range of values. Therefore, two uncertain parameters related to the generalized Hoek–Brown failure criterion are modeled as random variables. These are the Geological Strength Index (GSI) and the uniaxial compressive strength of the intact rock (UCS). Besides, deformation modulus (E_i) of intact rocks related to finite element calculation is also selected as random variables. According to different types of rock mass discontinuities, GSI range of sandstone slope was roughly classified into 3 groups: 60–70 for massive slope, 40–50 for thin bedded slope with interlocking blocks, and 25–35 for bedded slope with complex folding. The GSI range selection was referring to some typical rock mass examples for different rock formations in Hoek and Brown (2019). The range of UCS and E_i of natural sandstone without wetting–drying cycling was set up to 50–100 MPa and 14–16 GPa, respectively (Hoek and Brown, 1997). The COV of sandstone material properties (UCS and E_i) before and after wetting–drying cycles is assumed to be constant, as shown in Table 1. The statistics of UCS and E_i subjected to 1, 5, 10, 15, 20, 25, and 30 wetting–drying cycles are presented in Figure 2A and

Figure 2B, respectively. In current probabilistic analysis, the safety factor of slope will be recomputed 1,000 times (number of samples = 1,000), using a different set of randomly generated input variables for each analysis.

RESULTS

Rock Mass Deformation Modulus Deterioration

As mentioned above, the deterioration law of intact rock deformation modulus (E_i) has been presented as Eq. 4. Using Eq. 9, the rock mass deformation modulus (E_m) in the sandstone slopes at different stages of wetting–drying cycling was obtained. The range of rock masses E_m considering various GSI groups is shown in Table 1. From Figure 2C, it can be seen that with the value of N increasing, E_m decreased gradually. At the initial wetting and drying cycles, the E_m of sandstone rock mass degenerated rapidly. With the increase in the value of N , the rate of E_m decrease had a tendency to slow down. The main deterioration process occurred before 10 wetting–drying cycles. Taking the slope with GSI of 25–35 as an example, the range of E_m value is



0.8–1.8 GPa without wetting–drying cycling. When the value of N was respectively 1, 5, 10, 15, 20, 25, and 30, the E_m of sandstone was reduced to 0.76–1.60, 0.60–1.30, 0.54–1.10, 0.5–1.07, 0.47–1.00, 0.43–0.93, and 0.42–0.89 GPa. It shows that E_m dropped dramatically as N was 1, 5, and 10, then E_m decreased gently after 10 cycles. It is also clear that E_m was decreasing as GSI was decreasing. E_m with a GSI of 60–70 is approximately 10 times of that with a GSI of 25–35.

Safety Factor of Sandstone Slope

Safety factors (F_s) of the study slope were computed though FEM software RS2 based on the generalized Hoek–Brown criterion. **Figure 2D** shows the safety factor of sandstone slope after different numbers of wetting–drying cycles. As Monte Carlo simulation was carried out, the results of safety factor show dispersion, which includes maximum, mean, and minimum values. It can be seen from **Figure 2D** that after 30 wetting–drying cycles, the mean F_s of the slope with a GSI of 60–70 drops from 4.84 to 3.82; the mean F_s with a GSI of 50–70 drops from 2.93 to 2.48; the mean F_s with a GSI of 50–70 drops from 1.89 to 1.63. The changing trend of mean safety factors indicated that sandstone slope stability had undergone different amounts of degradation after wetting–drying cycling.

For sandstone slope with different GSI ranges, the relationship between mean F_s and “ $N+1$ ” could be fitted by logarithmic curves as follows:

$$\begin{aligned} \text{For GSI} = 60 - 70 : F_s &= -0.298 \ln(N + 1) + 4.8743 ; R^2 \\ &= 0.995 \end{aligned} \quad (10)$$

$$\begin{aligned} \text{For GSI} = 40 - 50 : F_s &= -0.123 \ln(N + 1) + 2.9292 ; R^2 \\ &= 0.995 \end{aligned} \quad (11)$$

$$\begin{aligned} \text{For GSI} = 25 - 35 : F_s &= -0.074 \ln(N + 1) + 1.8921 ; R^2 \\ &= 0.998 \end{aligned} \quad (12)$$

Taking the slope with a GSI of 25–35 as an example, **Figure 3** displays a plot of the shear strain of the slope with the strength reduction method after different numbers of wetting–drying cycling. Once the slope failure happens in FEM, the well-formed shear band would be presented as shown in **Figure 3**. The maximum shear strain occurs at both the upper layer and the cyclic wetting–drying layer when subjected to 1, 5, and 10 wetting–drying cycles, while it mainly occurs at the cyclic wetting–drying layer when subjected to 15, 20, 25, and 30 wetting–drying cycles. The mean safety factor of the slope without wetting–drying cycling (0 wetting–drying cycle) is 1.89. While, the mean safety factors of the slope subjected to 1, 5, 10, 15, 20, 25, and 30 wetting–drying cycles are 1.84, 1.76, 1.72, 1.69, 1.67, 1.65, and 1.63, respectively. As shown in **Figure 3**, the slope stability decreases as the number of wetting–drying cycles increases.

DISCUSSION

As mentioned above, considering different types of rock mass discontinuities, the slope composed by sandstone was classified into 3 categories in this study: massive slope of high GSI values, thin bedded slope with interlocking blocks of medium GSI values,

and bedded slope with complex folding of low GSI values. From **Figure 2D**, it is clear that F_s with a certain GSI range decreases as the number of wetting–drying cycles increases, and that F_s was reduced with the decrease in GSI during a certain wetting–drying cycle. In probabilistic analysis, the F_s of the slope with a high GSI varies more widely than that with a low GSI. It indicates that both wetting–drying cycling and rock mass discontinuities affect slope stability. However, the influence of wetting–drying cycling on slope stability deterioration becomes small after 10 wetting–drying cycles, while GSI is the dominant factor of slope stability.

It could be understood that wetting–drying cycling affects the microstructure of sandstone, while GSI affects the macrostructure of the whole rock slope. As known, wetting–drying cycles can dissolve some minerals and weaken the cement among grains in sandstone. However, the remaining minerals are not easy to dissolve after 10 wetting–drying cycles. Meanwhile, the pore structure in rock is hard to expand during subsequent wetting–drying cycling. Therefore, the strength of the sandstone and F_s of the slope with the same GSI is slightly reduced after 10 wetting–drying cycles. When the influence of wetting–drying cycling on slope stability is limited, the GSI turns out to be the dominant factor affecting slope stability.

In this study, the range of natural sandstone mechanical properties is selected to be representative of those referred to in the literature, and applied in strength deterioration relationships (see **Eqs 3 and 4**) developed by authors, and then the rock mass mechanical properties and safety factor were obtained. However, the mechanical properties of intact sandstone in a specific site could be different from the values selected in this study. The only normal distribution was assumed for GSI and mechanical properties in the probabilistic analysis. Other distribution types like lognormal could be applied in future research.

CONCLUSION

The rock mass mechanical properties and the safety factors of the slope under different wetting–drying cycles were analyzed based on generalized Hoek–Brown failure criterion. Some conclusions have been drawn:

- 1) Wetting–drying cycles have a remarkable influence on mechanical properties of sandstone rock mass at initial stages ($N = 1, 5$, and 10). After that, the rock mass strength is reduced gently or nearly kept constant with increasing number of wetting–drying cycles.
- 2) With the number of wetting–drying cycles (N) increasing, the F_s of sandstone slope at different GSI ranges decreases, and the relationship between F_s and the value of $N+1$ could be fitted by logarithmic curves. The most deteriorating process of F_s of sandstone slope with constant GSI happens during the initial stages of wetting–drying cycles.
- 3) Both wetting–drying cycling and GSI influence slope stability. The influence of wetting–drying cycling on slope stability becomes small after 10 wetting–drying cycles, while GSI then becomes the dominant factor of slope stability.

DATA AVAILABILITY STATEMENT

The raw data supporting the conclusion of this article will be made available by the authors, without undue reservation.

AUTHOR CONTRIBUTIONS

Drafting of article: KK; experiment design: SH; analysis and interpretation of data: KK and SH; numerical modeling: KK and IF; revisions of the manuscript: WL, HC, and YZ.

FUNDING

This research is financially supported by Jiangsu Shuangchuang Doctoral Program (Grant No. JSSCBS20210825), the Fundamental Research Funds for the Central Universities (Grant No. JUSRP121059), Chongqing Natural Science Foundation (Grant No. cstc2021jcyj-msxmX1114), Major science and technology projects of Anhui Province (Grant No. 201903a07020008), and the Scientific Research Fund of Institute of Engineering Mechanics, China Earthquake Administration (Grant No. 2019D08). These sources of funding are all gratefully acknowledged.

REFERENCES

- Griffiths, D. V., and Fenton, G. A. (2004). Probabilistic Slope Stability Analysis by Finite Elements. *J. Geotechnical Geoenvironmental Eng.* 130 (5), 507–518. doi:10.1061/(ASCE)1090-0241(2004)130:5(507)
- Guo, Z., Chen, L., Yin, K., Shrestha, D. P., and Zhang, L. (2020). Quantitative Risk Assessment of Slow-Moving Landslides from the Viewpoint of Decision-Making: A Case Study of the Three Gorges Reservoir in China. *Eng. Geology*. 273, 105667. doi:10.1016/j.enggeo.2020.105667
- Hoek, E., and Brown, E. T. (1997). Practical Estimates of Rock Mass Strength. *Int. J. Rock Mech. Mining Sci.* 34, 1165–1186. doi:10.1016/S1365-1609(97)80069-X
- Hoek, E., and Brown, E. T. (2019). The Hoek-Brown Failure Criterion and GSI - 2018 Edition. *J. Rock Mech. Geotechnical Eng.* 11, 445–463. doi:10.1016/j.jrmge.2018.08.001
- Hoek, E., Carranza-Torres, C., and Corkum, B. (2002). “Hoek-Brown Failure Criterion-2002 Edition,” in Proceedings of the 5th North American rock mechanics symposium and 17th tunnelling association of Canada conference, Toronto, Canada: Toronto: University of Toronto, 1, 267–273.
- Hoek, E., and Diederichs, M. S. (2006). Empirical Estimation of Rock Mass Modulus. *Int. J. Rock Mech. Mining Sci.* 43, 203–215. doi:10.1016/j.ijrmms.2005.06.005
- Hoek, E., and Marinos, P. (2000). Predicting Tunnel Squeezing Problems in Weak Heterogeneous Rock Masses. *Tunnels tunnelling Int.* 32 (11), 45–51.
- Huang, S., Wang, J., Qiu, Z., and Kang, K. (2018). Effects of Cyclic Wetting-Drying Conditions on Elastic Modulus and Compressive Strength of Sandstone and Mudstone. *Processes* 6 (12), 234. doi:10.3390/pr6120234
- Huang, X., Guo, F., Deng, M., Yi, W., and Huang, H. (2020). Understanding the Deformation Mechanism and Threshold Reservoir Level of the Floating

- Weight-Reducing Landslide in the Three Gorges Reservoir Area, China. *Landslides* 17, 2879–2894. doi:10.1007/s10346-020-01435-1
- Kang, K., Zerkal, O. V., Ponomarev, A. A., and Fomenko, I. K. (2021). Probabilistic Slope Stability Assessment under Seismic Conditions Based on the Generalized Hoek-Brown Criterion. *Soil Mech. Found. Eng.* 58, 223–229. doi:10.1007/s11204-021-09732-0
- Li, C., Criss, R. E., Fu, Z., Long, J., and Tan, Q. (2021). Evolution Characteristics and Displacement Forecasting Model of Landslides with Stair-step Sliding Surface along the Xiangxi River, Three Gorges Reservoir Region, China. *Eng. Geology*. 283, 105961. doi:10.1016/j.enggeo.2020.105961
- Liao, K., Wu, Y., Miao, F., Li, L., and Xue, Y. (2020). Time-varying Reliability Analysis of Majiagou Landslide Based on Weakening of Hydro-Fluctuation belt under Wetting-Drying Cycles. *Landslides* 18, 267–280. doi:10.1007/s10346-020-01496-2
- Miao, F., Wu, Y., Xie, Y., Yu, F., and Peng, L. (2016). Research on Progressive Failure Process of Baishuihe Landslide Based on Monte Carlo Model. *Stoch Environ. Res. Risk Assess.* 31, 1683–1696. doi:10.1007/s00477-016-1224-8
- Rocscience (2021). *Rocscience RS2*, 11, 012.
- Sun, G., Zheng, H., Tang, H., and Dai, F. (2015). Huangtupo Landslide Stability under Water Level Fluctuations of the Three Gorges Reservoir. *Landslides* 13, 1167–1179. doi:10.1007/s10346-015-0637-7
- Tang, H., Yong, R., and Ez Eldin, M. A. M. (2016). Stability Analysis of Stratified Rock Slopes with Spatially Variable Strength Parameters: the Case of Qianjiangping Landslide. *Bull. Eng. Geol. Environ.* 76, 839–853. doi:10.1007/s10064-016-0876-4
- Zhang, Y., Zhang, Z., Xue, S., Wang, R., and Xiao, M. (2020). Stability Analysis of a Typical Landslide Mass in the Three Gorges Reservoir under Varying Reservoir Water Levels. *Environ. Earth Sci.* 79 (1). doi:10.1007/s12665-019-8779-x

Conflict of Interest: The authors declare that the research was conducted in the absence of any commercial or financial relationships that could be construed as a potential conflict of interest.

Publisher's Note: All claims expressed in this article are solely those of the authors and do not necessarily represent those of their affiliated organizations, or those of the publisher, the editors, and the reviewers. Any product that may be evaluated in this article, or claim that may be made by its manufacturer, is not guaranteed or endorsed by the publisher.

Copyright © 2022 Kang, Huang, Liu, Cheng, Fomenko and Zhou. This is an open-access article distributed under the terms of the Creative Commons Attribution License (CC BY). The use, distribution or reproduction in other forums is permitted, provided the original author(s) and the copyright owner(s) are credited and that the original publication in this journal is cited, in accordance with accepted academic practice. No use, distribution or reproduction is permitted which does not comply with these terms.



Multi-Source Information Fusion Correlation Analysis of Bedrock Deterioration on Slopes Under Leaching Erosion

Wen Zhong^{1,2,3}, Zhiqi Feng^{1,2}, Bo Li^{4*}, Zequn Zhang^{1,2}, Peng Zeng^{1,2}, Zhongqun Guo^{1,5}, Kaijian Hu^{1,2} and Xiaojun Wang¹

¹Key Laboratory of Mining Engineering of Jiangxi Province, Jiangxi University of Science and Technology, Ganzhou, China, ²School of Resource and Environmental Engineering, Jiangxi University of Science and Technology, Ganzhou, China, ³State Key Laboratory of Geomechanics and Geotechnical Engineering, Institute of Rock and Soil Mechanics, Chinese Academy of Sciences, Wuhan, China, ⁴Faculty of Materials Metallurgy and Chemistry, Jiangxi University of Science and Technology, Ganzhou, China, ⁵School of Civil and Surveying & Mapping Engineering, Jiangxi University of Science and Technology, Ganzhou, China

OPEN ACCESS

Edited by:

Wen Nie,
Jiangxi University of Science and
Technology, China

Reviewed by:

Jun Peng,
The University of Hong Kong, Hong
Kong SAR, China
Chunyang Zhang,
Wuhan University of Technology,
China
Ming Tao,
Central South University, China

*Correspondence:

Bo Li
libo_smile@hotmail.com

Specialty section:

This article was submitted to
Geohazards and Georisks,
a section of the journal
Frontiers in Earth Science

Received: 25 January 2022

Accepted: 01 March 2022

Published: 24 March 2022

Citation:

Zhong W, Feng Z, Li B, Zhang Z,
Zeng P, Guo Z, Hu K and Wang X
(2022) Multi-Source Information
Fusion Correlation Analysis of Bedrock
Deterioration on Slopes Under
Leaching Erosion.
Front. Earth Sci. 10:862110.
doi: 10.3389/feart.2022.862110

To explore the effect of leaching erosion on the deterioration mechanism of ionic rare earth slope bedrock. The E-TOPSIS method and fuzzy grey correlation method were used to fuse and analyze the multi-source heterogeneous information such as porosity, pH, mass, volume, density, P-wave and characteristic strength of bedrock specimens. The dominant response parameters of bedrock deterioration of slopes under leaching erosion were obtained, and the multi-source information fusion correlation analysis model was established. The results show that compared with the basic physical parameters of bedrock, the influence of leaching erosion on the pore structure of bedrock is more significant; the pore space and leaching solution pH show obvious dominant responsiveness in the E-TOPSIS analysis with soaking duration. Basically, from the results of fuzzy grey correlation analysis, the micropore of bedrock specimens continued to increase after the decrease in the early stage of soaking, and the porosity varied significantly; the micropore and porosity of bedrock specimens had the highest correlation with the characteristic strength of bedrock, followed by the pH of leaching solution.

Keywords: ion-absorbed rare earth mine slopes, bedrock, leaching erosion, deterioration, multi-source information fusion

1 INTRODUCTION

Ion-adsorption rare earth ores are the weathering products of granites and other igneous rocks containing rare earth hydroxyl water ions. These rare earth ions are adsorbed into the surface of clay minerals such as kaolinite and illite during the permeation of aqueous solutions, forming ion-adsorbed rare earth deposits (Huang et al., 2015; Guo et al., 2020). The Gannan region of China is rich in medium and heavy rare earth elements, which are in short supply in the world. Rare earth materials are a strategic resource of global concern and are known as the mother of new materials and industrial gold (Chen, 2011; Dutta et al., 2016; Zhong et al., 2021). At present, rare earth mining mainly adopts *in-situ* leaching mining method (Liang et al., 2018), in which the leaching solution is used to replace the rare earth elements enriched in rare earth slopes. The leaching solution is a

complex solution containing multiple ions, where the main chemical components of the leaching solution are sulfuric acid, ammonium sulfate and ionic rare earth elements (Silva et al., 2019). Influenced by the mining method of ionic rare earth mines, their slope bedrock has been subjected to long-term erosion by the leaching solution, resulting in different degrees of deterioration of bedrock mechanical properties, which in turn affects the stability of ion-adsorbed rare earth mine slopes (Fan et al., 2017; Zhao et al., 2018; Luo F. Y. et al., 2021). Therefore, the study of the deterioration mechanism about the mechanical properties of ionic rare earth slope bedrock under the erosion of leaching solution provides theoretical basis for the work in disaster warning of ionic rare earth mine slopes.

In recent decades, researchers have conducted numerous studies on the deterioration mechanisms of rocks under the corrosive action of acid solutions, and fruitful results have been obtained. Acid solution erosion affects the macroscopic physical and mechanical properties of rocks to different degrees (Miao et al., 2016; Ni et al., 2017; Luo T et al., 2021). This is due to the water-chemical interactions between the acidic solution and its crystalline mineral particles inside the rock specimen, including ion exchange, dissolution, hydrolysis, and erosion, which change the mineral particle connectivity as well as the mineral composition and structure of the rock (Huang et al., 2021). When erosion of acidic solutions occurs, the roughness of the rock surface increases, while the mass and longitudinal velocity gradually decrease with increasing erosion time (Geng et al., 2019) and the porosity tends to increase (Miao et al., 2018).

The mechanical properties of rock are affected by liquid immersion (Zhang et al., 2020), especially under the condition of acid solution immersion, and their mechanical properties vary with soaking duration. The construction of mathematical models for characterize the degree of rock deterioration under different soaking duration conditions is a scientific problem that needs to be solved urgently, and scholars have studied the characterization of the degree of deterioration through the perspective of mathematical analysis. In this paper, E-TOPSIS method and fuzzy grey correlation analysis are chosen to characterize the degree of bedrock deterioration of ionic rare earth mine slopes under the effect of leaching erosion. The TOPSIS method was founded by Hwang and Yoon in 1981, which ranks evaluation targets by calculating the distance of evaluation targets from the optimal solution and the worst solution, and selects the evaluation targets that are closest to the optimal solution and farthest from the worst solution (Behzadian et al., 2012); one particularly important step is the determination of evaluation parameter weights, and this paper chooses The entropy method (EM), which does not need to consider subjective preferences and only needs objective data to calculate weights, is chosen as the method for weight determination in this paper (Chen, 2019). In previous studies, this approach is called entropy-based TOPSIS (abbreviated as E-TOPSIS). Grey system theory, founded by Deng Julong in 1982, focuses on the study of problems involving small samples and low information content, and deals with uncertain systems with partially known information by generating, mining and extracting useful information from the available information so that the operational behavior of the system and its evolutionary

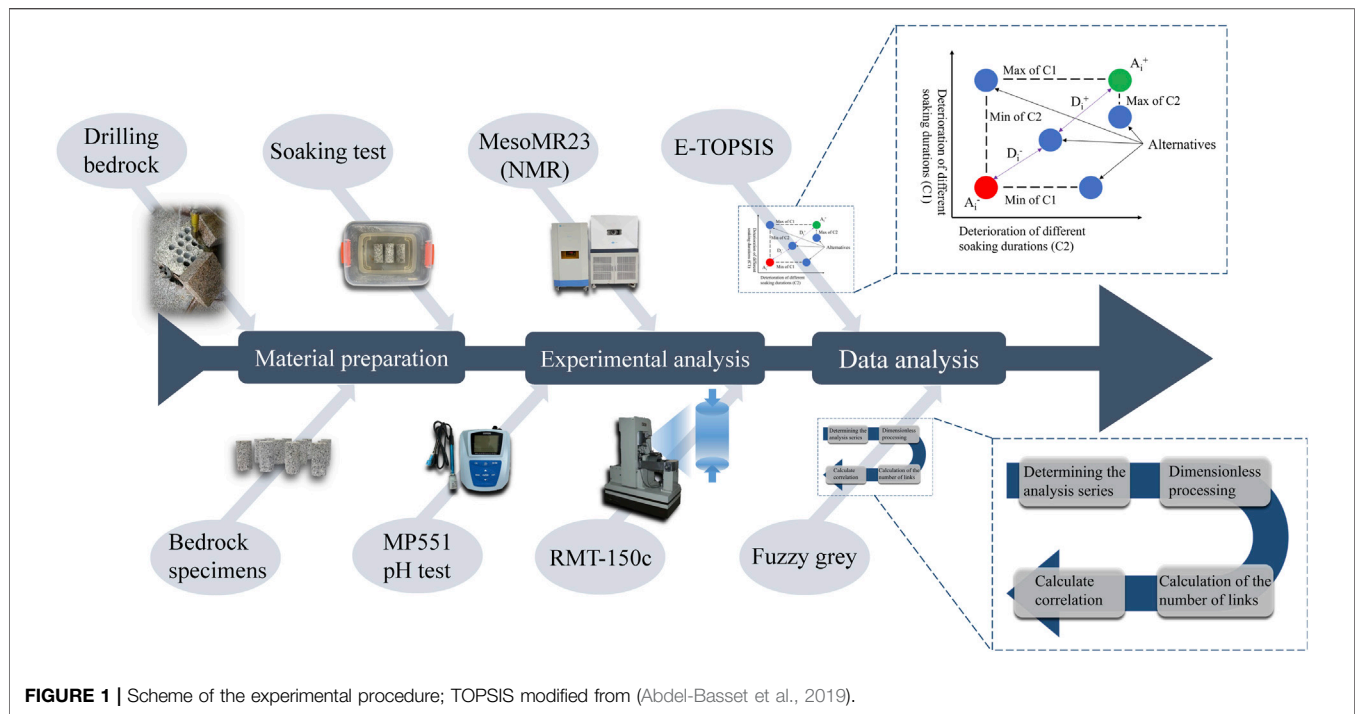
laws can be correctly described and effectively monitored (Deng, 1983). The TOPSIS preference method can reflect the overall similarity between the alternative target and the ideal target by means of function curves, but cannot well reflect the difference between the change trend of factors within the target and the ideal target; the grey correlation method can well illustrate the difference between the change trend of factors within the alternative target and the ideal target, and is applicable to the poor information evaluation where some information is known and some information is unknown environment, but has shortcomings in the overall judgment of system goals (Si et al., 2018).

The existing analyses mainly focus on the analyses of a single local characteristic parameter of the slope bedrock, and few studies have been reported on the overall information of multiple sources of slope bedrock deterioration under leaching erosion. In order to study the effects of leaching erosion on the physical and mechanical properties of slope bedrock, this paper integrates E-TOPSIS and fuzzy grey correlation analysis to analyze the porosity, pH, mass, volume, density, wave velocity, and characteristic strength of slope bedrock under leaching erosion and other multi-source heterogeneous information, and tries to establish a model of slope bedrock deterioration under leaching erosion and extract the physical parameters that can characterize the degree of bedrock deterioration under different soaking durations.

2 MATERIALS AND METHODS

2.1 Materials

The specimens in this paper were taken from the bedrock of the slope of an ionic rare earth mine in Gannan, China, and the sampling depth was about 5–10 m below the bedrock. The leaching solution used in this experiment were taken from a rare earth mine in Ganan, which has a pH value of 3.392 and its main chemical components are NH_4^+ , SO_4^{2-} and ionic rare earth elements. The leaching solution is an acidic solution, which has an erosive effect on the bedrock of the slope. The corresponding ionic rare earth leaching equation is: $\text{Clay-RE}^{3+} + 3\text{NH}_4^+ \rightarrow \text{Clay-3NH}_4^+ + \text{RE}^{3+}$ (RE^{3+} is rare earth ion). According to the International Society for Rock Mechanics (ISRM) test protocol, a standard cylindrical specimen with a height of 100 mm and a height-to-diameter ratio of 2:1 was made (Figure 1). Quartz, feldspar, black mica, hornblende, and other minerals determined by X-ray diffraction using an Empyrean type apparatus are the principal rock-forming mineral compositions of the granite specimens. To ensure the homogeneity of the specimens, all bedrock specimens were taken from the same rock block, and the bedrock specimen with less variability of P-wave was selected as the material for this test (Zhong et al., 2021). In order to avoid the end effect of the bedrock specimen during the test, the end parallelism of the bedrock specimen is controlled within ± 0.02 mm, the end face and the bedrock specimen axis are guaranteed to be mutually perpendicular, and the maximum deviation of the end face and axial perpendicular angle is controlled within ± 0.25 .



2.2 Methods

2.2.1 Experimental Methods

In this paper, the erosion of bedrock by leaching solution during *in-situ* leaching is investigated by means of laboratory simulation tests. In order to eliminate the influence of chance errors on the test results during the test, the selected bedrock specimens were divided into six groups of six bedrock specimens each and numbered, in order, as the first group (GS1-1 to GS1-6), the second group (GS2-1 to GS2-6), . . . , and the sixth group (GS6-1 to GS6-6). Each group of bedrock specimens was placed in an infiltration cell made of inert corrosion-resistant material, and the leaching solution was poured into the cell and all bedrock specimens were buried. The first group of bedrock specimens was used as the control group without immersion treatment, and the remaining five groups of bedrock specimens were subjected to immersion treatment for 30, 60, 90, 120 and 150 days, respectively. After immersion, the bedrock specimens were dried, and characteristics such as mass and P-wave of the dry bedrock specimens were measured (Table 1).

In order to investigate the effect of soaking duration on the microstructure of granite and the pH of the leaching solution, the pore distribution condition of the bedrock specimens with different soaking durations was measured using a MesoMR23-060H-I model NMR analyzer, and the pH of the leaching solution under different duration conditions was measured using an MP551 pH/ion concentration measuring instrument.

The uniaxial compression test of bedrock specimens under different immersion time conditions was performed using a digitally controlled electro-hydraulic servo tester - RMC-150C, developed and produced by the Chinese Academy of Sciences.

2.2.2 E-TOPSIS Methods

The E-TOPSIS method is an improvement of the traditional TOPSIS method, in which the weights of the parameters are first determined by the entropy weight method, and then the ranking of the evaluation objects is determined by the TOPSIS method using the technique of approximating the ideal solution. The main calculation steps of the E-TOPSIS method are as follows (Behzadian et al., 2012; Chen, 2021):

- ① Assuming that there are m evaluation targets (different soaking durations, the same below) and n evaluation indicators (parameters, the same below) for each evaluation target, construct a judgment matrix.

$$X = (x_{ij})_{m \times n} \quad (i = 1, 2, \dots, m; j = 1, 2, \dots, n) \quad (1)$$

- ② Normalization of the judgment matrix:

$$x_{ij} = \frac{x_{ij}}{x_{\max}} \quad (2)$$

where x_{ij} refers to the maximum value under the same index.

- ③ Calculate the information entropy:

$$e_{ij} = -k \sum_{i=1}^m P_{ij} \ln P_{ij} \quad (3)$$

where $P_{ij} = \frac{x_{ij}}{\sum_{i=1}^m x_{ij}}$; $k = \frac{1}{\ln m}$.

- ④ Define the weights of the indicators.

$$\omega_j = \frac{1 - e_j}{\sum_{j=1}^n (1 - e_j)} \quad (4)$$

where $\omega_j \in [0, 1]$, and $\sum_{j=1}^n \omega_j = 1$.

⑤ Calculate the weighting matrix:

$$R = (r_{ij})_{m \times n}, r_{ij} = \omega_j \cdot x_{ij} (i = 1, 2, \dots, m; j = 1, 2, \dots, n) \quad (5)$$

⑥ Determine the optimal and inferior solutions:

$$A_j^+ = \max(r_{1j}, r_{2j}, \dots, r_{mj}), A_j^- = \min(r_{1j}, r_{2j}, \dots, r_{mj}) \quad (6)$$

⑦ Calculate the Euclidean distance of each solution from the optimal and inferior solutions:

$$D_i^+ = \sqrt{\sum_{j=1}^n (A_j^+ - r_{ij})^2}, D_i^- = \sqrt{\sum_{j=1}^n (A_j^- - r_{ij})^2} \quad (7)$$

⑧ Calculate the composite evaluation index:

$$C_i = \frac{D_i^-}{D_i^+ + D_i^-}, C_i \in [0, 1] \quad (8)$$

where the larger the value, the lower the degree of deterioration.

2.2.3 Fuzzy Grey Correlation Methods

Fuzzy grey correlation is the degree of similarity or dissimilarity of dynamic trends between objects and factors, and it is a method to study and analyze the correlation between things based on the degree of similarity of time series curves between factors. The main calculation steps of the fuzzy grey correlation analysis method are as follows (Liu et al., 2016).

① Determining the analysis series:

Let $X_0 = \{x_0(t), t = 1, 2, \dots, m\}$ be the reference series and $X_i = \{x_i(t), t = 1, 2, \dots, m; i = 1, 2, \dots, n\}$ be the comparison sequence.

② Dimensionless processing:

$$x_i(t) = \frac{x_i(t)}{\bar{x}_i}, t = 1, 2, \dots, m; i = 1, 2, \dots, n \quad (9)$$

where t corresponds to the time period and i corresponds to a row (i.e., a feature) in the comparison series.

③ Calculation of the number of links:

$$\zeta_i(t) = \frac{\min_i \min_t \Delta_i(t) + \rho \max_i \max_t \Delta_i(t)}{\Delta_i(t) + \rho \max_i \max_t \Delta_i(t)} \quad (10)$$

where $\rho \in (0, \infty)$, is the resolution factor. The smaller the ρ is, the greater the resolving power is, and the general value of ρ is (0, 1), depending on the situation. This paper takes $\rho = 0.5$ (Liu et al., 2016).

④ Calculate the correlation

$$r_i = \frac{1}{n} \sum_{t=1}^n \zeta_i(t), t = 1, 2, \dots, n \quad (11)$$

where r_i refers to the correlation between the comparison series and the reference series.

3 EXPERIMENTAL RESULTS

3.1 Uniaxial Compression Experimental Results

According to the test results, the combination of axial strain method and axial stiffness method (Zhao et al., 2021b; Zhao et al., 2021c) was used to classify the compression-density stage, linear elastic deformation stage, plastic deformation stage and post-peak deformation damage stage of each bedrock specimen. And because of the limited pages, only the characteristic stresses and damage modes of GS1-1, GS2-1, GS3-1, GS4-1, GS5-1 and GS6-1 specimens are shown in this paper (Figure 2).

From Figure 2, it can be seen that there are more significant differences in stress-strain curves and characteristic stress stages of ionic rare earth slope bedrock specimens under different soaking durations conditions.

In the compression stage, the pores inside the bedrock specimen gradually become smaller under the action of axial pressure, and the stress-strain curve of the bedrock specimen is concave, and the length of the concave section and the degree of concavity both reflect the pore development of the bedrock specimen. From Figure 2, it can be found that the concave section of the stress-strain curve of the bedrock specimen gradually grows and the degree of concavity gradually deepens after soaking, which is a significant change compared with that of the unleached specimen. This is due to the fact that the dissolution of mineral particles inside the bedrock gradually deepens with the increase of soaking duration, and the pore development becomes more and more significant.

In the linear elastic deformation stage, the stress-strain curve is linear, and the pores inside the bedrock specimen gradually compact with the increase of axial pressure and then enter the deformation stage. Young's modulus E is an important index to describe the resistance to deformation of solid materials, and the more severely the rock is eroded, the smaller the E value (Zhao et al., 2020). The specimens of unleached bedrock showed the typical damage characteristics of granite, and the elastic phase was more obvious, with the increase of soaking duration, Young's modulus and elastic phase strain both showed different degrees of decrease. From Figure 2, it can be seen that the elastic stage strain decreased by 8–9% at 30 days of soaking, and the elastic stage strain was stable after 30 days, as can be seen from Figure 3, the Young's modulus of the bedrock specimens gradually decreases, and the depreciation rate reaches 46.66% in the late stage of soaking compared with that in the unleached ore. The above analysis shows that the effect of the leaching solution is relatively more significant mainly in the first 30 days of soaking, and remains relatively stable thereafter. Decrease in Young's

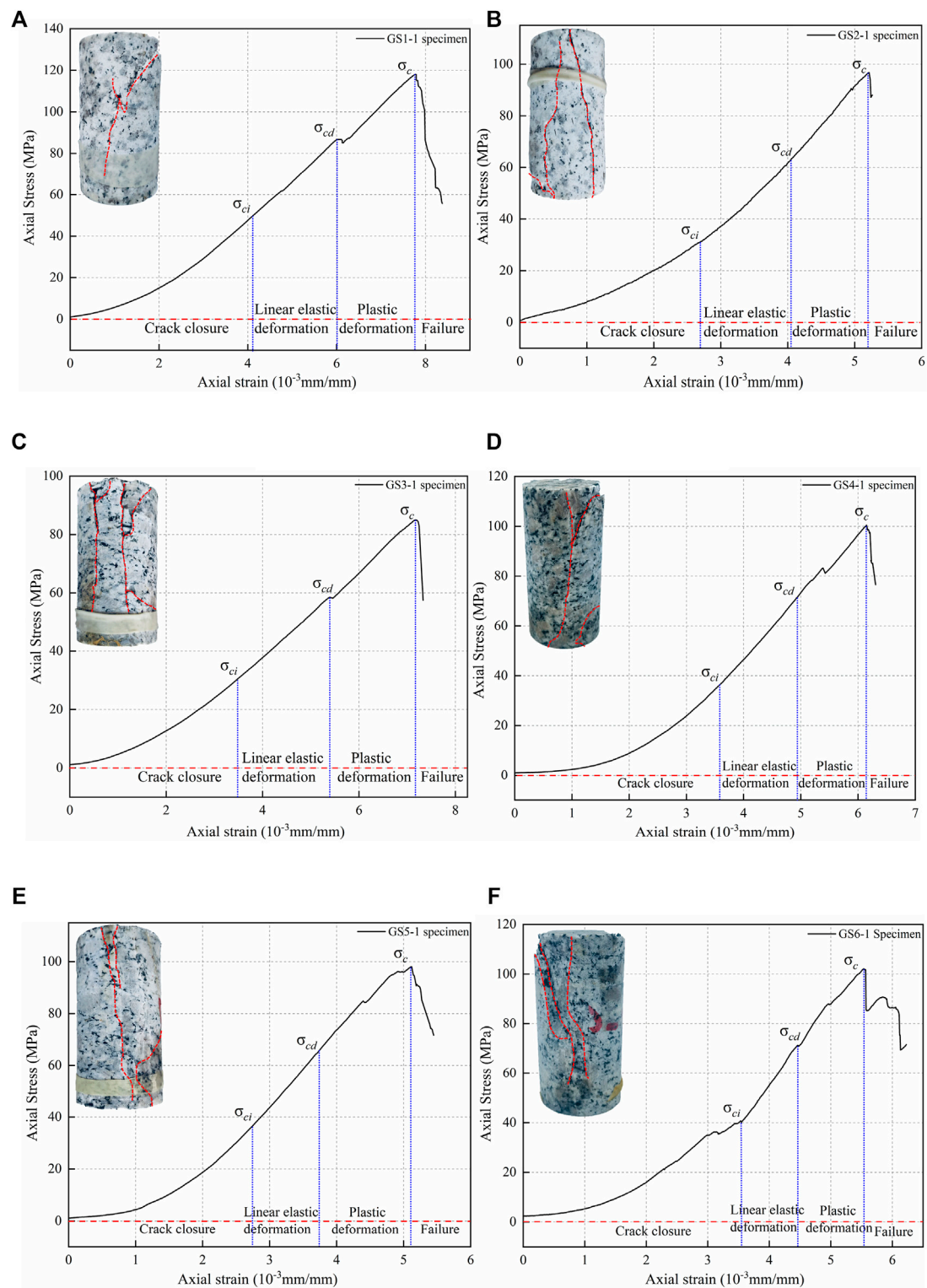
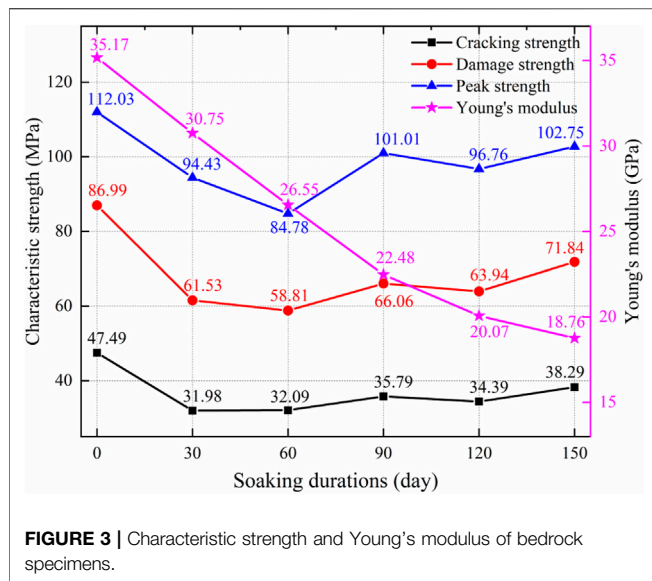


FIGURE 2 | Typical uniaxial compressive stress-strain curves for bedrock specimens under leaching erosion. (A) GS1-1; (B) GS2-1; (C) GS3-1; (D) GS4-1; (E) GS5-1; (F) GS6-1.



modulus and elastic stage strain indicates that the mechanical properties of bedrock are more significantly affected by the erosion of leaching.

In the plastic deformation stage, with the continuous increase of axial pressure, the internal microfractures of the bedrock specimen are generated, connected and penetrated, and the bedrock specimen appears plastic deformation until destruction. From **Figure 2**, it can be seen that the percentage of plastic stage and the relative deformation gradually increase with the increase of soaking duration, which indicates that the bedrock specimens are gradually affected by erosion.

In the post-peak damage stage, unlike the brittle performance of the bedrock specimen when it was not leached, with the increase of soaking time, the bedrock specimen showed different degrees of flow damage, ductility increased, and the peak softening stage appeared. From **Figure 2**, it can be seen that the damage form of bedrock specimens changed from penetration damage in the natural state to penetration damage and flake flaking damage at 150 days of soaking, and the softening effect of leaching erosion was significant, and a certain strength could be maintained after the damage. The bedrock specimens showed brittle damage before 90 days of soaking, and with the increase of soaking duration, the number of internal microcracks also increased, and the pores inside the specimens were connected and penetrated to form a certain degree of lamellar defect structure, which led to the peak softening stage and lamellar spalling damage of the bedrock specimens, and at this time the specimens had a tendency to change from brittle to ductile in the form of breakage.

The above analysis shows that with the increase of soaking duration, the bedrock specimen is gradually deepened by erosion, the pore development is more and more significant, the compressive stage of rock stress-strain curve is gradually obvious, the elastic stage is gradually shortened, the plastic stage is gradually reduced and the peak softening stage appears, and the bedrock damage form shows the trend of

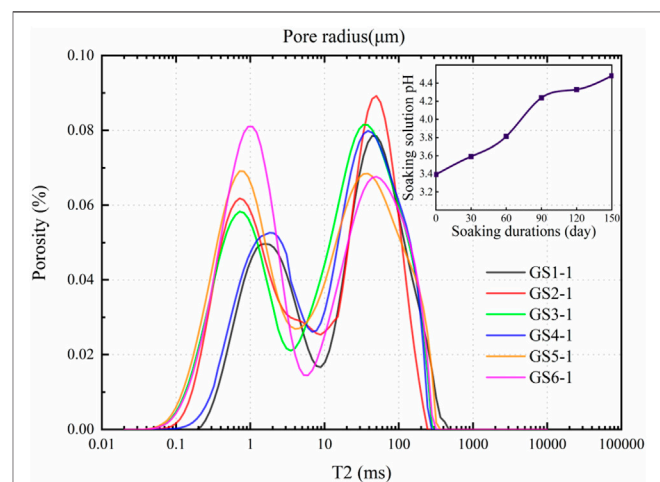
brittle to ductile development with the increase of soaking duration.

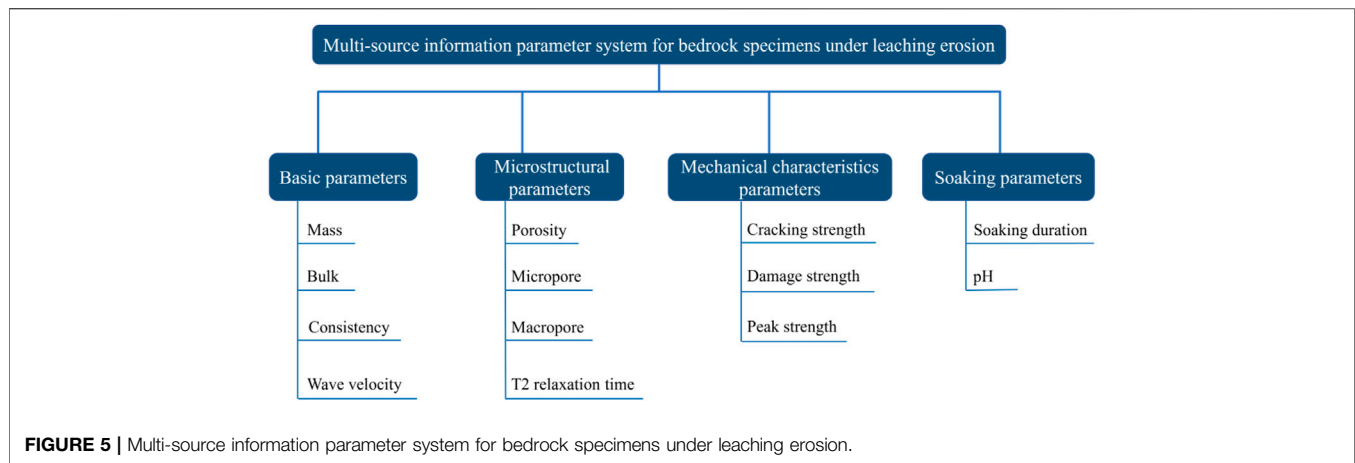
In order to investigate the effect of erosion on the characteristic strength of bedrock specimens, statistical analysis of the test results was conducted (**Figure 3**). The trend of the three characteristic strengths under the leaching erosion was basically the same, and the characteristic strengths decreased significantly in the period of 0–30 days; the peak strength of the three characteristic strengths maintained a faster rate of decrease in the period of 30–60 days, and the cracking strength and damage strength decreased slowly. The three characteristic strengths were the lowest in the period of 60 days of soaking, indicating that the deterioration of the bedrock specimens was the highest in the period of 60 days of soaking. In the remaining soaking duration except for a small decrease in the three characteristic intensities at 90–120 days, the overall trend is increasing, indicating that the deterioration of the bedrock specimens is gradually reduced.

3.2 Pore Evolutionary Characteristics

In order to investigate the effect of soaking duration on the microstructure of granite and the pH of the leaching solution, the pore distribution of the bedrock specimens with different soaking durations was measured by NMR analyzer, and the pH of the leaching solution under different duration conditions was measured by pH/ion concentration measurement instrument. Because of the limited pages, only the NMR test results of GS1-1, GS2-1, GS3-1, GS4-1, GS5-1 and GS6-1 specimens under different soaking duration conditions and the pH measurement of the leaching solution are shown in this paper (**Figure 4**).

Figure 4 shows the trends of porosity and pH of leaching solution with soaking duration. It can be seen from the figure that the porosity of the specimens increased with the soaking duration and then fluctuated within a certain range, in which the macropore of the specimens increased first with the increase of the soaking duration and continued to increase after a certain retreat at 90 days; the micropore of the specimens was the highest





at 60 days and then tended to decrease. The variation of pores inside the specimens caused the variation of characteristic strength, and the transformation of macropore and micropore inside the bedrock specimens was visible at 90 days, and the characteristic strength of bedrock specimens decreased faster at this time, when combined with the trend of characteristic strength variation of bedrock specimens. This phenomenon was also mirrored in the pH of the leaching solution, which steadily increased with the length of leaching duration, with the maximum rate of variation between 60 and 90 days.

3.3 Multi-Source Information Fusion Analysis Parameter Selection

Combined with the mechanical mechanism of bedrock specimen deterioration under chemical solution erosion (Zhao et al., 2021a), the effect of leaching erosion on the internal microstructure of granite specimens, including mineral deconstruction, microfractures, intergranular voids, lattice defects and microdefects, was considered comprehensively. Following the principles of independence, comprehensiveness and quantifiability in the selection of parameters, four parameters of physical properties, fine structure, mechanical characteristics parameters and soaking conditions of the bedrock specimens were selected in this paper to establish a more comprehensive analysis system of granite deterioration under leaching erosion. The specific parameters are shown in **Figure 5**.

3.3.1 Basic Physical Parameters

Four parameters, such as mass, volume, density and wave velocity, were analyzed. For granite in natural state, the basic physical parameters are not the same, which leads to the difference of deterioration degree of different bedrock specimens in the same area. The basic physical parameters are important indicators for the evaluation and analysis of bedrock specimen outside the laboratory. In the field, limited by equipment and time constraints, it is not possible to conduct exhaustive laboratory tests including composition analysis and

other tests, so the analysis of the basic physical parameters such as mass, volume, density and P-wave is necessary.

3.3.2 Microstructural Parameters

Four parameters of porosity, macropore, micropore, and NMR T2 relaxation time (T2) were analyzed. In the preliminary laboratory test analysis of bedrock mechanics, in addition to the analysis of the basic physical parameters of bedrock specimen, we often start from the microstructure parameters of bedrock specimens (Li et al., 2019), following the principle of quantifiability, this paper selects the pore parameters of bedrock specimens as the parameters of microstructure analysis.

3.3.3 Mechanical Characteristics Parameters

The Cracking strength, Damage strength and Peak strength are also called the characteristic strength of the bedrock specimen deterioration process. The characteristic strength of the rock is based on the development of the crack activity state stage before the peak of the rock damage process, the stress corresponding to the end point of the linear elastic stage is the starting crack strength, the stress corresponding to the end point of the stable development stage of the crack is the damage strength, and the stress corresponding to the end point of the unstable development section of the crack is the peak strength. These parameters are the visual representation of the development of the deterioration mechanism of the bedrock specimen. Adding these strengths to the parameter system as a comparison sequence can make the analytical model results more accurate.

3.3.4 Soaking Parameters

The parameters were analyzed in terms of both leaching duration and pH of the leaching solution. Ionic rare earth mining is often carried out by pool leaching and heap leaching, and with the replacement of rare earth ions during the leaching period, a large amount of leach solution will be stored in the collection lane for a long time, and the bedrock of ionic rare earth slopes will be at risk of deterioration under the action of leaching solution (Fang et al., 2018). In this paper, the leaching duration is used as the time

TABLE 1 | The average basic physical and mechanical parameters of each group of bedrock specimens.

Soaking durations (day)	m_1 (g)	m_2 (g)	V (cm ³)	ρ (g/cm ³)	v_1 (m/s)	v_2 (m/s)
0	510.17	510.17	192.69	2.65	4328.67	4328.67
30	511.73	511.89	193.93	2.64	4357.24	4399.50
60	512.22	511.93	193.92	2.64	4413.08	4427.33
90	509.78	511.02	194.33	2.63	4472.57	4446.00
120	510.53	508.107	192.86	2.63	4439.52	4444.67
150	509.65	508.332	192.88	2.64	4379.65	4400.83

m_1 : Average mass of each group of bedrock specimens before leaching; m_2 : Average mass of each group of bedrock specimens after leaching; v_1 : Average P-wave of each group of bedrock specimens before leaching; v_2 : Average P-wave of each group of bedrock specimens after leaching.

TABLE 2 | Calculation results of entropy value method.

Target	Information entropy value e	Positive ideal solution A_j^+	Negative ideal solution A_j^-	Weighting factor w (%)
Porosity	0.9982	0.20	0.15	7.27
pH	0.9971	0.52	0.39	11.59
Macropore	0.9917	0.48	0.29	33.65
Micropore	0.9985	0.09	0.07	6.00
T2	0.9898	172.05	99.86	41.37
Mass	0.9999	0.53	0.53	0.01
Volume	0.9999	0.02	0.02	0.01
Density	0.9999	0.00	0.00	0.00
P-wave	0.9999	4.14	4.03	0.09

TABLE 3 | Table of TOPSIS calculation results.

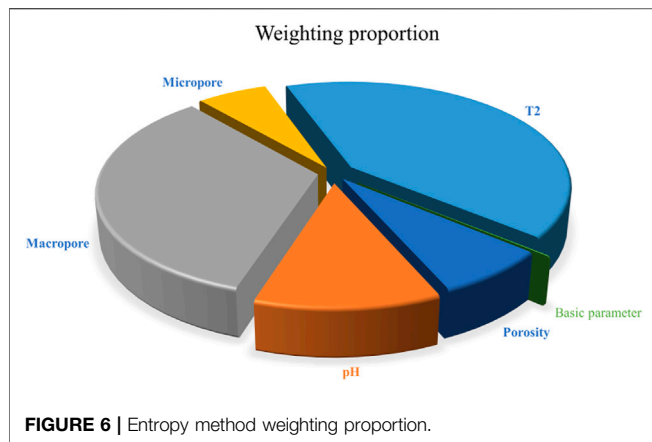
	Positive ideal solution distance	Negative ideal solution distance	Relative proximity	Sort results
	D+	D-	c	
C ₁	0.23	72.19	0.99	1
C ₂	70.79	1.40	0.02	5
C ₃	72.19	0.13	0.01	6
C ₄	40.06	32.12	0.44	3
C ₅	56.45	15.73	0.21	4
C ₆	40.06	32.12	0.44	2

parameter for model analysis, and an attempt is made to analyze the difference in the degree of deterioration of bedrock specimens under different leaching durations and to find out the characteristic parameters of dominant response accompanying the deterioration. It has been shown that the granite will show obvious deterioration under acidic solution soaking, and the pH variation of the solution after soaking is an important indicator for the analysis of the degree of granite deterioration under acidic conditions (Han et al., 2016; Huang et al., 2020).

3.4 Deterioration Analysis of Bedrock Mechanical Properties Based on E-TOPSIS Method

In order to obtain the dominant response of parameters for bedrock specimen deterioration under different soaking

durations, the judgment matrix under different soaking durations was established by the parameter system in **Figure 5**, and the entropy values and weights of different soaking durations were calculated according to **Eqs 1–4**, respectively (**Table 2**); the Euclidean distances of the parameter values from the optimal solution (A_j^+) and the worst solution (A_j^-) and the closeness to the optimal solution were calculated according to **Eqs 5–8**, respectively, and the scores were ranked (**Table 3**). In the E-TOPSIS method analysis, the mechanical parameters of bedrock specimen are a developmental characterization of the deterioration mechanism of the bedrock specimen, and their values are linearly related to the degree of deterioration of the bedrock specimen, so the characteristic parameters of the bedrock specimen are not brought into the analytical model as analytical parameters.



As can be seen from **Table 2**, the larger difference between the positive ideal solution A_j^+ and the negative ideal A_j^- solution in the parameter layer, the greater the degree of variability is indicated, and the larger the entropy value is, indicating that the parameter has a lower responsiveness to the degree of deterioration of the bedrock specimen at different soaking durations, and thus the smaller the weight is. Conversely the smaller the entropy value of the parameter, the larger the weight. Among the parameter weights, the NMR t2 relaxation time and large pores have the largest weight (>30%); the pH value of the soaking solution also has a larger weight (>10%); the porosity and micropore have a smaller weight (>5%); and the basic physical parameters of the bedrock specimen (mass, volume, density, and P-wave) have the smallest weight (<0.1%).

The weighting results are shown in **Figure 6**. From the size of the weights, it can be seen that the NMR T2 relaxation time occupies the largest weight, while the macropore and the pH of the leaching solution are second, and the porosity and micropore are smaller, indicating that along with the variation of the soaking duration, the parameter with the most dominant response to it is the NMR t2 relaxation time, and from the microscopic level. At the microscopic level, the response of macropore to soaking is more prominent compared to porosity and macropore.

Table 3 shows the comprehensive scores ρ of the response parameters of bedrock specimens under different soaking durations according to TOPSIS method based on the entropy results, where the smaller the Euclidean distance ρ between the comprehensive scores of the parameter system and the positive ideal solution, and the larger the Euclidean distance ρ from the negative ideal solution, the better. The results were $c_1 > c_6 > c_4 > c_5 > c_2 > c_3$, indicating the response of the parameter system to the degree of deterioration at different soaking durations, where the degree of deterioration was lowest at 0 days of soaking, followed by 150 days of soaking, and the highest degree of deterioration was observed at 60 days of soaking. By comparing with the peak strength of bedrock specimens at different soaking durations, it was found that the model results were consistent with the degradation degree of bedrock specimens. It indicates that the E-TOPSIS method has

TABLE 4 | Fuzzy grey correlation coefficient table.

	Micropore	Macropore	Porosity	pH	T2
ζ_{a0}	0.5236	0.3815	0.4448	0.4432	0.7801
ζ_{a30}	0.9354	0.7080	0.8115	1.0000	0.7614
ζ_{a60}	0.5499	0.7376	0.6255	0.7780	0.6401
ζ_{a90}	0.8103	0.7394	0.9613	0.7764	0.6764
ζ_{a120}	0.8784	0.5689	0.6979	0.6900	0.7476
ζ_{a150}	0.7361	0.6949	0.9841	0.8214	0.7193
ζ_{b0}	0.5388	0.3976	0.4610	0.4593	0.8571
ζ_{b30}	0.9035	0.7017	0.7949	0.9589	0.8577
ζ_{b60}	0.5943	0.7976	0.6762	0.8414	0.6920
ζ_{b90}	0.8650	0.7658	0.9836	0.8292	0.7029
ζ_{b120}	0.9199	0.6021	0.7354	0.7273	0.7864
ζ_{b150}	0.7901	0.7185	1.0000	0.8428	0.7722
ζ_{c0}	0.6087	0.3865	0.4781	0.4755	0.5216
ζ_{c30}	0.9052	0.7590	0.9276	0.8358	0.6159
ζ_{c60}	0.4792	0.6793	0.5572	0.7254	0.5726
ζ_{c90}	0.9265	0.5964	0.7923	0.8689	0.5423
ζ_{c120}	1.0000	0.5486	0.7189	0.7078	0.7908
ζ_{c150}	0.7049	0.6181	0.9468	0.7556	0.6846

ζ_a : Cracking strength; ζ_b : Damage strength; ζ_c : Peak strength.

TABLE 5 | Fuzzy grey correlation table.

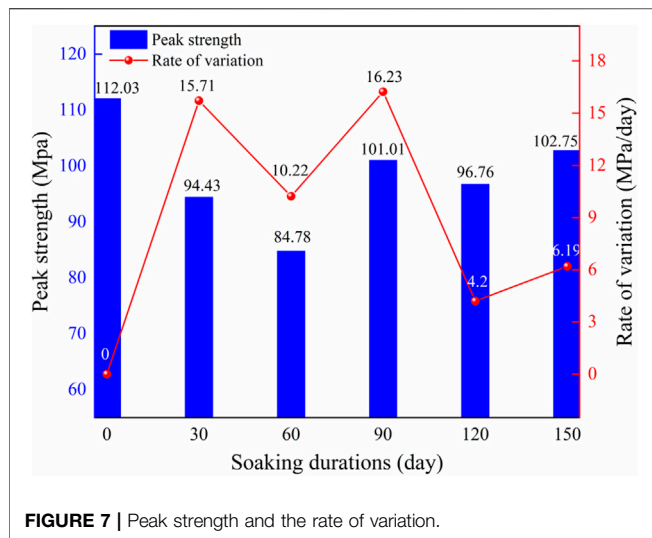
	Micropore	Macropore	Porosity	pH	T2
Cracking strength	0.7686	0.6639	0.7752	0.7765	0.7780
Damage strength	0.7389	0.6384	0.7542	0.7515	0.7028
Peak strength	0.7707	0.5980	0.7368	0.7282	0.6213

some analytical ability to explain the deterioration degree of bedrock specimens under different soaking durations. In order to reveal the response of each parameter in this parameter system to the characteristic intensity of bedrock specimens, further fuzzy grey correlation analysis is required.

3.5 Study on Mechanical Property Deterioration of Bedrock Based on Fuzzy Grey Correlation Analysis Algorithm

Combined with the E-TOPSIS method analysis, the differences in the basic physical parameters of the bedrock specimens under the leaching erosion conditions have a small effect on the parameter system as a whole, so the soaking parameters and microstructural parameters are analyzed as the focus in the fuzzy grey correlation analysis. The fuzzy grey correlation coefficients of the parameter system on the characteristic strength of the bedrock specimens were calculated according to **Eqs 9, 10**, respectively, **Table 4**, and then their correlations were calculated according to **Eq. 11**, **Table 5**.

Table 4 and **Table 5** show the correlation coefficients and correlations of each parameter with the average cracking strength, average damage strength and average peak strength of the bedrock specimens under different soaking time conditions, respectively. The correlation between micropore, porosity and pH of the leaching solution is larger, followed by macropore and NMR T2 relaxation time.

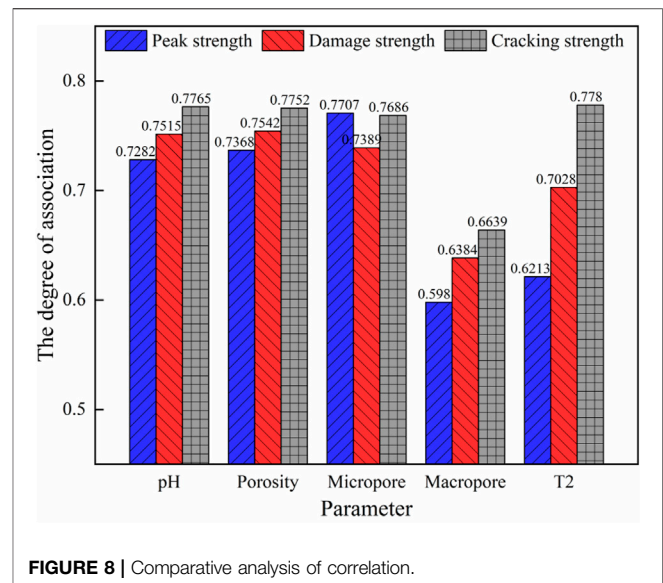


4 DISCUSSION

Uniaxial compressive strength is an important parameter for evaluating the stability of bedrock of ionic rare earth ore slopes, and some rock-forming mineral components under the erosion of leaching solution undergo different degrees of chemical decomposition and precipitation-adsorption reactions, causing different degrees of variations in their uniaxial compressive strength (Zhang and Zhao, 2013; Wang et al., 2020). In order to study the effect of leaching solution on the uniaxial compressive strength of bedrock specimens of ionic rare earth ore slopes, the average uniaxial compressive strength of bedrock specimens and its variation rate under different soaking duration conditions were statistically analyzed (Figure 7).

As can be seen from Figure 7, the mechanical properties of the bedrock of the slope are different with different soaking duration conditions. The peak strength of the bedrock specimens decreased from 112.03 MPa in the natural state to 102.75 MPa at 150 days of soaking, with a decrease of about 8.28%, which is obvious. The mechanical properties of the bedrock fluctuate greatly due to the influence of leaching erosion, and the peak strength of the bedrock specimens decreases the most at the early stage of soaking, and then rebound at 90 days, after which it fluctuates in a small range. The analysis is due to the fact that at the early stage of soaking, the micropore of the bedrock specimen gradually increased by the erosion of the leaching solution, and the internal structure of the bedrock specimen was damaged, resulting in the decrease of mechanical strength.

The fusion analysis of the mechanical parameters of the slope bedrock with its physical parameters under different soaking duration conditions shows that the micropore, macropore and porosity of the bedrock specimens, the NMR T2 relaxation time and the pH of the leaching solution are correlated with the characteristic stress parameters of the bedrock specimens to some extent. In order to explore the dominant response factors of mechanical parameters of bedrock specimens under different soaking duration conditions. In this paper, the



correlations of characteristic stress parameters of bedrock specimens under the conditions of different response factors were compared and analyzed (Figure 8).

As can be seen from Figure 8, in the fuzzy grey correlation analysis, the correlation between all parameters and the characteristic strength is high, and the parameter with the most significant difference from other parameters is the micropore, which has a higher correlation with the peak strength than the damage strength and cracking strength. Combined with the analysis in Figure 4, it can be seen that the micropore has the highest percentage at 60 days of soaking, and then starts to decrease. This is related to the pattern of damage of bedrock specimens under uniaxial compression. Combined with Figure 3, it can be seen that the trends of the three characteristic strengths are roughly the same, with the characteristic strength of bedrock specimens continuously decreasing at the beginning of the soaking period, reaching the highest degree of deterioration at 60 days, rebounding sharply at 90–120 days of soaking, and fluctuating in a small range thereafter. The above results of test indicate that there is a more significant correlation between micropore and the characteristic strength of bedrock specimens.

The results of the previous test showed that the pH value of the leaching solution continued to increase with the increase of soaking durations, presumably due to the chemical reaction between the leaching solution and the bedrock specimen to generate new minerals, resulting in a decrease in concentration. The porosity ratio of the bedrock specimens when not leached was mostly micropore and less macropore; the porosity continued to increase from soaking to 90 days, and the micropore ratio reached the maximum at 60 days; the macropore continued to decrease after reaching a high point at 30 days of soaking, and gradually increased during 90–120 days of soaking.

In the fuzzy ash correlation analysis, the correlation coefficient of parameters is an important quantitative index to judge the

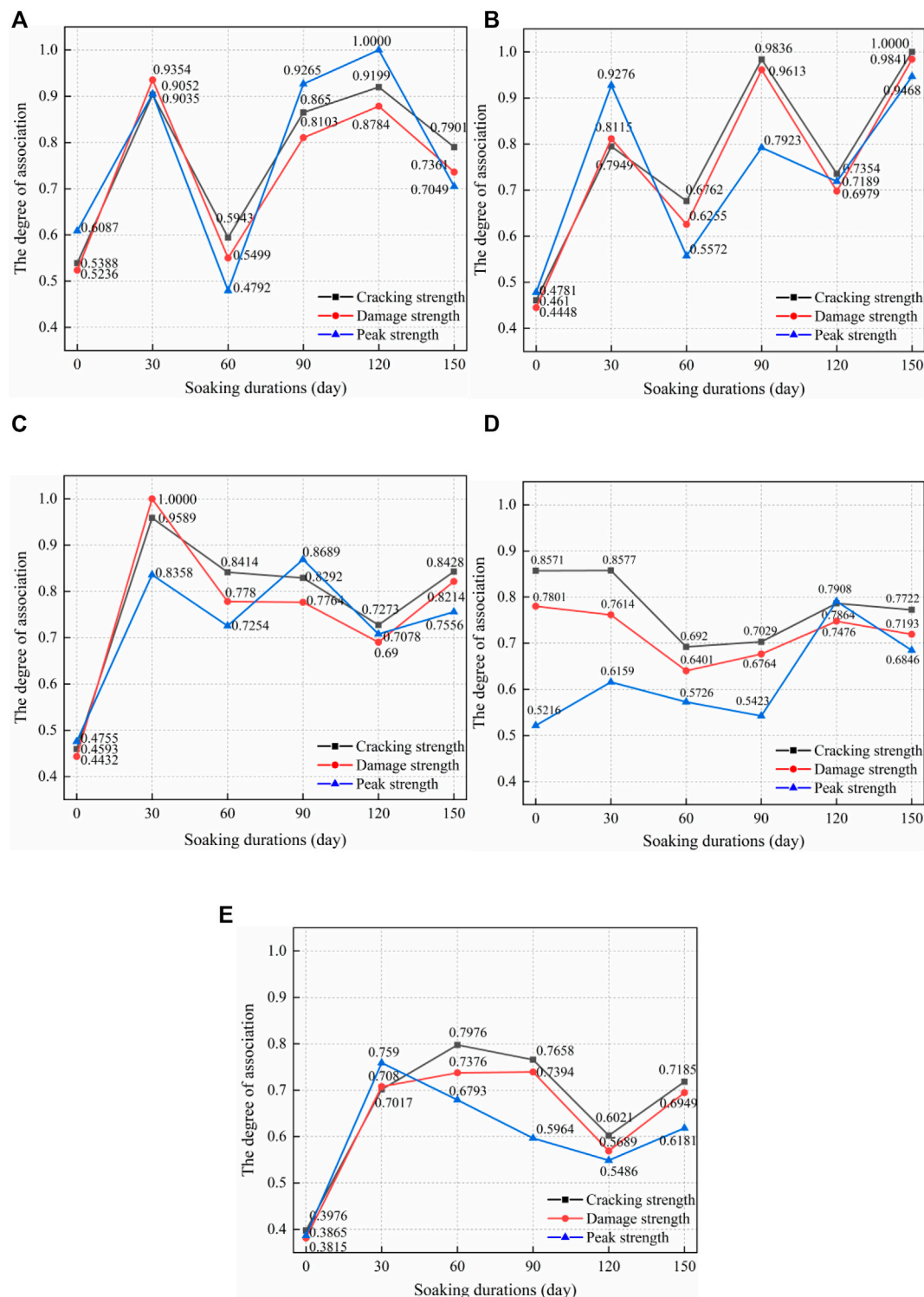


FIGURE 9 | Comparison of the correlation coefficient under different parameters. (A) Micropore; (B) Porosity; (C) pH; (D) T2; (E) Macropore.

correlation between the reference and comparison sequences, and the more obvious variations of the correlation coefficient of parameters indicates the higher correlation between the reference and comparison sequences (Liang et al., 2018). The

analysis of the fuzzy grey results shows that the correlation coefficient of pH of the leaching solution varies significantly at the beginning of soaking, and the fluctuation becomes slower with the increase of soaking duration, **Figure 9C**; the correlation

coefficient of micropore fluctuates sharply from 0 to 90 days of soaking and slows down at the end of soaking, **Figure 9A**; the correlation coefficient of macropore shows an increasing trend at the beginning of soaking until the fluctuation at the end of soaking, **Figure 9E**. And the porosity correlation coefficient shows strong fluctuations throughout the soaking process, indicating that the microscopic pore variations of bedrock specimens under leaching erosion is highly correlated with the deterioration activity of bedrock specimens, **Figure 9B**; combined with **Figure 9D**, the correlation coefficient curve of NMR T2 relaxation time decreases at the beginning of soaking and fluctuates significantly at the end of soaking. NMR T2 relaxation time is an important parameter reflecting the variations of bedrock pore structure, and the fluctuation variation of the correlation coefficient of NMR T2 relaxation time is roughly related to the variation trend of the characteristic intensity of bedrock specimens. From the above analysis, it can be seen that there is a more significant correlation between the trends of micropore and porosity of bedrock specimens and the internal deterioration activities of bedrock specimens, followed by the pH value of leaching solution.

5 CONCLUSION

In this paper, the E-TOPSIS method and fuzzy ash correlation analysis were combined to fuse the multi-source heterogeneous information of porosity, pH, mass, volume, density, p-wave and characteristic strength of ionic rare earth slope bedrock under leaching erosion. This research can serve as a theoretical foundation for predicting slope hazards in ionic rare earth mines. From the research, the following results were drawn:

- 1) The bedrock parameters of ionic rare earth slopes have the characteristic of changing with the variation of soaking duration. The E-TOPSIS method with the advantage of analysis under different time conditions and the fuzzy grey correlation method are selected to fuse the characteristic parameters of slope bedrock under leaching erosion. The entropy weight method shows that the influence of leaching erosion on the pore parameters is more significant.
- 2) Under the leaching erosion, the mechanical properties of the bedrock specimens showed a significant decrease and then a significant recovery, followed by fluctuations in a small range.

REFERENCES

- Abdel-Basset, M., Manogaran, G., Gamal, A., and Smarandache, F. (2019). A Group Decision Making Framework Based on Neutrosophic TOPSIS Approach for Smart Medical Device Selection. *J. Med. Syst.* 43 (2), 38. doi:10.1007/s10916-019-1156-1
- Behzadian, M., Khanmohammadi Otaghsara, S., Yazdani, M., and Ignatius, J. (2012). A State-Of-The-Art Survey of TOPSIS Applications. *Expert Syst. Appl.* 39 (17), 13051–13069. doi:10.1016/j.eswa.2012.05.056
- Chen, P. (2019). Effects of Normalization on the Entropy-Based TOPSIS Method. *Expert Syst. Appl.* 136, 33–41. doi:10.1016/j.eswa.2019.06.035

Along with the deterioration phenomenon, the pore parameters of the bedrock specimens show a dominant response to the pH of the leaching solution. The results of the E-TOPSIS composite analysis are consistent with the ranking of the degradation of the bedrock specimens at different soaking durations.

- 3) The micropore of bedrock specimen accounted for the highest percentage at 60 days of soaking, and the porosity varied significantly during the soaking period. The results of the fuzzy ash correlation analysis showed that the correlation between the micropore, the porosity and the characteristic strength of bedrock was the most significant, followed by the pH of the leaching solution.

DATA AVAILABILITY STATEMENT

The original contributions presented in the study are included in the article/Supplementary Material, further inquiries can be directed to the corresponding author.

AUTHOR CONTRIBUTIONS

Drafting of article: WZ and ZF; planning and supervision of the research: BL; analysis and interpretation of data: ZZ and PZ; acquisition of data: ZG, KH, and XW.

FUNDING

This work was supported by the National Natural Science Foundation of China (51764014, 51874148, 51904119, 52004106, and 52104086), the Natural Science Foundation of Jiangxi Province (20192BAB206018 and 20192BCBL23010), the Postdoctoral Research Foundation of China (2017M622099), the Open Research Fund of State Key Laboratory of Geomechanics and Geotechnical Engineering (Z017024), the Education Commission Program of Jiangxi Province (GJJ160674), the Postdoctoral Research Foundation of Jiangxi Province (2018KY03), the Youth Jinggang Scholars Program in Jiangxi Province (QNJG2019054), the Jiangxi thousand talents program (jxsq2018102092), the Innovative Leading Talents Program in Ganzhou ((2020)60).

- Chen, P. (2021). Effects of the Entropy Weight on TOPSIS. *Expert Syst. Appl.* 168, 114186. doi:10.1016/j.eswa.2020.114186
- Chen, Z. (2011). Global Rare Earth Resources and Scenarios of Future Rare Earth Industry. *J. Rare Earths* 29 (1), 1–6. doi:10.1016/s1002-0721(10)60401-2
- Deng, J. (1983). Gray System Overview. *World Sci.* 07, 3–7.
- Dutta, T., Kim, K.-H., Uchimiya, M., Kwon, E. E., Jeon, B.-H., Deep, A., et al. (2016). Global Demand for Rare Earth Resources and Strategies for green Mining. *Environ. Res.* 150, 182–190. doi:10.1016/j.envres.2016.05.052
- Fan, X., Xu, Q., Scaringi, G., Dai, L., Li, W., Dong, X., et al. (2017). Failure Mechanism and Kinematics of the Deadly June 24th 2017 Xinmo Landslide, Maoxian, Sichuan, China. *Landslides* 14 (6), 2129–2146. doi:10.1007/s10346-017-0907-7

- Fang, X., Xu, J., and Wang, P. (2018). Compressive Failure Characteristics of Yellow sandstone Subjected to the Coupling Effects of Chemical Corrosion and Repeated Freezing and Thawing. *Eng. Geology*. 233, 160–171. doi:10.1016/j.enggeo.2017.12.014
- Geng, H., Zhang, S., Zhi, J., Zhang, R., Ren, J., and Ro, C.-U. (2019). Acid Solution Decreases the Compressional Wave Velocity of sandstone from the Yungang Grottoes, Datong, China. *Herit Sci*. 7, 11. doi:10.1186/s40494-019-0245-2
- Guo, Z.-q., Lai, Y.-m., Jin, J.-f., Zhou, J.-r., Sun, Z., and Zhao, K. (2020). Effect of Particle Size and Solution Leaching on Water Retention Behavior of Ion-Absorbed Rare Earth. *Geofluids* 2020, 1–14. doi:10.1155/2020/4921807
- Han, T., Shi, J., Chen, Y., and Li, Z. (2016). Effect of Chemical Corrosion on the Mechanical Characteristics of Parent Rocks for Nuclear Waste Storage. *Sci. Tech. Nucl. Installations* 2016, 1–11. doi:10.1155/2016/7853787
- Huang, X.-W., Long, Z.-Q., Wang, L.-S., and Feng, Z.-Y. (2015). Technology Development for Rare Earth Cleaner Hydrometallurgy in China. *Rare Met.* 34 (4), 215–222. doi:10.1007/s12598-015-0473-x
- Huang, X., Pang, J., Liu, G., and Chen, Y. (2020). Experimental Study on Physicomechanical Properties of Deep Sandstone by Coupling of Dry-Wet Cycles and Acidic Environment. *Adv. Civil Eng.* 2020, 1–17. doi:10.1155/2020/2760952
- Huang, Z., Zeng, W., Gu, Q., Wu, Y., Zhong, W., and Zhao, K. (2021). Investigations of Variations in Physical and Mechanical Properties of Granite, sandstone, and marble after Temperature and Acid Solution Treatments. *Construction Building Mater.* 307, 124943. doi:10.1016/j.conbuildmat.2021.124943
- Li, J., Kaunda, R. B., Zhu, L., Zhou, K., and Gao, F. (2019). Experimental Study of the Pore Structure Deterioration of Sandstones under Freeze-Thaw Cycles and Chemical Erosion. *Adv. Civil Eng.* 2019, 1–12. doi:10.1155/2019/9687843
- Liang, X., Ye, M., Yang, L., Fu, W., and Li, Z. (2018). Evaluation and Policy Research on the Sustainable Development of China's Rare Earth Resources. *Sustainability* 10 (10), 3792. doi:10.3390/su10103792
- Liu, S. F., Tao, L. Y., Xie, N. M., and Yang, Y. J. (2016). On the New Model System and Framework of Grey System Theory. *J. Grey Syst.* 28 (1), 1–15. Available at: <http://ieeexplore.ieee.org/stamp/stamp.jsp?tp=&arnumber=7301810>
- Luo, F. Y., Zhang, G., and Ma, C. H. (2021). On the Soil Slope Failure Mechanism Considering the Mutual Effect of Bedrock and Drawdown. *Int. J. Geomechanics* 21 (2), 12. doi:10.1061/(asce)gm.1943-5622.0001903
- Luo, T., Fan, G., Guo, B., and Zhang, S. (2021). Experimental Study on the Influence of Hydro-Chemical Erosion on Morphology Parameters and Shear Properties of limestone Fractures. *Acta Geotech.* 16 (12), 3867–3880. doi:10.1007/s11440-021-01365-9
- Miao, S., Cai, M., Guo, Q., Wang, P., and Liang, M. (2016). Damage Effects and Mechanisms in Granite Treated with Acidic Chemical Solutions. *Int. J. Rock Mech. Mining Sci.* 88, 77–86. doi:10.1016/j.ijrmms.2016.07.002
- Miao, S., Wang, H., Cai, M., Song, Y., and Ma, J. (2018). Damage Constitutive Model and Variables of Cracked Rock in a Hydro-Chemical Environment. *Arab J. Geosci.* 11 (2), 14. doi:10.1007/s12517-017-3373-6
- Ni, J., Chen, Y.-L., Wang, P., Wang, S.-R., Peng, B., and Azzam, R. (2017). Effect of Chemical Erosion and Freeze-Thaw Cycling on the Physical and Mechanical Characteristics of Granites. *Bull. Eng. Geol. Environ.* 76 (1), 169–179. doi:10.1007/s10064-016-0891-5
- Si, S.-L., You, X.-Y., Liu, H.-C., and Zhang, P. (2018). DEMATEL Technique: A Systematic Review of the State-Of-The-Art Literature on Methodologies and Applications. *Math. Probl. Eng.* 2018, 1–33. doi:10.1155/2018/3696457
- Silva, R. G., Morais, C. A., Teixeira, L. V., and Oliveira, É. D. (2019). Selective Precipitation of High-Quality Rare Earth Oxalates or Carbonates from a Purified Sulfuric Liquor Containing Soluble Impurities. *Mining, Metall. Exploration* 36 (5), 967–977. doi:10.1007/s42461-019-0090-6
- Wang, Y., Zhang, H., Lin, H., Zhao, Y., and Liu, Y. (2020). Fracture Behaviour of central-flawed Rock Plate under Uniaxial Compression. *Theor. Appl. Fracture Mech.* 106, 102503. doi:10.1016/j.tafmec.2020.102503
- Zhang, C., Wang, Y., and Jiang, T. (2020). The Propagation Mechanism of an Oblique Straight Crack in a Rock Sample and the Effect of Osmotic Pressure under In-Plane Biaxial Compression. *Arab J. Geosci.* 13 (15), 736. doi:10.1007/s12517-020-05682-3
- Zhang, Q. B., and Zhao, J. (2013). A Review of Dynamic Experimental Techniques and Mechanical Behaviour of Rock Materials. *Rock Mech. Rock Eng.* 47 (4), 1411–1478. doi:10.1007/s00603-013-0463-y
- Zhao, K., Wu, W., Zeng, P., Yang, D., Liu, Y., Wang, L., et al. (2021a). Numerical and Experimental Assessment of the Sandstone Fracture Mechanism by Non-uniform Bonded Particle Modeling. *Rock Mech. Rock Eng.* 54 (12), 6023–6037. doi:10.1007/s00603-021-02620-x
- Zhao, K., Yang, D., Gong, C., Zhuo, Y., Wang, X., and Zhong, W. (2020). Evaluation of Internal Microcrack Evolution in Red sandstone Based on Time-Frequency Domain Characteristics of Acoustic Emission Signals. *Construction Building Mater.* 260, 120435. doi:10.1016/j.conbuildmat.2020.120435
- Zhao, K., Yang, D., Zeng, P., Gong, C., Wang, X., and Zhong, W. (2021b). Accelerating Creep Stage of Red Sandstone Expressed and Quantitatively Identified Based on Acoustic Emission Information. *Rock Mech. Rock Eng.* 54 (9), 4867–4888. doi:10.1007/s00603-021-02529-5
- Zhao, K., Yang, D., Zeng, P., Huang, Z., Wu, W., Li, B., et al. (2021c). Effect of Water Content on the Failure Pattern and Acoustic Emission Characteristics of Red sandstone. *Int. J. Rock Mech. Mining Sci.* 142, 104709. doi:10.1016/j.ijrmms.2021.104709
- Zhao, Y. Y., Zhang, G., Hu, D. S., and Han, Y. Z. (2018). Centrifuge Model Test Study on Failure Behavior of Soil Slopes Overlying the Bedrock. *Int. J. Geomechanics* 18 (11), 11. doi:10.1061/(asce)gm.1943-5622.0001292
- Zhong, W., Ouyang, J., Yang, D., Wang, X., Guo, Z., and Hu, K. (2021). Effect of the In Situ Leaching Solution of Ion-Absorbed Rare Earth on the Mechanical Behavior of Basement Rock. *J. Rock Mech. Geotechnical Eng.* 14 (6). [in press]. doi:10.1016/j.jrmge.2021.12.002

Conflict of Interest: The authors declare that the research was conducted in the absence of any commercial or financial relationships that could be construed as a potential conflict of interest.

Publisher's Note: All claims expressed in this article are solely those of the authors and do not necessarily represent those of their affiliated organizations, or those of the publisher, the editors and the reviewers. Any product that may be evaluated in this article, or claim that may be made by its manufacturer, is not guaranteed or endorsed by the publisher.

Copyright © 2022 Zhong, Feng, Li, Zhang, Zeng, Guo, Hu and Wang. This is an open-access article distributed under the terms of the Creative Commons Attribution License (CC BY). The use, distribution or reproduction in other forums is permitted, provided the original author(s) and the copyright owner(s) are credited and that the original publication in this journal is cited, in accordance with accepted academic practice. No use, distribution or reproduction is permitted which does not comply with these terms.



Experimental Study of Dynamic Characteristics of Tailings With Different Reconsolidation Degrees After Liquefaction

Wensong Wang^{1,2}, Guansen Cao^{2,3*}, Ye Li¹, Yuxi Zhou¹, Ting Lu², Ya Wang² and Binbin Zheng⁴

¹State Key Laboratory of Geohazard Prevention and Geoenvironment Protection, Chengdu University of Technology, Chengdu, China, ²State Key Laboratory of Coal Mine Disaster Dynamics and Control, Chongqing University, Chongqing, China, ³Zijin Mining Company Limited, Shanghang, China, ⁴School of Management Science and Engineering, Shandong Technology and Business University, Yantai, China

OPEN ACCESS

Edited by:

Wen Nie,
Jiangxi University of Science and
Technology, China

Reviewed by:

Fujiao Tang,
Harbin Institute of Technology, China
Peng Feng,
Chengdu University, China
Changbo Du,
Liaoning Technical University, China

*Correspondence:

Guansen Cao
caogs_zijin@163.com

Specialty section:

This article was submitted to
Geohazards and Georisks,
a section of the journal
Frontiers in Earth Science

Received: 15 February 2022

Accepted: 16 March 2022

Published: 11 April 2022

Citation:

Wang W, Cao G, Li Y, Zhou Y, Lu T,
Wang Y and Zheng B (2022)
Experimental Study of Dynamic
Characteristics of Tailings With
Different Reconsolidation Degrees
After Liquefaction.
Front. Earth Sci. 10:876401.
doi: 10.3389/feart.2022.876401

The construction period of most tailing ponds generally lasts for more than 10 years or even decades. During this period, it may be affected by more than one earthquake and is often subjected to vibrations generated by mining activities. The tailings liquefied by earthquakes or vibrations may experience dynamic loads again. Due to the low permeability of tailings, the reconsolidation process of tailings after liquefaction is prolonged. Therefore, changes in the nature of the tailings caused by previous earthquakes will affect the performance of the tailing dam in the subsequent earthquakes. Dynamic triaxial tests and bending element tests were conducted on two kinds of tailings from a copper mine in Southwest China to study this process. The tailing specimens will undergo two consolidation processes and subsequent cyclic loads during the test. The influence of reconsolidation degree, confining pressure, and particle size on the dynamic characteristics and wave velocity of the tailings after liquefaction under cyclic loading was measured. The results show that the reconsolidation degree significantly affects the trend of the excess pore water pressure ratio changing with the increase in the cycle number of loads. The reconsolidation process after liquefaction of tailings will improve its liquefaction resistance. The relationship between the ratio of the cycle number of liquefaction after reconsolidation to the cycle number of first liquefaction and the reconsolidation degree is proposed. In the entire experimental process, the shear wave velocity of the tailings gradually decreases when applying the cyclic load and gradually increases during the consolidation process, including the first consolidation before cyclic loading and reconsolidation after liquefaction. The research results are of great significance to the safe disposal of tailings, especially those in earthquake-prone areas.

Keywords: tailings, dynamic characteristic, liquefaction, consolidation degree, wave velocity, earthquake

1 INTRODUCTION

A tailing pond is formed by the accumulation of tailings discharged from metal and non-metal mines, which has a high potential risk of debris flow (Vick, 1990; Wei et al., 2013). Once a tailing pond is damaged, it will lead to vast environmental pollution along with casualties and property losses (Villavicencio et al., 2014; Martin-Crespo et al., 2015; Santamarina et al., 2019; Chen et al., 2021). According to relevant statistics, seismic liquefaction is the second significant factor responsible for the failure of a tailing pond (Rico et al., 2008). The laboratory test is a meaningful way to explore the dynamic characteristics of tailings, which can provide a basis for revealing the seismic instability mechanism of tailing dams. Several scholars have studied the dynamic characteristics of tailings such as cyclic shear stress ratio (CSR), dynamic shear modulus (G_d), initial shear modulus (G_0), damping ratio (λ_d), shear wave velocity (V_s), and excess pore water pressure (μ_d), etc (Wijewickreme et al., 2005; James et al., 2011; Liu et al., 2012; Cao et al., 2019; Lu et al., 2021).

The collapse of some dams is not due to seismic loading during an earthquake but rather due to reduction in shear strength or liquefaction resistance after an earthquake. The construction period of a tailing pond continues for dozens of years, during which it may have to withstand several accidental earthquakes. The influence of earthquakes on tailing dams is very complicated. The changes in the nature of tailings caused by the previous earthquake will affect the performance of the tailing dam during the subsequent earthquake. The Kayakari tailing reservoir in Japan did not suffer damage in the major earthquake of 2003, while in the minor earthquake of 2011, liquefaction occurred, and the dam broke. Ishihara et al. (2015) have conducted a series of *in situ* experiments and established relevant models for verification. The results show that the overall stability of the tailing dam decreases to some extent even if the earthquake does not directly destroy the dam; however, the strength of the tailings and the stability of the tailings reservoir will increase with the increase of time after the earthquake and reconsolidation of the tailings with the dissipation of excess pore pressure. Therefore, in addition to focusing on whether the dam will be damaged in the earthquake, the research on the dynamic stability of the tailing dam should also pay attention to whether or when the post-earthquake tailing dam can recover to the pre-earthquake stability, that is, the post-earthquake tailing consolidation to what extent can restore the original strength. It is of great significance to study the change in mechanical properties during the reconsolidation process of tailings after an earthquake.

Some researchers have studied the post-liquefaction behavior of sand, silt, and clay with various factors, including densities, fine content, and reconsolidated degrees (U_{re}). Ashour et al. (2009) presented equations to assess the undrained response of liquefied sand based on drained test behavior, indicating that the post-cyclic excess pore pressure and associated residual effective confining pressure govern the post-liquefaction undrained behavior of sand. Wang et al. (2013) studied the effect of limited excess pore pressures on silt, indicating that an

excess pore pressure ratio of greater than 0.70 was a prerequisite for significant volume reduction, and thus an increase in undrained shear strength due to reconsolidation after cyclic loading. Soroush and Soltani-Jigheh (2009) measured the behavior of clay under monotonic, cyclic, and post-cyclic loading and found that during post-cyclic monotonic shearing, the clay behaves similarly to over-consolidated soil; the larger the particle size is, the higher the over-consolidation ratio would be. According to previous studies, the dynamic and mechanical properties of post-liquefied soil are affected by factors such as effective confining pressure (σ'_c), U_{re} , CSR, particle size, and other factors. However, most scholars focused more on the residual strength and deformation characteristics of post-liquefied soils with a monotonic shear method and seldom paid attention to the liquefaction resistance with recyclic loading. Tailing dams usually contain a lot of fine grains, resulting in poor permeability, which will make them more prone to liquefaction and collapse (Karim and Alam, 2014). Therefore, it is necessary to study the dynamic response of post-liquefied tailings under cyclic loading during the reconsolidation process under the influence of multifactor coupling.

In this study, a dynamic triaxial test system was adopted to carry out the cyclic loading test again on the tailing specimens with different degrees of reconsolidation after the first liquefaction and the second liquefaction was achieved. Several cyclic loading tests with different U_{re} , σ'_c , and CSR were conducted on two types of tailing specimens. This study aims to obtain the change in excess pore water pressure and shear wave velocity during the cyclic reloading process with variant U_{re} . In particular, the liquefaction resistance of tailings under different U_{re} was compared. The research results can provide a basis for further understanding of the stability change law and failure mechanism of tailing dams in earthquake-prone areas.

2 TEST MATERIALS, METHODS, AND PROCEDURES

2.1 Source of Test Materials

The tailing materials being examined in this study are chosen from the Xiaodae copper tailing pond located 2.8 km in the southwest of Huili County, Liangshan Prefecture, Sichuan Province, China, as shown in **Figure 1**. The Xiaodae tailing pond is surrounded by mountains in three directions, with the bottom of the terrain shaped like a "V." The north side of the terrain is higher than the south, with the slope being 8–10. The total dam height is 187.5 m, and its total final capacity is 953.61 million m³. It is a typical upstream tailing pond.

The Xiaodae tailing pond is located in the Himalayan earthquake zone. The Himalayan earthquake zone is one of the largest earthquake areas in China and the region where earthquakes occur most intensely and frequently. In the vicinity of the Xiaodae tailing pond, the 7.7 magnitude Tonghai earthquake (5 January 1970), 7.0 magnitude Lijiang earthquake (3 February 1996), 8.0 Wenchuan earthquake (12 May 2008), and 7.0 magnitude Yaan earthquake (20

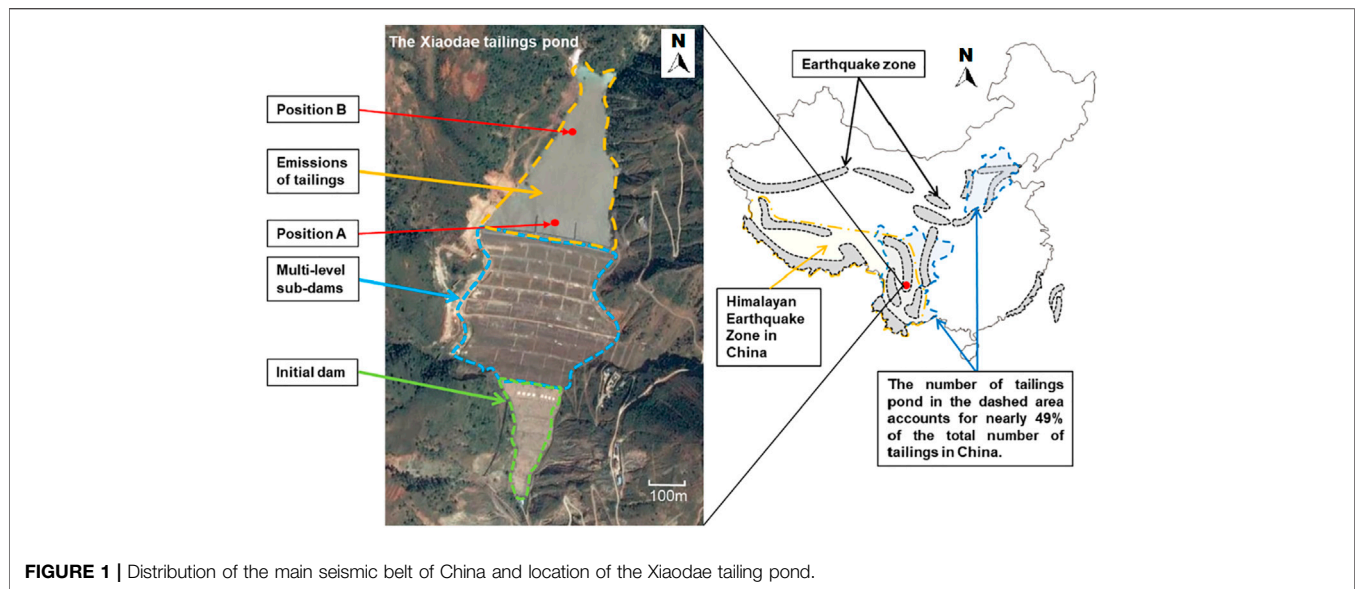


FIGURE 1 | Distribution of the main seismic belt of China and location of the Xiaodae tailing pond.

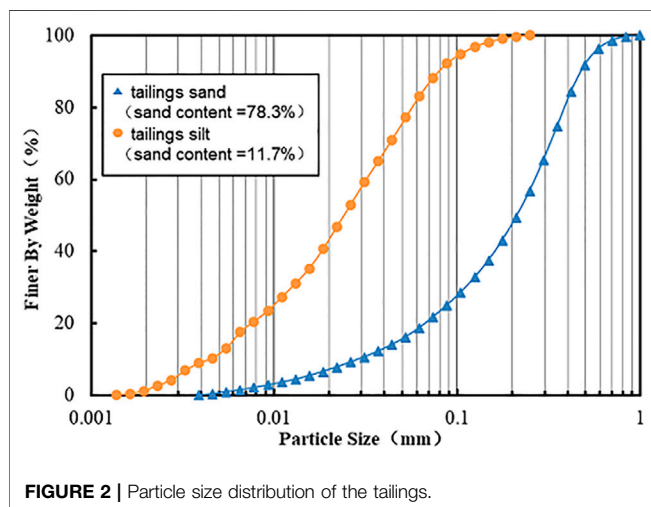


FIGURE 2 | Particle size distribution of the tailings.

April 2013) have occurred. China's seismic belt and mineral resource distribution area have considerably overlapped. There are currently about 8,000 tailing ponds in China, nearly half of which are distributed in the two major earthquake areas (North China and Southwest China) shown in **Figure 1**. Therefore, it is necessary to study the dynamic characteristics of the Xiaodae tailings for variant consolidation degrees after cyclic loading.

2.2 Physical and Mechanical Properties of Test Materials

2.2.1 Particle Size Distribution

The Xiaodae tailing pond is constructed using the upstream method. Therefore, on the top beach surface near the sub-dams, the particle size of the tailings is larger; whereas, at the tail part of the beach, it is finer. Previous studies have shown that particle size has a great effect on the dynamic properties of soils

(Gratchev et al., 2006; Yilmaz et al., 2008). Therefore, on the typical top beach surface shown in **Figure 1**, two Xiaodae copper tailings were collected, taken from the front position (position A) and tail position (position B). The particle size distribution curves of tailings were obtained by using an S3500 light-scattering particle size analyzer (manufactured by Microtrac, Inc., Montgomeryville, PA, United States) and shown in **Figure 2** and **Table 1**. The clay content (particle size ≤ 0.005 mm), silt content (0.005 mm $<$ particle size ≤ 0.074 mm), and sand content (particle size > 0.074 mm) in the coarse tailings in the test are 0.9, 20%, 20.8%, and 78.3%, respectively. The abovementioned particle contents in fine tailings are 13.1%, 75.2%, and 11.7%, respectively. Both tailings have a uniformity coefficient greater than 5 and a curvature coefficient between 1 and 3, so they are both granular materials with good particle gradation. The mineralogy and chemical composition of the tailings have been described in detail in our published article (Cao et al., 2019).

2.2.2 Static Characteristics

According to the National Standard of the People's Republic of China "Standards for Geotechnical Test Methods" (GB/T 50123–2019), the physical properties and static mechanical properties of two tailings were obtained by tests, including density, moisture content, liquid and plastic limit, cohesion, and internal friction angle, as listed in **Table 2**. According to another National Standard of the People's Republic of China "Safety Regulation for Tailings Pond" (GB 39496–2020), the test results show that the two types of tailings can be named tailing sand and tailing silt.

2.2.3 Dynamic Characteristics

The dynamic characteristic parameters of soil usually include liquefaction resistance, shear modulus, and damping ratio. The dynamic characteristics of the test tailings were obtained by dynamic triaxial tests. Generally, liquefaction resistance is

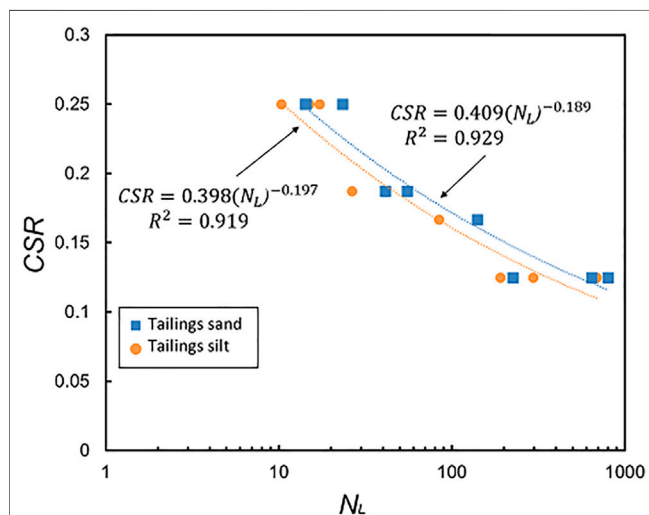
TABLE 1 | Particle size distribution parameters of the tailings.

Category	Clay content (%)	Silt content (%)	Sand content (%)	D ₅₀ (mm)	C _u	C _c
Tailing sand	0.9	20.8	78.3	0.024	9.66	1.74
Tailing silt	13.1	75.2	11.7	0.211	7.75	1.36

D_{50} refers to the average particle size, C_u refers to the uniform coefficient, and C_c refers to the curvature coefficient.

TABLE 2 | Physical property and static mechanical property parameters of the tailings.

Category	Specific gravity	Dry density (g/cm ³)	Void ratio e	Natural moisture content (%)	Effective cohesion c (kPa)	Effective internal friction angle φ (°)	Liquid limit (%)	Plastic limit (%)
Tailings sand	2.85	1.51	0.89	12	7	34	22	17
Tailings silt	2.86	1.54	0.86	15	12	29	24	18

**FIGURE 3** | Number of liquefaction failure cycles (N_L) versus the cyclic shear stress ratio (CSR) of the tailings.

expressed by the relationship between the CSR and number of liquefaction failure cycles N_L , as given in **Eqs 1, 2** (Lu et al., 2021).

$$CSR = \tau / \sigma'_c, \quad (1)$$

$$CSR = a \cdot N_L^b, \quad (2)$$

where τ and σ'_c are shear stress and effective confining pressure, respectively; a and b are the fitting parameters that depend on some common factors of tailings such as density, particle structure and size, stress history, etc. The results of the liquefaction resistance are shown in **Figure 3**. Comparing the experimental results of the liquefaction resistance of the tailing sand and tailing silt, it can be seen that the empirical equation **Eq. 2** can fit well in the relationship between the CSR and failure cycle number of tailings.

The dynamic deformation characteristics of soil are usually expressed by the relationship between the dynamic shear modulus ratio (G_d/G_0)/damping ratio (λ_d) and dynamic

shear strain (γ_d). G_d , G_0 , and λ_d can be obtained by analyzing the hysteresis curve and shear wave velocity (Lu et al., 2021). In **Figure 4**, $G_d/G_0 \sim \gamma_d$ and $\lambda_d \sim \gamma_d$ of the test tailings were compared to previous relevant findings on natural sands (Seed and Idriss, 1970; Ishihara, 1996; Rollins et al., 1998; Stokoe et al., 2004). It can be seen from **Figure 4** that compared with natural sand, the dynamic shear modulus ratio and damping ratio of tailings are more sensitive to changes in dynamic shear strain. When the dynamic shear strain exceeds 0.001, compared with the natural sand, the attenuation of the dynamic shear modulus ratio and increase of the damping ratio of the tailings are both faster; especially when the dynamic shear strain exceeds 0.01, the damping ratio of the tailings will be significantly larger than that of natural sand. The abovementioned phenomenon reflects the particularity of the dynamic behavior of tailings under cyclic loading.

2.3 Test Methods and Procedures

All tests in the study were performed in stress-controlled loading mode on a DYN-TTS-type dynamic triaxial instrument (manufactured by GDS Instruments, Hampshire, United Kingdom). The loading waveform is controlled by a servo system as a sine wave with a vibration frequency of 1 Hz. The tailings specimens were prepared by following the requirements of the Standards for Geotechnical Test Methods (GB/T 50123-2019). The samples collected from the Xiaodae tailing pond were reconstructed into cylindrical specimens with diameter of 50 mm and height of 100 mm using the wet tamping method. The test specimens were prepared according to the dry density and natural moisture content listed in **Table 2**. After the specimen preparation was completed, vacuum saturation was first conducted, and then the multistage back pressure saturation in the pressure chamber was performed until the saturation degree reached 95%. The specimens were subjected to the first consolidation under different confining pressures (100 kPa, 200 kPa, and 400 kPa), and the pore water pressure dissipated to 0 kPa as the consolidation was completed. It should be pointed out that, considering that the liquefaction depth of tailing dam during

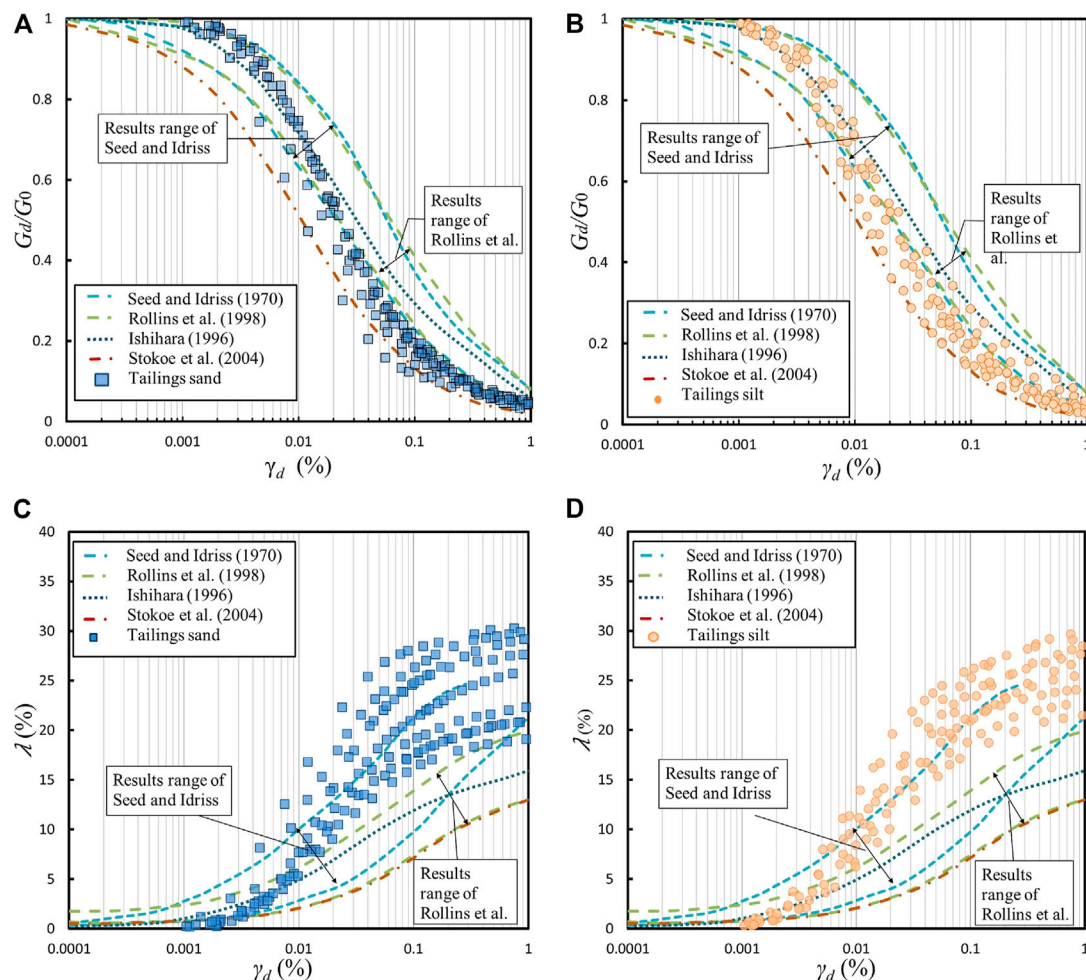


FIGURE 4 | Comparison of the dynamic deformation characteristics of the tailings and natural sands: (A) $G_d/G_0 \sim \gamma_d$ curves of the tailings sand; (B) $G_d/G_0 \sim \gamma_d$ curves of the tailings silt; (C) $\lambda_d \sim \gamma_d$ curves of the tailings sand; and (D) $\lambda_d \sim \gamma_d$ curves of the tailings silt.

earthquakes generally does not exceed 20 m, the maximum confining pressure in the test was set to 400 kPa, which corresponds to the maximum principal stress at a depth of 20 m.

During the loading stage, cyclic loading of specific CSRs was applied to the tailing specimens until the excess pore water pressure was equal to the effective confining pressure, thereby obtaining the liquefied specimens. This process stimulates the liquefaction of tailings caused by earthquakes. Then, the specimens were reconsolidated, that is, being consolidated again. During the reconsolidation process, the excess pore water pressure was controlled to reach a preset U_{re} in order to simulate different stages of the pore water migration and dissipation process at the site after an earthquake. After reconsolidation, the second cyclic loading with the same CSRs as the first loading was applied to the specimens. When the excess pore water pressure reached the confining pressure again, the reloading process ended. The shear wave velocity was measured by the bender element test after each consolidation was completed. The data such

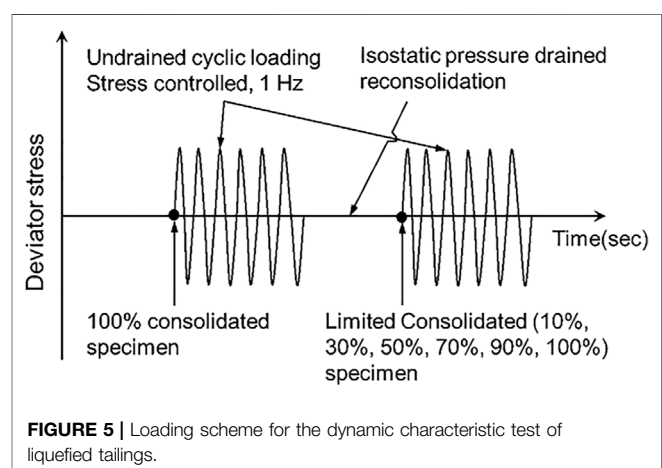
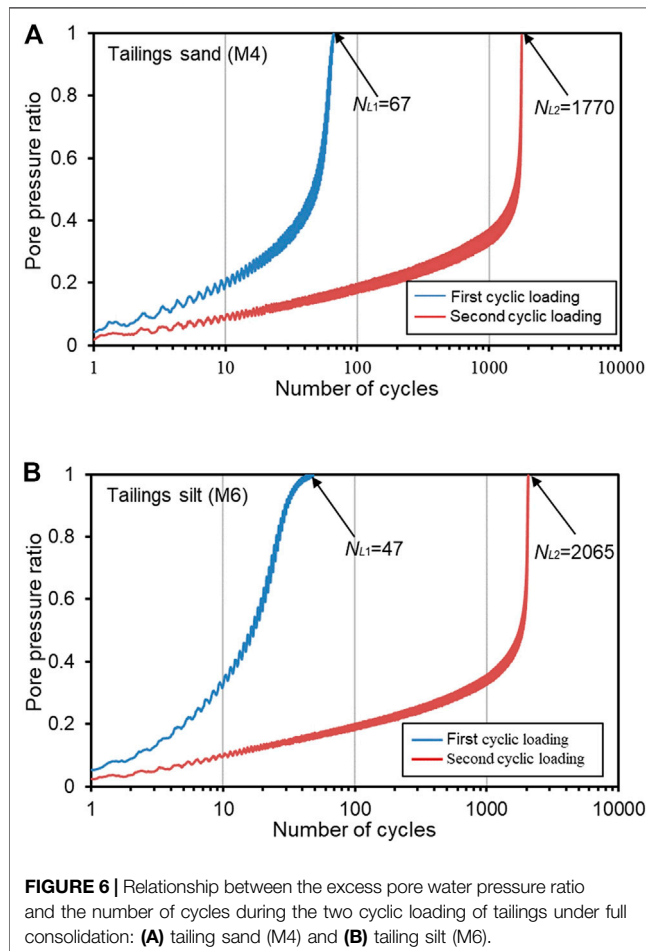


FIGURE 5 | Loading scheme for the dynamic characteristic test of liquefied tailings.

as the number of loading cycles, axial strain, pore water pressure, and shear wave velocity were collected and recorded in real time during the test process. The detailed

TABLE 3 | Test scheme for dynamic characteristics of liquefied tailings.

Test number	Sample category	Effective confining pressure (kPa)	Cyclic shear stress ratio	Vibration frequency (Hz)	Degree of reconsolidation (%)
M1	Tailings sand	100	0.25	1	20, 40, 60, 80, 100
M2	Tailings sand	200	0.25	1	20, 40, 60, 80, 100
M3	Tailings sand	400	0.25	1	20, 40, 60, 80, 100
M4	Tailings sand	400	0.188	1	10, 30, 50, 70, 90, 100
M5	Tailings silt	100	0.25	1	20, 40, 60, 80, 100
M6	Tailings silt	400	0.188	1	10, 30, 50, 70, 90, 100

**FIGURE 6** | Relationship between the excess pore water pressure ratio and the number of cycles during the two cyclic loading of tailings under full consolidation: (A) tailing sand (M4) and (B) tailing silt (M6).

experimental scheme and testing process are shown in Figure 5 and Table 3.

3 RESULT ANALYSIS AND DISCUSSION

3.1 Excess Pore Water Pressure

Considering the M4 and M6 test groups as examples, the changes of excess pore water pressure of tailing sand and tailing silt after liquefaction under the cyclic reloading were analyzed. The σ'_c and CSR in the two groups of tests were both 400 kPa and 0.188, respectively. In this study, the number of liquefaction failure cycles in the two

cyclic loading processes was defined as N_{L1} and N_{L2} , respectively.

Figure 6 shows the relationship between the excess pore water pressure ratio (μ_d/σ'_c) and number of cycles for the tailing sand and tailing silt during the two cyclic loading processes. After the liquefied tailings are fully consolidated again, the number of liquefaction failure cycles is significantly larger than the original one. This is due to the increased compaction of the tailings due to vibration and subsequent drainage consolidation (Geng et al., 2021). The liquefaction number of tailing silt increased from 47 to 2065 and that of tailing sand increased from 67 to 1770. That is, compared with tailing sand, the effect of the first vibration on the liquefaction resistance of tailing silt was more significant. This phenomenon reflects that after the tailings are subjected to dynamic loads such as earthquakes if they are sufficiently consolidated, their liquefaction resistance will be enhanced. Meanwhile, the effect of the vibro-consolidation method in the process of tailing dam construction is also confirmed.

The relationship between the excess pore water pressure ratio and number of cycles of tailings after liquefaction with different U_{re} is shown in Figure 7. Figure 7 shows that with the increase in the U_{re} , the number of the liquefaction failure cycles increases, indicating an increase in liquefaction resistance. When the U_{re} is low (such as 10%~70% in Figure 7), the excess pore water pressure ratio is approximately linear with the logarithm of the number of cycles; when U_{re} is high (such as 90% and 100% in Figure 7), the excess pore water pressure ratio is approximately piecewise linear with the logarithm of the number of cycles: with the increase in the cycle numbers, the increase of the excess pore water pressure ratio can be divided into two stages: when the pore pressure ratio is less than 0.5, its increase rate is relatively low; when it exceeds 0.5, the pore pressure ratio increases rapidly. Bi et al. (2016) explained this phenomenon, arguing that the porosity nonuniformity of the particle system affects the occurrence of particle dislocation, and the porosity nonuniformity of the particle system becomes weaker as the pore pressure increases.

The dynamic pore pressure model of soil describes the development law of excess pore water pressure under the action of cyclic loading and is usually expressed by the relationship between the excess pore water pressure ratio and cycle number ratio (the ratio of the number of cycles to the number of liquefaction failures, N/N_L). Figure 8 shows the dynamic pore pressure models of tailings after liquefaction with different U_{re} . When the U_{re} is low, the dynamic pore

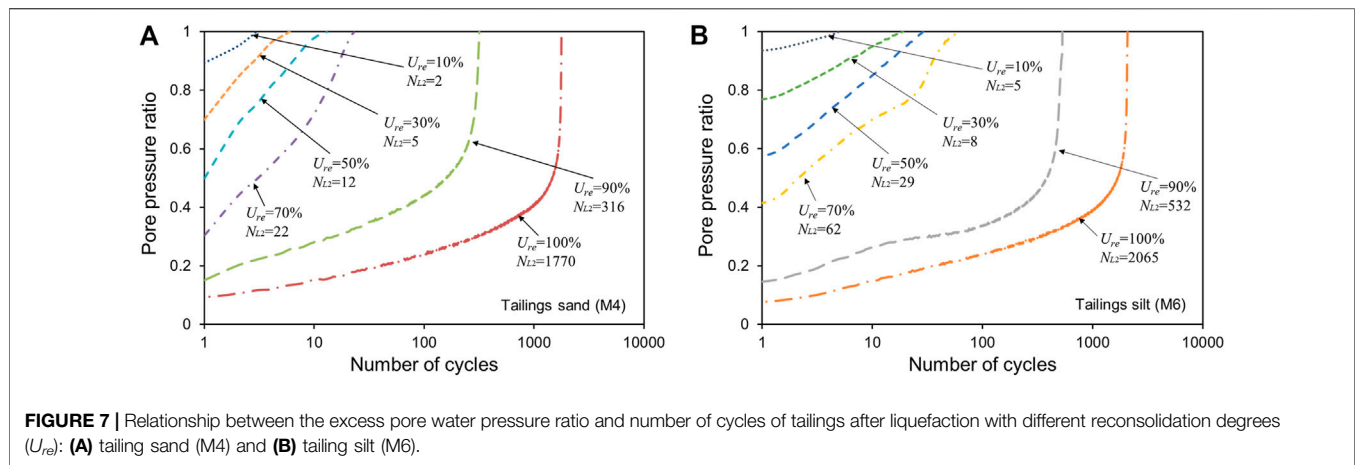


FIGURE 7 | Relationship between the excess pore water pressure ratio and number of cycles of tailings after liquefaction with different reconsolidation degrees (U_{re}): (A) tailing sand (M4) and (B) tailing silt (M6).

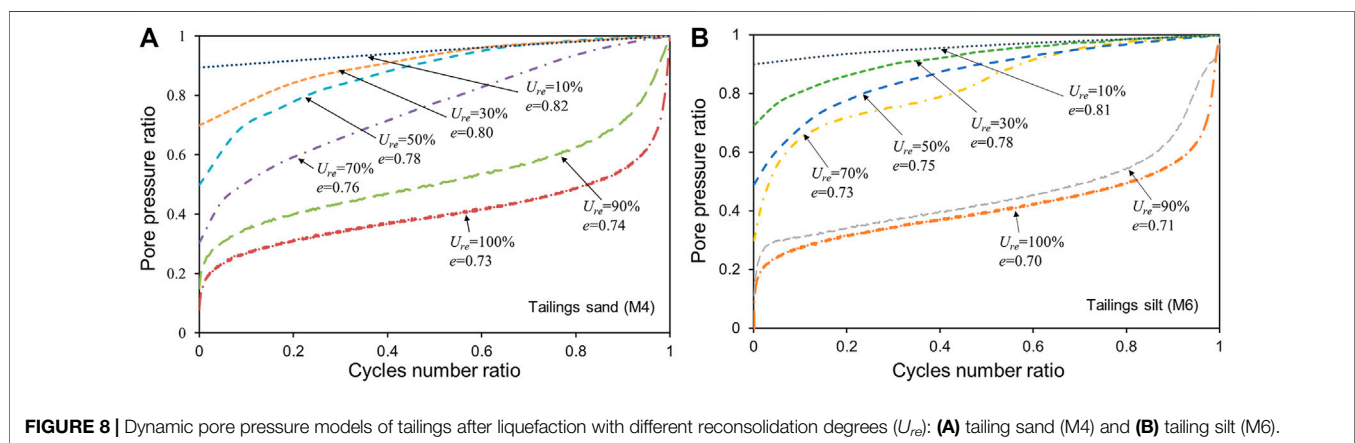


FIGURE 8 | Dynamic pore pressure models of tailings after liquefaction with different reconsolidation degrees (U_{re}): (A) tailing sand (M4) and (B) tailing silt (M6).

pressure models of the two tailings are both convex type; with the increase of U_{re} , the dynamic pore pressure model gradually evolves into a convex-concave type. **Figure 8** also shows the void ratios corresponding to different U_{re} calculated according to the drainage volume during the reconsolidation drainage process. With the increase of U_{re} , the void ratio gradually decreases, and the particle structure of the tailings changes from a loose state to a dense state, resulting in a change in the shape of the dynamic pore pressure model. The same phenomenon was obtained in the experimental studies of natural sands by Papadopolou et al. (2010) and Monkul et al. (2015), indicating that tailings have a strong similarity with natural sands in the evolution law of dynamic pore pressure, wherefore it is also prone to liquefaction under vibration.

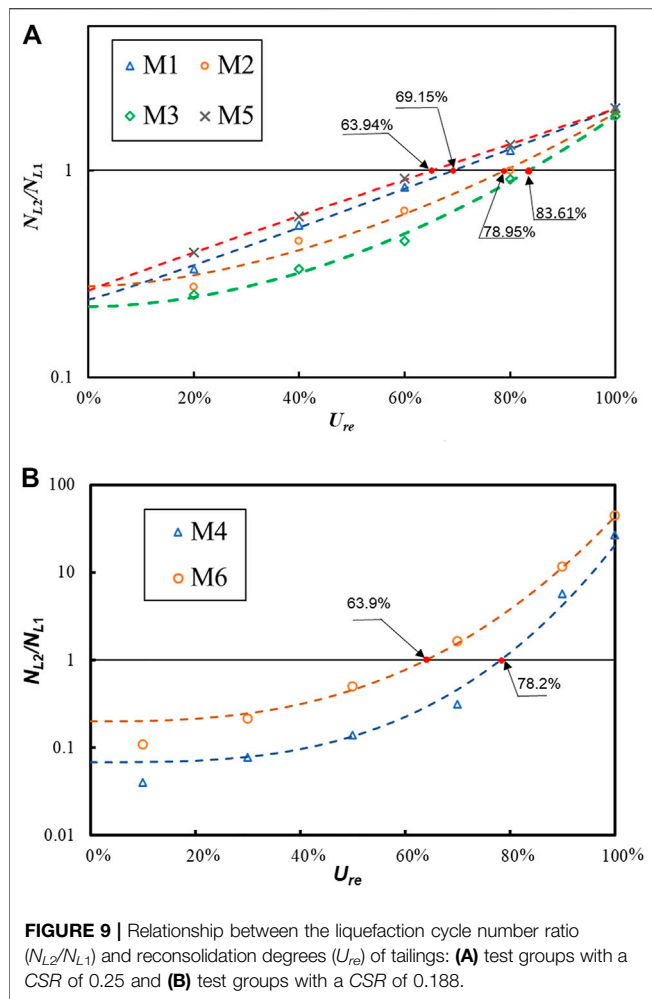
3.2 Liquefaction Resistance

From the test results of the two cyclic loadings, it can be seen that the reconsolidation effect after the cyclic loading increases the liquefaction resistance of the tailings. The results of a series of experiments conducted by Ishihara et al. (2015) show that while the earthquake reduces the overall stability of the tailing dam in the short term, the strength of the tailings gradually increases over time as reconsolidation effects occur. Similar

conclusions are also found in the work of Wang et al. (2013), who studied the undrained shear strength of fully reconsolidated liquefied silt, which was 4.2 times that of the original silt. The ratio of the second liquefaction failure cycle number (N_{L2}) to the first liquefaction failure cycle number (N_{L1}) of the same specimen can quantitatively characterize the influence of the reconsolidation effect on the liquefaction resistance of tailings. In the study, the ratio N_{L2}/N_{L1} is named as the liquefaction cycle number ratio. The liquefaction cycle number ratios of tailings with various U_{re} were calculated, as shown in **Figure 9** and **Eq. 3**.

$$\lg\left(\frac{N_{L2}}{N_{L1}}\right) = A\left(1 - \frac{\mu_d}{\sigma'_c}\right)^B + \lg C, \quad (3)$$

where A , B , and C are the fitting parameters, μ_d is the excess pore water pressure, σ'_c is the effective confining pressure, and $1 - \frac{\mu_d}{\sigma'_c}$ is equal to U_{re} . The results of the fitting parameters are shown in **Table 4**. All the goodness-of-fit of the six groups of test results using **Eq. 3** is close to 1, which confirms the applicability of the formula. When the N_{L2}/N_{L1} is equal to 1, **Eq. 3** implies that the liquefaction resistance of the tailings with this reconsolidation degree returns to that before cyclic loading.



It can be seen from the six sets of experimental results shown in **Figure 9** that all the N_{L2}/N_{L1} increase with the increase of U_{re} . A reasonable explanation for this phenomenon is that the soil skeleton is completely remodeled during the development of liquefaction: although the effective stress is almost zero post liquefaction, the particles are rearranged to form a new skeleton structure with stronger stability potential; during the reconsolidation process, the excess pore water pressure gradually dissipates, the newly formed particle skeleton structure becomes dense and stable, and its liquefaction resistance exceeds that of the original tailings at pre-liquefaction (Wang and Wei, 2016).

The effective confining pressure of the three test groups of M1, M2, and M3 increased gradually, and the other conditions were the same. It can be seen from the data of M1, M2, and M3 in **Figure 9** that with the increase of the effective confining pressure, the N_{L2}/N_{L1} of the liquefied tailings under the same U_{re} gradually decreases. When N_{L2}/N_{L1} is equal to 1, the U_{re} of the three groups of M1, M2, and M3 are 69.15%, 78.95%, and 83.61%, respectively, that is, the U_{re} required to restore the liquefaction resistance before cyclic loading increases with the increase of the effective confining pressure. This may be due to the high confining

TABLE 4 | Fitting results of the relationship between the liquefaction cycle number ratio and reconsolidation degrees of tailings.

Test number	A	B	C	R2
M1	0.926	1.060	0.2365	0.99
M2	0.840	1.709	0.2748	0.97
M3	0.923	1.883	0.2193	0.98
M4	4.176	1.663	0.0018	0.96
M5	0.882	0.971	0.2623	0.99
M6	2.337	2.699	0.2043	0.97

pressure limiting the extent of particle skeletal structure remodeling during cyclic loading.

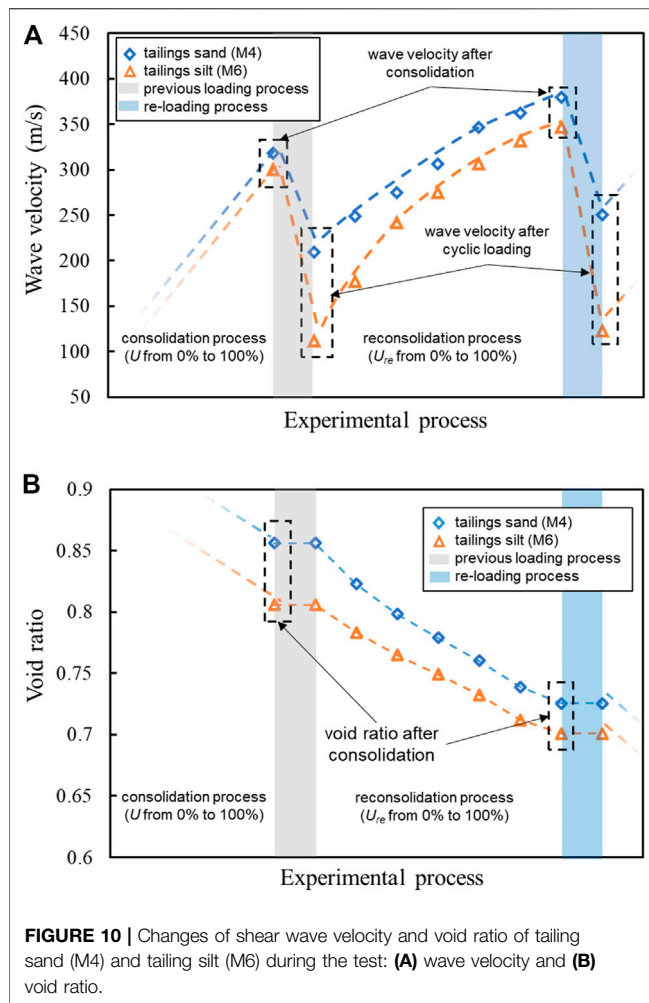
Comparing the results of M1 and M5 in **Figure 9A** and M4 and M6 in **Figure 9B**, we can analyze the difference in the relationship between N_{L2}/N_{L1} and U_{re} of tailing sand and tailing silt. Under the same other conditions, the N_{L2}/N_{L1} of tailing silt is significantly larger than that of tailing sand, indicating that tailing silt has a higher increase in liquefaction resistance than tailing sand after liquefaction and reconsolidation. McDowell and Bolton (1999) proposed that when a granular material has wide disparity in particle size, the small particles are kinematically unstable, and the large particles are stable. Therefore, due to the larger number of fine particles in tailing silt, its particle structure is better optimized after cyclic loading, resulting in its N_{L2}/N_{L1} being higher than that of tailing sand.

Meanwhile, comparing the results of M3 and M4 in **Figure 9** (with different CSR and other same conditions), it can be seen that the CSR has a significant impact on the shape of the relationship curve between N_{L2}/N_{L1} and U_{re} : the curve with a CSR of 0.188 is significantly steeper than that with a CSR of 0.25, indicating that a more significant increase in liquefaction resistance can be obtained by applying a cyclic load with a smaller CSR.

The N_{L2}/N_{L1} versus U_{re} results of the study provide a new rapid and feasible method for estimating the liquefaction resistances of tailings after an earthquake. By measuring the pore water pressure of the tailings after the earthquake to obtain the U_{re} , combined with the liquefaction resistance of the tailings before the earthquake, the liquefaction resistance of the tailings after the earthquake can be obtained without the need to carry out a large number of dynamic tests again. This has an important guiding significance for the post-earthquake risk assessment and emergency treatment of tailing ponds.

3.3 Shear Wave Velocity

Shear wave velocity is an important index to reflect the dynamic strength and dynamic deformation characteristics of soil (Kayabali, 1996; Rahman and Siddiqua, 2017). Taking the test results of M4 and M6 as examples, the shear wave velocity changes in tailing sand and tailing silt during cyclic loading and drainage consolidation were analyzed, as shown in **Figure 10A**. The shear wave velocities of the two tailings decreased significantly under cyclic loading and gradually recovered during the subsequent reconsolidation process. Many previous studies have shown that there is a strong correlation between the shear wave velocity of soil and its compactness, which can be expressed by void ratio due to the



different propagation velocities of waves in solids and liquids (Cao et al., 2019; Li et al., 2022). The change in the void ratio of the tailing specimens during the whole test process is shown in **Figure 10B**. During the consolidation process, the particle structure of tailings becomes tighter under confining pressure, the void ratio decreases, and the water in the pores is gradually discharged, resulting in a gradual increase in the shear wave velocity. Since the compactness of the tailings after reconsolidation exceeds that after the first consolidation, the wave velocity of the tailings after reconsolidation is also significantly higher than that after the first consolidation. It is worth noting that the void ratio of the specimen did not change during the two undrained cyclic loadings, but the shear wave velocity still decreased significantly. Whalley et al. (2012) pointed out that the wave velocity of soil is directly related to the effective stress in addition to the compactness: the generation of excess pore water pressure microscopically hinders the direct contact of adjacent particles, thereby increasing the proportion of the liquid medium in the propagation path of the wave. Therefore, under the action of cyclic loading, the increase of excess pore water pressure in the tailings (the decrease of effective stress) leads to the decrease of wave velocity.

Figure 10A also shows that the shear wave velocity of tailing sand is higher than that of tailing silt, and compared with the tailing sand, cyclic loading has a greater effect on the wave velocity of tailing silt. Akbari Paydar and Ahmadi (2016) also found in similar experiments on natural sands of different particle sizes that the higher the content of coarse particles, the higher the wave velocity, although the porosity ratio of sand with larger particle size is relatively lower. This may be because the larger the content of fine particles, the more complex the interlaced structure of particles and pore water, resulting in increased wave propagation time; the contact strength between fine particles is weak, and the contact between fine particles is easily destroyed during cyclic loading so that the proportion of the solid medium in the propagation path of the wave is reduced (Zhang et al., 2015).

4 CONCLUSION

In this study, a variety of dynamic triaxial tests and bending element tests were performed to analyze the dynamic characteristics and wave velocity characteristics of tailing sand and tailing silt with multiple reconsolidation degrees after liquefaction, from which the following conclusions are drawn:

During the process of cyclic reloading of the liquefied tailings, the development law of excess pore water pressure is related to the reconsolidation degree: when the reconsolidation degree is low, the excess pore water pressure ratio and the logarithm of the cycles number are approximately linear, and the dynamic pore pressure model is of convex type; when the reconsolidation degree is high, the excess pore water pressure ratio and the logarithm of the cycles number is approximately piecewise linear (when the excess pore water pressure ratio exceeds 0.5, its growth rate increases significantly), and the dynamic pore pressure model is convex-concave type.

The liquefaction resistance of the tailings increases with the reconsolidation degree and eventually exceeds that of the original tailings. A fitting formula is proposed to characterize the relationship between the reconsolidation degree and liquefaction resistance of reconsolidated tailings. The liquefaction resistance of reconsolidated tailings decreases with the increase of effective confining pressure and particle size, and the decrease of the cyclic shear stress ratio can make the relationship curve between the two liquefaction cycle ratio and reconsolidation degree steeper.

The shear wave velocity of tailings is affected by compaction, effective stress, and particle size. During the drainage consolidation process, the wave velocity increases gradually due to the increase in the compactness of the tailings; in the undrained cyclic loading process, although the compaction of the tailings does not change, the reduction of effective stress will also lead to the reduction of wave velocity. In addition, the effect of cyclic loading on wave velocity is more pronounced with decreasing particle size.

The research results can provide a basis for further understanding of the stability change law and failure mechanism of tailing dams and are of great significance to the safe disposal of tailings in earthquake-prone areas.

DATA AVAILABILITY STATEMENT

The raw data supporting the conclusion of this article will be made available by the authors, without undue reservation.

AUTHOR CONTRIBUTIONS

Conceptualization: WW and GC; data curation: GC and YL; formal analysis: WW, GC and TL; funding acquisition: WW and BZ; investigation: YZ, TL and YW; methodology: GC; project

administration: WW; supervision: BZ; validation: YL and YZ; visualization: GC and YZ; writing—original draft: WW and GC; writing—review and editing: WW.

FUNDING

This study was financially supported by the National Natural Science Foundation of China (51804051 and 51804178) and the Natural Science Foundation of Chongqing, China (cstc2019jcyj-bshX0022).

REFERENCES

- Akbari Paydar, N., and Ahmadi, M. M. (2016). Effect of Fines Type and Content of Sand on Correlation between Shear Wave Velocity and Liquefaction Resistance. *Geotech. Geol. Eng.* 34 (6), 1857–1876. doi:10.1007/s10706-016-9995-8
- Ashour, M., Norris, G., and Nguyen, T. (2009). Assessment of the Undrained Response of Sands under Limited and Complete Liquefaction. *J. Geotech. Geoenviron. Eng.* 135 (11), 1772–1776. doi:10.1061/(ASCE)GT.1943-5606.0000114
- Bi, Z., Huang, W., Sun, Q., and Sun, S. (2016). Experimental Analysis of Cyclic Loading on a Cohesionless Granular System. *Granular Matter* 18 (1), 10. doi:10.1007/s10035-016-0611-7
- Cao, G., Wang, W., Yin, G., and Wei, Z. (2019). Experimental Study of Shear Wave Velocity in Unsaturated Tailings Soil with Variant Grain Size Distribution. *Constr. Build. Mater.* 228, 116744. doi:10.1016/j.conbuildmat.2019.116744
- Chen, X., Jing, X., Chen, Y., Pan, C., and Wang, W. (2021). Tailings Dam Break: The Influence of Slurry with Different Concentrations Downstream. *Front. Earth Sci.* 9, 726336. doi:10.3389/feart.2021.726336
- Geng, W., Wang, W., Wei, Z., Huang, G., Jing, X., Jiang, C., et al. (2021). Experimental Study of Mesoscale Deformation Characteristics of Unsaturated Tailings with Different Moisture Content. *Water* 13 (1), 15. doi:10.3390/w13010015
- Gratchev, I. B., Sassa, K., Osipov, V. I., and Sokolov, V. N. (2006). The Liquefaction of Clayey Sands under Cyclic Loading. *Eng. Geol.* 86 (1), 70–84. doi:10.1016/j.enggeo.2006.04.006
- Ishihara, K., Ueno, K., Yamada, S., Yasuda, S., and Yoneoka, T. (2015). Breach of a Tailings Dam in the 2011 Earthquake in Japan. *Soil Dyn. Earthquake Eng.* 68, 3–22. doi:10.1016/j.soildyn.2014.10.010
- Ishihara, K. (1996). *Soil Behavior in Earthquake Geotechnics*. Oxford, UK: Clarendon Press.
- James, M., Aubertin, M., Wijewickreme, D., and Wilson, G. W. (2011). A Laboratory Investigation of the Dynamic Properties of Tailings. *Can. Geotech. J.* 48 (11), 1587–1600. doi:10.1139/T11-060
- Karim, M. E., and Alam, M. J. (2014). Effect of Non-plastic silt Content on the Liquefaction Behavior of Sand-silt Mixture. *Soil Dyn. Earthquake Eng.* 65, 142–150. doi:10.1016/j.soildyn.2014.06.010
- Kayabali, K. (1996). Soil Liquefaction Evaluation Using Shear Wave Velocity. *Eng. Geol.* 44 (1–4), 121–127. doi:10.1016/S0013-7952(96)00063-4
- Li, J., Kong, L., and Jin, L. (2022). Stress History and Time Effect on Shear Modulus of Expansive Soils. *Arab J. Geosci.* 15 (1), 35. doi:10.1007/s12517-021-09342-y
- Liu, H.-m., Yang, C.-h., Zhang, C., and Mao, H.-j. (2012). Study on Static and Dynamic Strength Characteristics of Tailings Silty Sand and its Engineering Application. *Saf. Sci.* 50 (4), 828–834. doi:10.1016/j.ssci.2011.08.025
- Lu, T., Wang, W., Wei, Z., Yang, Y., and Cao, G. (2021). Experimental Study on Static and Dynamic Mechanical Properties of Phosphogypsum. *Environ. Sci. Pollut. Res.* 28 (14), 17468–17481. doi:10.1007/s11356-020-12148-2
- Martín-Crespo, T., Gómez-Ortiz, D., Martín-Velázquez, S., Esbrí, J. M., de Ignacio-San José, C., Sánchez-García, M. J., et al. (2015). Abandoned Mine Tailings in Cultural Itineraries: Don Quixote Route (Spain). *Eng. Geol.* 197, 82–93. doi:10.1016/j.enggeo.2015.08.008
- McDowell, G. R., and Bolton, M. D. (1999). A Micro Mechanical Model for Isotropic Cyclic Loading of Isotropically Clastically Compressed Soil. *Gm* 1 (4), 183–193. doi:10.1007/s100350050024
- Monkul, M. M., Gültekin, C., Gülver, M., Akın, Ö., and Eseller-Bayat, E. (2015). Estimation of Liquefaction Potential from Dry and Saturated sandy Soils under Drained Constant Volume Cyclic Simple Shear Loading. *Soil Dyn. Earthquake Eng.* 75, 27–36. doi:10.1016/j.soildyn.2015.03.019
- Papadopolou, A., Kallioglou, P., Tika, T., Papadopoulos, S., and Batum, E. (2010). Liquefaction Resistance of Silty Sands and Dynamic Properties of Cohesive Soils from Düzce, Turkey. *J. Earthquake Eng.* 14 (3), 351–362. doi:10.1080/13632460903387095
- Rahman, M. Z., and Siddiqua, S. (2017). Evaluation of Liquefaction-Resistance of Soils Using Standard Penetration Test, Cone Penetration Test, and Shear-Wave Velocity Data for Dhaka, Chittagong, and Sylhet Cities in Bangladesh. *Environ. Earth Sci.* 76 (5), 207. doi:10.1007/s12665-017-6533-9
- Rico, M., Benito, G., Salgueiro, A. R., Díez-Herrero, A., and Pereira, H. G. (2008). Reported Tailings Dam Failures. *J. Hazard. Mater.* 152 (2), 846–852. doi:10.1016/j.jhazmat.2007.07.050
- Rollins, K. M., Evans, M. D., Diehl, N. B., and Iii, W. D. D. (1998). Shear Modulus and Damping Relationships for Gravels. *J. Geotech. Geoenviron. Eng.* 124 (5), 396–405. doi:10.1061/(asce)1090-0241(1998)124:5(396)
- Santamarina, J. C., Torres-Cruz, L. A., and Bachus, R. C. (2019). Why Coal Ash and Tailings Dam Disasters Occur. *Science* 364 (6440), 526–528. doi:10.1126/science.aax1927
- Seed, H. B., and Idriss, I. M. (1970). *Soil Moduli and Damping Factors for Dynamic Response Analyses*. Report EERC 70/10. Berkeley, California: University of California. Earthquake Engineering Research Center.
- Soroush, A., and Soltani-Jigheh, H. (2009). Pre- and post-cyclic Behavior of Mixed Clayey Soils. *Can. Geotech. J.* 46 (2), 115–128. doi:10.1139/T08-109
- Stokoe, K. H., Darendeli, M. B., Menq, F., and Choi, W. K. (2004). “Comparison of the Linear and Nonlinear Dynamic Properties of Gravels, Sands, Silts and Clays,” in Proceedings of the 11th International Conference on Soil Dynamics and Earthquake Engineering.
- Vick, S. G. (1990). *Planning, Design, and Analysis of Tailings Dams*. Vancouver, BC, Canada: BiTech Publishers.
- Villavicencio, G., Espinace, R., Palma, J., Fourie, A., and Valenzuela, P. (2014). Failures of Sand Tailings Dams in a Highly Seismic Country. *Can. Geotech. J.* 51 (4), 449–464. doi:10.1139/cgj-2013-0142
- Wang, G., and Wei, J. (2016). Microstructure Evolution of Granular Soils in Cyclic Mobility and post-liquefaction Process. *Granular Matter* 18 (3), 51. doi:10.1007/s10035-016-0621-5
- Wang, S., Luna, R., and Yang, J. (2013). Postcyclic Behavior of Low-Plasticity silt with Limited Excess Pore Pressures. *Soil Dyn. Earthquake Eng.* 54, 39–46. doi:10.1016/j.soildyn.2013.07.016
- Wei, Z., Yin, G., Wang, J. G., Wan, L., and Li, G. (2013). Design, Construction and Management of Tailings Storage Facilities for Surface Disposal in China: Case Studies of Failures. *Waste Manag. Res.* 31 (1), 106–112. doi:10.1177/0734242x12462281
- Whalley, W. R., Jenkins, M., and Attenborough, K. (2012). The Velocity of Shear Waves in Unsaturated Soil. *Soil Tillage Res.* 125, 30–37. doi:10.1016/j.still.2012.05.013
- Wijewickreme, D., Sanin, M. V., and Greenaway, G. R. (2005). Cyclic Shear Response of fine-grained Mine Tailings. *Can. Geotech. J.* 42 (5), 1408–1421. doi:10.1139/T05-058
- Yilmaz, Y., Mollamahmutoglu, M., Ozaydin, V., and Kayabali, K. (2008). Experimental Investigation of the Effect of Grading Characteristics on the

Liquefaction Resistance of Various Graded Sands. *Eng. Geol.* 100 (3-4), 91–100. doi:10.1016/j.enggeo.2007.12.002

Zhang, Q., Yin, G., Wei, Z., Fan, X., Wang, W., and Nie, W. (2015). An Experimental Study of the Mechanical Features of Layered Structures in Dam Tailings from Macroscopic and Microscopic Points of View. *Eng. Geol.* 195, 142–154. doi:10.1016/j.enggeo.2015.05.031

Conflict of Interest: Author GC is employed by Zijin Mining Company Limited.

The remaining authors declare that the research was conducted in the absence of any commercial or financial relationships that could be construed as a potential conflict of interest.

Publisher's Note: All claims expressed in this article are solely those of the authors and do not necessarily represent those of their affiliated organizations, or those of the publisher, the editors, and the reviewers. Any product that may be evaluated in this article, or claim that may be made by its manufacturer, is not guaranteed or endorsed by the publisher.

Copyright © 2022 Wang, Cao, Li, Zhou, Lu, Wang and Zheng. This is an open-access article distributed under the terms of the Creative Commons Attribution License (CC BY). The use, distribution or reproduction in other forums is permitted, provided the original author(s) and the copyright owner(s) are credited and that the original publication in this journal is cited, in accordance with accepted academic practice. No use, distribution or reproduction is permitted which does not comply with these terms.



Risk Evolution Study of Tailings Dam Failures Disaster Based on DEMATEL-MISM

Binbin Zheng^{1,2}, Jiahe Wang¹, Tingting Feng¹, Wensong Wang^{3*}, Yuxi Zhou³, Guansen Cao⁴ and Yufei Wang¹

¹School of Management Science and Engineering, Shandong Technology and Business University, Yantai, China, ²Shandong Emergency Management Institute, Shandong Technology and Business University, Yantai, China, ³State Key Laboratory of Geohazard Prevention and Geoenvironment Protection, Chengdu University of Technology, Chengdu, China, ⁴Zijin Mining Company Limited, Shanghai, China

OPEN ACCESS

Edited by:

Wen Nie,
Jiangxi University of Science and
Technology, China

Reviewed by:

Lixin Wu,
Central South University, China
Jiaqiu Xu,
Harbin Institute of Technology, China
Ma Heng,
Liaoning Technical University, China

*Correspondence:

Wensong Wang
www.cdut.edu.cn

Specialty section:

This article was submitted to
Geohazards and Georisks,
a section of the journal
Frontiers in Earth Science

Received: 28 March 2022

Accepted: 11 May 2022

Published: 27 May 2022

Citation:

Zheng B, Wang J, Feng T, Wang W,
Zhou Y, Cao G and Wang Y (2022) Risk
Evolution Study of Tailings Dam
Failures Disaster Based on DEMATEL-
MISM.
Front. Earth Sci. 10:906486.
doi: 10.3389/feart.2022.906486

Tailings pond engineering is a complex and extensive system with many risk factors that can trigger a dam failure. It is important to clarify the evolutionary relationships among the factors and to enhance effective management to reduce the risk of dam failure. In this paper, an effective and reliable method for analyzing the evolution of tailings pond dam failure risk by combining DEMATEL and MISM is proposed. Firstly, 35 risk factors affecting tailings pond failure were summarized. An index system for evaluating the influence factors of dam failure was constructed from four aspects: personnel, management, environment, and system. Secondly, the Decision-making Trial and Evaluation Laboratory (DEMATEL) was used to study the influence relationships among the factors, for analyzing and identifying the key causal factors. Subsequently, the Modified Interpretative Structural Model Method (MISM) was used to classify the cause factors into five levels of influence as well as to determine the degree of integrated influence between the risk factors. Finally, an evolutionary model of tailings pond dam failure risk was constructed based on the results of the analysis. The results of the study indicated the followings: 1) System risk accounted for 58.58% of the total weight, while personnel risk accounts for 15.51%. To maintain the stability of the tailings pond system, personnel risk should not be neglected in addition to focusing on systemic factors. 2) Rainfall intensity was an essential causal factor. Focusing on rainfall intensity and taking appropriate measures effectively reduced the risk of dam failure. The height of the dam and the depth of the seepage line accounted for a large proportion of the causal factors, making it possible to control the height of the dam and accurately monitor the depth of the seepage line to improve the stability of the dam. 3) In the tailings pond dam risk evolution model, there were 30 factors with higher mutability and correlation, which played a transitional role in risk transfer. A risk factor transfer network diagram was established for this purpose as a diagnostic map. The research results can provide new methods and ideas for tailings dam failure risk analysis research and practice.

Keywords: tailings ponds, DEMATEL, MISM, influence factors, risk evolution

INTRODUCTION

A tailings pond is an artificial mudflow hazard source with high potential energy. Its operation directly affected both the life and property safety of mining enterprises and the downstream public (Yang et al., 2019; Zheng et al., 2021; Wang et al., 2022). More than 8,000 tailings were currently located in China. Of these, 16% were residents or important facilities within 1 km distance downstream, which were highly susceptible to serious safety accidents, major environmental emergencies with mass incidents, which seriously threatened the safety of personnel lives as well as property and social harmony (Wang et al., 2018). The high frequency of accidents and the serious consequences has drawn the high attention of government and mining companies. In addition, as safety, reliability and automation of modern tailings pond systems have increased, its concealment and coupling increases as well. (Cao et al., 2019; Wilson et al., 2021). As the increase in system complexity leads to the transformation of the nature of the accident, the various potential interactions within the system become equally complex. Therefore, it is important to comprehensively analyze the evolution of tailings dam failure risk, clarify the interrelationships among risk factors and the degree of influence, as well as to identify key risk factors for tailings dam failure control.

The identification of hazards and the determination of their characteristics are important part of system safety management (Zhen et al., 2022). It not only defines the scope of research for subsequent accident analysis and prevention, and post-disaster rescue, but also provides a decision basis for managers. Tailings ponds are risky system projects with numerous risk factors that induce failure and increasingly sophisticated risk analysis methods. There are various methods and models commonly used for risk analysis, such as the physical modeling method (Yin et al., 2011; Nie et al., 2017), factor analysis method (Xin et al., 2011), laboratory experiment method (Xu and Wang, 2015), evaluation model method (Mei and Wu, 2012), etc. In order to reveal on the mechanism of dam failure, Marti et al. (2021) studied the mechanism and causes of the sudden collapse of the Aznalcollar tailings pond and the results indicated progressive damage, which was caused by the brittle reaction of the clay and the high pore pressure left by the incomplete consolidation of the dam foundation. Salgueiro et al. (2008) evaluated the risk of tailings dam failure based one-FonRisk combined with relevant data. Based on GIS, combined with ARIMA and 3S (RS, GIS, GPS) technologies, Nie et al. (2022) developed a 3D tailings dam visualization and early warning system to achieve high-precision prediction and real-time warning of disasters. The safety of tailings ponds was systematically studied in terms of their material properties, failure, environmental impacts and the rehabilitation of tailings pond after a dam failure by Kossoff et al. (2014). Nevertheless, the current risk analysis of tailings pond has mainly focused on single factors or the lack of correlation between multiple factors. It has been proven that tailings dam failure was a complex multi-factor coupled evolutionary process. Thus, the analysis requires consideration of the integrated

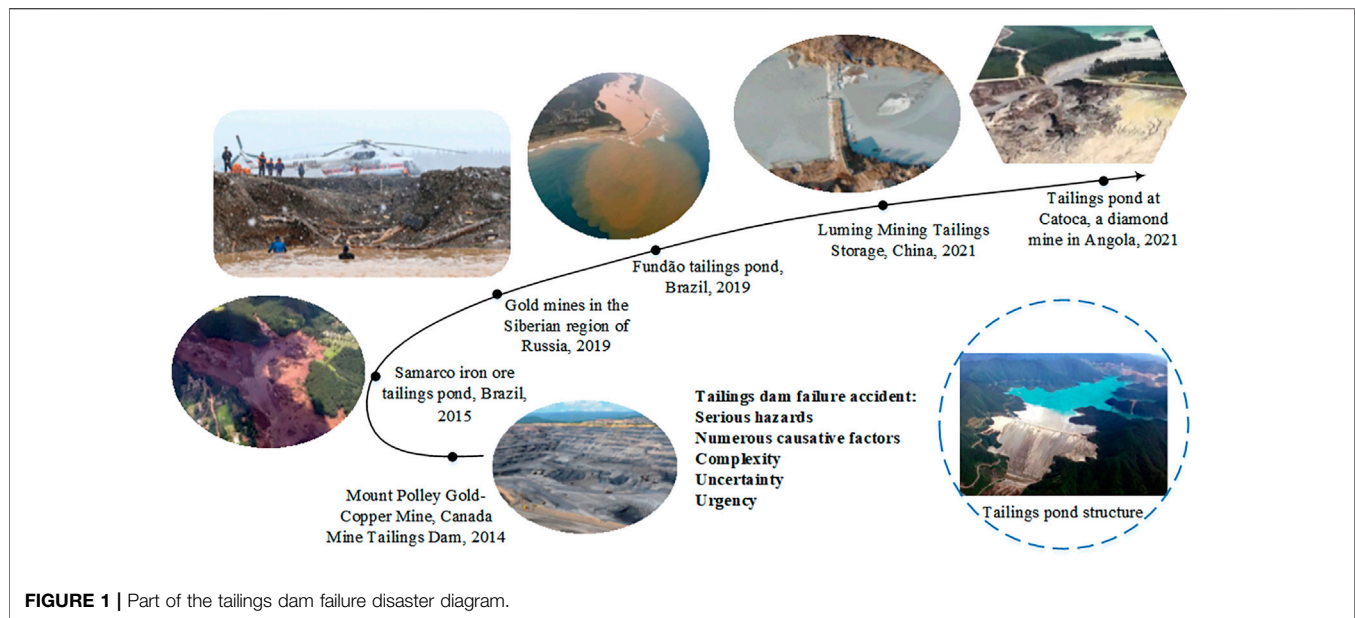
influence relationship among the factors together with the risk evolution process, followed by effective risk control.

In the field of complex systems, research has gradually begun to consider the interrelationships among the factors and their impact on system stability. Meng et al. (2019) used an integrated approach of the Decision-making Trial and Evaluation Laboratory (DEMATEL) and Bayesian networks (BN) to analyze the vulnerability risk of dynamic evolution of offshore platforms, effectively identifying the root causes of chain fire and explosion accidents. Fazli et al. (2015) used the DEMATEL method to identify supply chain risk interdependencies for crude oil. The analytical network process (ANP) approach was then applied to assess the importance of each risk and identify the best response strategy. Soner (2021) combined fuzzy sets and the DEMATEL method to analyze accidents in confined spaces onboard ships. DEMATEL and the Technique for Order Preference by Similarity to an Ideal Solution (TOPSIS) models were constructed by Li et al. (2022) to prioritize and calculate risk values for hydrogen production units to identify, assess and manage vulnerabilities in hydrogen production units. Effective tools for risk assessment and management of hydrogen were production units. Risks are prioritized using the DEMATEL method by Zhang et al. (2019). An analysis of their interdependencies is then carried out to identify key risks. The DEMATEL research methodology can be used to construct a structural model involving the causal relationships of complex factors, has proven to be an effective tool that can be used to recognize the interdependences among the elements of a system and identify the critical elements.

The structure of the tailings pond is sophisticated and the risk is not significantly transmitted in the factors that trigger dam failure (Zhong et al., 2021). Consequently, it was urgent to study the risk of tailings dam failure from the perspective of complex systems theory. In this paper, the DEMATEL method was used to analyze and collate the importance of 35 risk factors. Considering that the classical Interpretative Structural Model (ISM) method has relatively complicated calculations when the amount of data is large, we used the cause-effect extraction method to improve it to suit the analysis of tailings pond risk evolution. The cause-effect extraction method was improved to dig deeper into the implicit conduction structure between the factors and to reflect more accurately the level to which each factor belongs. Based on the above analysis, we had sorted out the evolution path of tailings pond dam failure risk and thus proposed a risk prevention and control strategy for tailings pond dam failure.

CAUSAL ANALYSIS OF TAILINGS DAM FAILURE

In recent years, several serious and catastrophic accidents have occurred due to engineering failures in tailings ponds. Several tailings pond accidents and their contributing causes are shown in **Figure 1**. The destructive force of a tailings pond failure is enormous, causing environmental pollution and personnel casualties. Qualified geological conditions are particularly



important for the proper operation of tailings pond. The investigation report of the Mount Polley tailings dam showed that the cause of the dam failure was the glacial lake layer nearly 8 m below the base of the dam around the failure gap, the strength of which did not reach the design strength of the tailings pond. Design changes should first ensure tailings pond system stability. The Brazilian Samarco dam design changes affected the sand drainage and the continuous increase of the dam body (load increase) led to the liquefaction of the sand, which eventually led to the accident. The construction of the tailings pond should be carried out strictly according to the requirements at the early stage. As the filtering layer of the tailings pond in Brazil Fundão was not properly done, a large number of clogged fine particles were found in the drainage ditch, which significantly reduced the drainage capacity and led to the rising water level of the dam, resulting in an eventual pipe surge. Quality of safety personnel in tailings pond also indirectly affect the safe operation of it. The weak awareness of safety management personnel in the Luming tailings pond destroyed the tailings pond drainage shaft due to substandard engineering quality, which in turn led to massive leakage of tailings. Through case studies, field research, and literature analysis, the risks of tailings pond failures have been categorized into four main areas: personnel, management, environment, and systems.

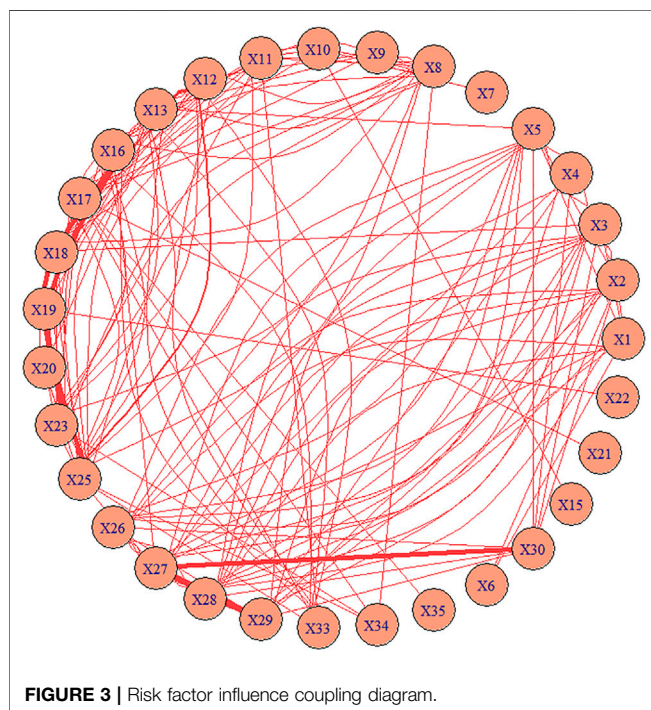
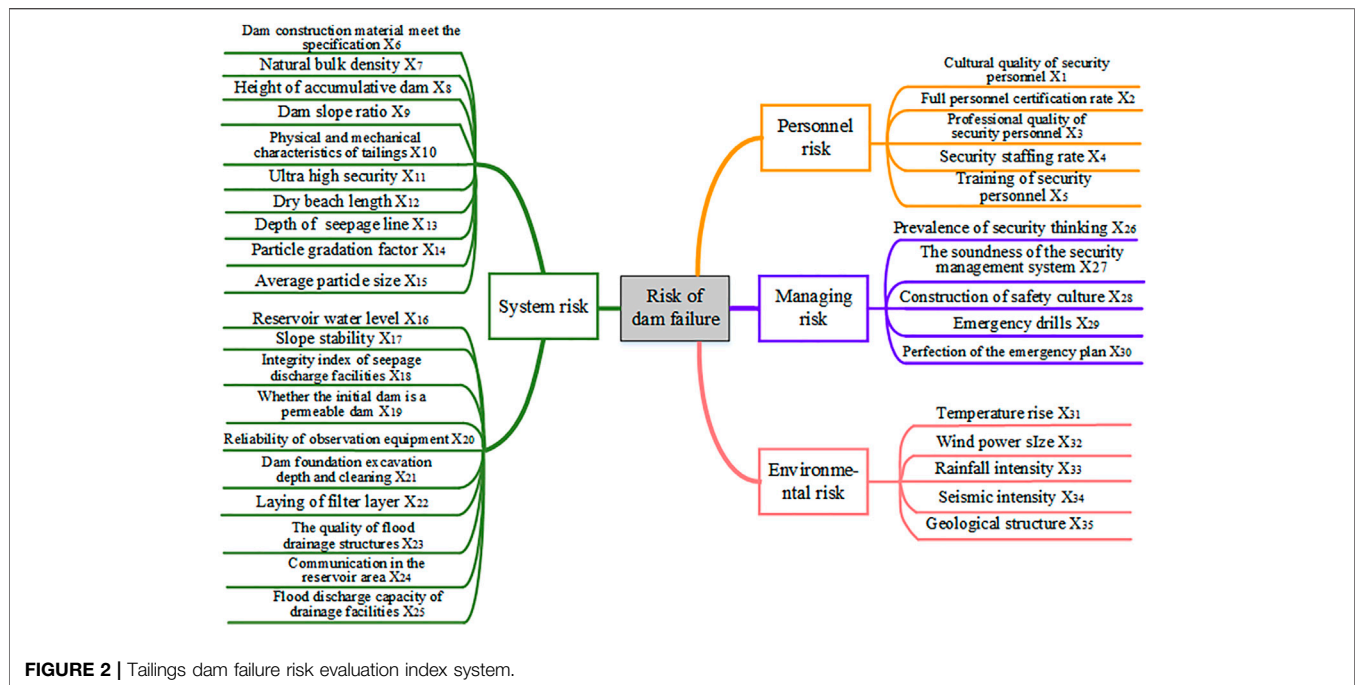
- 1) Unsafe behavior of personnel: a range of behaviors such as illegal construction and production by the operators, non-implementation of the safety production responsibility system, and failure to make major design changes following specifications would undoubtedly lead to the dam failure in long-term tailings operations (Zhen et al., 2021).
- 2) Inadequate management system: chaotic safety and production management, lack of implementation of various safety measures, and deficiencies in daily management (Hatje et al., 2017; Cheng et al., 2021).

- 3) Unsuitable environment: encountering over-standard flooding which led to roof topping, and earthquakes that led to liquefaction of the tailings sediment layer resulting in unsuitable initial siting of the tailings pond (Clarkson and Williams, 2021).
- 4) Instability of the system: seepage failure, overtopping failure, high a saturation line, steep a slope, and rapid a rise of the dam, resulting in unstable damage to the dam, leading to a dam failure (Li et al., 2022).

Based on the above four aspects, the causes of tailing pond dam failure were systematically analyzed from the perspective of the whole life cycle of tailing pond. The 35 risk factors that may induce tailings pond failure were identified and a tailings pond failure risk evaluation index system was constructed, as shown in **Figure 2**.

CONSTRUCTION OF RISK ANALYSIS MODEL BASED ON DEMATEL-MISM

An influence relationship scoring table among 35 factors affecting the stability of tailings pond was designed based on the risk index, and enterprise tailings pond safety managers and university experts were invited to score the results. We designed a matrix scoring table to score the degree of influence among the 35 factors on a scale of 1–10. A risk factor coupling relationship diagram was drawn based on the expert scoring results, as shown in **Figure 3**. The flood discharge capacity of drainage facilities (X_{25}) has a stronger relationship with the dry beach length (X_{12}) in the safe operation of the actual tailings pond, so the lines are thicker. The training of security personnel (X_5) has a lesser degree of influence with natural bulk density X_7 , thus the connection is not shown. The thickness of the lines represented the degree of influence among the factors and reflected the complex



influence relationship among the factors. It can be seen from the figure that the occurrence of a tailings pond dam failure was a complex and dynamic process. The relationships among the many influencing factors in this process were unclear and coupled with each other. However, the transfer pattern between risk factors was not obvious and the identification of important risk factors was challenging, posing certain difficulties

for risk evolution analysis and effective control. Accordingly, the rational approach of classifying numerous factors into different levels and establishing an efficient with transparent risk evolution model was necessary (Yi-qing et al., 2014).

DEMATEL was a system analysis method using graphical and matrix tools. The dependencies of the elements of a tailings storage system were effectively analyzed by it. The importance of each element of the system was distinguished by determining the causal relationships between the elements and the state of the system. The classical ISM was used to study a conceptual system through mathematical topological operations and to obtain a minimal hierarchical directed topological map. Nonetheless, faced with multi-indicator data, a large amount of computation was involved, and it was not easy to better discern the connections among hierarchies. Traditional models were therefore optimized by using the cause-result extraction method. Apply the ISM rule of equality for the reachable and common sets to obtain the hierarchical distribution. In the paper, the Modified Interpretative Structural Model (MISM) method was used in this paper to investigate the numerous inter-element connectivity structure in tailings pond systems. The advantage was the ability to reveal the internal conduction patterns of the tailings pond system through the complex relationships between the elements of the tailings pond system.

A combination of DEMATEL and MISM was used to construct a risk evolution model, and the analysis steps were as follows:

Step 1: Determine the indicators for tailings pond failure study indicators. The interrelationships between the 35 factors

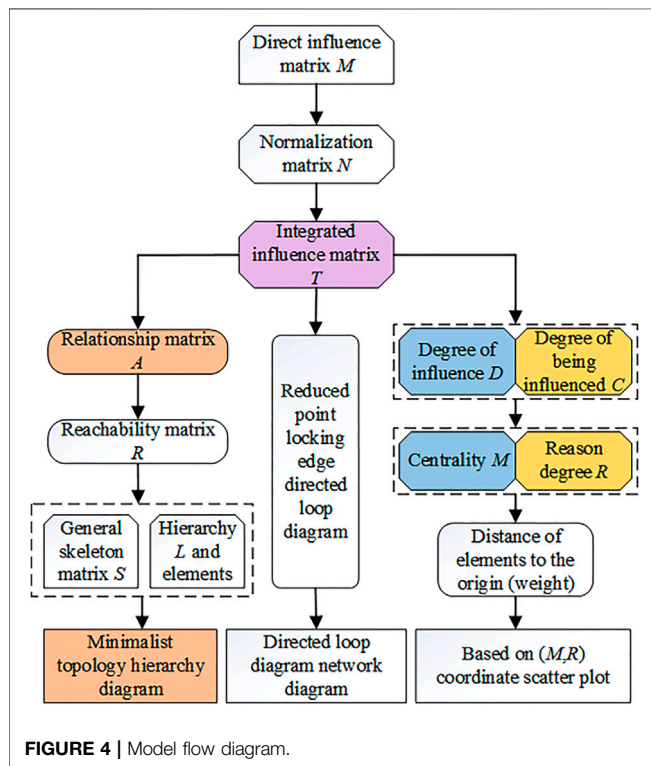


FIGURE 4 | Model flow diagram.

were quantified to obtain the direct influence matrix. Finally, a direct influence matrix was constructed.

$$M = (a_{ij})_{n \times n}, \quad (1)$$

Where: M is the direct influence matrix; a_{ij} is the effect of a factor i on a factor j ; n is the number of factors.

Step 2: The canonical direct influence matrix was obtained by normalizing the original relationship matrix.

$$\text{Max var} = \max \left(\sum_{j=1}^n a_{ij} \right), \quad (2)$$

$$N = \left(\frac{a_{ij}}{\text{Max var}} \right)_{n \times n} \quad (3)$$

Where: Maxvar is the maximum value of the sum of each row in the M matrix; the canonical direct influence matrix was defined N .

Step 3: From the normalized direct influence matrix, the integrated influence matrix was calculated.

$$T = (N + N^2 + \dots) = \sum_{k=1}^{\infty} N^k \rightarrow T = N(I - N)^{-1}, \quad (4)$$

Where T is the integrated influence matrix, N is the canonical direct influence matrix, and I is the unit matrix, i.e., a matrix with diagonal values of 1 and other values of 0.

Step 4: The influence degree, affected degree, centrality degree, and cause a degree of the factors were obtained from the integrated influence matrix.

$$D_i = \sum_{j=1}^n t_{ij} \quad (i = 1, 2, 3, \dots, n), \quad (5)$$

$$C_i = \sum_{j=1}^n t_{ij} \quad (i = 1, 2, 3, \dots, n), \quad (6)$$

$$M_i = D_i + C_i, \quad (7)$$

$$R_i = D_i - C_i, \quad (8)$$

Where D is the sum of the values in each row of the matrix T , representing the combined influence of each row on all other elements, that is, the degree of influence. C is the sum of the values of each column T , which represents the combined influence of the column element on all other elements, namely, the degree of being influenced. Effectiveness and degree of influence of the element i are added to obtain the centrality of the element as M_i . t_{ij} represents the elements of row i and column j of the T matrix. Within the evaluation index system, the centrality of an element is obtained by subtracting the influence degree of the element from that of the element. The reason degree is R_i . If the reason degree is greater than 0, it means that the factor has a great influence on other factors and is called the reason factor. Conversely, if the reason degree is less than 0, the factor is referred to as an outcome factor.

Step 5: Plot centrality and causality based on the calculated centrality with an explanation.

$$\lambda = \bar{X} + \sqrt{\frac{\sum_{i=1}^n (x_{ij} - \bar{x})^2}{n^2}}, \quad (9)$$

$$d = \sqrt{M^2 + R^2}, \quad (10)$$

Where λ is the threshold value, x_{ij} belongs to the integrated influence matrix, and \bar{x} is the average of all elements in the integrated influence matrix. d indicates the distance of the element from the origin on the cause result diagram.

Step 6: Coupling with MISM, the risk factor poles were delineated and the evolutionary path of the tailings pond breach risk factor was systematically identified.

$$A \rightarrow D \rightarrow M \rightarrow S \rightarrow \text{Topology hierarchy diagram}, \quad (11)$$

Where A is the adjacency matrix obtained after processing the integrated influence matrix T . D is the multiplication matrix joined to the unit matrix ($D = A + I$) where I is the unit matrix, and the multiplication matrix can be derived from the reachable matrix M by the Boolean matrix operation. The general skeleton matrix S can be derived by reducing the edges of the reachable matrix to remove the same path, and the general skeleton matrix can be used to derive the element hierarchy and inter-element relationships to derive a set of directed topology diagrams.

$$(A + I)^{k-1} \neq (A + I)^k = (A + I)^{k+1} = M. \quad (12)$$

$$S' = M' - (M' - 1)^2 - 1. \quad (13)$$

The MISM reachable matrix D was obtained, and the selected factors were calculated by DEMATEL to obtain the integrated influence matrix T . The key to the establishment of

TABLE 1 | Centrality and causality of dam failure risk factors.

Risk factors	Centrality M	Reason degree R	Center degree sorting	Attribute
X_1	0.0740	0.0241	19	Reason
X_2	0.1014	0.0291	15	Reason
X_3	0.1275	0.0313	10	Reason
X_4	0.0684	0.0080	21	Reason
X_5	0.1251	0.0154	11	Cause
X_6	0.0569	-0.0122	24	Result
X_7	0.0369	0.0092	27	Cause
X_8	0.1664	0.0218	3	Cause
X_9	0.0737	0.0081	20	Cause
X_{10}	0.0578	0.0200	23	Cause
X_{11}	0.1005	-0.0044	16	Result
X_{12}	0.1574	-0.0195	7	Result
X_{13}	0.1924	-0.0098	2	Result
X_{14}	0.0293	0.0020	31	Reason
X_{15}	0.0354	-0.0030	28	Result
X_{16}	0.2017	-0.0083	1	Result
X_{17}	0.1652	-0.0577	4	Result
X_{18}	0.1123	-0.0168	12	Result
X_{19}	0.0581	0.0118	22	Reason
X_{20}	0.0531	-0.0051	25	Result
X_{21}	0.0271	-0.0098	32	Result
X_{22}	0.0239	-0.0164	33	Result
X_{23}	0.1428	-0.0311	8	Result
X_{24}	0.0301	-0.0175	29	Result
X_{25}	0.1630	-0.0313	5	Result
X_{26}	0.1112	0.0209	13	Reason
X_{27}	0.1623	0.0733	6	Reason
X_{28}	0.1382	0.0238	9	Reason
X_{29}	0.1092	-0.0385	14	Result
X_{30}	0.0957	-0.0579	17	Result
X_{31}	0.0061	0.0001	34	Cause
X_{32}	0.0037	-0.0002	35	Result
X_{33}	0.0941	0.0151	18	Cause
X_{34}	0.0521	0.0221	26	Cause
X_{35}	0.0297	0.0034	30	Cause

an adjacency matrix is to determine the threshold value λ . In a tailings pond safety system, if the influencing degree of a factor to another factor exceeds λ , the stimulus will receive a response, i.e., the factor can directly affect another factor; if the influencing degree of a factor to another factor is smaller than λ , the stimulus will receive no response, i.e., the factor shows no effect on another factor. Based on the T matrix, the normalization process was carried out according to **Equation 9**, and the t_{ij} factors representing the influence relationship in the direct influence matrix T were set to 1, and those less than λ were set to 0. (Take $\lambda = 0.00129$). The point reduction from the reachable matrix M means that the loop in the reachable matrix is treated as a point and is called a point reduction. After the point reduction, the reachable matrix M' is obtained, and then the edge reduction operation is performed. The essence of the edge reduction operation is to remove the duplicate paths by **Eq. 13**. M' is reduced to obtain S' , the skeleton matrix, and the loop elements are substituted to obtain the general skeleton matrix S .

As a result, the relationship structure of the connection matrix was defined, and the adjacency matrix A was obtained, which in turn

obtained the reachability matrix M . In the reachable matrix, each variable has a reachable set $R(e_i)$, a prior set $Q(e_i)$, and a common set $T(e_i)$. The extraction rule of MISM is that when $T(e_i) = R(e_i)$ the element is removed and placed at the top of the hierarchy, and then continue to select the remaining elements that meet the extraction rules. Then, the remaining elements are selected to meet the extraction rules and extracted at each level. When the elements of the strongly connected domain were greater than or equal to two, the strongly connected region was called a cycle. The hierarchical classification was performed using the causal rotation hierarchical extraction principle. Its advantage was that it reflected the hierarchy over elements more accurately than classical methods and better reflected the dialectic of causality. Following edge locking, point reduction, stratification, and sub-region, the determination of the influence relationships among the factors was carried out, from which the MISM multi-level ladder was obtained.

Step 7: Using the Euclidean distance formula to calculate the influence system weights of each factor, the calculated MISM contraction point factors are expanded. Combined with the integrated influence matrix T , the probabilities of the

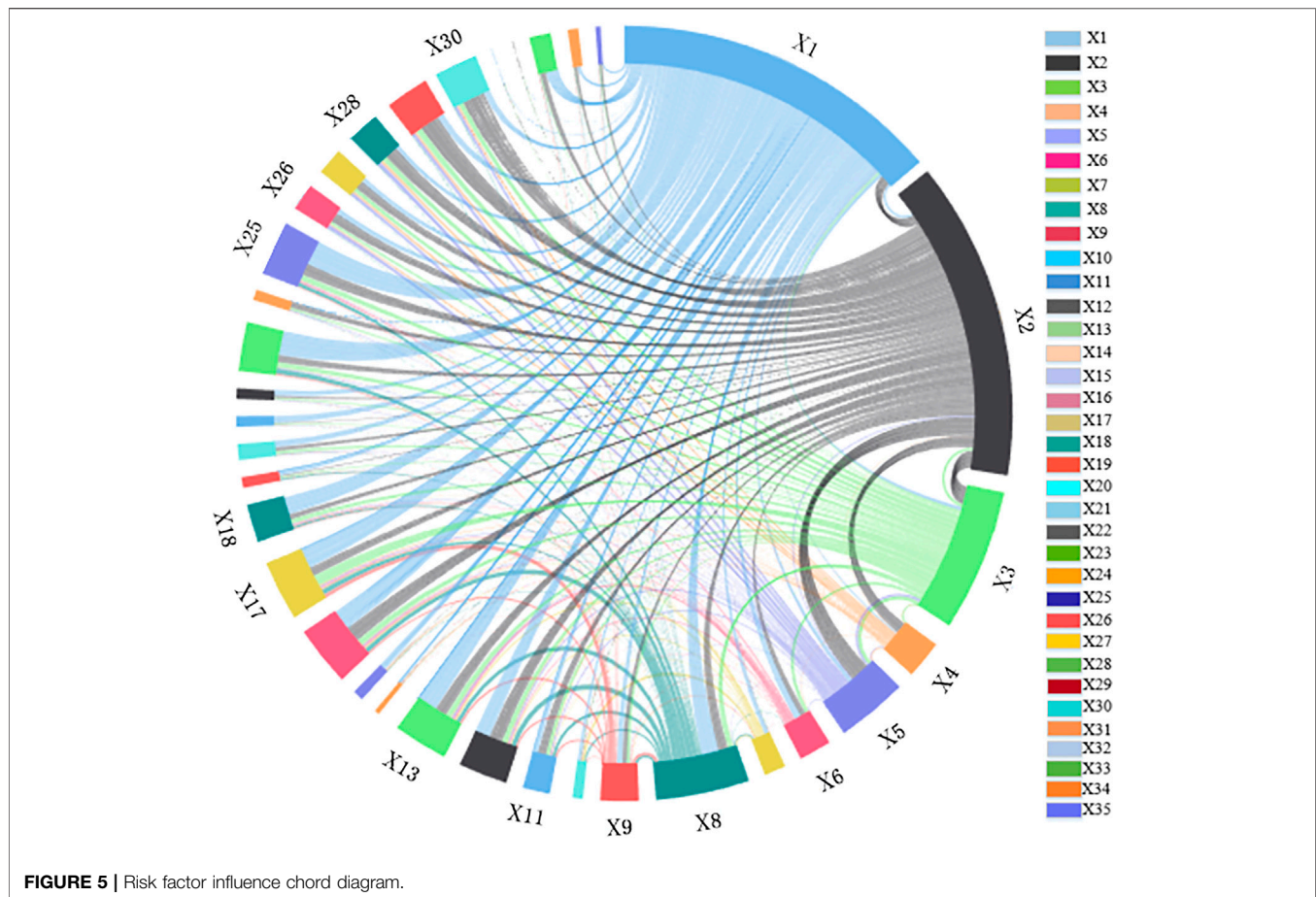


FIGURE 5 | Risk factor influence chord diagram.

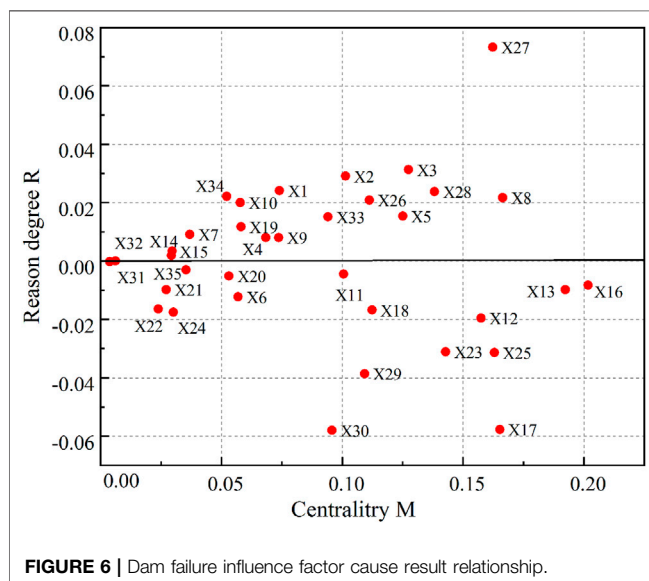


FIGURE 6 | Dam failure influence factor cause result relationship.

internally conducted paths and the contraction point matrix were determined. The specific flow diagram of the model calculation is shown in Figure 4 below.

RISK EVOLUTION ANALYSIS OF TAILINGS DAM BREAK

Dam Failure Risk Influence Degree Analysis

The direct influence matrices were obtained by analyzing expert opinions and relevant information and normalizing the direct influence matrices. They were used in Eqs 2–4 to calculate the normalized influence matrix and the comprehensive influence matrix. The causality and centrality of the indicator system were calculated by Eqs 5–8, which were used to analyze the causal relationships. Equations 9–13 were used to calculate the hierarchical ladder structure of the MISM and normalize the causality and centrality to derive the influence weights of the different system elements. The positions of different factors in the system are found in sequence, and the interactions among different factors are marked. Finally, a hierarchical model was established. Factor attributes were classified according to their cause degree values and if it was positive, the attribute was a causal factor. Conversely, the factor was an outcome factor, and the results were shown in Table 1. Where the cause factor is more likely to influence other factors in the system than the effect factor. The large centrality of the reservoir water level (X_{16}) and the depth of seepage line (X_{13}) in Table 1 indicated that when changes occur in the tailings pond system, they are likely to cause

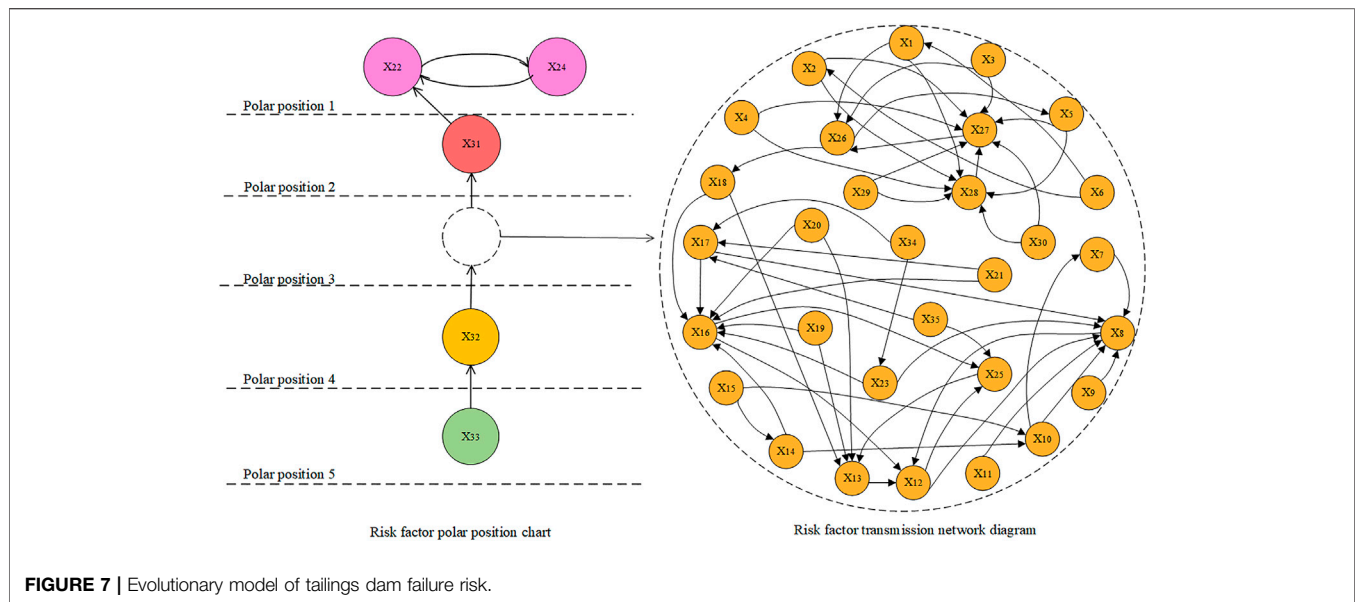


FIGURE 7 | Evolutionary model of tailings dam failure risk.

variation in other risk factors in the system. The large degree of the cause of personnel risk components showed that the occurrence of accidents had an important relationship with the management and behavior of personnel.

A chord diagram of the risk factors was drawn by visually displaying the calculated integrated influence matrix T and comparing the combined influence of the factors, as in **Figure 5**. The perimeter consisted of 35 factors, which were weighted differently due to the degree of the combined influence of the different factors. As a consequence, the length of the perimeter had some variation, and the chord between the factors varied with the magnitude of the influence value. It is evident from the figure that factors such as the cultural quality of security personnel (X_1) and the full personnel certification rate (X_2) were relatively high in proportion to their influence in the complex system of the tailings pond. This indicates that the safety qualities of personnel play a more important role in the system and that the risks posed by personnel influenced all other factors in the system more extensively. Unsafe personnel behavior can greatly affect the stability of tailings pond. As pointed out in the study by Armstrong et al., the low level of personnel quality had led to an increase in the number of tailings pond failures in recent years (Armstrong et al., 2019).

The degree of influence and centrality of each factor was obtained by calculating the degree to which its factor influenced and was influenced by other factors. Centrality was the principle by which core and non-core factors were judged, indicating the position and magnitude of the factor's role in the evaluation indicator system. Dematel was used to analyze each factor, and **Figure 6** shows the distribution of centrality of each factor. One of the rules for determining non-core factors was based on the distribution of centrality values in the graph. A distribution with leftward

centrality indicated a non-core factor of influence, which was excluded from the risk analysis. The magnitude of centrality depends on the degree of stability within the system. **Table 1** shows that the centrality of X_{31} , X_{32} , and X_{35} had small centrality, indicating that factors such as temperature rise, wind and geological structure were relatively stable and reliable. On the other hand, the causes and centrality of X_8 and X_{27} were relatively large. Risks associated with the height of the dam and the robustness of the safety management system should be taken into account as they may affect other factors. The reason degree and centrality of X_{13} and X_{16} were relatively large, indicating that the depth of seepage line and reservoir water level were susceptible to other factors, so the risk caused by the reservoir level and seepage should be noted. In addition, in the study by Cheng et al. through Spatio-temporal pattern mining of global tailings dam failure events, it was found that regular drainage inspection, risk assessment, monitoring and early warning of tailings dams in key areas still need to be strengthened for disaster mitigation (Cheng et al., 2021).

Dam Failure Risk Area and Polar Position Division

MISM was applied to classify the 35 factors into different levels of influence, with the risk evolution being divided into five poles according to the calculation results. In the process of risk transmission evolution, the influencing factors were coupled with each other. Considering the mutual coupling effect among the 35 factors, a risk evolution model of tailings dam failure was established, as shown in **Figure 7**.

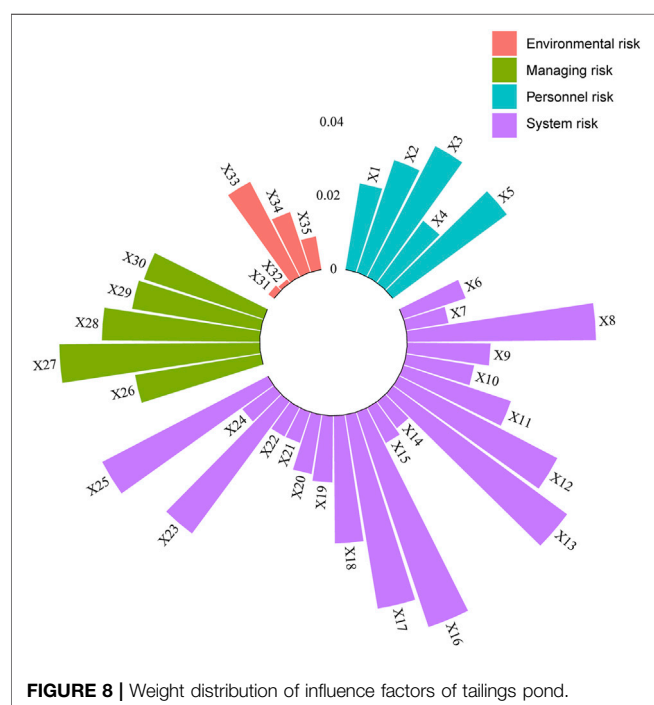
As can be seen in **Figure 7** the evolutionary model of tailings pond dam failure risk was divided into five relative positions

TABLE 2 | Risk factor influence weighting.

Risk factors	X ₁	X ₂	X ₃	X ₄	X ₅	X ₆	X ₇	X ₈	X ₉	X ₁₀	X ₁₁	X ₁₂	X ₁₃
Weights	2.4%	3.2%	4.0%	2.1%	3.8%	1.8%	1.2%	5.1%	2.3%	1.9%	3.1%	4.8%	5.9%
Risk Factors	X ₁₄	X ₁₅	X ₁₆	X ₁₇	X ₁₈	X ₁₉	X ₂₀	X ₂₁	X ₂₂	X ₂₃	X ₂₄	X ₂₅	X ₂₆
Weights	0.9%	1.1%	6.1%	5.3%	3.5%	1.8%	1.6%	0.9%	0.9%	4.5%	1.1%	5.1%	3.4%
Risk Factors	X ₂₇	X ₂₈	X ₂₉	X ₃₀	X ₃₁	X ₃₂	X ₃₃	X ₃₄	X ₃₅				
Weights	5.4%	4.3%	3.5%	3.4%	0.2%	0.1%	2.9%	1.7%	0.9%				

TABLE 3 | Systematic risk influence weights.

Systemic risk components	Personnel risk (%)	System risk (%)	Managing risk (%)	Environmental risks (%)
Weights	15.51	58.58	20.07	5.84

**FIGURE 8 |** Weight distribution of influence factors of tailings pond.

where the risk would be transferred between five poles. Various factors could also have a direct or indirect effect on each other. Collectively, the intensity of rainfall (X₃₃) was located at the fifth pole of the fundamental factors and was the root cause of the dam failure hazard. Rainfall intensity should always be monitored, and advanced protective measures should be taken during high rainfall events. The polar 3 contained a large number of intermediate factors, forming a closed loop. In this way, it demonstrated that many factors were prone to sudden and simultaneous changes, increasing the probability of tailings pond failure, and it played a crucial role in the evolution of the risk. The laydown of the filter layer (X₂₂) located at polar 1 and the communication of the reservoir area (X₂₄) was hidden risk factors that need to be controlled during the operation of

the tailings pond, because of their long-term and profound influence on the safety management of tailings pond. The weights of each risk factor were calculated and shown in **Tables 2, 3**. To visualize the influence weight of each factor, based on the data in **Table 2**, the weight distribution of the influence factors of the tailings pond was drawn, as shown in **Figure 8**. The weights of X₁₃, X₁₆, X₂₅, and X₂₇ were higher and the depth of the saturation line, the water level in the reservoir area, the discharge capacity of the drainage facilities, and the soundness of the security management system were all prone to cause damage and lead to dam failure accidents. In terms of system risk composition, the tailing pond carried a relatively high weighting of system risk. However, the risks posed by personnel and management should not be ignored.

The 30 features presented at polar position 3 were prone to collective mutations. Any change in one of ring factors would alter the rest. Without effective measures, it could result in a rapid transfer of risk and even lead to a dam failure. The integrated influence matrix *T* was adopted as the conditional probability of its occurrence further exploring transmission paths and frequency probabilities. The probability greater than 10% was selected as the main transmission path and the risk factor transmission network was mapped, as shown in **Figure 7**. The risk factor transmission network could be used to identify and diagnose unexpected risks. Under the circumstances of a sudden change in an easily observable factor, the factors in the transmission network could be reviewed and repaired by correlation. The likelihood of subsequent risk derivation was greatly reduced, while a large number of risk hazards were eliminated and could be used as a guide for emergent risk mapping. As a result, the method was found to have good applicability in tailings pond failure risk analysis.

DISCUSSION

In previous tailings pond risk analyses, a number of studies have been carried out to consider the effects of a single factor and

studied the mechanism of dam failure in depth (Wang and Zhang, 2017). The research on single-factor causation had been quite effective and had opened up new perspectives on effective dam failure prevention and monitoring. However, dam failures had occurred in the presence of adequate monitoring facilities and safety staffing. The reason for a dam failure is that it is the result of many factors acting together. Changes in individual factors do not cause safety personnel to think, but it probably hides a more profound phenomenon. Many factors within a tailings pond are highly interrelated, where a minor change in a single factor can cause sudden changes in other factors. The gradual accumulation of dam failure risk sources combined with the inability of safety personnel to detect these risk sources ultimately led to the dam failure.

The DEMATEL-MISM tailings pond dam failure risk evolution model based on multi-factor interactions established in this paper and the risk transfer of 35 factors on tailings pond dam failure risk were investigated. We found the existence of a collective mutation and risk transfer network that can be used as an effective map for tailings pond dam failure risk diagnosis. At the same time, the weights of each factor in the influence system are determined, which can monitor the tailings pond from various aspects and ensure the safe operation of the tailings pond. The results of this paper verify that tailings pond dam failures are caused by multi-factor mutations. However, the derivation and transmission of risk in actual engineering is dynamic and changing (Liu et al., 2019). Follow-up studies are recommended to consider the time series of risk transmission mechanisms and the probability of risk transmission among multiple factors.

CONCLUSION

Tailings pond failures are composed of personnel, system, management and environmental risk factors. Based on safety theory and complex systems theory, this paper established a whole-life cycle tailings dam failure risk index system. It also explored the risk transmission paths between different factors, divided the influencing elements at different levels to determine the influence weighting ratio of different factors. A causal risk analysis was conducted on tailings dam failure accidents, and 35 dam failure risk factors were summarized. The causal relationships among the

factors were identified and the importance of each element in the system was classified according to its centrality.

DEMATEL method was used to calculate the degree of cause and centrality of each factor and to determine the degree of influence among the 35 factors. Moreover, a hierarchy with 30 factors that were prone to variability while rapidly transmitting risk internally was derived in conjunction with the MISIM approach. It is concluded that network diagrams for the transmission of variability-prone factor effectively provided diagnostic and mapping functions. Depending on the weighting of each factor, not only the internal risks of the system needed to be focused on, but also the personnel and management risks could not be ignored and needed to be strengthened. Besides, a hierarchical structure among the factors was determined, which more intuitively reflected the relationship among the influencing effects of the factors within the tailings pond system. The factors associated with the risk network could be reviewed and repaired, greatly reducing the likelihood of subsequent risk derivation while eliminating many risk hazards. Thus, taken as an emerging risk map, it could provide a better perspective and direction for reducing the occurrence of dam failure hazard events.

DATA AVAILABILITY STATEMENT

The raw data supporting the conclusions of this article will be made available by the authors, without undue reservation.

AUTHOR CONTRIBUTIONS

Conceptualization: BZ and JH; Data curation: GC and WW; Formal analysis: TF, YZ, and YW; Funding acquisition: WW and BZ; Investigation: YZ, TF, and YW; Methodology: BZ; Project administration: WW; Supervision: BZ; Validation: GC and JH; Visualization: GC and TF; Writing—original draft: BZ and JH; Writing—review and editing: WW.

FUNDING

This study was financially supported by the National Natural Science Foundation of China (51804178, 51804051).

REFERENCES

- Armstrong, M., Petter, R., and Petter, C. (2019). Why Have So Many Tailings Dams Failed in Recent Years? *Resour. Policy* 63, 101412. doi:10.1016/j.resourpol.2019.101412
- Cao, G., Wang, W., Yin, G., and Wei, Z. (2019). Experimental Study of Shear Wave Velocity in Unsaturated Tailings Soil with Variant Grain Size Distribution. *Constr. Build. Mater.* 228, 116744. doi:10.1016/j.conbuildmat.2019.116744
- Cheng, D., Cui, Y., Li, Z., and Iqbal, J. (2021). Watch Out for the Tailings Pond, a Sharp Edge Hanging over Our Heads: Lessons Learned and Perceptions from the Brumadinho Tailings Dam Failure Disaster. *Remote Sens.* 13 (9), 1775. doi:10.3390/rs13091775
- Clarkson, L., and Williams, D. (2021). An Overview of Conventional Tailings Dam Geotechnical Failure Mechanisms. *Min. Metallurgy Explor.* 38 (3), 1305–1328. doi:10.1007/s42461-021-00381-3
- Fazli, S., Kiani Mavi, R., and Vosooghizadeh, M. (2015). Crude Oil Supply Chain Risk Management with DEMATEL-ANP. *Operational Res.* 15 (3), 1–28. doi:10.1007/s12351-015-0182-0
- Hatje, V., Pedreira, R. M. A., de Rezende, C. E., Schettini, C. A. F., de Souza, G. C., Marin, D. C., et al. (2017). The Environmental Impacts of One of the Largest Tailing Dam Failures Worldwide. *Sci. Rep.* 7 (1), 10706–10713. doi:10.1038/s41598-017-11143-x
- Kossoff, D., Dubbin, W. E., Alfredsson, M., Edwards, S. J., Macklin, M. G., and Hudson-Edwards, K. A. (2014). Mine Tailings Dams: Characteristics, Failure, Environmental Impacts, and Remediation. *Appl. Geochem.* 51, 229–245. doi:10.1016/j.apgeochem.2014.09.010

- Li, Q., Geng, J., Song, D., Nie, W., Saffaro, P., and Liu, J. (2022). Automatic Recognition of Erosion Area on the Slope of Tailings Dam Using Region Growing Segmentation Algorithm. *Arabian J. Geosciences* 15 (5), 1–15. doi:10.1007/s12517-022-09746-4
- Liu, J., Liu, R., Zhang, Z., Cai, Y., and Zhang, L. (2019). A Bayesian Network-Based Risk Dynamic Simulation Model for Accidental Water Pollution Discharge of Mine Tailings Ponds at Watershed-Scale. *J. Environ. Manag.* 246, 821–831. doi:10.1016/j.jenvman.2019.06.060
- Martí, J., Riera, F., and Martínez, F. (2021). Interpretation of the Failure of the Aznalcollar (Spain) Tailings Dam. *Mine Water Environ.* 40, 189–208. doi:10.1007/s10230-020-00712-8
- Mei, G. D., and Wu, Z. Z. (2012). Research on the Dam-Break Hazard Vulnerability Assessment Index System and Methods of Tailings Pond. *App. Mech. Mat.* 204–208, 3450–3456. doi:10.4028/www.scientific.net/amm.204-208.3450
- Meng, X., Chen, G., Zhu, G., and Zhu, Y. (2019). Dynamic Quantitative Risk Assessment of Accidents Induced by Leakage on Offshore Platforms Using DEMATEL-BN. *Int. J. Nav. Archit. Ocean Eng.* 11 (1), 22–32. doi:10.1016/j.ijnaoe.2017.12.001
- Nie, W., Krautblatter, M., Leith, K., Thuro, K., and Festl, J. (2017). A Modified Tank Model Including Snowmelt and Infiltration Time Lags for Deep-Seated Landslides in Alpine Environments (Aggenalm, Germany). *Nat. Hazards Earth Syst. Sci.* 17 (9), 1595–1610. doi:10.5194/nhess-17-1595-2017
- Nie, W., Luo, M., Wang, Y., and Li, R. (2022). 3D Visualization Monitoring and Early Warning System of a Tailings Dam-Gold Copper Mine Tailings Dam in Zijinshan, Fujian, China. *Front. Earth Sci.* 10, 800924. doi:10.3389/feart.2022.800924
- Salgueiro, A. R., Pereira, H. G., Rico, M.-T., Benito, G., and Díez-Herreo, A. (2008). Application of Correspondence Analysis in the Assessment of Mine Tailings Dam Breakage Risk in the Mediterranean Region. *Risk Anal.* 28 (1), 13–23. doi:10.1111/j.1539-6924.2008.00998.x
- Soner, O. (2021). Application of Fuzzy DEMATEL Method for Analysing of Accidents in Enclosed Spaces Onboard Ships. *Ocean. Eng.* 220 (9), 108507. doi:10.1016/j.oceaneng.2020.108507
- Wang, F., and Zhang, Q.-L. (2017). Systemic Estimation of Dam Overtopping Probability: Bayesian Networks Approach. *J. Infrastruct. Syst.* 23 (2), 04016037. doi:10.1061/(asce)is.1943-555x.0000328
- Wang, K., Yang, P., Hudson-Edwards, K., Wen-sheng, L. Ü., and Lei, B. U. (2018). Status and Development for the Prevention and Management of Tailings Dam Failure Accidents. *Chin. J. Eng.* 40 (5), 526–539. doi:10.13374/j.issn2095-9389.2018.05.002
- Wang, W., Cao, G., Li, Y., Zhou, Y., Lu, T., Wang, Y., et al. (2022). Experimental Study of Dynamic Characteristics of Tailings with Different Reconsolidation Degrees after Liquefaction. *Front. Earth Sci.* 10, 876401. doi:10.3389/feart.2022.876401
- Wilson, R., Toro, N., Naranjo, O., Emery, X., and Navarra, A. (2021). Integration of Geostatistical Modeling into Discrete Event Simulation for Development of Tailings Dam Retreatment Applications. *Miner. Eng.* 164, 106814. doi:10.1016/j.mineng.2021.106814
- Xin, Z., Xiaohu, X., and Kaili, X. (2011). Study on the Risk Assessment of the Tailings Dam Break. *Procedia Eng.* 26, 2261–2269. doi:10.1016/j.proeng.2011.11.2433
- Xu, B., and Wang, Y. (2015). Stability Analysis of the Lingshan Gold Mine Tailings Dam under Conditions of a Raised Dam Height. *Bull. Eng. Geol. Environ.* 74 (1), 151–161. doi:10.1007/s10064-014-0602-z
- Yang, Y., Wei, Z., Cao, G., Yang, Y., Wang, H., Zhuang, S., et al. (2019). A Case Study on Utilizing Geotextile Tubes for Tailings Dams Construction in China. *Geotext. Geomembranes* 47 (2), 187–192. doi:10.1016/j.geotextmem.2018.12.007
- Yi-qing, Z., Xuan, T., Zhong-xue, L., and Liang-yong, T. (2014). Dynamic Modeling and Simulation of Hazard and Risk Evolution for Mine Tailing Ponds. *Chin. J. Eng.* 36 (9), 1158–1165. doi:10.13374/j.issn1001-053x.2014.09.005
- Yin, G., Li, G., Wei, Z., Wan, L., Shui, G., and Jing, X. (2011). Stability Analysis of a Copper Tailings Dam via Laboratory Model Tests: A Chinese Case Study. *Miner. Eng.* 24 (2), 122–130. doi:10.1016/j.mineng.2010.10.014
- Zhang, L., Sun, X., and Xue, H. (2019). Identifying Critical Risks in Sponge City PPP Projects Using DEMATEL Method: A Case Study of China. *J. Clean. Prod.* 226, 949–958. doi:10.1016/j.jclepro.2019.04.067
- Zhen, Z., Wu, X., Ma, B., Zhao, H., and Zhang, Y. (2022). Propagation Network of Tailings Dam Failure Risk and the Identification of Key Hazards. *Sci. Rep.* 12 (1), 1–17. doi:10.1038/s41598-022-08282-1
- Zhen, Z., Zhang, Y., Hu, M., Zhao, H., and Zhang, Y. (2021). Propagation Laws of Reclamation Risk in Tailings Ponds Using Complex Network Theory. *Metals* 11 (11), 1789. doi:10.3390/met11111789
- Zheng, B., Wang, J., Zhang, D., Zhao, L., and Wang, W. (2021). Laboratory Experimental Study of the Evaporation and Mechanical Behaviour of Deposited Tailings. *Environ. Sci. Pollut. Res.* 28 (47), 67565–67576. doi:10.1007/s11356-021-14951-x
- Zhong, W., Ouyang, J., Yang, D., Wang, X., Guo, Z., and Hu, K. (2021). Effect of the In Situ Leaching Solution of Ion-Absorbed Rare Earth on the Mechanical Behavior of Basement Rock. *J. Rock Mech. Geotechnical Eng.* doi:10.1016/j.jrmge.2021.12.002

Conflict of Interest: Author GC is employed by Zijin Mining Company Limited.

The remaining authors declare that the research was conducted in the absence of any commercial or financial relationships that could be construed as a potential conflict.

Publisher's Note: All claims expressed in this article are solely those of the authors and do not necessarily represent those of their affiliated organizations, or those of the publisher, the editors and the reviewers. Any product that may be evaluated in this article, or claim that may be made by its manufacturer, is not guaranteed or endorsed by the publisher.

Copyright © 2022 Zheng, Wang, Feng, Wang, Zhou, Cao and Wang. This is an open-access article distributed under the terms of the Creative Commons Attribution License (CC BY). The use, distribution or reproduction in other forums is permitted, provided the original author(s) and the copyright owner(s) are credited and that the original publication in this journal is cited, in accordance with accepted academic practice. No use, distribution or reproduction is permitted which does not comply with these terms.



Influence of Clay Content on Crack Evolution of Clay–Sand Mixture

Xiangang Jiang^{1,2*}, Qin Huang¹, Zongliang Zhang³, Luis E. Vallejo⁴, Xiaoqing Chen⁵, Wanyu Zhao⁵, Hongyan Deng⁶, Xingrong Liu⁷, Danqing Song⁸ and Zhuo Chen¹

¹College of Civil Engineering, Sichuan Agricultural University, Dujiangyan, China, ²Sichuan Higher Education Engineering Research Center for Disaster Prevention and Mitigation of Village Construction, Sichuan Agricultural University, Dujiangyan, China, ³HYDROCHINA Kunming Engineering Corporation, Kunming, China, ⁴Department of Civil and Environmental Engineering, University of Pittsburgh, Pittsburgh, PA, United States, ⁵Key Laboratory of Mountain Hazards and Surface Process, Institute of Mountain Hazards and Environment, CAS, Chengdu, China, ⁶College of Civil Engineering, Southwest Jiaotong University, Chengdu, China, ⁷Geological Hazards Prevention Institute, Gansu Academy of Sciences, Lanzhou, China, ⁸State Key Laboratory of Hydrosience and Engineering, Department of Hydraulic Engineering, Tsinghua University, Beijing, China

OPEN ACCESS

Edited by:

Haijun Qiu,
Northwest University, China

Reviewed by:

Jun Li,
Sichuan University of Science and
Engineering, China
Cui Kai,
Lanzhou University of Technology,
China

*Correspondence:

Xiangang Jiang
41446@sicau.edu.cn

Specialty section:

This article was submitted to
Geohazards and Georisks,
a section of the journal
Frontiers in Earth Science

Received: 08 April 2022

Accepted: 02 May 2022

Published: 17 June 2022

Citation:

Jiang X, Huang Q, Zhang Z, Vallejo LE,
Chen X, Zhao W, Deng H, Liu X,
Song D and Chen Z (2022) Influence of
Clay Content on Crack Evolution of
Clay–Sand Mixture.
Front. Earth Sci. 10:915478.
doi: 10.3389/feart.2022.915478

Clay particles have an important influence on the cracking of clay–sand mixture, but the quantitative relationships between the clay content and crack evolution of the clay–sand mixture are still not clear. In order to explore the crack evolution process of the clay–sand mixture under different clay content conditions, we prepared nine groups of saturated clay–sand mixture samples with different clay contents and carried out drying experiments and Brazilian tests. The geometric dimensions and development forms of soil cracking were quantitatively analyzed by taking pictures of the sample cracks, image processing, and weighing the variation of the soil mass at the corresponding time during the drying process. The results showed that when the clay content was greater than 50%, the development process of the clay–sand mixture cracks can be divided into three stages: the formation stage of main cracks, the generation stage of the autonomously derived secondary fractures, and the stage of cracks widening. When it was less than 50%, the cracks in the development process of clay–sand mixture cracks had the characteristics of short length, dense crack spacing, no main cracks, and no obvious stage. The clay could add the tensile strength of the mixture and restrain crack development. The clay content had a significant effect on the shrinkage cracking and crack development process of soil, which shows that with the increase in the clay content, the tensile strength increases and restrains the crack development; the crack rate increases continuously and the width of cracks become larger; the lower the clay content, the lower is the crack rate and the smaller is the average crack width. The water content of samples with different clay soil contents all nonlinearly decreased with the increase in drying time, and the corresponding residual water content increased with the increase in the clay soil content at the same time. The water content of initial cracking, stable crack length, stable crack width, and stable block of the clay–sand mixture increased with the increase in the clay content, and the water content of the stable crack length was the same as that of the stable block number.

Keywords: clay, evolution, drying curve, crack geometrical size, Brazilian test

1 INTRODUCTION

When the soil loses water during the drying process, it shrinks and generates cracks on the surface of the soil. The generation of cracks would change the structure of the soil, increase the permeability of the soil, and greatly reduce the strength and stability of the soil, which causes various geological engineering problems and natural disasters (Morris et al., 1992; Albrecht and Benson, 2001; Tang et al., 2008; Ma et al., 2020; Liu et al., 2021; Yang et al., 2022).

Many researchers studied the characteristics of soil cracks from different aspects. In the aspect of crack geometry characteristics and evolution, Baer et al. (2009) analyzed the crack morphology and crack surface variation characteristics of silt loam based on the fractal theory, providing a method to quantify soil cracks, and their patterns considered fractal dimension; Miller et al. (1998) introduced a crack strength factor which can describe the development process of soil surface cracks quantitatively; Vogel et al. (2005a) and Vogel et al. (2005b) stated that the Minkowski function is a useful function to investigate the development modes of soil cracks quantitatively; Yuan and Yin (2004) used the remote optical microscope and made a quantitative analysis of the crack evolution law through the gray entropy of the crack image; Liu et al. (2013) developed a computer image processing method to describe the number of crack intersection nodes, length, number of cracks, number of blocks, block area, and crack rate of cracks. In terms of the causes and influencing factors, scholars believe that the occurrence of cracks in clay soil has a certain relationship with soil shrinkage. When soil shrinkage is inhibited or the surface tensile stress exceeds the cohesive strength between soil particles, cracks are prone to occur (Towner, 1987; Fleureau et al., 2015). Morris et al. (1992) found that some parameters of the soil, such as compressive modulus, Poisson's ratio, shear strength, and tensile strength, have a certain influence on the development and growth of soil cracks; Wang et al. (2017) indicated that with the increase in the dry-wet cycle, the crack rate and mean crack width also decreased; by drying experiments of lean clay, Zeng et al. (2019) and Zeng et al. (2020) found that the total length of cracks increases with the increase in interface roughness, and the total length of cracks decreases with the increase in soil thickness; Tang et al. (2008) analyzed the geometric characteristics of clayey soil cracks at different temperatures and considered that the crack rate, crack width, and crack length increase with the increasing temperature, and the shapes of the crack intersection notes were generally "+" and "T". However, the aforementioned studies were mostly focused on cohesive soil, and the mixtures which are common in nature and engineering fields were rare to report.

Fine and coarse particle mixtures are a type of common soil composed of coarse particles, such as block stones, gravel, and sand and fine particles, such as silt, sand, and clay (Medley, 2001). Under the change in external environments, such as temperature changes, cracks often appear in the mixture, which affects the soil's structure, strength, and seepage characteristics. The fine particle content in mixed soil is one of the decisive factors affecting their properties, which has been widely concerned by

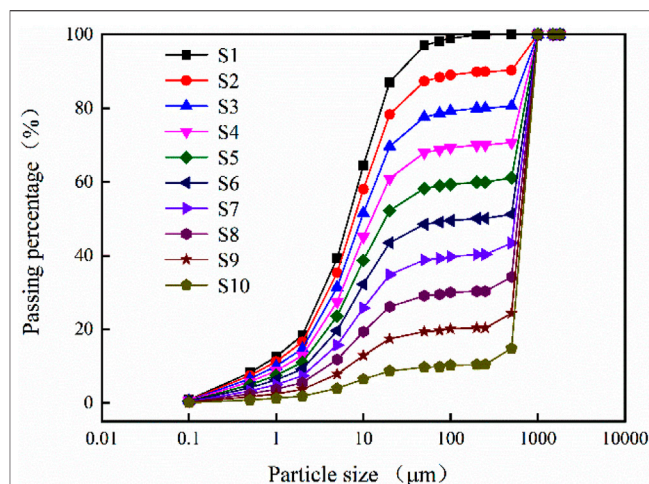


FIGURE 1 | Particle size distribution.

researchers (Sridharan and Prakash, 1998; Vallejo and Mawby, 2000; Vallejo, 2001; Chik and Vallejo, 2005; Ouyang and Takahashi, 2015; Guo and Cui, 2020). Although there are abundant research studies on the relationships between fine particle content and the strength, permeability, and pore change of mixed soil (Vallejo, 2001; Rahardjo et al., 2008), there is still a lack of relevant research on how the content of clay affects the development of cracks in mixed soils and the relationship between the content of clay and the geometry parameters of cracks.

This article aimed to explore the crack process and evolution characteristics of mixtures with different clay contents. The mixture of clay and quartz sand was selected as the research object. In this study, drying experiments and Brazilian tests were conducted. The Brazilian tests were designed to get the tensile strengths of different clay contents and how the clay contents help the crack development. Through the drying experiments, first, the evolution process and morphology of the geometric size of the surface cracks during the drying process of the soil were analyzed. Second, the quantitative relationships between the clay soil content and tensile strength and soil crack parameters (such as crack rate, crack length, and crack width) are studied with drying experiments and Brazilian tests. Finally, the influence of water content change during the crack development process was discussed.

2 EXPERIMENTAL MATERIALS AND METHODS

2.1 Experimental Materials and Preparation

The clay mineral component used in this experiment is kaolinite, which is one of the main mineral components of clay. The experimental material was the mixed soil of clay and quartz sand. The clay content of the artificially prepared material was 100, 90, 80, 70, 60, 50, 40, 30, 20, and 10%, and the corresponding sample number was S1–S10. The Malvern particle size analyzer

was used to investigate the size distribution of fine particle mixtures, and the screening device was used to achieve the size distribution of sands. The particle grading curve of the experimental material is shown in **Figure 1**.

The preparation process of the materials for the drying experiment is as follows. First, clay particles and quartz sands were dried up. Second, the corresponding mass was weighed according to the design requirements, and the clay and quartz sands were mixed evenly. The prepared mixed soil was put into a circular container with a diameter of 200 mm, and the thickness of the sample was 10 mm. The surface of the circular container was covered with a filter paper larger than the diameter of the container, and it was bound to the container with rubber reinforcement. Then, the container with the sample was placed in the distilled water cooled after boiling, and the water was ensured to overflow the top of the vessel. In this way, water could enter the container through a filter paper covering the surface of the container. The sample was placed in water for 72 h to saturate the sample. It was reported that 40°C is the global average maximum temperature (Middel et al., 2014), and at such temperature, the soil in the field would dry the fastest naturally. Therefore, 40°C was selected as the experimental temperature. During the drying process, the sample was weighed and photographed until the crack remained stable.

For Brazilian tests, the experimental materials were prepared the same way as the drying experiments. For soil sample preparation before Brazilian tests, the material was mixed with some water, and the water content was 8.3%.

2.2 Image Processing Method

Photographs were taken for soil cracks during the drying process, and the photographs were processed through image processing software to get crack geometry parameters. The processing steps are as follows: first, the photographs were preliminarily cut through the image processing software to make the image size 1,200 × 1,200 (pixels). Second, we created the image by binarization and skeletonization. Finally, according to the crack images after binarization and skeletonization, the crack rate, crack length, average crack width, and other parameters were calculated. In the analysis process, the processed image is expressed in the form of pixel value, and the relationship between the pixel value and the actual size of the image is as follows (Luo et al., 2020):

$$A_i = \beta_{i1} A_{i0}, \quad (1)$$

$$L_i = \beta_{i2} L_{i0}, \quad (2)$$

$$\beta_{i2} = \sqrt{\beta_{i1}}, \quad (3)$$

$$\beta_{i1} = \frac{A_i}{A_{i0}}, \quad (4)$$

$$R_s = \frac{A_i}{A_1}, \quad (5)$$

$$w_i = \frac{A_{i0}}{L_{i0}} \beta_{i2}, \quad (6)$$

where A_{i0} and L_{i0} are the crack pixel area and crack pixel length of the specimen, respectively; A_i and L_i are the actual crack area and actual crack length area, respectively; β_{i1} is the area conversion

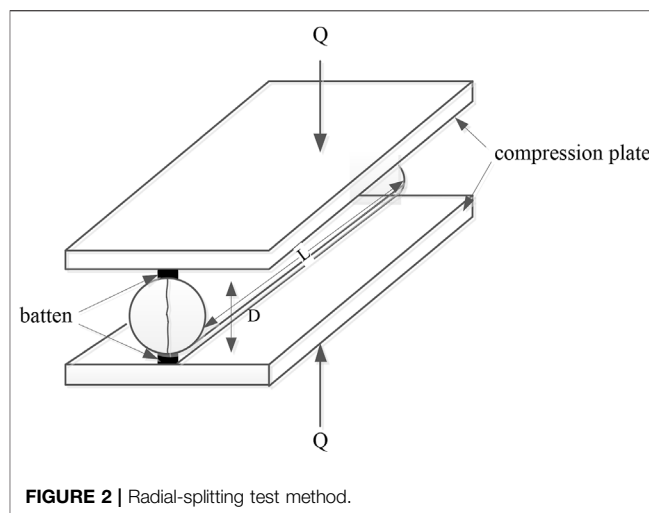


FIGURE 2 | Radial-splitting test method.

coefficient; β_{i2} is the length conversion coefficient; A_1 is the actual initial surface area of the sample, which is 31,400 mm² in the test; A_{i0} is the initial pixel area in the sample image; R_s is the crack rate of the sample, and w_i is the average width of the crack.

2.3 Method of Brazilian Test

Brazilian test is the most common method for determining the tensile strength of soils. The test is an indirect tensile strength test method, also called the radial-splitting test. In this test, a cylindrical specimen was placed horizontally between compression plates (Jiang et al., 2015). One batten was put above, and one was put below the specimen, which is used to distribute the applied load evenly along the entire length, as shown in **Figure 2**. In order to cause tensile radial failure in the specimen, load was applied on the top of the batten. At that moment, the lateral stress along the diameter is the tensile strength of the specimen with elasticity theory. The tensile strength σ_t is obtained using the following relationship:

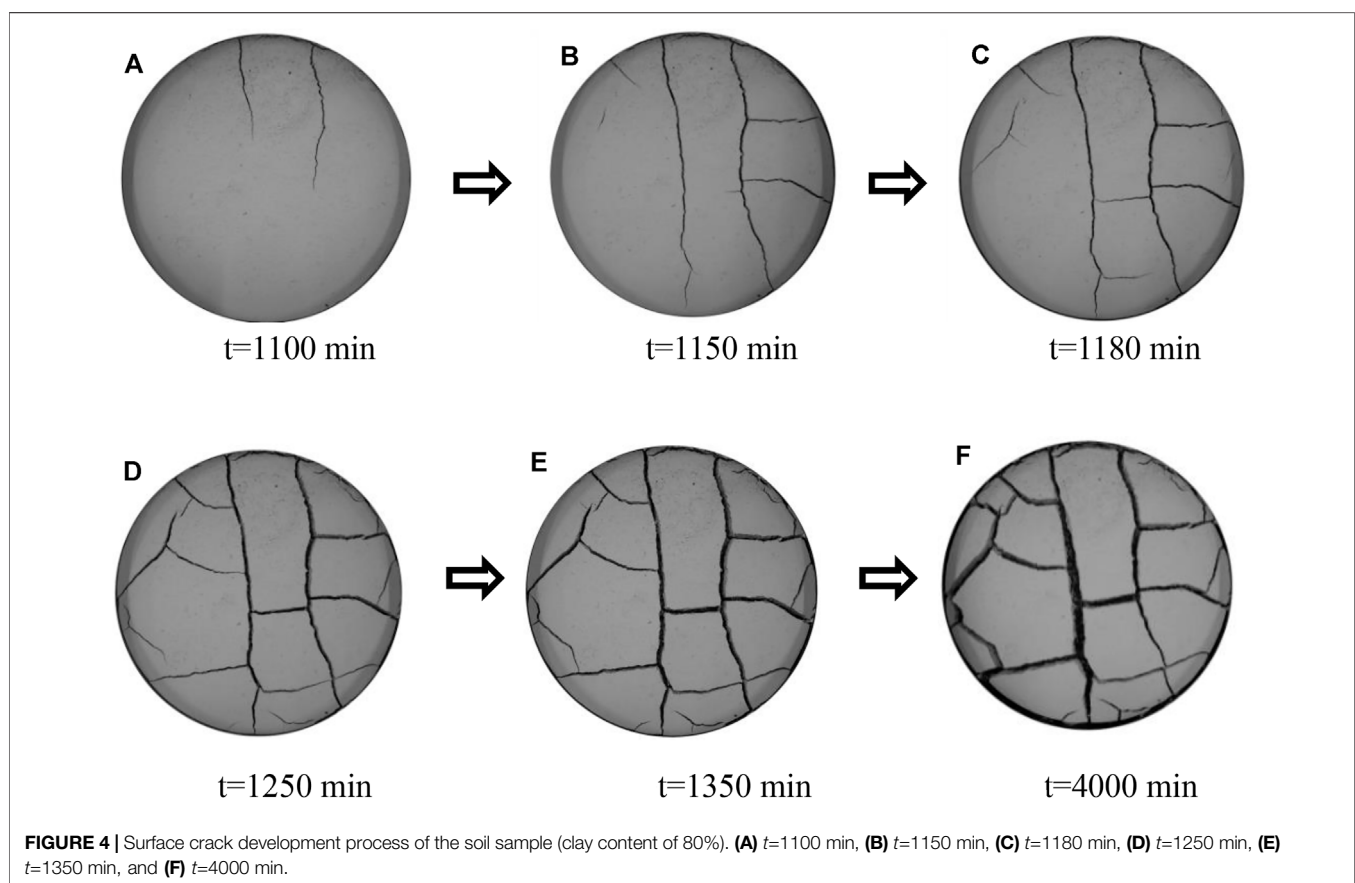
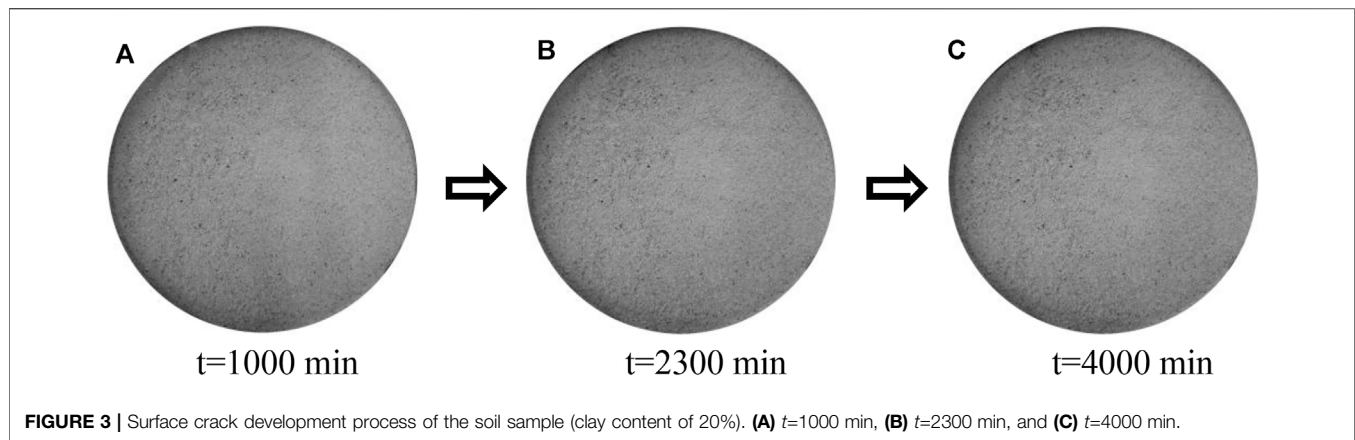
$$\sigma_t = \frac{2Q}{\pi DL}, \quad (7)$$

where Q is the applied load, N; D is specimen diameter, m; and L is the specimen length, m.

3 EXPERIMENTAL RESULTS

3.1 Development Process of Cracks

Figure 3 and **Figure 4** show the timing of drying time from sample drying. We found that the development process and shape of the cracks are related to the clay content from the experiments. When the clay content was less than 30%, there were few cracks or no cracks on the surface of the soil sample (take sample S9 as an example) (**Figure 3**). When the clay content was more than or equal to 30% and less than or equal to 50%, the development process of cracks was basically the same. It is shown that with the continuous drying, short and small cracks appeared at the specimen boundary first. Then,



the cracks on the specimen surface developed from the boundary to the center of the specimen, and the cracks stopped growing when cracks intersect with other cracks. For all cracks, their lengths were short, and there was no main crack in the soil.

When the clay content was more than 50%, the formation and development process of cracks were basically similar and could be divided into three stages. This takes sample S3 as an example to illustrate, which is shown in **Figure 4**.

The first stage: the formation stage of the main crack. With the drying of the sample, cracks first appeared around the boundary of the sample and whose number was little, that is, generally one or two. Then, the crack tip extended to the center of the sample and continued to grow through the center of the soil until the crack tip reached the boundary of the soil sample. These kinds of first-formed cracks were the main cracks, and these cracks divided the soil into several blocks (**Figures 4A and B**).

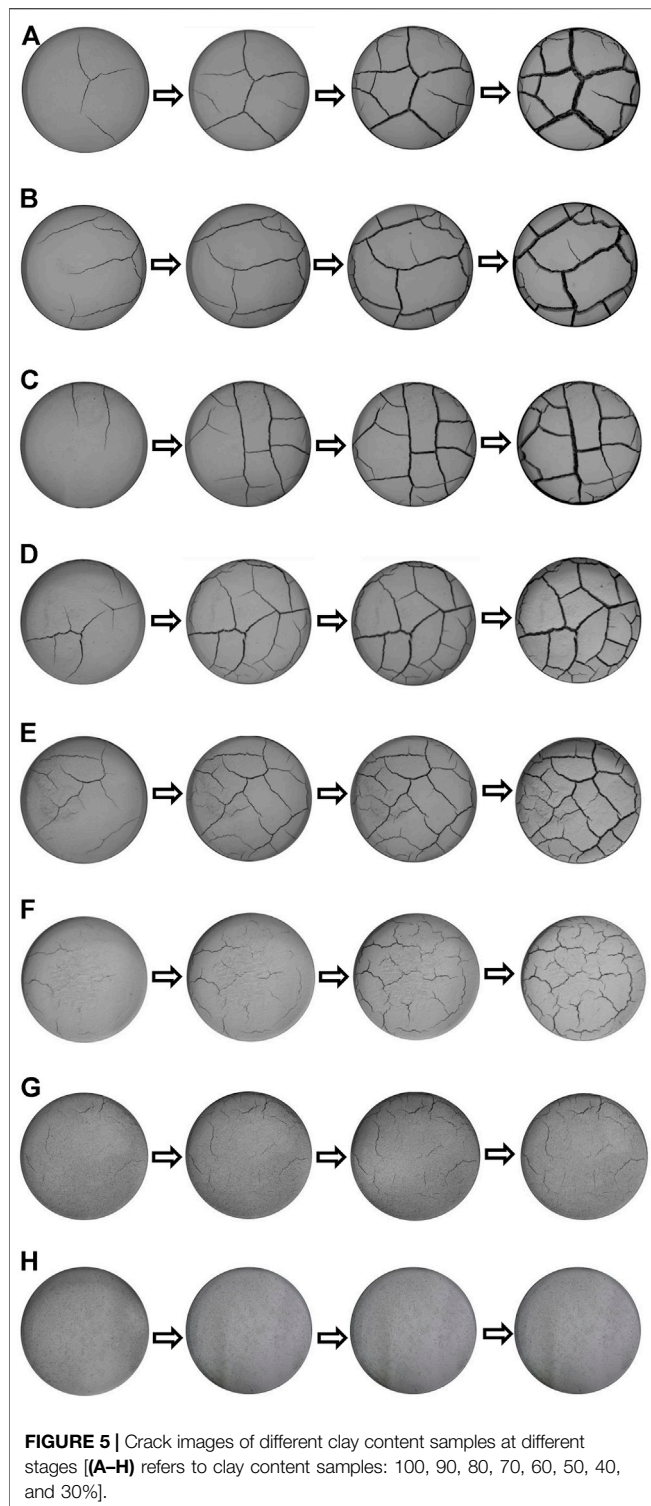


FIGURE 5 | Crack images of different clay content samples at different stages [(A–H) refers to clay content samples: 100, 90, 80, 70, 60, 50, 40, and 30%].

The second stage: the stage of self-derived secondary cracks. After the main cracks passed through the whole soil sample, new cracks were generated from the main crack and extended to the periphery of the sample, and the direction was approximately perpendicular to the main crack (**Figures 4C and D**). These self-derived new cracks are called secondary cracks, which will divide

the primary block into more secondary blocks until they are intersected with adjacent cracks perpendicularly, and then stop growing. With the development of drying, more new cracks may emerge from the secondary cracks and divide the secondary blocks into smaller blocks. In this stage, the variation of crack width was small, but the length of the cracks increased rapidly. In addition, the number of blocks did not change after the length of cracks stopped growing.

The third stage: The stage of cracks widening. As the drying time continued, the crack length did not develop, and there were no new cracks. The number, shape, and development direction of the cracks did not change. The cracks only gradually widened and finally stabilized until the end of drying, as shown in **Figures 4E and F**. When the experiments finished, the width and length of the main cracks were wider and longer than the secondary cracks.

3.2 Crack Development Mode

The crack development process of each sample was recorded by photographs, which can be processed with image processing software. **Figure 5** shows the morphological characteristics of cracks. It can be seen that the cracks of the S1–S5 sample are almost straight-line, while the cracks of the S6–S8 sample are mostly arc with relatively few straight lines. The mutual cracks of samples with different clay content all show a “T” shape, and the intersection angle between cracks is mostly 90°. The separated blocks are mostly triangle, quadrilateral, pentagon, and hexagon, especially since most of the blocks are quadrilateral. From the **Figures S1(a), S2(a), S3(a), S4(a), S5(a), S6(a), S7(a), S8(a)**, it can be seen that at the initial time, with the decreasing of clay content, the cracks of the samples become shorter and thinner, and the crack width becomes smaller. As the drying time increased, new cracks were generated from both the specimen boundary and the initial cracks, and the original blocks were divided [**Figure 5 S1–S8 (b–c)**]. The number and shape of the blocks were unchanged when the fracture length became stable [**Figure 5 S1–S8(d)**]. **Figure 5D** shows that when the clay content is 100%, the block separated by cracks around the boundary of the specimen is dominated by a triangle, and the blocks inward the center are mainly quadrilateral. When the clay contents were 50, 60, 70, 80, and 90%, there are two forms of shapes of triangle and quadrangle around the boundary of the specimen, and the interior is still dominated by a quadrilateral. Moreover, when the clay content is 50–100%, the number of blocks increases with decrease of the clay content. When the clay content is less than 50%, the number decreased, and the block shape around the sample is irregular and difficult to identify. However, the block shape inside the sample was mostly quadrilateral, and the cracks are approximately arc.

3.3 Characteristics of the Crack Geometry Size and Tensile Strength for Different Clay Contents

The geometric parameters of cracks with different clay soil contents are shown in **Figure 6**. The figure indicates that, in the initial stage, the soil samples with higher clay contents (80–100%) basically did not produce cracks, and while the clay

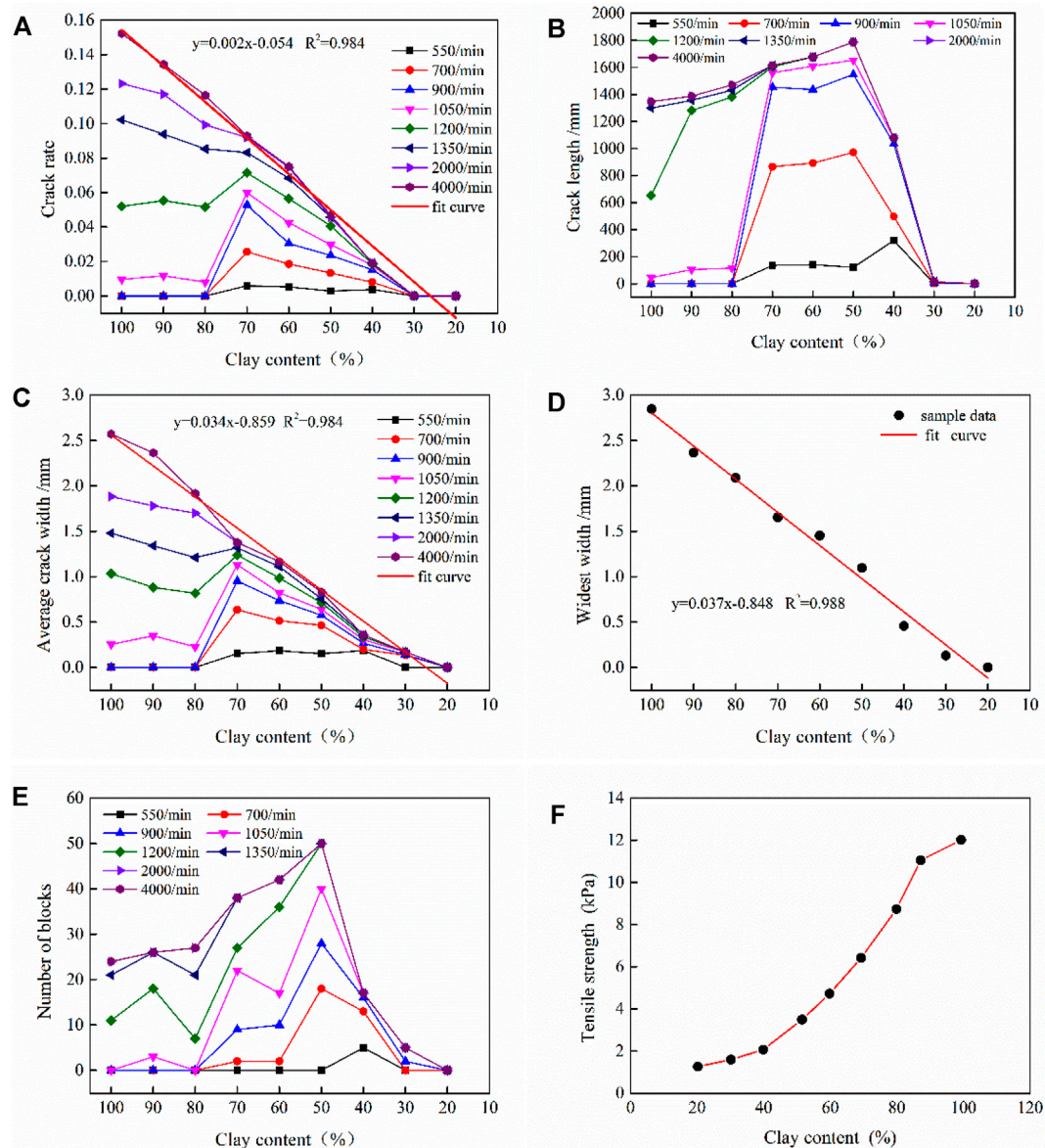


FIGURE 6 | Relationship between the crack parameter and tensile strength and clay content: **(A)** relationship between the crack rate and clay content. **(B)** Relationship between the crack length and clay content. **(C)** Relationship between the average crack width and clay content. **(D)** Relationship between the maximum crack width and clay content. **(E)** Relationship between the number of blocks and clay content. **(F)** Relationship between the tensile strength and clay content.

content was lower (except 20% clay content of the sample, as it did not crack), such as 30–70%, the cracks had started to generate. This means that the clay soil content has an inhibitory effect on the crack's generation (**Figure 6A**). From the crack development process, the crack rate increased with the development of time, especially before 1,350 min, and the crack rate first increased and then decreased with the increase in the clay content, and the critical clay content was 70%. After 1,350 min, there was a monotonic relationship between the crack rate and the clay content (**Figure 6A**). After the crack finish development, the crack rate of the sample with the highest clay soil content was

15.22%, while the crack rates of the sample with the clay content decreasing, in turn, were 13.43, 11.64, 9.28, 7.51, 4.68, 1.91 and 0.01%, respectively. It indicated that the crack rate increases with the increase in the clay content, and the clay content has a promoting effect on the final crack area (**Figure 6A**). Moreover, there is a linear relationship between the crack rate and the clay content at the final moment. **Figure 6B** shows the change curve of the total crack length under different clay content conditions. It can be seen from the figure that the crack length decreases with the increase in the clay content. In the period of 550 and 1,050 min, the total crack length decreased the fastest between

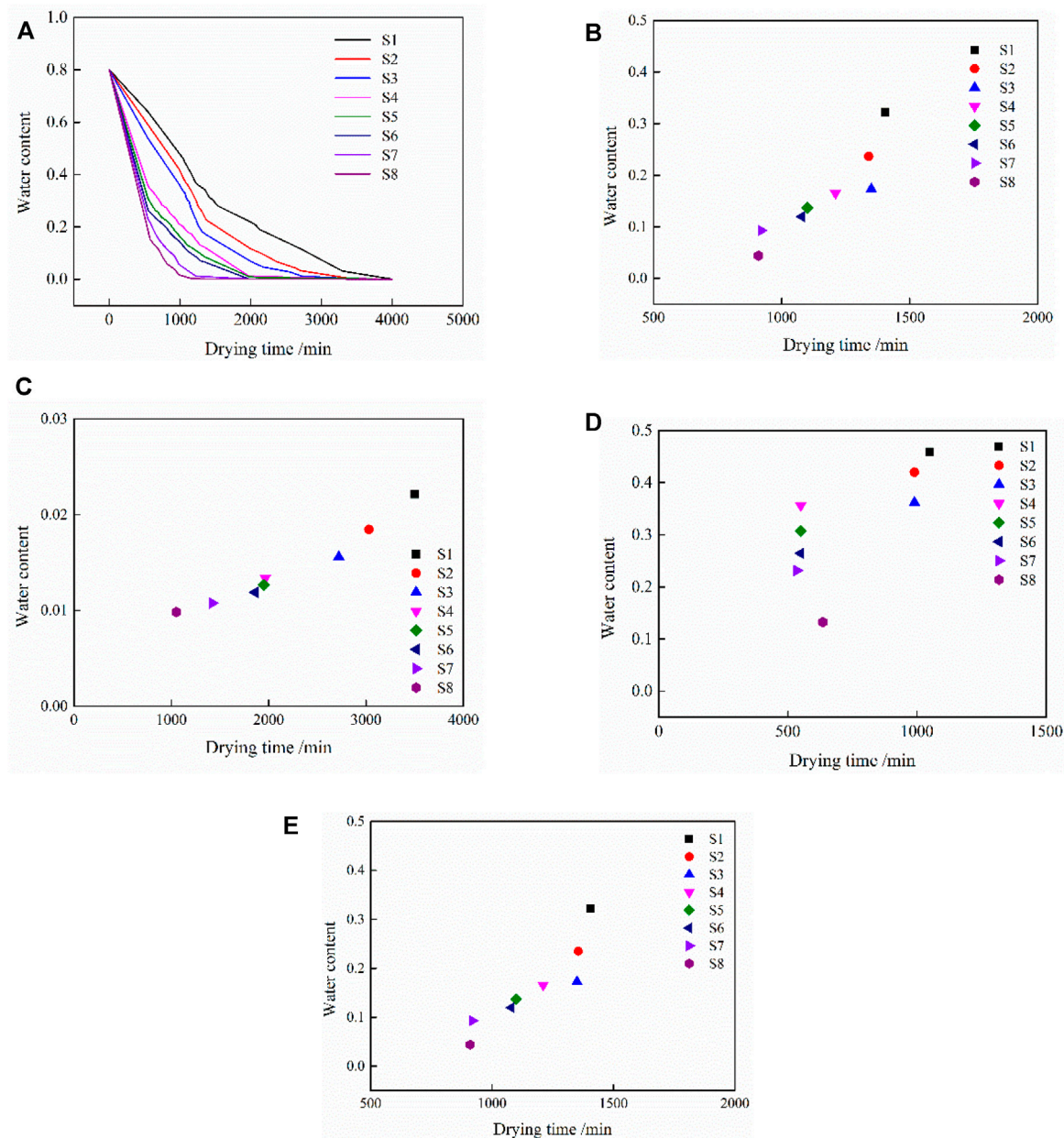


FIGURE 7 | Variation of the water content during the drying process: **(A)** Relationship between the water content and drying time for different materials. **(B)** Relationship between water content and time for different materials when the number of blocks was stable. **(C)** Relationship between the water content and time for different materials when the width of crack was stable. **(D)** Relationship between the water content and time for different materials when the first crack occurred. **(E)** Relationship between water content and time for different materials when the length of crack was stable.

70 and 80% clay content. In addition, after the cracks were stable, the crack length increased first and then decreased with the decrease in the clay content.

Figure 6C shows the average width variation curve of the cracks with different soil clay contents. It can be seen that the various characteristics of the average crack width are consistent with that of the crack rate with clay content. In addition, there is a linear relationship between the average crack width and the clay content. The curve of the maximum crack width of the sample

shows that after the completion of the drying experiments, the maximum crack width of the sample with the most clay soil content is 2.84 mm, and the maximum crack width of the sample with the least clay soil content is 0.13 mm. It indicated that the maximum crack opening degree of the sample is obviously affected by the clay content. In addition, **Figure 6D** shows a significant linear correlation between the clay content and maximum crack width. The variation curve of the number of sample blocks with different clay soil contents (**Figure 6E**) shows

that during the whole process of crack development, the number of blocks of the soil is the most with a clay content of 50% and the minimum number of blocks with a clay content of 30%. It means that with the increase in the content of clay soil, the number of soil blocks separated by cracks increase first and then decrease. In particular, a clay content of 50% is the inflection point (Figure 6E).

Figure 6F shows the relationship between tensile strength and clay content. It indicates that the tensile strength increases with the increase in the clay content. Combined with the abovementioned results, this figure demonstrates that the clay adds tensile strength to the mixtures, which helps the samples to develop no cracks.

3.4 Variation of the Water Content in the Cracking Process of Mixed Soil and Its Influence on Crack Development

The relationships between the water content and time for different clay contents are shown in Figure 7. It can be seen from the figure that the water content of the samples with different clay contents decreases non-linearly with the increase in drying time. Moreover, the higher the clay content, the greater was the remained water content at the same time during the drying process. Corresponding to the geometric parameters of the crack mentioned in Section 3.3, this section selects the water content at the first crack occurred time (w_1), water content when the length of the crack reaches its maximum value (w_2), water content when the width of the crack reaches its maximum value (w_3), and water content when the number of blocks reaches its maximum value (w_4). These parameters reflect the characteristics of water content in the process of crack development. Figure 7 shows that the w_1 of S1–S8 samples are 45.92, 42.02, 36.19, 35.62, 30.73, 26.45, 23.17, and 13.24%, respectively. It indicates that the w_1 increases with the increase in the clay content. It reflects that w_1 is greatly affected by the clay content. For S1–S8 samples, the w_2 values were 32.20, 23.50, 17.31, 16.52, 13.68, 11.97, 9.28 and 4.38%, respectively. It means that w_2 increases with the increase in the clay soil content. The figure shows the clay of 70% is the critical clay content for the difference between w_2 and w_1 . When the clay content is greater than or equal to 70%, the difference decreases with the increase in the clay content; otherwise, the difference increases with the increase of the clay content. In addition, the w_4 is the same as w_2 . It indicates that when the crack length is stable, the number of blocks separated by the crack is basically stable. From the moment when the crack width is stable, the w_3 for the highest clay content is 2.01%, while w_3 values with the clay content decreasing, in turn, were 1.85, 1.56, 1.34, 1.27, 1.19, 1.08 and 0.98%. It means the difference of w_3 for different clay contents is not much.

4 DISCUSSION AND CONCLUSION

In this study, the development process and morphology of soil cracks under different clay soil contents were analyzed by drying experiments. In particular, with image processing software, the geometric dimensions of the cracks were quantitatively analyzed. In this study, the clay particles mainly consisted of kaolin minerals. In such a way, the previous results may be applicable to the kaolin

minerals. In addition, the montmorillonite mineral is also one kind of clay mineral in nature. Although the montmorillonite mineral was not considered in this study, the results of other researchers have shown that the results in this study are applicable to the montmorillonite mineral. For example, the intersection angle between cracks in soils is both 90°, and the cracks are both mainly vertically intersected during the drying process for the montmorillonite and kaolin minerals (Tang et al., 2010; Tang et al., 2011; Costa et al., 2013). Also, after the crack development and stability, there is a linear relationship between the crack rate and clay content for both the montmorillonite mineral and the kaolin mineral (Xia et al., 2016). However, there are some differences during the process of fracture evolution for montmorillonite and kaolin. For example, the residual water content for the first crack that occurred for montmorillonite is higher than that of kaolin (El Hajjar et al., 2019). The main reason is that there is a large hydrated part in the form of bound water for the matrix of montmorillonite. This requires a temperature of 200°C to evaporate and crystalline water that does not leave the paste until temperatures above 550°C (Wakim, 2005). During the drying process, the montmorillonite has a greater influence on the shrinkage limit water content and shrinkage limit suction of soil than that of kaolin (Fleureau et al., 2015). This difference may lead to different sizes of cracks during the process of the crack development for the two clay minerals.

The conclusions are as follows:

- 1) For samples with clay content less than 30%, there are about no cracks on the surface of the soil sample. For samples with clay content greater than 50%, the formation and development of cracks are divided into three stages. The first stage is mainly the formation and elongation of the main crack; the second stage is mainly the formation of secondary cracks, and new secondary cracks are derived from secondary cracks; the third stage is mainly the crack width widening tends to be stable. For samples with the clay soil content more than or equal to 30% and less than or equal to 50%, the formation and development of cracks have no stage characteristics. The cracks are generated from the perimeter and develop to the center of the sample, and there are no main cracks, the length of the crack is short, and the spacing is small.
- 2) The clay content has a significant influence on the crack form. When the clay content is high, the cracks show a straight-line shape, and when the clay soil content is less, the cracks are mostly in the form of arc-shape. The internal cracks in the soil with different clay contents are mainly quadrilateral. When the clay contents are 100%, 50%–90%, and less than 50%, the shape of the block around the soil is mainly trilateral, trilateral and quadrilateral, and irregular, respectively. The clay content could restrain the crack development by increasing the tensile strength of soils.
- 3) The clay content has an inhibitory effect on the initial time of sample cracking. With the increase in the clay soil content, the maximum crack width, the average crack width, and the crack rate increase. When the cracks are stable, there is a linear relationship between the crack rate, average crack width, maximum crack width, and clay soil content; when the clay content is between 100 and 50%, the crack length increases

with the decrease in the clay content, while the total length of cracks between 50 and 30% decreases with the decrease in the clay content.

- 4) During the drying process, the mixed soil samples with higher clay soil content have higher remained water content at the same time. The water content responding to the moment of initial cracking, the crack length, width, and the block unchanged increases with the increasing of the clay content. The remained water content of soils when the number of block stable reached its maximum value is the same as that of when the length of the crack reached its maximum value.

DATA AVAILABILITY STATEMENT

The original contributions presented in the study are included in the article, further inquiries can be directed to the corresponding author.

REFERENCES

- Albrecht, B. A., and Benson, C. H. (2001). Effect of Desiccation on Compacted Natural Clays. *J. Geotech. Geoenviron. Eng.* 127 (1), 67–75. doi:10.1061/(asce)1090-0241(2001)127:1(67)
- Baer, J. U., Kent, T. F., and Anderson, S. H. (2009). Image Analysis and Fractal Geometry to Characterize Soil Desiccation Cracks. *Geoderma* 154 (1–2), 153–168. doi:10.1016/j.geoderma.2009.10.008
- Chik, Z., and Vallejo, L. E. (2005). Characterization of the Angle of Repose of Binary Granular Materials. *Can. Geotech. J.* 42 (2), 683–692. doi:10.1139/t04-118
- Costa, S., Kodikara, J., and Shannon, B. (2013). Salient Factors Controlling Desiccation Cracking of Clay in Laboratory Experiments. *Géotechnique* 63 (1), 18–29. doi:10.1680/geot.9.p.105
- El Hajjar, A., Ouahbi, T., Eid, J., Taibi, S., Bouchemella, S., and Eid, J. (2019). “Desiccation and Cracking Behaviour of Clayey Soils: Experimental Characterization and Mechanisms Identification,” in *Soil Mechanics Geotech Eng, ECSMGE, Reykjavik, Iceland 1st - 6th of September 2019*. doi:10.32075/17ECSMGE-2019-0998
- Fleureau, J. M., Wei, X., Ighil-Ameur, L., Hattab, M., and Bicalho, K. V. (2015). *Experimental Study of the Cracking Mechanisms of Clay during Drying*. Proceedings of the 15th Pan-American Conference on Soil Mechanics and Geotechnical Engineering, Buenos Aires, Argentina. 2101–2108. Stand Alone, 2101–2108. doi:10.3233/978-1-61499-603-3-2101
- Guo, C., and Cui, Y. (2020). Pore Structure Characteristics of Debris Flow Source Material in the Wenchuan Earthquake Area. *Eng. Geol.* 267 (1), 105499. doi:10.1016/j.enggeo.2020.105499
- Jiang, X., Cui, P., and Ge, Y. (2015). Effects of Fines on the Strength Characteristics of Mixtures. *Eng. Geol.* 198, 78–86. doi:10.1016/j.enggeo.2015.09.011
- Liu, C., Tang, C.-S., Shi, B., and Suo, W.-B. (2013). Automatic Quantification of Crack Patterns by Image Processing. *Comput. Geosci.* 57, 77–80. doi:10.1016/j.cageo.2013.04.008
- Liu, Z., Qiu, H., Ma, S., Yang, D., Pei, Y., Du, C., et al. (2021). Surface Displacement and Topographic Change Analysis of the Changhe Landslide on September 14, 2019, China. *Landslides* 18 (4), 1471–1483. doi:10.1007/s10346-021-01626-4
- Luo, Z. G., Wang, S. J., Zhang, J. W., and Yang, Z. B. (2020). Thickness Effect on Crack Evolution of Expansive Soil. *J. Geotech. Eng.* 42 (10), 1922–1930. (in Chinese). doi:10.11779/CJGE202010018
- Ma, S., Qiu, H., Hu, S., Yang, D., and Liu, Z. (2020). Characteristics and Geomorphology Change Detection Analysis of the Jiangdingya Landslide on July 12, 2018, China. *Landslides* 18, 383–396. doi:10.1007/s10346-020-01530-3
- Medley, E. W. (2001). Orderly Characterization of Chaotic Franciscan Melanges. *Eng. Geol.* 19 (4), 20–32.
- Middel, A., Häb, K., Brazel, A. J., Martin, C. A., and Guhathakurta, S. (2014). Impact of Urban Form and Design on Mid-Afternoon Microclimate in Phoenix Local Climate Zones. *Landsc. Urban Plan.* 122, 16–28. doi:10.1016/j.landurbplan.2013.11.004
- Miller, C. J., Mi, H., and Yesiller, N. (1998). Experimental Analysis of Desiccation Crack Propagation in Clay Liners. *J. Am. Water Resour. Assoc.* 34 (3), 677–686. doi:10.1111/j.1752-1688.1998.tb00964.x
- Morris, P. H., Graham, J., and Williams, D. J. (1992). Cracking in Drying Soils. *Can. Geotech. J.* 29 (2), 263–277. doi:10.1139/t92-030
- Ouyang, M., and Takahashi, A. (2015). Influence of Initial Fines Content on Fabric of Soils Subjected to Internal Erosion. *Can. Geotech. J.* 53 (2), 299–313. doi:10.1139/cgj-2014-0344
- Rahardjo, H., Indrawan, I. G. B., Leong, E. C., and Yong, W. K. (2008). Effects of Coarse-Grained Material on Hydraulic Properties and Shear Strength of Top Soil. *Eng. Geol.* 101 (3–4), 165–173. doi:10.1016/j.enggeo.2008.05.001
- Sridharan, A., and Prakash, K. (1998). Characteristic Water Contents of a Fine-Grained Soil-Water System. *Géotechnique* 48 (3), 337–346. doi:10.1680/geot.1998.48.3.337
- Tang, C.-S., Shi, B., Liu, C., Suo, W.-B., and Gao, L. (2011). Experimental Characterization of Shrinkage and Desiccation Cracking in Thin Clay Layer. *Appl. Clay Sci.* 52 (1–2), 69–77. doi:10.1016/j.clay.2011.01.032
- Tang, C. S., Cui, Y. J., Tang, A. M., and Shi, B. (2010). Experiment Evidence on the Temperature Dependence of Desiccation Cracking Behavior of Clayey Soils. *Eng. Geol.* 114 (3–4), 261–266. doi:10.1016/j.enggeo.2010.05.003
- Tang, C. S., Shi, B., Liu, C., Zhao, L. Z., and Wang, B. J. (2008). Influencing Factors of Geometrical Structure of Surface Shrinkage Cracks in Clayey Soils. *Eng. Geol.* 101 (3–4), 204–217. doi:10.1016/j.enggeo.2008.05.005
- Towner, G. D. (1987). The Mechanics of Cracking of Drying Clay. *J. Agric. Eng. Res.* 36 (2), 115–124. doi:10.1016/0021-8634(87)90118-1
- Vallejo, L. E. (2001). Interpretation of the Limits in Shear Strength in Binary Granular Mixtures. *Can. Geotech. J.* 38 (5), 1097–1104. doi:10.1139/t01-029
- Vallejo, L. E., and Mawby, R. (2000). Porosity Influence on the Shear Strength of Granular Material-Clay Mixtures. *Eng. Geol.* 58 (2), 125–136. doi:10.1016/s0013-7952(00)00051-x
- Vogel, H. J., Hoffmann, H., Leopold, A., and Roth, K. (2005b). Studies of Crack Dynamics in Clay Soil: II. A Physically Based Model for Crack Formation. *Geoderma* 125 (3–4), 213–223. doi:10.1016/j.geoderma.2004.07.008

AUTHOR CONTRIBUTIONS

XJ and QH designed this research and drafted the manuscript. ZZ and LV helped with the language. XC, WZ, HD, XL, DS, and ZC provided ideas and discussion throughout the progress. All authors have read and agreed to the published version of the manuscript.

FUNDING

This work was supported by the National Natural Science Foundation of China (Grant No. U19A2049), the Second Tibetan Plateau Scientific Expedition and Research Program (Grant No. 2019QZKK0906), the National Natural Science Foundation of China (Grant Nos. 42177149 and 41925030), Gansu Province's 2021 Key Talent Project (Grant No. 2021RCXM066), and the Gansu Academy of Sciences Applied Research and Development Project (Grant No. 2021JK-07).

- Vogel, H. J., Hoffmann, H., and Roth, K. (2005a). Studies of Crack Dynamics in Clay Soil: I. Experimental Methods, Results, and Morphological Quantification. *Geoderma* 125 (3-4), 203–211. doi:10.1016/j.geoderma.2004.07.009
- Wakim, J. (2005). *Influence des solutions aqueuses sur le comportement mécanique des roches argileuses*. France, Paris: Thèse de l'École Nationale Supérieure des Mines de Paris.
- Wang, C., Zhang, Z.-Y., Liu, Y., and Fan, S.-M. (2017). Geometric and Fractal Analysis of Dynamic Cracking Patterns Subjected to Wetting-Drying Cycles. *Soil Tillage Res.* 170, 1–13. doi:10.1016/j.still.2017.02.005
- Xia, D. S., Liu, Q. B., Xiang, W., Wang, J. E., and Ai, M. (2016). Impact of Montmorillonite Content on Desiccation Cracks on Clay Surface. *J. Yangtze River Sci. Res. Inst.* 33 (9), 83–86+92. (in Chinese). doi:10.11988/ckyyb.20150607
- Yang, D. D., Qiu, H. J., Ma, S. Y., Liu, Z. J., Du, C., Zhu, Y. R., et al. (2022). Slow Surface Subsidence and its Impact on Shallow Loess Landslides in a Coal Mining Area. *Catena* 209, 105830. doi:10.1016/j.catena.2021.105830
- Yuan, J. P., and Yin, Z. Z. (2004). Quantitative Index of Fissure and Strength Characteristics of Fissured Expansive Soils. *J. Hydraul. Eng.* 1 (06), 108–113. (in Chinese). doi:10.13243/j.cnki.slxb.2004.06.019
- Zeng, H., Tang, C.-S., Cheng, Q., Inyang, H. I., Rong, D.-Z., Lin, L., et al. (2019). Coupling Effects of Interfacial Friction and Layer Thickness on Soil Desiccation Cracking Behavior. *Eng. Geol.* 260, 105220. doi:10.1016/j.enggeo.2019.105220
- Zeng, H., Tang, C. S., Cheng, Q., Zhu, C., Yin, L. Y., and Shi, B. (2020). Drought-Induced Soil Desiccation Cracking Behavior with Consideration of Basal Friction and Layer Thickness. *Water Resour. Res.* 56 (7), e2019WR026948. doi:10.1029/2019wr026948

Conflict of Interest: ZZ was employed by the company HYDROCHINA Kunming Engineering Corporation.

The remaining authors declare that the research was conducted in the absence of any commercial or financial relationships that could be construed as a potential conflict of interest.

Publisher's Note: All claims expressed in this article are solely those of the authors and do not necessarily represent those of their affiliated organizations, or those of the publisher, the editors, and the reviewers. Any product that may be evaluated in this article, or claim that may be made by its manufacturer, is not guaranteed or endorsed by the publisher.

Copyright © 2022 Jiang, Huang, Zhang, Vallejo, Chen, Zhao, Deng, Liu, Song and Chen. This is an open-access article distributed under the terms of the Creative Commons Attribution License (CC BY). The use, distribution or reproduction in other forums is permitted, provided the original author(s) and the copyright owner(s) are credited and that the original publication in this journal is cited, in accordance with accepted academic practice. No use, distribution or reproduction is permitted which does not comply with these terms.



Spatial and Temporal Analysis of Quantitative Risk of Flood due to Climate Change in a China's Plateau Province

Baolin Wu^{1,2,3}, Zhengtao Zhang^{1,4,2,3*}, Xinrui Guo⁵, Cheng Tan^{1,2,3}, Chengfang Huang^{1,2,3} and Jun Tao⁶

¹Key Laboratory of Environmental Change and Natural Disasters, Ministry of Education, Beijing Normal University, Beijing, China, ²Academy of Disaster Reduction and Emergency Management, Ministry of Emergency Management and Ministry of Education, Beijing, China, ³Faculty of Geographical Science, Beijing Normal University, Beijing, China, ⁴State Key Laboratory of Earth Surface Processes and Resource Ecology (ESPRE), Beijing Normal University, Beijing, China, ⁵College of Global Change and Earth System Science, Beijing Normal University, Beijing, China, ⁶School of National Safety and Emergency Management, Beijing Normal University, Beijing, China

OPEN ACCESS

Edited by:

Haijun Qiu,
Northwest University, China

Reviewed by:

Jianmin Qiao,
Shandong Normal University, China
Qiang Zou,
(CAS), China

*Correspondence:

Zhengtao Zhang
zhangzhengtao@bnu.edu.cn

Specialty section:

This article was submitted to
Geohazards and Georisks,
a section of the journal
Frontiers in Earth Science

Received: 29 April 2022

Accepted: 16 May 2022

Published: 24 June 2022

Citation:

Wu B, Zhang Z, Guo X, Tan C,
Huang C and Tao J (2022) Spatial and
Temporal Analysis of Quantitative Risk
of Flood due to Climate Change in a
China's Plateau Province.
Front. Earth Sci. 10:931505.
doi: 10.3389/feart.2022.931505

The Qinghai–Tibet Plateau is a region sensitive to climate change with significant changes in topography, and the increase in extreme precipitation in the region easily leads to landslides and debris flows. To mitigate the effects of climate change, the Chinese government has pledged to an emission reduction target that achieves a “carbon peak” in 2030 and being “carbon neutral” in 2060 at a huge cost. In order to explore the quantitative flood risk at the county level in Qinghai province (the core province of the Qinghai–Tibet Plateau) and the contribution of emission reduction efforts to risk mitigation, this article constructs a loss rate curve based on the data of more than 1,000 single flood disasters from 2009 to 2019 through government cooperation and the data of observed cumulative precipitation. Combined with the latest CMIP6 climate model data, the temporal and spatial variation characteristics of the flood loss ratio in Qinghai province from 2020 to 2060 are quantitatively characterized. The results show the following: 1) the curve of the flood loss rate in Qinghai province from 2020 to 2060 may present a trend of “rising in the early stage, stable in the middle stage, and declining in the late stage” under low (SSP126) and medium (SSP245) emission scenarios and presents a trend of rising fluctuation under the high-emission (SSP585) scenario. The flood loss ratio under SSP585 is 10 times higher than that under SSP126; 2) the flood risk of 44 counties from 2020 to 2060 in Qinghai province may be concentrated in the southeast region, with Jiuzhi county, Banma county, Nangqian county, Gande county, and Dari county being the most prominent; (3) compared with SSP585, the Qinghai province in SSP126 may cumulatively avoid about 24 billion CNY in economic losses from 2020 to 2060 and avoid nearly 600 million CNY in losses per year, which is equivalent to 93% of Qinghai province's special funds for ecological and environmental protection in 2019. The research aims to provide theoretical and data support for flood disaster risk prevention and management in China's high-altitude areas and to promote the initiative of emission reduction in China and even the world.

Keywords: Qinghai–Tibet Plateau, risk assessment, flood, loss rate, carbon neutral

1 INTRODUCTION

The regional extreme precipitation intensity and global warming degree represent an approximate linear relationship (high confidence) (IPCC, 2021). According to the CMIP5 scenarios, the relevant meteorological indices of the Qinghai–Tibet Plateau have a greater range of variation than the global meteorological indices, and its response to climate change is more obvious (**Supplementary Table S1**) (Wu and You, 2019). Also, the Tibetan Plateau in China is a region sensitive to climate change due to its unique and complex high-altitude geographical conditions (Duan et al., 2016). The risk of regional extreme precipitation may be further amplified in this region (Ma et al., 2021) and more vulnerable to induce mass movement disasters such as landslides and debris flow (Ma et al., 2021; Liu et al., 2022; Yang et al., 2022). This change will threaten the lives and property of people on the Qinghai–Tibet Plateau and even downstream regions (Zhou et al., 2022).

In order to further reduce the impact of climate change, the Chinese government has set the carbon emission reduction target of “carbon peak by 2030 and carbon neutral by 2060” and formulated strong emission reduction measures. Due to the Tibetan Plateau’s high sensitivity to climate change response and the positive relationship between regional extreme precipitation and climate change, the assessment of future flood risk changes in the region can reflect the effectiveness of emission reduction in China and even the world to a certain extent. The current risk assessment of extreme flood has experienced a process from qualitative methods to semi-qualitative and semi-quantitative methods and then to quantitative methods. The qualitative methods mainly used questionnaire survey, data analysis, and other methods combined with expert experience to determine the relative risk degree (Meihua et al., 2008; Zelenáková, 2009; Wang et al., 2018). With the maturity of the disaster risk theory, the research on disaster risk assessment mostly adopts the method of multi-factor weighted syntheses of categories like hazards, exposure, and fragility (Guo et al., 2021; Lv et al., 2021). However, as all relevant indicators need to be uniform in dimension, the result is a “relative” risk level of “low/medium/high.” In order to meet the evaluation needs of the “absolute” degree of disaster risk, the loss function or expected loss function based on disaster statistics and the intensity of hazard to calculate the loss rate curve is built to evaluate the results measured by the monetary value of economic losses or the number of affected populations (Delalay et al., 2020; Su et al., 2021), but this method also puts high requirements for the reliability, timing, and comprehensiveness of basic data (Li et al., 2016).

Qinghai province is the core province of the Qinghai–Tibet Plateau in China, and it is urgent to carry out a risk assessment for flood disasters. Due to the relatively low social and economic development of Qinghai province and the backward construction of disaster management departments, there is a lack of sufficient public historical disaster data in this area. Therefore, the

qualitative and semi-quantitative methods are mostly used for disaster risk assessment (Jinhu et al., 2007; Dou and Yan, 2013; Zou et al., 2013; Chen et al., 2021; Weidong et al., 2021). However, with the government’s increasing demand for the assessment of the “absolute” degree of flood risk in Qinghai province and also with the exploration of the contribution of emission reduction efforts to the risk reduction degree, the quantitative method for the Qinghai flood disaster becomes an urgent work. Some research studies use information diffusion methods such as the Monte Carlo method to supplement missing historical disaster data, but this brings large uncertainty compared to actual information (Kalyanapu et al., 2012; Peng et al., 2017; Koc and Işık, 2021).

In this article, the disaster data composed of more than 1,000 single flood disasters in the flood season (May–October) in Qinghai province from 2009 to 2019 were obtained by cooperating with the disaster management departments of Qinghai province, and the accumulated precipitation during a flood disaster process was obtained by combining the observed daily precipitation data. Based on the aforementioned data, the expected loss function is constructed by the regression prediction model and probability density analysis method. In addition, daily precipitation grid data of 22 climate models (CMIP6) and future GDP grid data (SSP database) were used to evaluate the flood disaster loss rate curves of 44 counties in Qinghai province from 2020 to 2060 under three scenarios. This study takes the low-emission scenario SSP126 as the “carbon neutral” target scenario, medium-emission scenario SSP245, and high-emission scenario SSP585, which were used as comparative reference scenarios to evaluate the temporal and spatial variation characteristics of flood risk at provincial and county scales in Qinghai province from 2020 to 2060 (O’Neill et al., 2016; Ridder et al., 2022). The purpose was to analyze the contribution of emission reduction to reducing flood disaster risk in Qinghai province and identify the potential “positive impact” brought by China’s emission reduction efforts, providing data and method support for formulating sustainable disaster prevention and mitigation policies and social-economic development policies in Qinghai province, and also promoting China and the global initiative to reduce emissions.

2 METHODOLOGY

2.1 Study Area

Qinghai, a province in western China located in the northeast of the Qinghai–Tibet Plateau, is 1200 km long from east to west and more than 800 km wide from north to south, accounting for 1/13th of China’s total area. The average altitude of the province is over 3000 m above sea level. Its topography shows downward elevation from west to east and a saddle shape from north to south (**Figure 1A**). The annual precipitation in Qinghai province is 15.4–732.5 mm with a general distribution landscape of gradual decrease from southeast to northwest. In most areas of the

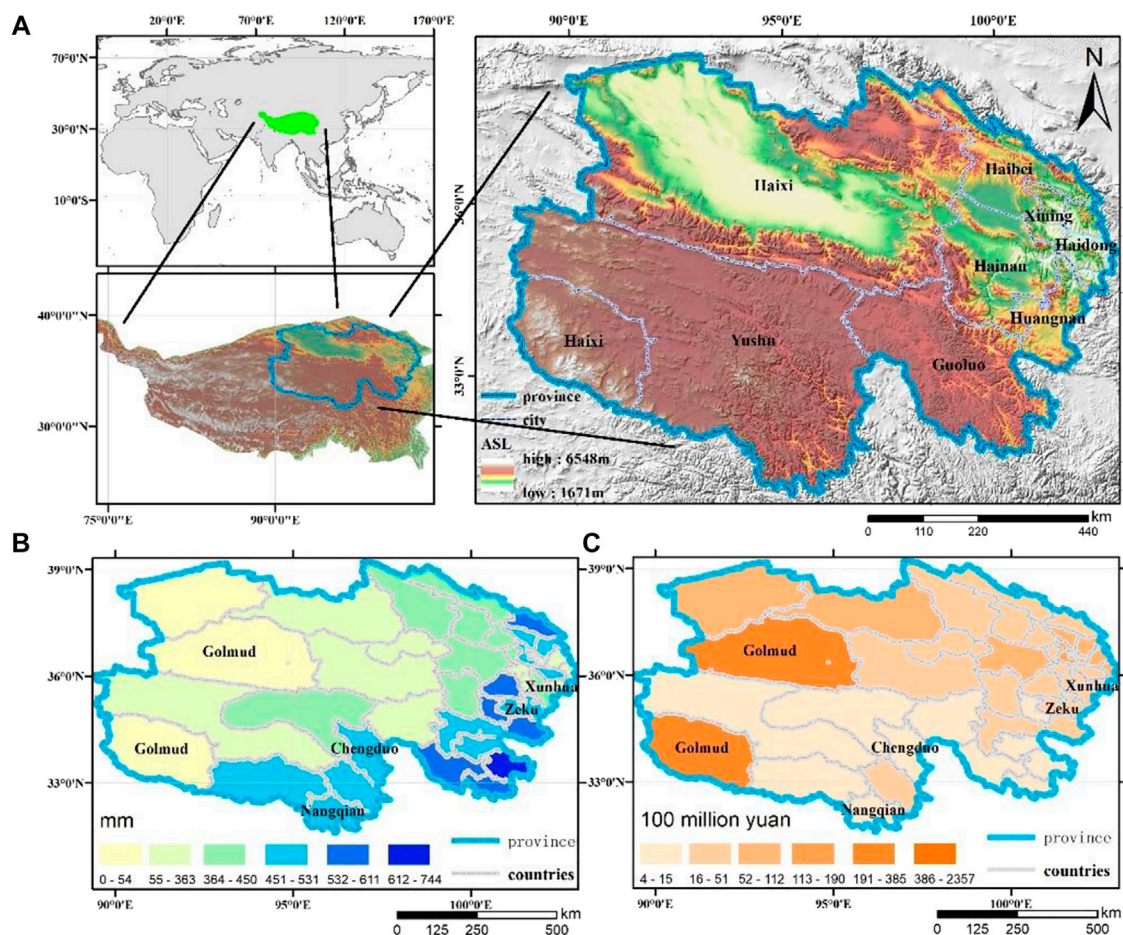


FIGURE 1 | Distribution landscape of natural and economic characteristics of Qinghai province. **(A)** Geographical location of Qinghai province and the Qinghai–Tibet Plateau, and the terrain of Qinghai province; **(B)** average precipitation distribution in Qinghai province from 2009 to 2019; **(C)** GDP distribution of Qinghai province in 2019.

province, the annual precipitation is below 400 mm and features sharp seasonal fluctuations that the precipitation in the flood season accounts for more than 70% of its annual total. The topography makes it easy for heavy rain to develop into flash floods, and even geological disasters, such as debris flow and landslides.

The precipitation distribution in Qinghai province from 2009 to 2019 shows that the east is rainier than the west, while the south is rainier than the north (**Figure 1B**). Jiuzhi county in the southeast of Qinghai province has the highest annual average precipitation in the province. The precipitation of counties in Qinghai province is mainly in the flood season (June to September), accounting for more than 65% of the annual precipitation. The spatial and temporal distribution of landslide and debris flow disasters coincides with that of rainstorm and flood disasters caused by precipitation in the eastern part of the Qinghai–Tibet Plateau (Lin et al., 2020). As the risks of flood hazards are high in the east and low in the west, those in Chengduo county, Nangqian county, Zeku county, and Xunhua county possess high-risk curves. According to the GDP distribution in 2019 (**Figure 1C**), except

Golmud county, we can see that the economically developed areas in Qinghai are mainly in Xining city and its surrounding regions. The high direct losses (DEL) all happened in the northeast of Qinghai province, and Xining city and its surrounding areas are the most severely affected, showing an ascending trend from southwest to northeast. A total of 11 counties in Qinghai province suffered direct economic losses of over 100 million CNY each from 2009 to 2019, with Xunhua county suffering the highest DEL of 593 million CNY.

2.2 Data

From 2009 to 2019, Qinghai province counted 1,512 county-level flood and secondary disasters, such as landslides and debris flow data, including the direct economic losses, affected population, dead population, and damaged farmland. The meteorological data include daily precipitation and daily mean temperature data of 41 meteorological stations in Qinghai province from 2009 to 2019. The social statistical data are the annual GDP data of 44 counties in Qinghai province from 2009 to 2019. The specific information is shown in **Table 1**:

TABLE 1 | History data.

Data type	Disaster data			Meteorological data	
	Direct economic loss	Death population	The affected population	Precipitation	Air temperature
Number	1512	-	-	41 × 11 × 365	41 × 11 × 365
Unit	CNY	-	-	mm	°C
Spatial scale	County	County	County	County	County
Time scale	Day	Day	Day	Day	Day

TABLE 2 | Future data.

Data type	Meteorological data	Social-economic statistic data
	Precipitation	GDP
Scenario	SSP126/245/585	SSP126/245/585
Unit	mm	USD
Spatial-scale resolution	100–500 km	1 km
Time-scale resolution	Day	Year

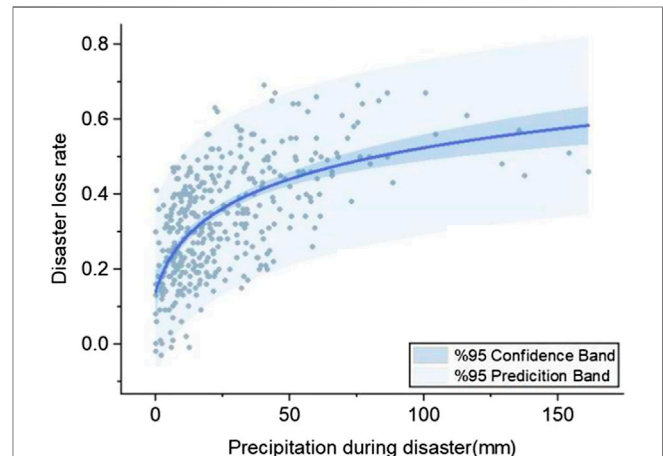
Future flood disaster risk assessment uses CMIP6 (<https://esgf-node.llnl.gov/search/cmip6/>) future climate scenarios data from 2020 to 2060, including daily scale precipitation data of 22 GCM models (**Supplementary Table S2**) under different scenarios with different spatial resolutions. Future emission scenarios include CMIP6's latest SSPs (Shared Socioeconomic Pathways and the Representative Concentration Pathways): SSP126, SSP245, and SSP585. The SSPs are the updated RCP (Representative Concentration Pathway) scenarios SSP126, SSP245, and SSP585, representing the low social vulnerability and low-emission scenario, medium social vulnerability and medium-emission scenario, and high social vulnerability and high-emission scenario, respectively. The future economic forecast data adopt the future GDP grid data of three emission scenarios under the SSP database during the period 2020–2060. Detailed information is listed in **Table 2**:

2.3 MATERIALS AND METHODS

This article mainly includes three parts: 1) construction of an expected loss model based on historical data; 2) future climate model data extraction; 3) future risk assessment of flood disaster in Qinghai province.

In this study, the single-process precipitation of 377 flood disasters in Qinghai province from 2009 to 2019 was fitted with the corresponding loss rate of flood by polynomial fitting, and the expected loss curve of rainstorm flood disasters in Qinghai province is determined as follows:

$$\begin{aligned}
 R_Curve^{his} &\rightarrow V \\
 &- \text{Best} \left\{ f_x \left(QRloss_{i,j}^{his}, \sum_{d=1}^n pr_{i,j}^{his} \right) (x = 1, 2, 3 \dots) \right\} \\
 &= \alpha + \ln(Accpr^{his} + \gamma),
 \end{aligned} \quad (1)$$

**FIGURE 2** | Expected loss curve.

where x is the function fitting mode, and this formula selects the best fitting function through linear fit and nonlinear curve fit (e.g., convolution, exponential, growth/sigmoidal, logarithm, polynomial, power, and rational); i is the i th county; j is the j th flood precipitation process; d is the accumulated days of flood disaster; $Accpr^{his}$ is the single rainstorm flood disaster-accumulated precipitation; $\alpha = -0.08092$ $[-0.17124, 0.0094]$; $\beta = -0.12987$ $[-0.15164, -0.1081]$; $\gamma = 5.38928$ $[2.13541, 8.64315]$; and $QRloss$ is the loss rate of flood disaster:

$$QRloss_{i,j}^{his} = \frac{\log_{10} \left(DL_{i,j}^{year} \cdot \frac{GDP_i^{year}}{Def_i^{year=2015}} \right)}{\log_{10} \left(\frac{GDP_i^{year}}{Def_i^{year=2015}} \right)}, \quad (2)$$

where DL^{year} is the direct economic loss of a single flood disaster, GDP^{year} is the current GDP (Gross domestic product), and $Def_i^{year=2015}$ is the GDP deflator set 2015 = 100.

Figure 2 shows the trend that the loss rate of flood disaster changes with the change of precipitation during the disaster process. It can be seen from the expected loss curve in **Figure 2** that with the increase of the process precipitation, the loss rate increases rapidly in the range of 0–20 mm process precipitation and increases more slowly after 20 mm process precipitation, showing a “logarithmic” shape as a whole.

The precipitation data of the future CMIP climate model were interpolated by quadratic spline interpolation with a uniform accuracy of $0.0083^\circ \times 0.0083^\circ$ (1 km). The formula for future precipitation data and GDP data is as follows:

$$GDP_i^{future} = \sum_{g=1}^m GDP_{i,g}^{future}, \quad (3)$$

$$Accpr_i^{future} = \frac{\sum_{d=1}^n \sum_{g=1}^m pr_{i,g}^{future}}{m}, \quad (4)$$

where g is the number of grid points in a region, GDP_i^{future} is the projected future GDP, $Accpr_i^{future}$ is the projected future process precipitation.

DL_i^{future} (direct economic losses of future flood disasters) can be obtained by Eqs. 2, 3, 4:

$$DL_i^{future} = f\left(GDP_i^{future} \cdot \frac{GDP_i^{future}}{Def_i^{year=2015}}, QRloss_i^{future}\right). \quad (5)$$

The ratio of direct economic loss (P) is calculated as the “absolute” value of the future flood disaster risk assessment in Qinghai province through the formula in Eq (6):

$$P_i^{future} = \frac{DL_i^{future}}{GDP_i^{year=2015}}. \quad (6)$$

The quantiles of 90%, 98%, and 99% of precipitation in the historical flood disaster process are selected as the threshold values of flood disasters that occur once in 10 years, once in 50 years, and once in 100 years, respectively, and the threshold values are used to evaluate the risk of extreme flood disasters in the future. Taking the 10-year flood risk as an example:

$$P_{10}^{future} = P_i\{Accpr_i^{future} \geq Accpr_{90}^{his}\}. \quad (7)$$

Take 5% and 95% of the multi-model data set under each scenario as the error range of precipitation for future flood disasters. Under the high-emission scenario (SSP585), the GDP loss ratio in 2055 is 0.7%, and the uncertainty caused by the multi-model 95% and 5% data is in the range of (0.00003%, 70%), that is, it causes the loss of 29,400 CNY to 205.8 billion CNY. The reason for such a large error is that the multi-mode data of CMIP6 vary greatly in the high-altitude area of the Qinghai–Tibet Plateau. Therefore, only the mean value data of 22 models are used to calculate the future flood disaster loss ratio.

3 EVALUATION RESULTS AND ANALYSIS OF RAINSTORM AND FLOOD DISASTER IN QINGHAI PROVINCE

3.1 The Loss Rate Assessment in Qinghai Province From 2009 to 2019

Figure 2 shows the changing trend of the loss rate of flood in the context of precipitation fluctuations during the disaster. As can be seen from the expected loss curve in the figure, with the increase of precipitation, the loss rate rises rapidly in the precipitation range of 0–20 mm and then more and more slowly after 20 mm, presenting a “logarithmic” change trend as a whole.

Due to the large vertical elevation difference in Qinghai province, small precipitation can quickly give rise to runoffs and confluences to form flash floods, but more precipitation is needed in plain areas to cause regional floods. Combined with the loss rate of Y-axis, “small and frequent” flood disasters are more likely to occur in Qinghai province, but the losses caused by the accumulation of those disasters cannot be ignored. According to the distribution of precipitation and loss rate of the flood, the disaster with the highest loss rate in history is not the one with the heaviest precipitation. Due to the underdeveloped economy in some areas in Qinghai province, the number of hazard-affected bodies is small. With the continuous growth of precipitation, most of those bodies exposed to the affected area of the disaster are damaged, so the losses reach the peak value. In addition, for relatively developed areas with insufficient disaster protection capacity, rainstorms and floods often lead to landslides, debris flows, and other geological disasters, resulting in a high loss rate with low precipitation.

3.2 The Temporal Variation Features of the Loss Ratio Changes From 2020 to 2060

1) Annual trend analysis of the loss ratio in Qinghai province from 2020 to 2060

Figure 3 shows the annual change curve of the loss ratio of flood in Qinghai province from 2020 to 2060 under the scenarios SSP126, SSP245, and SSP585, calculated based on the historically expected loss curve, the future precipitation, and the forecast data of GDP. The shaded part is the error range caused by the 95% confidence interval of the expected loss curve. On the whole, the scenarios SSP126 and SSP245 show a trend of “rising in the early stage, stable in the middle stage, and declining in the late stage,” while scenario SSP585 shows a rising trend of fluctuation, which is becoming wilder. From 2050 to 2060, the fluctuation degree will reach its peak. The average annual loss ratios under the three scenarios are 0.231%, 0.249%, and 0.429%, respectively. The higher the emission force is, the higher the overall loss rate will be.

In scenario SSP126, the year with the highest loss ratio will be around 2040 and the highest loss ratio (0.499%) will be found in 2037 while the lowest loss ratio (0.075%) in 2058. In the figure, the most obvious increase and decrease changes will be found from 2037 to 2038 and from 2055 to 2058, with the loss ratio increasing by 0.3560% and decreasing by 0.290%, respectively. From 2020 to 2060, the total loss ratio will reach 9.4808%.

In scenario SSP245, the highest loss ratio (0.522%) will be found in 2048, while the lowest loss ratio (0.121%) in 2020. From 2047 to 2048, the most obvious loss ratio increase will be 0.3688%, while from 2048 to 2049, the most obvious loss ratio decrease will be 0.2193%. The total loss ratio through the period from 2020 to 2060 is expected to reach 10.1938%.

In scenario SSP585, the loss ratio will reach a peak (0.8063%) in 2058, while the lowest loss ratio (0.125%) was seen in 2020. The most obvious increase and decrease changes will be found during the periods 2055–2058 and 2058–2060, with the loss ratio increasing by 0.364% and decreasing by 0.371%, respectively. The cumulative loss ratio from 2020 to 2060 will be 17.6011%.

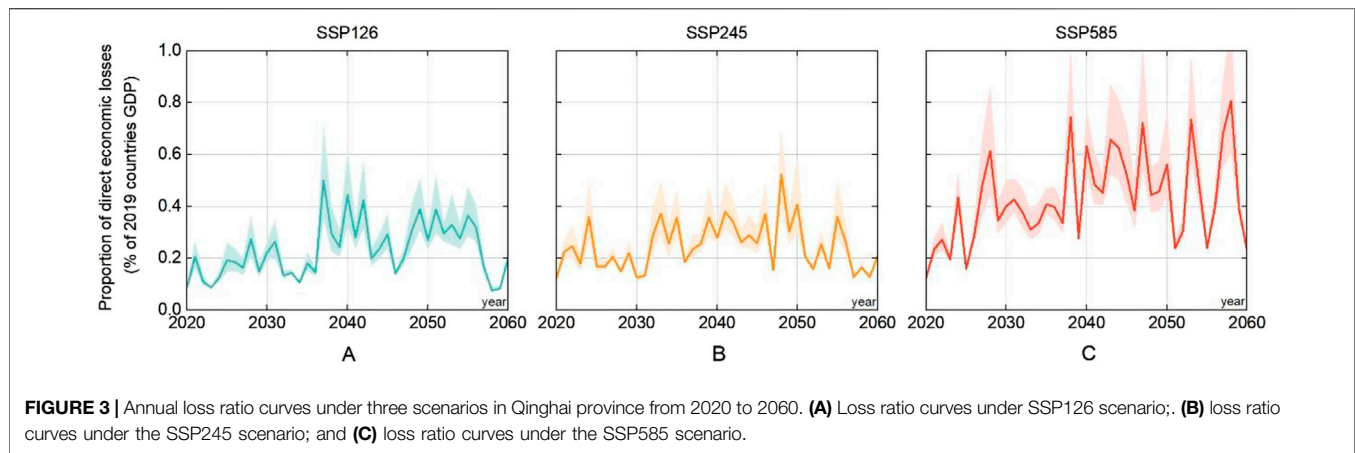


FIGURE 3 | Annual loss ratio curves under three scenarios in Qinghai province from 2020 to 2060. **(A)** Loss ratio curves under SSP126 scenario; **(B)** loss ratio curves under the SSP245 scenario; and **(C)** loss ratio curves under the SSP585 scenario.

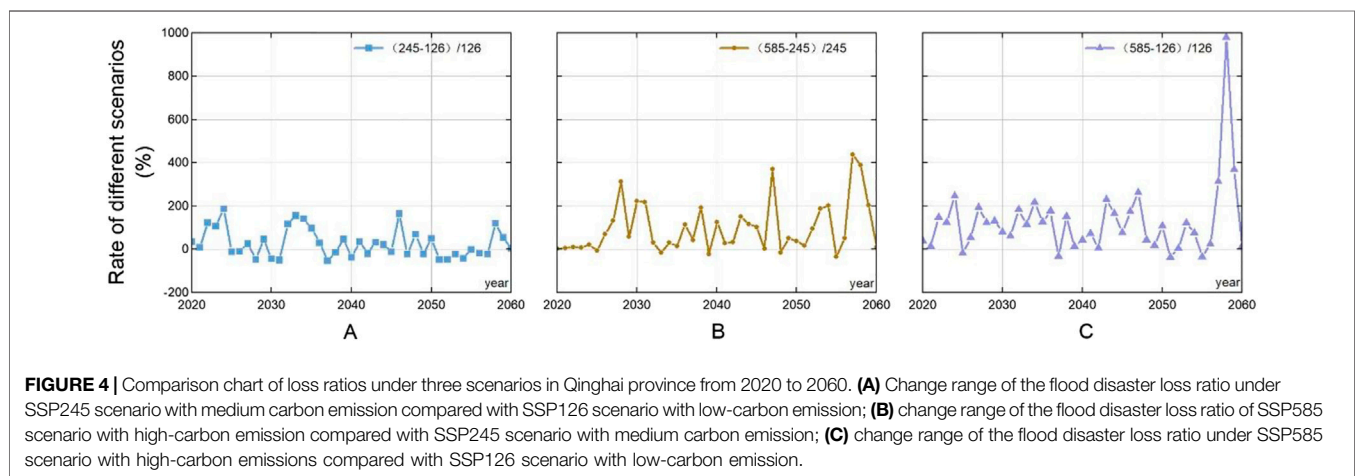


FIGURE 4 | Comparison chart of loss ratios under three scenarios in Qinghai province from 2020 to 2060. **(A)** Change range of the flood disaster loss ratio under SSP245 scenario with medium carbon emission compared with SSP126 scenario with low-carbon emission; **(B)** change range of the flood disaster loss ratio of SSP585 scenario with high-carbon emission compared with SSP245 scenario with medium carbon emission; **(C)** change range of the flood disaster loss ratio under SSP585 scenario with high-carbon emissions compared with SSP126 scenario with low-carbon emission.

With the time going on, the maximum loss ratio in the SSP585 scenario will be constantly refreshed, and its fluctuation range will become larger and larger.

Based on the aforementioned variation trends of the loss ratio and precipitation in the three scenarios, the lowest value (0.075%) of the flood risk loss ratio in Qinghai province is found in scenario SSP126 and the highest value (0.8063%) in scenario SSP585. The increasing trend and fluctuation range of the loss ratio of SSP585 are significantly larger than those of SSP126 and SSP245.

2) Comparative analysis of the difference in losses under three scenarios in Qinghai province from 2020 to 2060

Based on the assessment results of flood disaster loss ratios through the period of 2020–2060 under the scenario SSP126/245/585 in Qinghai province, **Figure 4** further analyzes the disparity of future flood loss ratios among the three scenarios.

The ratio of actual loss to GDP in 2019 under the future scenarios SSP126/245/585 shows significant differences in maximum value, minimum value, and inter-annual fluctuation. The difference between SSP585 and SSP126 is greater than that between SSP585 and SSP245, and that between SSP245 and SSP126 is the smallest.

Compared with that under the scenario SSP126 with low emission, the change extent of annual flood disaster loss under scenario SSP245 with medium emission (**Figure 4A**) shows that the loss ratio under SSP245 during 2020–2060 is 0.017% high. In most of the years, the loss of SSP245 is higher than that of SSP126, and the widest discrepancy between them will be 186.745% in 2024. In the next 41 years, the cumulative loss ratio of SSP245 will be 0.713% higher than that of SSP126. Given the GDP, 294 billion CNY, of Qinghai province in 2019, the DEL of flooding in the province will increase by about 2.1 billion CNY. **Figure 4B** shows that under SSP585, the annual average loss ratio is 0.1807% higher than that of SSP245, and the loss caused by flood will increase by 436.566% to the peak (2057), with an average annual increase of 97.777%. From 2020 to 2060, the difference of cumulative disaster loss ratios will be 7.4073%. Given the GDP of Qinghai province in 2019, the loss of flood in the province under the SSP585 scenario will increase by about 21.777 billion CNY compared with that under the SSP245 scenario.

From 2020 to 2060, the annual average loss ratio under the SSP585 scenario is 0.198% higher than that under scenario SSP126. In 41 years, the loss ratio of flood disasters under the SSP585 scenario was less than that under the SSP126 scenario only by 4 years. At the same time, the difference in the GDP loss

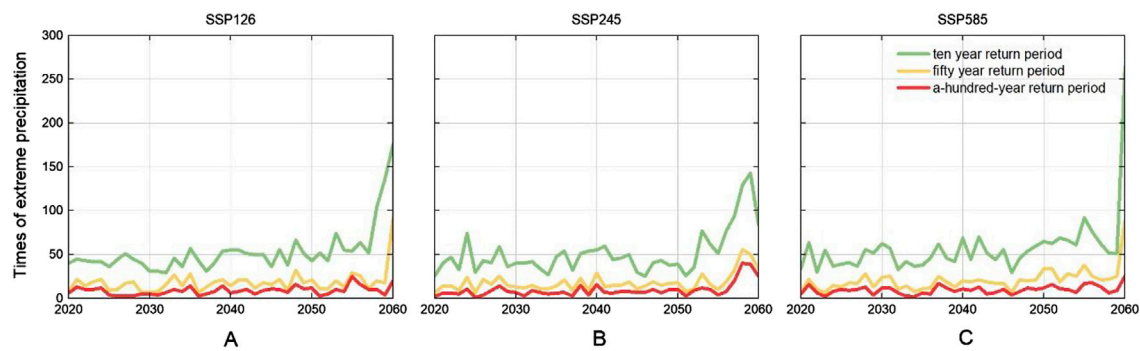


FIGURE 5 | Extreme flood frequency in Qinghai province from 2020 to 2060. **(A)** 10/50/100-year return period flood frequency under the SSP126 scenario; **(B)** 10/50/100-year return period flood frequency under the SSP245 scenario; and **(C)** 10/50/100-year return period flood frequency under the SSP585 scenario.

ratio between the two scenarios varies greatly from year to year, and the loss of scenario SSP585 is 126% higher than that of scenario SSP126 a year on average. The loss caused by the flood disaster will increase by nearly 10 times than that in 2058 (980.733%). This is mainly because under scenario SSP585, the loss ratio of flood will fluctuate greatly during 2050–2060, and its extreme value will also be seen in 2058.

The aforementioned results show that from 2020 to 2060, compared with scenario SSP585, the loss ratio of flood in Qinghai province will decrease by 8.12% under scenario SSP126, which is to achieve carbon emission reduction targets. With the emission reduction action of China's "carbon neutrality and carbon peak" target, only the loss caused by the flood in Qinghai can drop by 23.874 billion CNY (based on the GDP of Qinghai province of 294 billion CNY in 2019) from 2020 to 2060, about saving 600 million CNY per year on average, equivalent to 93% of Qinghai's 2019 provincial special fund for ecological and environmental protection (626 million CNY). From the perspective of disaster risk, the results can quantitatively reveal the hidden "benefits" behind the costs for China to achieve the "carbon neutrality and carbon peak" target.

3) Analysis of the frequency of flood return period in Qinghai province from 2020 to 2060

During 2020–2060 in Qinghai province, the occurrences of extreme floods within a 10-, 50-, and 100-year return period (**Figure 5**) show that the frequency of those extreme disasters occurring within the 10-year return period is greater than that occurring within the 50-year return period and 100-year return period under scenario SSP126/245/585, and all of them show a fluctuant-rising trend. In particular, around 2058, there has been a significant increasing trend.

Under scenario SSP126, the average annual occurrences of 10-, 50-, and 100-year return period flooding in Qinghai province from 2020 to 2060 will amount to 53, 19, and 9, respectively. In 2057, the number of extreme floods occurring within the 10-year return period will increase sharply and will reach 176 in 2060. In 2060, the number of the 50-year return period flood will be 91 and

the number of 100-year return period floods will rise to its peak of 25 in 2055.

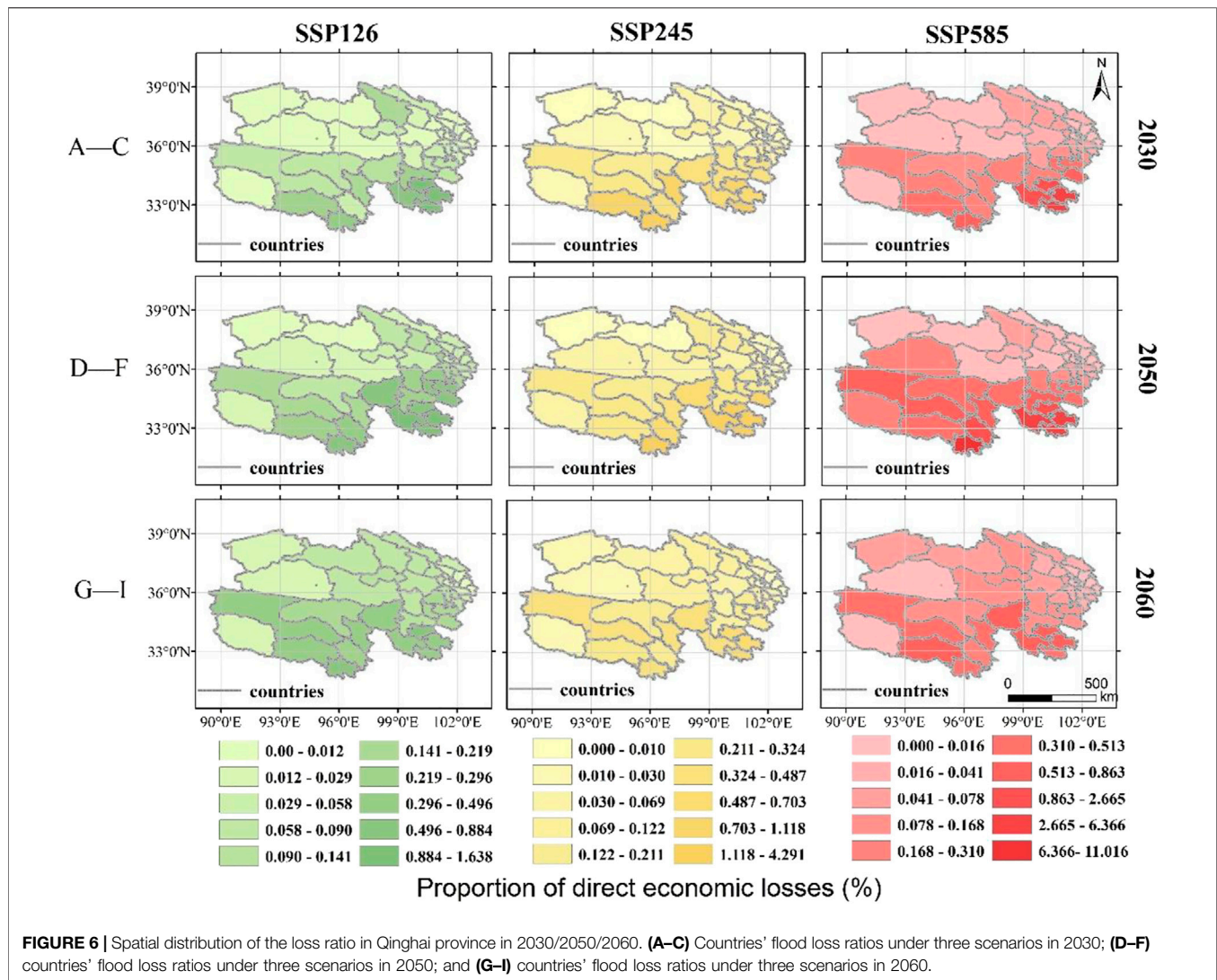
Under the scenario SSP245, the average number of 10-, 50-, and 100-year return period floods in Qinghai province in the future will be 52, 19, and 10 per year, respectively. The frequency of occurrences of these three types of flood return periods shows a slow-rising trend and will increase significantly in 2056. In 2059, the number of extreme floods during the 10-year return period will increase to a peak of 143. Both that number of 50-year return period and 100-year return period flood will reach peaks of 56 and 40 in 2058, respectively.

Under scenario SSP585, the average number of 10-, 50-, and 100-year return period floods in Qinghai province in the future will be 58, 21, and 10 per year, respectively. In 2060, the number of these three types of extreme floods will reach their peaks of 265, 90, and 26, respectively.

By comparing the total number of extreme disasters of different return periods, the frequency of flood of diverse return periods under scenario SSP585 is significantly higher than that under SSP126 and SSP245. From 2020 to 2060, the smaller the emission reduction, the higher the frequencies of extreme rainstorms and flood disasters and their peaks.

In conclusion, under three scenarios in Qinghai province from 2020 to 2060, the occurrence frequencies of the extreme flood occurring within a 10-, 50-, and 100-year return period all show an increasing trend. However, compared with scenario SSP126, under scenario SSP585 with high emission, extreme flood disasters occurring within the 100-year return period may have 37 extra cases, those within the 50-year return period may have 94 extra cases, and those within the 10-year return period may have 167 extra cases.

According to casualties caused by diverse return periods of flood from historical disaster data, if the emission reduction target (SSP126 scenario) could be achieved, it might lower the casualties by the numbers of 58, 77, and 88, respectively, due to minimizing the occurrence of 10-year return period/50-year return period/100-year return period flood (compared with SSP585 scenario). Therefore, measures to reduce emissions may significantly cut the potential loss of life caused by floods.



3.3 The Spatial Distribution Characteristics of the Loss Ratio in Typical Years and Typical Countries

1) Analysis of the characteristics of a county loss ratio of rainstorm and flood disasters in Qinghai province in typical years

Figure 6 shows the distribution of the loss ratio of rainstorm and flood disasters in each county of Qinghai province in 2030, 2050, and 2060 under three scenarios. The disaster loss ratio in Qinghai province will be in a descending pattern from southeast to northwest in three typical years. The southeast of Qinghai province suffers a bigger loss than other regions of the province, while the west and north suffer less. In Qinghai province, the counties of Banma, Dari, Gande, Jiuzhi, and Nangqian will all have high or mid-high loss ratios under scenarios SSP126, SSP245, and SSP585, and the eastern part of Qinghai will suffer mid-high loss ratios, the central and southwestern parts

will have medium loss ratios, and the western part will be subjected to low or very low loss ratios.

According to the figure for 2030, the distribution pattern of the high and low values of the loss ratio in each county under the three emission scenarios is similar. Under scenario SSP126, the areas with the highest loss ratios are Jiuzhi, Banma, Gande, Dari, and Nangqian counties successively. The loss ratios of Jiuzhi, Banma, and Gande counties are all higher than 1%, and the sum of that is 3.17%, accounting for more than half of the total loss ratio of rainstorm and flood disasters in 2030. Under scenario SSP245, the loss ratios of Banma, Nangqian, and Gande counties are the highest, with a sum of 3.67%. Under scenario SSP585, the loss ratios of Jiuzhi, Banma, Dari, and Gande counties are significantly higher than those of other regions, and the sum of that is 4.56%, accounting for nearly 60% of the province. In 2050, the counties of Banma, Jiuzhi, Dari, Gande, and Nangqian will be the five counties with the highest loss ratios of rainstorm and flood disasters in Qinghai under the three scenarios, and the sum of their loss ratios will be 5.784%, 14.830%, and 27.611%,

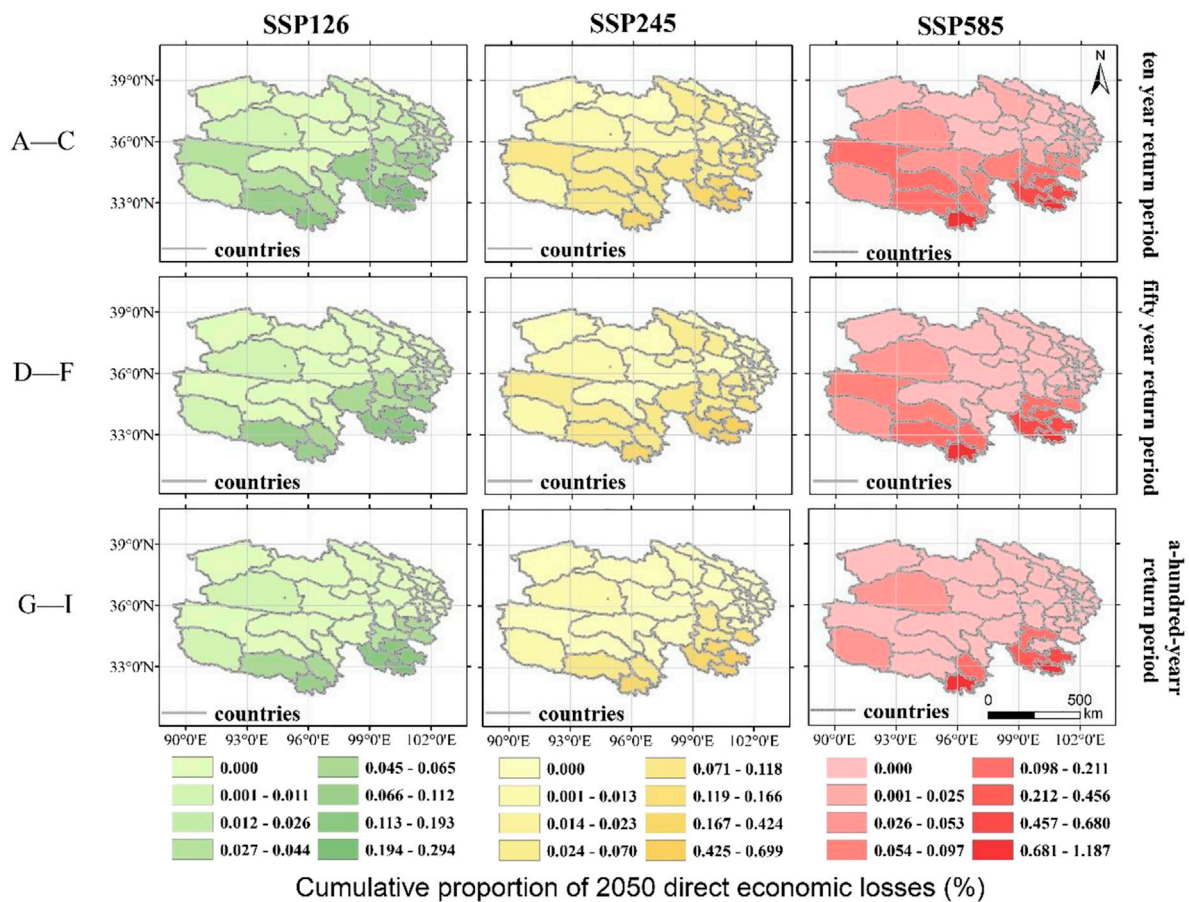


FIGURE 7 | Spatial distribution of the cumulative loss ratio of extreme rainstorms and flood disasters in Qinghai province in 2050. (A–C) countries' cumulative flood loss ratios of the 10-year return period under three scenarios; (D–F) countries' cumulative flood loss ratios of the 50-year return period under three scenarios; and (G–I) countries' cumulative flood loss ratios of 100-year return period under three scenarios.

respectively, under the low-, medium- and high-emission scenarios, accounting for 48.5%, 72.0%, and 79.0% of the province, respectively. In 2060, the counties of Banma, Jiuzhi, Dari, Gande, and Nangqian still suffer higher loss ratios, but the sum of their loss ratios is 2.40%, 2.82%, and 3.10%, respectively, under the low-, medium-, and high-emission scenarios, accounting for 36.9%, 42.4%, 42.9% of the province, respectively.

Under the three scenarios of SSP126, SSP245, and SSP585, the loss ratios of each county in Qinghai province will reach the peak in 2050 and drop to a trough in 2060, which is consistent with the results. Before China achieves a carbon peak in 2030, fossil fuels will stay as its main energy. So, carbon dioxide emissions may reach a peak, which may increase the frequency and intensity of flood disasters to some extent, leading to the reduction of the disaster loss ratio later than carbon peaking. China plans to achieve carbon neutrality by 2060, and the reduction of the disaster loss ratio caused by social and economic transformation will be earlier than achieving that goal and reaching its lowest point in 2060. With the growth of carbon emissions, more regions will suffer high losses in the province, causing more extreme and concentrated flood disasters.

2) The distribution of extreme flood loss ratios in Qinghai province in 2050

In 2050, by adding and counting the loss ratios of the extreme flood of different return periods for each county in Qinghai province, the spatial loss distribution characteristics of extreme floods with different intensities in specific years in Qinghai province are shown in Figure 7.

Under the same scenario, 10-, 50-, and 100-year return period flood disasters all have the greatest losses in the counties of Banma, Jiuzhi, Gande, Dari, and Nangqian. The spatial impact of the extreme flood is similar to the distribution of the high and low values of flood loss ratios in typical years in Qinghai. With the growing rate of emissions, the area affected by the extreme flood (especially the 10-year return period flood) decreases, but the cumulative loss ratio of the key disaster areas affected by the extreme flood will rise. Therefore, the higher the emission scenario is, the stronger the extreme of flood will be, and the disaster-prone areas such as Banma, Jiuzhi, Gande, Dari, and Nangqian counties will suffer higher risks.

Among the 44 counties in Qinghai province, the three counties with the highest frequencies (1–2 times) of 100-year return period flood in 2050 are Banma county, Jiuzhi county, and Yushu City. The losses caused by floods to these three areas account for 0.042%–1.187% of their GDP, respectively. The ranges of their total loss ratio are from 0.26% to 1.187%, 0.176%–0.625%, and 0.048%–0.185%, respectively. In addition, the spatial distribution of cumulative loss ratios of flood in 2050 also has significant unevenness in Qinghai province, and the counties with higher cumulative loss ratios are mainly concentrated in the southern part such as Banma county, Gande county, Dari county, Jiuzhi county, and Yushu City.

4 DISCUSSION AND CONCLUSION

4.1 Discussion

- 1) In the past, due to the improvement of China's disaster statistics system (mostly after the Wenchuan earthquake in 2008) (Guo et al., 2016) and the strength of the actual disaster statistics department in Qinghai province, data before 2009 are difficult to obtain. However, in this article, there are still 1,512 disaster data from 2009 to 2019 and more than 100,000 daily precipitation data. In addition, climate change and economic development in Qinghai province start to increase during the period 2009–2019. Therefore, the historical disaster data from 2009 to 2019 can represent the future trend to a certain extent.
- 2) This study only analyzed the difference of future precipitation change dominated by the single precipitation factor, without integrating temperature and precipitation calculation to synthesize the loss rate. This may result in insufficient consideration of flood disasters caused by temperature changes in the plateau region. However, some studies (Ping et al., 2014; Ji et al., 2015) on the risk of flood disaster in plateau areas also show that the flood disaster is more related to extreme precipitation. In addition, the influence of pressure and temperature on precipitation is taken into account in future precipitation dates in the CMIP6 climate model. Still, a comprehensive temperature and precipitation assessment of floods in Qinghai province will be the focus of future research.
- 3) The future meteorological data used in this study are from the CMIP6 global climate model (GCM). Although this model is the most authoritative future climate prediction data at present, its simulation accuracy is still limited for county-level areas (Kim et al., 2020) and also for high-altitude areas (Zhu et al., 2020; Zhu and Yang, 2020; Lun et al., 2021), which may bring some uncertainties to the results. For example, there may be errors in the accuracy of the simulation effect for the relatively developed areas in the northeast of Qinghai province, such as Xining, the capital city of Qinghai province. If smaller scale meteorology model data are available, historical model data can be corrected from historical site data to obtain more accurate future model data. The ideal data may take a regional climate model (RCM) to simulate the precipitation for Qinghai province in the future, but the RCM

parameter setting needs field experiment and experience estimation (Weigel et al., 2021), and this could also bring the subjective experience of error and uncertainty. In order to reduce the uncertainty, this study uses 22 models of collection and data processing methods.

- 4) This study demonstrates the contribution of emission reduction through the assessment of regional flood disaster risk. But the direct correlation between the risk reduction of flood disasters and the intensity of emission reduction is not shown. Although many studies have shown that floods are closely related to extreme precipitation and the positive relationship between regional extreme precipitation and climate change, the assessment of future flood risk changes in the region can reflect the effectiveness of emission reduction only to a certain extent. Therefore, the quantitative calculation of the relationship between disaster risk and emission reduction in the direction of future research and the further demand of government disaster reduction departments.

4.2 CONCLUSION

Based on the disaster data of more than 1,000 flood disasters from 2009 to 2019, observed precipitation data, and future precipitation and GDP data, this study constructed the loss rate curve of cumulative precipitation and disaster loss, evaluated the quantitative risk of flood disasters at the district- and county-scale in Qinghai province from 2020 to 2060, and compared the temporal and spatial distribution characteristics of loss rate differences under different scenarios and return periods. The main conclusions are as follows:

- 1) The flood disaster loss ratios of Qinghai province in 2020–2060 present a trend of “rising in the early stage, stable in the middle stage, and declining in the late stage,” under low- (SSP126) and medium- (SSP245) emission scenarios, and presenting a trend of rising fluctuation under the high-emission (SSP585) scenario, respectively, are (0.075%, 0.499%), (0.121%, 0.522%), and (0.125%, 0.806%). The results show that the future flood disaster risk of Qinghai province under the high-emission SSP585 scenario is significantly higher than that under the low-emission SSP126 scenario, and the maximum risk difference may reach up to 10 times.
- 2) Compared with the high-emission SSP585 scenario, the cumulative loss of Qinghai province in 2020–2060 under the emission reduction target scenario SSP126 will be reduced by 8.1203%. Based on Qinghai's 2019 GDP of 294 billion CNY, the emission reduction target will avoid a potential economic loss of nearly 24 billion CNY in the future and an average of 582 million CNY per year, which is equivalent to 93% of Qinghai's 2019 provincial special fund for ecological and environmental protection of 626 million CNY. In addition, the frequency of extreme flood disasters over a 100-year return period, 50-year return period, and 10-year return period may also be reduced by 37 times, 94 times, and 167 times, respectively, avoiding in total 223 casualties.

- 3) Without considering the impact of climate model accuracy and resolution on the assessment accuracy of northeastern Qinghai province, the high-value areas of the flood disaster loss ratio caused by 44 counties in Qinghai province in the future are mainly located in Banma county, Gande county, Dari county, Jiuzhi county, and Nangqian county in southeastern Qinghai province. Under SSP585, Jiuzhi county, Banma county, and Nangqian county may suffer the most severe losses from the flood disaster.

This study quantitatively reveals the spatial and temporal variation characteristics of flood risk and makes an application contribution to the improvement of flood risk assessment from “relative” risk degree to “absolute” risk degree in high-altitude regions. Therefore, this study provides data and method support for flood risk prevention and management in China’s high-altitude regions. More importantly, from the perspective of casualties and economic losses caused by flood disasters, this study evaluates the potential “positive impact” brought by multiple costs of emission reduction, providing theoretical and practical evidence for promoting the enthusiasm for emission reduction in China and even worldwide.

DATA AVAILABILITY STATEMENT

The raw data supporting the conclusion of this article will be made available by the authors, without undue reservation.

REFERENCES

- Chen, J., Liu, L., Pei, J., and Deng, M. (2021). An Ensemble Risk Assessment Model for Urban Rainstorm Disasters Based on Random Forest and Deep Belief Nets: a Case Study of Nanjing, China. *Nat. Hazards* 107, 2671–2692. doi:10.1007/s11069-021-04630-y
- Delalay, M., Ziegler, A. D., Shrestha, M. S., and Gopal, V. (2020). Methodology for Future Flood Assessment in Terms of Economic Damage: Development and Application for a Case Study in Nepal. *J. Flood Risk Manag.* 13, e12623. doi:10.1111/jfr3.12623
- Dou, R., and Yan, J. (2013). Spatial-temporal Variations of Drought and Flood Intensities in East of Qinghai Province during Last 52 Years. *J. Nat. Disasters* 22, e12365. doi:10.1371/journal.pone.0148072
- Duan, A., Xiao, Z., and Wu, G. (2016). Characteristics of Climate Change over the Tibetan Plateau under the Global Warming during 1979–2014. *Clim. Change Res.* 12, 374–381. doi:10.12006/j.issn.1673-1719.2016.039
- Guo, G., Liu, L., Li, Y., Gao, J., Lin, S., and Wu, S. (2021). A Vulnerability Curve Method to Assess Risks of Climate-Related Hazards at County Level. *Atmosphere* 12, 1022. doi:10.3390/atmos12081022
- Guo, X., Cui, P., Li, Y., Ma, L., Ge, Y., and Mahoney, W. B. (2016). Intensity-duration Threshold of Rainfall-Triggered Debris Flows in the Wenchuan Earthquake Affected Area, China. *Geomorphology* 253, 208–216. doi:10.1016/j.geomorph.2015.10.009
- Ji, Y., Zhou, G., Wang, S., and Wang, L. (2015). Increase in Flood and Drought Disasters during 1500–2000 in Southwest China. *Nat. Hazards* 77, 1853–1861. doi:10.1007/s11069-015-1679-9
- Jinhu, Y., Zhihong, J., Qiguo, Y., Xuying, S., and Yubi, Y. (2007). Analysis on Extreme Precipitation Event over the Northwest China in Flood Season. *J. Desert Res.* 27, 320–325.
- Kalyanapu, A. J., Judi, D. R., McPherson, T. N., and Burian, S. J. (2012). Monte Carlo-Based Flood Modelling Framework for Estimating Probability Weighted

AUTHOR CONTRIBUTIONS

BW computed data, made diagrams, and wrote the manuscript; ZZ directed the thesis idea and revised the full manuscript; XG helped in data processing and diagrams; CT provided data for the study area; CH provided methods for processing data and writing; JT provided suggestions for revision of the manuscript.

FUNDING

This research was funded by the Second Tibetan Plateau Scientific Expedition and Research Program (No.2019QZKK0606), the National Natural Science Foundation of China (No. 41907395; No. 42171074), the China Postdoctoral Science Foundation (2021M690425), and the Fundamental Research Funds for the Central Universities (No. 2021NTST28). The authors declare that they have no known competing financial interests or personal relationships that could have appeared to influence the work reported in this article.

SUPPLEMENTARY MATERIAL

The Supplementary Material for this article can be found online at: <https://www.frontiersin.org/articles/10.3389/feart.2022.931505/full#supplementary-material>

- Flood Risk. *J. Flood Risk Manage* 5, 37–48. doi:10.1111/j.1753-318X.2011.01123.x
- Kim, Y.-H., Min, S.-K., Zhang, X., Sillmann, J., and Sandstad, M. (2020). Evaluation of the CMIP6 Multi-Model Ensemble for Climate Extreme Indices. *Weather Clim. Extrem.* 29, 100269. doi:10.1016/j.wace.2020.100269
- Koc, K., and Işık, Z. (2021). Assessment of Urban Flood Risk Factors Using Monte Carlo Analytical Hierarchy Process. *Nat. Hazards Rev.* 22, 516. doi:10.1061/(asce)nh.1527-6996.0000516
- Li, N., Wang, Y., and Zhang, Z. (2016). Transformation of Natural Disaster Risk Assessment Method Based on Number and Content of Scientific Papers. *J. Catastrophology* 31, 8–14. doi:10.3969/j.issn.1000-811X.2016.03.002
- Lin, Q., Wang, Y., Glade, T., Zhang, J., and Zhang, Y. (2020). Assessing the Spatiotemporal Impact of Climate Change on Event Rainfall Characteristics Influencing Landslide Occurrences Based on Multiple GCM Projections in China. *Clim. Change* 162, 761–779. doi:10.1007/s10584-020-02750-1
- Liu, Y., Qiu, H., Yang, D., Liu, Z., Ma, S., Pei, Y., et al. (2022). Deformation Responses of Landslides to Seasonal Rainfall Based on InSAR and Wavelet Analysis. *Landslides* 19, 199–210. doi:10.1007/s10346-021-01785-4
- Lun, Y., Liu, L., Cheng, L., Li, X., Li, H., and Xu, Z. (2021). Assessment of GCMs Simulation Performance for Precipitation and Temperature from CMIP5 to CMIP6 over the Tibetan Plateau. *Int. J. Climatol.* 41, 3994–4018. doi:10.1002/joc.7055
- Lv, Y., Liu, S., and Zhong, G. (2021). Flood Risk Assessment in Small Watershed Based on Catastrophe Theory. *IOP Conf. Ser. Earth Environ. Sci.* 691, 012016. doi:10.1088/1755-1315/691/1/012016
- Ma, S., Qiu, H., Hu, S., Yang, D., and Liu, Z. (2021). Characteristics and Geomorphology Change Detection Analysis of the Jiangdingya Landslide on July 12, 2018, China. *Landslides* 18, 383–396. doi:10.1007/s10346-020-01530-3
- Meihua, Z., Yun, S., and Jingnai, Z. (2008). Trust in Local Disaster Reduction Ability and its Influences on Public Flood Risk Perception: Based on the

- Investigation and Analysis. *J. Catastrophol.* 23(4), 70–75. doi:10.3969/j.issn.1000-811X.2008.04.015
- O'Neill, B. C., Tebaldi, C., van Vuuren, D. P., Eyring, V., Friedlingstein, P., Hurtt, G., et al. (2016). The Scenario Model Intercomparison Project (ScenarioMIP) for CMIP6. *Geosci. Model. Dev.* 9, 3461–3482. doi:10.5194/gmd-9-3461-2016
- Peng, Y., Chen, K., Yan, H., and Yu, X. (2017). Improving Flood-Risk Analysis for Confluence Flooding Control Downstream Using Copula Monte Carlo Method. *J. Hydrologic Eng.* 22, 04017018. doi:10.1061/(asce)he.1943-5584.0001526
- Ping, H., Jinxiao, L., Guoqin, X., and Hongbo, L. (2014). Analysis of Precipitation Distribution and Drought and Flood Disasters in Chuxiong City on the Yunnan Plateau. *Earth Environ.* 42, 162–167. doi:10.14050/j.cnki.1672-9250.2014.02.005
- Ridder, N. N., Ukkola, A. M., Pitman, A. J., and Perkins-Kirkpatrick, S. E. (2022). Increased Occurrence of High Impact Compound Events Under Climate Change. *npj Clim. Atmos. Sci.* 5, 3. doi:10.1038/s41612-021-00224-4
- Su, X., Shao, W., Liu, J., Jiang, Y., and Wang, K. (2021). Dynamic Assessment of the Impact of Flood Disaster on Economy and Population under Extreme Rainstorm Events. *Remote Sens.* 13, 3924. doi:10.3390/rs13193924
- Wang, Z., Wang, H., Huang, J., Kang, J., and Han, D. (2018). Analysis of the Public Flood Risk Perception in a Flood-Prone City: The Case of Jingdezhen City in China. *Water* 10, 1577. doi:10.3390/w10111577
- Weidong, M., Fenggui, L., Qiang, Z., Qiong, C., Cungui, Z., Fei, L., et al. (2021). Estimation of Critical Rainfall for Flood Disasters in the Qinghai-Tibet Plateau. *J. Resour. Ecol.* 12, 600–608. doi:10.5814/j.issn.1674-764x.2021.05.003
- Weigel, K., Bock, L., Gier, B. K., Lauer, A., Righi, M., Schlund, M., et al. (2021). Earth System Model Evaluation Tool (ESMValTool) v2.0 - Diagnostics for Extreme Events, Regional and Impact Evaluation, and Analysis of Earth System Models in CMIP. *Geosci. Model. Dev.* 14, 3159–3184. doi:10.5194/gmd-14-3159-2021
- Wu, F., and You, Q. (2019). Temperature Change on the Tibetan Plateau under the Global Warming of 1.5°C and 2°C. *Clim. Change Res.* 12, 130–139. doi:10.12006/j.issn.1673-1719.2018.175
- Yang, D., Qiu, H., Ma, S., Liu, Z., Du, C., Zhu, Y., et al. (2022). Slow Surface Subsidence and its Impact on Shallow Loess Landslides in a Coal Mining Area. *Catena* 209, 105830. doi:10.1016/j.catena.2021.105830
- Zeleňáková, M. (2009). Preliminary Flood Risk Assessment in the Hornád Watershed. *WIT Trans. Ecol. Environ.* 124, 15–24. doi:10.2495/RM090021
- Zhou, W., Qiu, H., Wang, L., Pei, Y., Tang, B., Ma, S., et al. (2022). Combining Rainfall-Induced Shallow Landslides and Subsequent Debris Flows for Hazard Chain Prediction. *Catena* 213, 106199. doi:10.1016/j.catena.2022.106199
- Zhu, H., Jiang, Z., Li, J., Li, W., Sun, C., and Li, L. (2020). Does CMIP6 Inspire More Confidence in Simulating Climate Extremes over China? *Adv. Atmos. Sci.* 37, 1119–1132. doi:10.1007/s00376-020-9289-1
- Zhu, Y.-Y., and Yang, S. (2020). Evaluation of CMIP6 for Historical Temperature and Precipitation over the Tibetan Plateau and its Comparison with CMIP5. *Adv. Clim. Change Res.* 11, 239–251. doi:10.1016/j.accre.2020.08.001
- Zou, X., Liu, F., Zhang, Y., Chen, Q., Zhang, H., and Zhao, Z. (2013). County Scale-Based Risk Analysis of Flood Hazard in Qinghai-Tibet Plateau. *J. Nat. Disasters* 22, 181–188. doi:10.13577/j.jnd.2013.0524

Conflict of Interest: The authors declare that the research was conducted in the absence of any commercial or financial relationships that could be construed as a potential conflict of interest.

Publisher's Note: All claims expressed in this article are solely those of the authors and do not necessarily represent those of their affiliated organizations, or those of the publisher, the editors, and the reviewers. Any product that may be evaluated in this article, or claim that may be made by its manufacturer, is not guaranteed or endorsed by the publisher.

Copyright © 2022 Wu, Zhang, Guo, Tan, Huang and Tao. This is an open-access article distributed under the terms of the Creative Commons Attribution License (CC BY). The use, distribution or reproduction in other forums is permitted, provided the original author(s) and the copyright owner(s) are credited and that the original publication in this journal is cited, in accordance with accepted academic practice. No use, distribution or reproduction is permitted which does not comply with these terms.



Impacts of Risk Perception, Disaster Knowledge, and Emotional Attachment on Tourists' Behavioral Intentions in Qinling Mountain, China

Junqing Hao^{1,2,3*}, Han Tang¹, Jiawei Hao¹, Yanting Ma¹ and Xinxiang Jiang¹

¹Modern Enterprise Management Research Center, Xi'an University of Finance and Economics, Xi'an, China, ²School of Public Policy and Administration, Xi'an Jiaotong University, Xi'an, China, ³Key Laboratory of Degradation and Unused Land Reclamation Project, Ministry of Natural Resources, Xi'an, China

OPEN ACCESS

Edited by:

Haijun Qiu,
Northwest University, China

Reviewed by:

Fasuo Zhao,
Chang'an University, China
Xiaojun Yao,
Northwest Normal University, China

*Correspondence:

Junqing Hao
junqinghao@xaupe.edu.cn
54358526@qq.com

Specialty section:

This article was submitted to
Geohazards and Georisks,
a section of the journal
Frontiers in Earth Science

Received: 22 February 2022

Accepted: 12 May 2022

Published: 01 July 2022

Citation:

Hao J, Tang H, Hao J, Ma Y and
Jiang X (2022) Impacts of Risk
Perception, Disaster Knowledge, and
Emotional Attachment on Tourists'
Behavioral Intentions in Qinling
Mountain, China.
Front. Earth Sci. 10:880912.
doi: 10.3389/feart.2022.880912

With natural disasters occurring more frequently around the world, their impact on tourism is becoming a serious problem. The existing literature in the field of tourism disaster management focuses mostly on disaster impact analysis, risk assessment, and post-disaster recovery, while the impact of disaster on tourism and tourists is still a new topic. It is necessary to investigate the correlation between the natural disasters and the tourists' behavior. Taking the famous tourism destination, Qinling Mountain, located in the middle of China, as an example where frequent mountain disasters happened, we investigated 542 youth group tourists using a questionnaire survey and analyzed the influence of risk perception, disaster knowledge, and emotional attachment on tourists' travel behavioral intentions. The results showed that 1) risk perception has a negative effect on tourists' behavioral intentions; 2) disaster knowledge and tourism emotional attachment have a positive effect on tourists' behavioral intention; and 3) the moderation role of gender is not significant, while the moderation role of education level is significant. Therefore, this analysis is of great importance for research dealing with the theory of tourism disaster and the management practice of disaster-prone tourism destinations.

Keywords: risk perception, disaster tourism, emotional attachment, behavioral intention (BI), tourist

1 INTRODUCTION

Tourism, as a key leisure activity for public, is heavily dependent on natural environment. However, tourism destinations are threatened by natural disasters (Murphy and Bayley, 1989). The frequent occurrence of global natural disasters has affected safety and travel behaviors of tourists. For instance, Mount St. Helens in the United States erupted in 1980 and killed 57 people. In 2004, the tsunami and earthquake in Indonesia killed 292,000 people. In 2008, the Wenchuan earthquake in China caused damage to at least 111 A-level scenic spots; 456 natural ecological landscapes were destroyed, and many tourists were trapped. All these natural disasters pushed global researchers to focus on them.

However, tourists' pursuit of exciting and beautiful scenery even with a high risk of natural disasters continues to promote areas, becoming hot popular tourism destinations (Murphy and Bayley, 1989). Aso Volcano, located in the northeastern area of Kumamoto-ken, is one of the largest active volcanos in Japan whose latest volcanic eruption occurred in October 20, 2021. Meanwhile, Aso Volcano is also a global geopark and world-famous hot spring resort, where millions of tourists come for leisure. In 2017, a major debris flow disaster occurred at Jiuzhaigou which is a World

Natural Heritage Site in China, and as a consequence, the number of tourists dropped by 32.6% compared with the previous year. But the number of tourists increased rapidly when Jiuzhaigou reopened in October 2021.

Driven by the frequent occurrence of natural disasters and the development of tourism, studies dealing with both tourist behavior and disaster risk management are increasingly conducted by the scientific community (Arain, 2015). Tourists are not only the bearers of disasters, but also the practitioners of disaster risk management in tourism destination (Zhou et al., 2012). When facing disasters, every tourist will have irrational attitudes, such as panic, anger, and even disappointment, which will affect his/her effective response to natural disasters and preservation of his/her own safety (Hao and Dong, 2021). The analysis of the risk perception and attitude of tourists in the context of natural disasters and its impact on travel behavioral intentions is the main focus of tourism destination disaster management practice and tourism behavior theory research.

Most of the literature is focused on the fields of tourism disaster risk emergency response, tourism disaster risk assessment, disaster impact, and post-disaster recovery. For instance, a database management subsystem and disaster relief management subsystem have been established to construct a tourism emergency management and rescue system in case of occurrence of sudden natural disasters (Zhao, 2020). Based on the principle of safety, the ecological security of forest tourism scenic spots was evaluated after freezing natural disasters (Feng, 2020), and the impact of geological disasters on the perceived image of tourist destinations was analyzed (Mao and Zhang, 2013). In some countries where tourism being the important economic industry, a nonlinear relationship between tourism and economic growth was found after the Wenchuan earthquake in China (Kim and Marcouiller, 2015). Under the dual influence of natural disasters and internal conflicts, the vulnerability and resilience of domestic and international tourists in India are significantly different (Okuyama, 2018; Yang et al., 2022). Based on the data of in-depth interviews and semi-structured questionnaires in two types of communities in YuanYang County, Yunnan Province in China, Sun et al. (2015) analyzed the perception of disaster risk in tourism communities. The perceptions of local residents after the Wenchuan earthquake in China and residents of the Italian city L'Aquila community on disaster tourism destinations were explored. The study concluded that perceptions are both mixed and contradictory (Wright and Sharpley, 2018; Wang, 2019). A review of the literature suggests that there are still only few research studies that have been conducted on the impact of disasters on tourist behavior.

Therefore, the objectives of this study are to explore 1) the impact of tourists' emotional attachment, disaster knowledge, and disaster risk perception on tourists' behavioral intentions; and 2) the moderating effect of tourists' gender and education level on the relationship between disaster risk perception, disaster knowledge, emotional attachment, and tourists' behavioral intentions. Thus, the current study may have important implications for researchers and practitioners in understanding tourists' travel intentions and disaster risk perception and in

developing suitable plans for tourism management in disaster-prone destinations.

2 LITERATURE REVIEW AND THEORETICAL FRAMEWORK

2.1 Risk Perception

Existing studies hold that risk can be considered as a measure of uncertain results. Disaster risk refers to the level of potential impact and its potential occurrence probability in the future. Risk perception, which was first discussed by Bauer (1960) in the consumer behavior field, is defined as the expectation of loss caused by uncertainty about the outcome that is likely to occur given the consumer's choice (Ahyoung, 2021). A representative study was Slovic Paul's theory of "personality profile" in 1987 which measured risk perception using the psychometric paradigm of risk perception (Slovic, 1987). Many studies have also measured risk perception from multiple dimensions, such as functional, physical, economic, social, and psychological risks, rather than a single component (Hong, 2015; Ahyoung, 2021). In the context of disaster tourism issues, such as natural disasters and landslides, risk perception is a comprehensive embodiment of disaster risk, exposure, vulnerability, and disaster prevention and reduction ability (Pan et al., 2016). Risk perception refers to people's feelings and understanding of risks taken in the surrounding world, including personal experience based on intuitive judgment and subjective feelings (Meng et al., 2010). It is also people's beliefs, attitudes, judgments, and emotions about hazards and its potential benefits, as well as cultural and social tendencies in the broader sense (Wu and Zhang, 2012).

In previous studies, risk perception has been widely taken as a key variable that affects people's travel intentions or as barriers to leisure travel. Pahl et al. (2005) explored that if a person thinks that he is at risk and feels vulnerable because of natural disasters, he is more likely to take pro-environmental action. Thus, risk perception is positively related to tourists' behavioral intention.

2.2 Disaster Knowledge

Knowledge is "a fact or condition of knowing something with a considerable degree of familiarity through experience, association, and contact" (Zhou et al., 2022). Hoffmann and Muttarak (2017) revealed that those who had been influenced by disaster in the past 3 years show nearly three times more preparedness behavior. Meanwhile, other literature studies demonstrated that disaster could improve people's experiences, especially for those who perceived the severity of the hazard (Wiwik, 2020). According to these studies, tourists' disaster knowledge refers to tourists' information about natural disasters that happened in tourism attractions.

Some studies found insignificant correlations between disaster knowledge and people's experiences (Sim et al., 2018). A person who can obtain disaster knowledge through different channels will show an overall lower impact on his/her risk perception. A person who has experienced natural disasters has a significant impact on his/her risk perception. Persons with past flood experience and flood knowledge education are quite sensible

to flood risk perception (Okaka and Odhiambo, 2019). The fear of experiencing an earthquake positively and indirectly affects the risk perception of earthquake survivors (Bronfman et al., 2020). Chinese residents' perception level of flood disaster risk is relatively low (Zhou and Liu, 2019), while residents' perception level of geological disaster risk in the mining area is relatively high (Feng and Ning, 2020). Li et al. (2011) found that disaster knowledge, as the most critical variable, has a significant impact on people's psychological and behavioral processes when sudden disasters such as earthquakes occur. Gao (2019) believed that the perceived use of new media and tourism information will affect the tourism behavior of youth groups. Therefore, there is a positive correlation in the relationship between disaster knowledge and tourists' intentions because of the disaster experience.

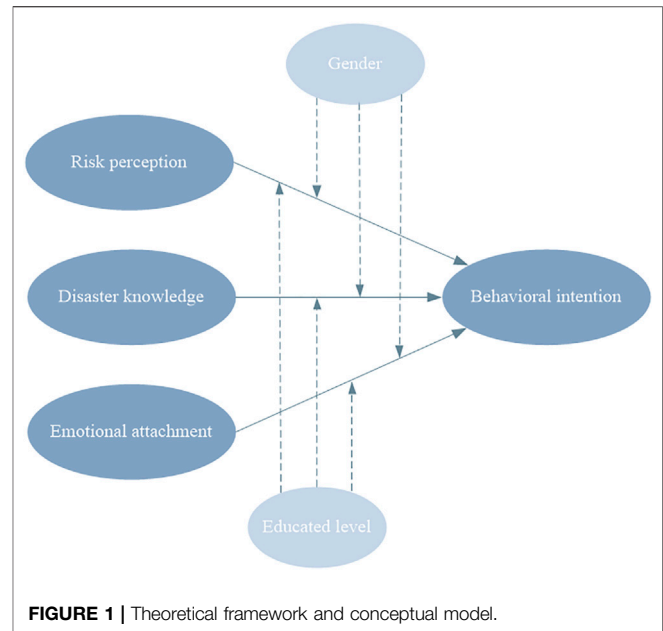
2.3 Emotional Attachment

Drawing upon the theory of attachment, place attachment refers to a person's complex emotional and affective response to a place or location, value, and attribution (Liu et al., 2021; Morais and Lin, 2010). It has been applied to investigate tourists' emotional, functional, affective, and social attachment to tourism destinations (Bowlby, 1969; Hidalgo and Hernandez, 2001; Kyle et al., 2004; Xu and Zhang, 2015). Place attachment has been conceptualized as a complex construct with multiple dimensions (Woosnam, et al., 2018). Researchers have proposed two (Hwang, 2005), three (Yuksel et al., 2010), and even four dimensions (Ramkinssoon et al., 2012) for place attachment.

Tourists' emotional attachment significantly affects their risk perception and travel behavioral attitude. A person's dependence on the place of disaster positively affects the perception of disaster risk. Participants from flood prone areas believe that the perception of flood risk is higher (Ullah et al., 2020). Most participants with a higher socio-economic status have higher risk perception of tsunami due to their residence being near the coastline (Gotham et al., 2018). By measuring risk perception, Shen et al. (2020) revealed that the presence of children or older people in the respondent's family induces a higher risk perception. There are significant differences in risk perception within the non-expert population and between the expert and non-expert populations (Pelling, 2011). Leiter (2011) found that risk and specific characteristics of individuals are important determinants of participants' perception of risk. Kim et al. (2016) found that an experience from past destinations only plays a regulatory role in the relationship between age and tourism risk perception (Jang et al., 2020). Therefore, there is a significant effect on emotional attachment for tourist behavioral intentions.

2.4 The Moderation of Gender and Education Level

Some studies found that women who had experienced geological disasters have higher risk perception of geological disasters and pay more attention to disaster knowledge (Yang et al., 2018).



Women with high levels of risk perception tend to have negative attitudes toward disaster reduction (Yang et al., 2018). Other studies revealed that educated youth have significant intention to travel to places where they have been in their youth time for work, and the yacht tourists' behavior and attitude have a significant positive impact on their travel behavioral intention (Liu and Jia, 2018; Gou et al., 2020). Young people are usually the main demographic of tourists in mountain tourism destinations. Hu et al. (2014) analyzed the characteristics of mountain tourism recreation behavior in Wugong Mountain in China and found that there are mainly young students and tourists who are satisfied and willing to revisit the mountain tourism area. Zheng et al. (2016) also found that vacationers in the Nankun Mountain in Guangdong Province of China are mostly young and middle-aged tourists. Varasteh et al. (2015) studied the travel behavior of international students studying in Malaysia and found that most international students tend to travel during semester holidays for the purpose of entertainment and exploring new places. Youth group tourists pay attention to the tourism safety measures applied in mountain areas, but they have low safety awareness and lack of knowledge on mountain tourism safety (Cen and Huang, 2011).

Thus, different groups, such as male and female, and high education level and low education level, had different impacts on the relationship between tourists' risk perception, disaster knowledge, emotional attachment, and their travel behaviors (Gao et al., 2017).

2.5 Tourists' Behavioral Intention

Tourists' behavioral intention is defined as "subjective judgments about how we will behave in the future" (Ahyoung, 2021). In regard to disaster tourism matters, tourists' behavioral intention can be described as the extent to which groups will take actions to

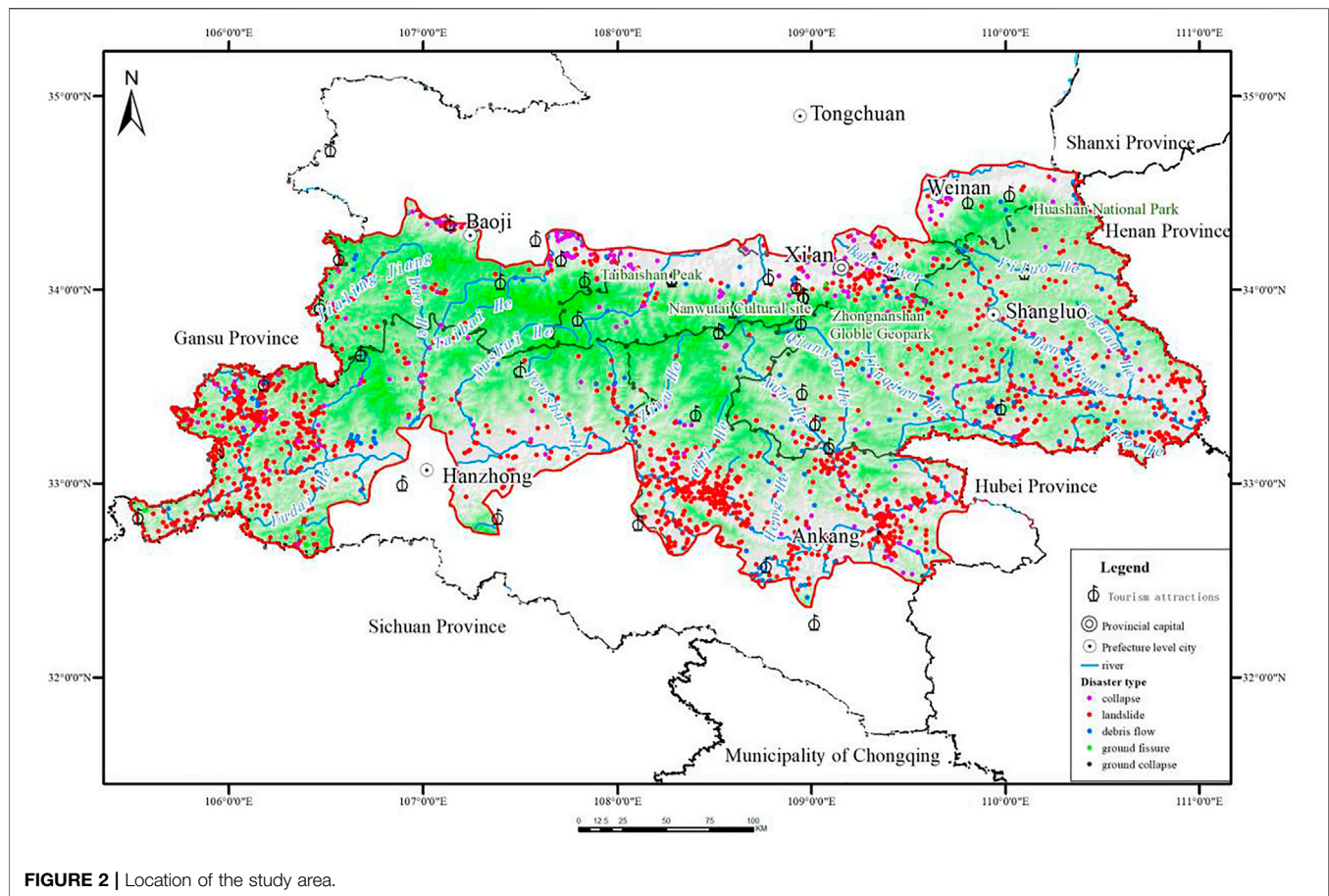


FIGURE 2 | Location of the study area.

continue their travel in various ways, such as overcoming all kinds of disaster impacts to visit tourist attractions in the future (Ramdas and Mohamed, 2014).

Based on the above literature review, we consider tourists' emotional attachment, disaster knowledge, and disaster risk perception as the main driving factors, and analyze the impacts on tourists' behavioral intentions in this study. Therefore, the following research framework and conceptual model of this study are developed (Figure 1).

3 METHODOLOGY

3.1 Study Area

The Qinling Mountain Range ($32^{\circ}28'53''$ – $34^{\circ}32'23''$ N, $105^{\circ}29'18''$ – $111^{\circ}01'54''$ E) in the hinterland of Shaanxi Province in China stretches from the Jialingjiang River in the west to the Bahe River in the east. This range is connected with the Sichuan Basin in the south and the Loess Plateau in the north, spanning six cities of Shaanxi Province—Xi'an, Baoji, Weinan, Hanzhong, Ankang, and Shangluo (Figure 2).

The Qinling Mountain and Huaihe River are the watersheds between northern and southern China. The Qinling Mountain Range is about 1,600 km long from east to west and 300 km wide on average from north to south.

The average elevation is about 1,500 m with the highest peak, Taibaishan Peak (3,771.2 m above sea level), located in Baoji City. Situated between the subtropical zone and the temperate zone with a mountainous continental climate, the Qinling Mountain has an obvious vertical zonality. The annual precipitation can reach 1,000–1,300 mm, creating climatic conditions very conducive to the formation and development of landslide and debris flow in Qinling Mountain.

Known as the “Central National Park of China,” rich natural resources and historical culture in Qinling Mountain feed numerous tourism attractions, such as the Huashan National Park, Zhongnanshan Global Geopark, and Nanwutai Cultural site, and their exotically beautiful landscapes attract tourist attention worldwide.

In fact, quite a few tourist attractions in Qinling Mountain frequently suffer heavy geological hazards (Ma et al., 2021). According to the investigation results of Shaanxi Geological Survey Department, landslide and debris flow that existed in the Qinling Mountain caused an average of 55 people missing or dead each year with a direct economic loss of 57 million RMB.

3.2 Questionnaire Development

To measure the constructs proposed in the conceptual model, a questionnaire was first developed based on previous studies and then tested on 30 college students. The final questionnaire was

TABLE 1 | Latent variables and measurement items used in the conceptual model.

Latent variable	Measurement item	Source
Risk perception	-Natural disasters in Qinling Mountains are severe -Natural disasters in Qinling Mountains are frequent -Natural disasters in Qinling Mountains occur with great intensity -Natural disasters in Qinling Mountains are horrible -Natural disasters in Qinling Mountains are worrying -Natural disasters in Qinling Mountains are anxious	Fuchs and Reichel (2006)
Disaster knowledge	-Tourist attractions of Qinling Mountains are in good order -Tourist attractions of Qinling Mountains are well-known -Tourist attractions of Qinling Mountains are well serviced -The emergency measures of tourist attractions are in place -The disaster information of tourist attractions is issued immediately -The disaster information of tourist attractions is accurate	Sun et al. (2015)
Emotional attachment	-The scenery of Qinling Mountains is unique -The scenery of Qinling Mountains is sacred -The history of Qinling Mountains is ancient -Travelling in Qinling Mountains is unforgettable -Travelling in Qinling Mountains is missing -Travelling in Qinling Mountains is excited	Tang et al. (2007)
Behavioral intention	-Once the natural disaster is over, I will still travel to Qinling Mountains -Once the natural disaster is over, I think it's still a good idea to travel to Qinling Mountains -Once the natural disaster is over, I am very happy to travel to Qinling Mountains -No matter what disaster happens, I will still travel to Qinling Mountains -No matter what disaster happens, I think it's still a good idea to travel to Qinling Mountains -No matter what disaster happens, I am very happy to travel to Qinling Mountains	Li et al. (2020)

composed of 24 measurement items, which are described in **Table 1**. A 5-point Likert-type scale was used to measure each statement of risk perception, disaster knowledge, emotional attachment, and behavioral intentions (from 1 = strongly disagree to 5 = strongly agree).

- 1) The measurement of disaster risk perception is based on the research items published in Fuchs and Reichel's (2006) tourism disaster risk perception, including six items in terms of the risk of disaster-causing factors and the vulnerability of the carrier.
- 2) The measurement of disaster knowledge is based on the scale of Sun et al. (2015). It refers to acquisition channels, timeliness, and accuracy of natural disaster information in Qinling Mountains. There are three items in total.
- 3) The emotional attachment of tourists is measured with six items that are based on the scale of Tang et al. (2007). Among them, emotion refers to the unique, sacred, and ancient history of Qinling Mountains, and attachment corresponds to the nostalgic, unforgettable, and exciting tourism experience of Qinling Mountains.
- 4) The measurement of tourists' behavioral intentions refers to the tourists' behavioral intention items of Li et al. (2020), and analyzes the tourists' behavioral intentions and willingness of tourists when confronted with disasters. There are three items in total.

3.3 Data Collection and Analysis Tool

This analysis investigates the perception and influencing factors of tourism disaster risk in Qinling Mountains using youth group tourists. The data are obtained from a questionnaire survey. The first survey was conducted during winter season in Qinling

Mountain in January 2021, and the second survey was conducted before the summer season in May 2021 to collect a comprehensive dataset. Two surveys were conducted in the form of electronic questionnaires, and a total of 542 questionnaires were received. Then, a range between 15 and 44 was defined as the age of youth group tourists. After screening, 511 questionnaires were considered valid, with an effective rate of 94.3%. The survey results were imported into SPSS 25.0 software for sample descriptive statistical analysis, and the results are shown in **Table 2**.

In terms of gender distribution, males accounted for 42.1% and females accounted for 57.9%. Concerning education level, most of them have a good education level: 279 tourists have a master's degree or above, accounting for 54.6%; 219 tourists have a college or bachelor's degree, accounting for 42.9%; and 13 tourists have a diploma of high school, vocational school, or technical secondary school and junior middle school or below, accounting for 2.6%. From the perspective of personal monthly income, 172 tourists earned below 1,000 RMB, accounting for 33.7%, followed by 5,000–10,000 RMB, 1,001–3,000 RMB, 3,001–5,000 RMB, and more than 10,000 RMB, accounting for 22.1, 20, 14.1, and 10.25%, respectively. In terms of current residence, 248 tourists currently live in Xi'an city which is the capital city of Shaanxi Province, accounting for 48.5%, while 20.2% live in other areas of Shaanxi Province and 31.3% live in other provinces. The occupations of the survey participants are mainly students; enterprise managers; personnel of public institutions; and professional, cultural, educational, scientific, and technological personnel, accounting for 53.6, 11.4, 11.2, 9, and 6.5%, respectively. There are a few state agency personnel, workers, service personnel, soldiers, farmers, and retirees, accounting for less than 10% of the total participants. Based

TABLE 2 | Sample description.

Category			Number	Proportion (%)	Category			Number	Proportion (%)
Gender	Male		215	42.1	Current residence	Xi'an city	248	48.5%	
	Female		296	57.9		Other areas of Shaanxi Province	103	20.2%	
Age	15–24		277	54.2	Occupational	Other provinces	160	31.3%	
	25–44		234	45.8		State organizations	15	2.9%	
Education degree	Junior middle school and below		2	0.4		Personnel of public institutions	46	9.0%	
	High school/vocational school/technical secondary school		11	2.2		Enterprise manager	57	11.2%	
	College/undergraduate		219	42.9		Professional/cultural educational/scientific and technological personnel	33	6.5%	
	Master's degree and above		279	54.6	Service personnel	10	2.0%		
	Below 1,000 RMB		172	33.7	Student	274	53.6%		
Monthly income	1,001–3,000 RMB		102	20.0	Worker	12	2.3%		
	3,001–5,000 RMB		72	14.1	Soldier	2	0.4%		
	5,000–10,000 RMB		113	22.1	Farmer	3	0.6%		
	More than 10,000 RMB		52	10.2	Retiree	1	0.2%		
					Other	58	11.4%		

TABLE 3 | Reliability testing.

Factor	Cronbach's alpha	Extracted item
Tourists' emotional attachment	0.951	6
Disaster knowledge	0.940	3
Disaster risk perception	0.946	6
Travel behavioral intention	0.919	3
The whole reliability	0.936	18

on the above analysis, the research object and data have been considered with enough quality to meet the research objective.

4 RESULTS

4.1 Reliability and Validity Testing

In order to test the adaptability between the item and the variable factor, a single-factor test was applied. The results show that a total of 4 factors and 18 items can be extracted and their eigenvalues are all greater than 1, and the interpretation rate of cumulative variance after rotation is 78.2%, indicating that 18 items in this study have good adaptability to variable factors.

In this study, SPSS software was used to analyze the reliability and validity of the questionnaire. In the reliability test, it is generally considered that if the Cronbach's alpha coefficient is greater than 0.7, the data would have high reliability. The Cronbach's alpha coefficients of the four variables in this study are shown in **Table 3**, as follows: 0.951, 0.940, 0.946, and 0.919, respectively, and the overall reliability is 0.936, indicating that the data are highly reliable and can be considered for further analyses. In addition to the reliability test, the content and structure validity were also examined. Since the variable measurement items draw on the mature scales of existing research, they have good content validity. A KMO test was conducted to test for structural validity. The KMO

value of this questionnaire is 0.920, and the significance in the Bartlett sphere test is 0.000, less than the significance level of 0.05, indicating that the research data have good discriminant validity.

4.2 Empirical Analysis of the Interaction Relationship

4.2.1 The Effect of Tourist Emotional Attachment on Tourist Behavioral Intentions

Taking the tourism emotional attachment as an independent variable and the tourists' behavioral intentions as a dependent variable, and using SPSS for linear regression analysis, we can get the result of the effect of disaster knowledge on tourists' behavioral intentions, as shown in **Table 4**.

It can be concluded from the aforementioned results that the regression equation between the variables is as follows: Travel Behavioral Intentions = 1.805 + 0.464* Travel Emotional Attachment. The model collinearity *VIF* is less than 5, indicating that there is no multicollinearity, and the results can be considered as true and reliable. The *p*-value is 0.000, which is less than the significance level of 0.05, indicating that travel emotional attachment significantly affects travel behavioral intentions. $R^2 = 0.153$, which means that travel emotional attachment explains travel attitude and behavior with the change of 15.3%. We found that the regression coefficient of tourism emotional attachment is 0.464, which is more than 0, indicating that tourism emotional attachment has a positive and significant impact on tourists' behavioral intentions.

4.2.2 The Effect of Disaster Knowledge on Tourist Behavioral Intentions

Taking the disaster knowledge of tourism destination as an independent variable and the tourists' behavioral intentions as a dependent variable, and by using SPSS for linear regression analysis, we can get the result related to the effect of the disaster knowledge on the tourists' behavioral intentions, as presented in **Table 5**.

TABLE 4 | Analysis of the impact of emotional dependence perception on tourists' behavioral intentions.

	Non-standardized coefficient		Standardized coefficient	<i>t</i>	Significance	VIF
	B	Standard error	Beta			
(Constant)	1.805	0.101		17.931	0.000	
Tourists' emotional attachment	0.464	0.048	0.392	9.599	0.000	1.000

TABLE 5 | Analysis of the impact of disaster knowledge perception on tourists' behavioral intentions.

	Non-standardized coefficient	Standardized coefficient		<i>t</i>	Significance	VIF
	B	Standard error	Beta			
(Constant)	1.542	0.118		13.103	0.000	
Disaster knowledge	0.520	0.050	0.418	10.378	0.000	1.000

TABLE 6 | Analysis of the impact of disaster risk perception on tourists' behavioral intentions.

	Non-standardized coefficient	Standardized coefficient		<i>t</i>	Significance	VIF
	B	Standard error	Beta			
(Constant)	2.041	0.119		17.181	0.000	
Disaster risk perception	−0.260	0.044	0.252	5.870	0.000	1.000

Based on the aforementioned results, the regression equation between variables is as follows: Tourists' Behavioral Intentions = $1.542 + 0.520 \times \text{Disaster knowledge}$. The model collinearity *VIF* is less than 5, indicating that there is no multicollinearity, and the results are true and reliable. The *p*-value is 0.000, less than the significance level of 0.05, indicating that the disaster knowledge significantly affects tourists' behavioral intentions. $R^2 = 0.175$, which indicates that the disaster knowledge can explain tourism behavior intentions with the reason for the change of 17.5%. We found that the regression coefficient of the disaster knowledge is 0.520, which is more than 0, indicating that the disaster knowledge has a significant positive impact on the tourists' behavioral intentions.

4.2.3 The Effect of Disaster Risk Perception on Tourists' Behavioral Intentions

Taking the disaster risk perception as an independent variable and the tourists' behavioral intentions as a dependent variable, and by using SPSS for linear regression analysis, we can get the result of the effect of the disaster risk perception on the tourists' behavioral intentions, as presented in **Table 6**.

Based on the aforementioned results, it can be concluded that the regression equation between variables is as follows: Tourists' Behavioral Intentions = $2.041 - 0.260 \times \text{Disaster Risk Perception}$. The model collinearity *VIF* is less than 5, indicating that there is no multicollinearity, and the results are true and reliable. The *p*-value is 0.000, which is less than the significance level of 0.05, indicating that disaster risk perception significantly affects tourism behavior. $R^2 = 0.063$, which means that disaster risk

perception can explain tourism behavior intentions with the change of 6.3%. We found that the regression coefficient of the disaster risk perception is −0.260, which is less than 0, indicating that the disaster risk perception negatively affects travel behavioral intentions.

4.3 Moderating Effect Analysis

4.3.1 Gender Moderating Effect

Hierarchical regression analysis was used in this study to analyze the moderating effect of gender. We investigated whether gender moderates the relationship between independent variables and youth group tourism behavioral propensity, as presented in **Table 7**.

From Model 1 in **Table 7**, it can be seen that tourism emotional attachment and disaster knowledge positively influence tourists' behavioral intentions and disaster risk perception negatively influences the travel behavioral intentions of youth groups. Model 2 added the moderating variable gender, and model 3 added the interaction of gender and independent variable based on output from model 2. The results showed that the interaction coefficient between gender and tourism emotional attachment was 0.073 ($p > 0.05$), the interaction coefficient between gender and disaster knowledge was 0.170 ($p > 0.05$), and the interaction coefficient between gender and disaster risk perception was 0.113 ($p > 0.05$). We can conclude that gender did not play a significant moderating role in the relationship between emotional attachment to tourism, disaster knowledge, perception of disaster risk, and youth group behavioral intentions.

TABLE 7 | Analysis of the moderating effect of gender.

Variable name	Travel behavioral intention		
	Model 1	Model 2	Model 3
Constant	1.805** (17.931)	1.704** (10.918)	1.695** (10.825)
Emotional attachment	0.464** (9.599)	0.462** (9.546)	0.466** (9.571)
Gender		0.066 (0.845)	0.067 (0.853)
GenderXTourists' emotional attachment			0.073 (0.755)
R^2	0.153	0.154	0.155
F	92.145	46.404	31.100
Constant	1.542** (13.103)	1.236** (6.992)	1.211** (6.838)
Disaster knowledge	0.520** (10.378)	0.531** (10.593)	0.546** (10.746)
Gender		0.178* (2.308)	0.176* (2.290)
GenderXDisaster knowledge			0.170 (1.702)
R^2	0.175	0.183	0.188
F	107.702	56.973	39.090
Constant	2.401** (17.181)	1.943** (11.401)	1.924** (11.262)
Risk perception	-0.260** (5.870)	-0.257** (5.794)	-0.262** (5.881)
Gender		0.067 (0.808)	0.068 (0.831)
GenderX Risk perception			0.113 (1.270)
R^2	0.063	0.065	0.068
F	34.459	17.544	12.248

** means $p < 0.01$, * means $p < 0.05$.

4.3.2 The Moderating Effect of Education Level

Taking tourism emotional attachment, disaster knowledge, and disaster risk perception as independent variables, and education level as a moderator variable, we studied, this time, whether education level played a moderating role in the relationship between the independent variables and the travel behavioral intentions of youth groups, as presented in **Table 8**.

From Model 1 in **Table 8**, it can be seen that tourism emotional attachment and disaster knowledge have a positive and significant impact on tourists' travel intentions; disaster risk perception has a negative impact on the travel behavioral intentions. Model 2 added the moderating variable of education level, and model 3 added the interaction term between education level and independent variable based on output from model 2. The results showed that the interaction coefficient between education level and tourism emotional attachment was 0.152 ($p > 0.05$), and the interaction coefficient between education level and disaster knowledge is 0.181 ($p < 0.05$). It indicated that education level has a significant moderation role between disaster knowledge and tourists' behavioral intentions, which indicates that high education level strengthens this relationship and low education level weakens it. At the same time, we did not find a significant moderation role of education level on emotional attachment and travel intentions. Education level did not play a

significant moderating role in risk perception and travel intentions.

5 DISCUSSION

Taking youth group tourists as our research object, this study analyzes the relationship between risk perception, disaster knowledge, and emotional attachment and the tourists' travel behavioral intentions in disaster-prone tourism destinations. We investigated the moderation role of tourists' gender and their education level and discussed the different interaction relationships with different gender and education level conditions. The research shows that disaster risk perception has a negative and significant effect on tourists' behavioral intentions, while disaster knowledge and tourism emotional attachment have significant and positive effects. In further study, we found the tourists' education level has a stronger moderation than their gender.

5.1 Tourists' Emotional Attachment Positively Affects Tourists' Travel Behavioral Intentions

Previous tourism and hospitality research published in the literature shows that tourism emotional attachment of a visitor will be beneficial to his/her travel attitudes and behavioral intentions (Kim et al., 2017). Yuksel et al. (2010) found a strong link between place attachment and visitors' satisfaction, a key determining factor of tourists' attitude (Prayag & Ryan, 2012). Tourism emotional attachment can be a good predictor of visitors' emotional experience of satisfaction and might have a direct effect on destination loyalty. It has been found that tourists' attachment has an indirect significant positive effect on their behavioral intentions (e.g., revisit intentions and travel purchase intentions) (Cheng et al., 2017).

According to the analysis results, young tourists' emotional attachment to Qinling Mountains positively and significantly affects their travel behavioral intentions. The higher the emotional attachment level of the youth group to Qinling, such as emotional experience and cognitive level, the stronger their behavioral willingness to travel to this area will be.

5.2 Disaster Knowledge Positively Affects Tourists' Travel Behavior Intentions

It is reasonable to assume that changing travel environment also impacts travelers' preference of travel services. The sociological concept of "cocooning" is widely used in social science to explain the human behavior when a person prefers to stay in his/her room instead of going out (Wut, et al., 2021).

According to the results of our empirical analysis, among youth group tourists who visited Qinling Mountains, the quality of disaster knowledge has a positive and significant impact on their travel behavioral intentions. When youth group tourists got access to the information of natural disasters in Qinling Mountains as comprehensively and accurately as possible, such

TABLE 8 | Analysis of the moderating effect of education level.

Variable name	Travel behavioral intention		
	Model 1	Model 2	Model 3
Constant	1.805** (17.931)	1.517** (5.782)	1.532** (5.850)
Tourists' emotional attachment	0.464** (9.599)	0.465** (9.616)	0.452** (9.255)
Education level		0.081 (1.187)	0.084 (1.228)
Education level×Tourists' emotional attachment			0.152 (1.786)
R^2	0.153	0.156	0.161
F	92.145	46.813	32.407
Constant	1.542** (13.103)	1.414** (5.418)	1.472** (5.626)
Disaster knowledge	0.520** (10.378)	0.519** (10.328)	0.508** (10.091)
Education level		0.037 (0.548)	0.029 (0.424)
Education level×Disaster knowledge			0.181* (2.088)
R^2	0.175	0.175	0.182
F	107.702	53.927	37.642
Constant	2.041** (17.181)	1.684** (5.880)	1.692** (5.972)
Risk perception	-0.260** (5.870)	-0.263** (5.946)	-0.264** (1.339)
Education level		0.099 (1.371)	(1.200)
Education level×Risk perception			0.097
R^2	0.063	0.067	0.069
F	34.459	18.199	12.623

** means $p < 0.01$, * means $p < 0.05$.

as the time, frequency, and damage degree of disaster, their travel intentions and travel behavioral intentions became more obvious.

5.3 Disaster Risk Perception Negatively Affects Tourists' Travel Behavioral Intentions

Existing research studies in the literature found that threat severity and susceptibility can induce “travel fear,” which leads to protection motivation and protective travel behaviors after the outbreak of the COVID-19 pandemic (Zheng, et al., 2021). Findings also revealed that “travel fear” can trigger different coping strategies, which increases people's psychological resilience and adoption of cautious travel behaviors. Second, disease has an impact on tourists' behaviors; one possible explanation is that travelers might develop adaptive behaviors (personal health interventions) which may prevent them from contracting the disease (Cahyanto, et al., 2016). The pandemic is also likely to change tourists' lifestyles, travel behaviors, and patterns (Guan, et al., 2020).

The analysis of the results concludes that the tourists' perception of disaster risk has a negative impact on the tourists' behavioral intentions of youth group tourists in Qinling Mountains. If the youth group has a greater perception of the risk of various natural disasters of Qinling Mountains, they may cancel their travel plans or change to

another destination. On the contrary, if they positively perceive the potential risk of Qinling Mountain, they may keep their travel plans.

5.4 Differences in the Relationship Between Different Genders and Education Level

According to the analysis results of the moderating effect of gender and education level, the moderating effect of gender is non-significant, but the moderation role of education level is significant which has a positive moderating effect on disaster knowledge for tourists' travel intentions. In other words, there is no significant difference between male tourists and female tourists with regard to their behavioral tendencies. Tourists with a high education level can comprehensively and accurately assimilate the information of various natural disasters about tourism destinations, which strengthens the relationship between disaster knowledge and their travel behavioral intentions.

6 CONCLUSION

6.1 Theoretical Implications

This analysis expands the theoretical study on risk perception of tourism disaster. First, on the basis of explaining the concepts of

disaster risk, risk perception, and tourism perception, combined with the current research literature, we constructed a research framework for analyzing the influencing factors of tourists' travel behavioral intentions in disaster-prone tourism destinations. Second, risk perception theory and TPB were applied jointly in this study, and risk perception and tourism emotional attachment were both taken as influencing factors to expand the category of influencing factors of tourists' behavioral intentions in TPB. Third, we analyzed the moderating role of tourists' gender and their education level, which enriches the research on the moderating effects in tourism disaster management studies.

6.2 Managerial Implications

The conclusion has great importance for policymakers dealing with the risk management in disaster-prone tourist destinations. On the one hand, tourism destinations can strengthen tourists' emotional experience of destinations through well-provided services, good tourist images, and unforgettable tourist experiences, and thereby promoting their willingness to travel again. On the other hand, tourism destinations need to release natural disaster knowledge comprehensively, such as the time and damage degree of disasters, through various channels via Internet, TV, and social media, to help tourists establish a positive risk perception. And, well-educated tourists should be regarded as the main source of tourists in the Qinling Mountains destination, take them as the target tourists for the Qinling Mountains, and promote and serve them well.

DATA AVAILABILITY STATEMENT

The raw data supporting the conclusions of this article will be made available by the authors, without undue reservation.

REFERENCES

- Arain, F. (2015). Knowledge-based Approach for Sustainable Disaster Management: Empowering Emergency Response Management Team. *Procedia Eng.* 118, 232–239. doi:10.1016/j.proeng.2015.08.422
- Bauer, R. (1960). *Dynamic Marketing for a Changing World*. Editor R. Handcock (Chicago: American Marketing Association), 389.
- Bowlby, J. (1969). *Attachment and Loss*. New York: Basic Books.
- Bronfman, N. C., Cisternas, P. C., Repetto, P. B., Castañeda, J. V., and Guic, E. (2020). Understanding the Relationship between Direct Experience and Risk Perception of Natural Hazards. *Risk Anal.* 40 (10), 2057–2070. doi:10.1111/risa.13526
- Cahyanto, I., Wiblishauser, M., Pennington-Gray, L., et al. Wiblishauser, M., Pennington-Gray, L., Schroeder, A. (2016). The Dynamics of Travel Avoidance: The Case of Ebola in the U.S. *Tour. Manag. Perspect.* 20, 195–203. doi:10.1016/j.tmp.2016.09.004
- Cen, Q., and Huang, Y. L. (2011). Investigation on the Current Situation of Mountain Tourism Security Based on Tourists' Cognition. *Ecol. Econ.* 10 (10), 147.
- Cheng, Y. Y., Patrick, P., and Jing, L. S. (2017). Yesterday once More? Autobiographical Memory Evocation Effects on Tourists' Post-travel Purchase Intentions toward Destination Products. *Tour. Manag.* 61, 263. doi:10.1016/j.tourman.2017.02.014

ETHICS STATEMENT

The studies involving human participants were reviewed and approved by the Ethics Committee of Xi'an University of Finance and Economics.

AUTHOR CONTRIBUTIONS

JUH contributed to conception and design of the study. HT and JIH organized the database and performed the statistical analysis. JUH and HT wrote the first draft of the manuscript. JIH, YM, and XJ wrote sections of the manuscript. All authors contributed to manuscript revision, read, and approved the submitted version.

FUNDING

This work was funded by the Key project of Natural Science Foundation of Shaanxi Province of China (Grant No. 2022JZ-63), the Key project of National Philosophy and Social Science Foundation of China (Grant No. 21ZDA066), Philosophy and Social Science Foundation of Xi'an (Grant No. 22JX46), and Key laboratory of Degraded and Unused Land Consolidation Engineering, the Ministry of Natural and Resources (Grant No. SXDJ 2019-07).

ACKNOWLEDGMENTS

We deeply appreciate and warmly thank Professor Huigang Liang, and the reviewer and editor, whose constructive and helpful comments substantially improved this manuscript.

- Feng, D. M., and Ning, L. J. (2020). Research on the Influencing Factors of Public Risk Perception of Geological Disasters in Coal Mining Areas--Taking Fushun West Open-Pit Mining Area as an Example. *Sci. Technol. Dev.* 16 (08), 901. doi:10.11842/chips.20191125001
- Feng, Z. B. (2020). Evaluation Method for Ecological Security of Forest Tourist Attractions after Freezing Disaster. *J. Catastrophology* 35 (1), 55.
- Fuchs, G., and Reichel, A. (2006). Tourist Destination Risk Perception: The Case of Israel. *J. Hosp. Leis. Mark.* 14 (2), 83–108. doi:10.1300/j150v14n02_06
- Gao, J., Li, M. J., and Wu, B. H. (2017). Study on the Relationship between Nostalgic Tourism Emotion and Behavior of Educated Youth. *Areal Res. Dev.* 36 (02), 61. doi:10.3969/j.issn.1003-2363.2017.02.012
- Gao, X. (2019). The Influencing Factors of New Media on Youth Group Tourism Behavior. *Youth Journal.* 23 (23), 23.
- Gotham, K. F., Campanella, R., Lauve-Moon, K., and Powers, B. (2018). Hazard Experience, Geophysical Vulnerability, and Flood Risk Perceptions in a Postdisaster City, the Case of New Orleans. *Risk Anal.* 38 (2), 345–356. doi:10.1111/risa.12830
- Gou, T., Tang, Y., and He, L. (2020). Effect of Destination Risk Perception on Travel Behavior Intention in Jiuzhaigou Scenic Spot after Earthquake. *Yunnan Geogr. Environ. Res.* 32 (04), 26.
- Guan, X., Gong, J., Xie, L., and Huan, T. C. (2020). Scale Development of Value Co-destruction Behavior in Tourism. *Tour. Manag. Perspect.* 36, 100–757. doi:10.1016/j.tmp.2020.100757

- Hao, J. Q., and Dong, Y. M. (2021). Analysis of Disaster Risk Perception and its Influence Factors in Qinling Mountain. *J. Catastrophology* 36 (3), 165. doi:10.3969/j.issn.1000-811X.2021.03.028
- Hidalgo, M. C., and Hernández, B. (2001). Place Attachment: Conceptual and Empirical Questions. *J. Environ. Psychol.* 21, 273–281. doi:10.1006/jevp.2001.0221
- Hoffmann, R., and Muttarak, R. (2017). Learn from the Past, Prepare for the Future: Impacts of Education and Experience on Disaster Preparedness in the Philippines and Thailand. *World Dev.* 96, 32–51. doi:10.1016/j.worlddev.2017.02.016
- Hong, I. B. (2015). Understanding the Consumer's Online Merchant Selection Process: The Roles of Product Involvement, Perceived Risk, and Trust Expectation. *Int. J. Inf. Manag.* 35, 322–336. doi:10.1016/j.ijinfomgt.2015.01.003
- Hu, M. W., Zhao, L. G., and Li, L. P. (2014). Analysis on the Characteristics of Mountain Recreation Behavior of Tourists in Wugong Mountain. *J. Pingxiang Univ.* 31 (05), 28.
- Jang, W. M., Kim, U.-N., Jang, D. H., Jung, H., Cho, S., Eun, S. J., et al. (2020). Influence of Trust on Two Different Risk Perceptions as an Affective and Cognitive Dimension during Middle East Respiratory Syndrome Coronavirus (MERS-CoV) Outbreak in South Korea: Serial Cross-Sectional Surveys. *BMJ open* 10 (3), e033026. doi:10.1136/bmjopen-2019-033026
- Kim, H., and Marcouiller, D. W. (2015). Considering Disaster Vulnerability and Resiliency: The Case of Hurricane Effects on Tourism-Based Economies. *Ann. Reg. Sci.* 54 (3), 945–971. doi:10.1007/s00168-015-0707-8
- Kim, H., Schroeder, A., and Pennington-Gray, L. (2016). Does Culture Influence Risk Perceptions? *Tour. Rev. Int.* 20 (1), 11–28. doi:10.3727/154427216x14581596798942
- Kim, S., Lee, Y.-K., and Lee, C.-K. (2017). The Moderating Effect of Place Attachment on the Relationship between Festival Quality and Behavioral Intentions. *Asia Pac. J. Tour. Res.* 22 (1), 49–63. doi:10.1080/10941665.2016.1176060
- Kyle, G. T., Mowen, A. J., and Tarrant, M. (2004). Linking Place Preferences with Place Meaning: An Examination of the Relationship between Place Motivation and Place Attachment. *J. Environ. Psychol.* 24 (4), 439–454. doi:10.1016/j.jenvp.2004.11.001
- Leiter, A. M. (2011). The Sense of Snow - Individuals' Perception of Fatal Avalanche Events. *J. Environ. Psychol.* 31 (4), 361–372. doi:10.1016/j.jenvp.2011.08.007
- Li, H. Q., Wang, S. H., Fan, C. M., and Jia, J. M. (2011). Study on Public Fear Psychology and Emergency Management in Sudden Disaster. *East China Econ. Manag.* 25 (09), 36. doi:10.3969/j.issn.1007-5097.2011.09.007
- Li, J., Nguyen, T. H. H., and Coca-Stefaniak, J. A. (2020). Coronavirus Impacts on Post-pandemic Planned Travel Behaviours. *Ann. Tour. Res.*
- Liu, J., and Jia, N. (2018). Research on the Influencing Mechanism of Yacht Travel Behavior Intention Based on TPB Extended Model. *Mar. Sci. Bull.* 37 (04), 378. doi:10.11840/j.issn.1001-6392.2018.04.003
- Liu, Z., Qiu, H., Ma, S., Yang, D., Pei, Y., Du, C., et al. (2021). Surface Displacement and Topographic Change Analysis of the Changhe Landslide on September 14, 2019, China. *Landslides* 18, 1471–1483. doi:10.1007/s10346-021-01626-4
- Ma, S., Qiu, H., Hu, S., Yang, D., and Liu, Z. (2021). Characteristics and Geomorphology Change Detection Analysis of the Jiangdingya Landslide on July 12, 2018, China. *Landslides* 18, 383–396. doi:10.1007/s10346-020-01530-3
- Mao, X. L., and Zhang, H. Z. (2013). Research on the Reconstruction of Tourist Destination Perception Image after Geological Disaster. *Resour. Dev. Mark.* 29 (9), 998. doi:10.3969/j.issn.1005-8141.2013.09.026
- Meng, B., Liu, M., and Li, Q. S. (2010). Theoretical Model of Risk Perception and Analysis of Influencing Factors. *China Saf. Sci. J.* 20 (10), 59. doi:10.3969/j.issn.1003-3033.2010.10.011
- Morais, D. B., and Lin, C.-H. (2010). Why Do First-Time and Repeat Visitors Patronize a Destination? *J. Travel & Tour. Mark.* 27 (2), 193–210. doi:10.1080/10548401003590443
- Murphy, P. E., and Bayley, R. (1989). Tourism and Disaster Planning. *Geogr. Rev.* 79 (1), 36–46. doi:10.2307/215681
- Okaka, F. O., and Odhiambo, B. D. O. (2019). Households' Perception of Flood Risk and Health Impact of Exposure to Flooding in Flood-Prone Informal Settlements in the Coastal City of Mombasa. *Ijccsm* 11 (4), 592–606. doi:10.1108/ijccsm-03-2018-0026
- Okuyama, T. (2018). Analysis of Optimal Timing of Tourism Demand Recovery Policies from Natural Disaster Using the Contingent Behavior Method. *Tour. Manag.* 64, 37–54. doi:10.1016/j.tourman.2017.07.019
- Pahl, S., Harris, P. R., Todd, H. A., and Rutter, D. R. (2005). Comparative Optimism for Environmental Risks. *J. Environ. Psychol.* 25, 1–11. doi:10.1016/j.jenvp.2004.12.004
- Pan, Y. Y., Su, C. N., and Zhao, X. (2016). Risk Assessment and Regionalization of Storm Surge Disaster in Coastal Areas: A PPDC Model Based on Hybrid Algorithm Optimization. *Statistics Inf. Forum* 31 (2), 21. doi:10.3969/j.issn.1007-3116.2016.02.004
- Pelling, M. (2011). Urban Governance and Disaster Risk Reduction in the Caribbean: the Experiences of Oxfam GB. *Environ. Urbanization* 23 (2), 383–400. doi:10.1177/0956247811410012
- Prayag, G., and Ryan, C. (2012). Antecedents of Tourists' Loyalty to Mauritius. *J. Travel Res.* 51 (3), 342–356. doi:10.1177/0047287511410321
- Ramdas, M., and Mohamed, B. (2014). Impacts of Tourism on Environmental Attributes, Environmental Literacy and Willingness to Pay: a Conceptual and Theoretical Review. *Procedia - Soc. Behav. Sci.* 144, 378–391. doi:10.1016/j.sbspro.2014.07.307
- Ramkinssoon, H., Weiler, B., and Smith, G. (2012). Place Attachment and Pro Environmental Behavior in National Parks: The Development of a Conceptual Framework. *J. Sustain. Tour.* 20 (2), 257. doi:10.1080/09669582.2011.602194
- Shen, Y., Lou, S., Zhao, X., Ip, K. P., Xu, H., and Zhang, J. (2020). Factors Impacting Risk Perception under Typhoon Disaster in Macao SAR, China. *Ijerph* 17 (20), 7357. doi:10.3390/ijerph17207357
- Sim, T., Hung, L.-S., Su, G.-W., and Cui, K. (2018). Interpersonal Communication Sources and Natural Hazard Risk Perception: a Case Study of a Rural Chinese Village. *Nat. Hazards* 94 (3), 1307–1326. doi:10.1007/s11069-018-3478-6
- Slovic, P. (1987). Perception of Risk. *Science* 236 (4799), 280–285. doi:10.1126/science.3563507
- Sun, Y. H., Zhou, H. J., and Wei, Y. J. (2015). A Study on the Difference of Disaster Risk Perception in Tourism Communities-Aa Case Study of Hani Rice Terraces. *Tour. Trib.* 30 (12), 46. doi:10.3969/j.issn.1002-5006.2015.12.009
- Tang, W. Y., Zhang, J., Luo, H., Yang, X. Z., and Li, D. H. (2007). Analysis on the Characteristics of Tourists' Sense of Place in Jiuzhaigou Natural Scenic Spot. *J. Geogr. Sci.* (06), 599.
- Ullah, F., Saqib, S. E., Ahmad, M. M., and Fadlallah, M. A. (2020). Flood Risk Perception and its Determinants Among Rural Households in Two Communities in Khyber Pakhtunkhwa, Pakistan. *Nat. Hazards* 104 (1), 225–247. doi:10.1007/s11069-020-04166-7
- Varasteh, H., Marzuki, A., and Rasoolimanesh, S. M. (2015). International Students' Travel Behaviour in Malaysia. *Anatolia* 26 (2), 200–216. doi:10.1080/13032917.2014.934698
- Wang, S. (2019). Residents' Perceptions of Community-Based Disaster Tourism: The Case of Yingxiu, China. *Asia Pac. J. Tour. Res.* 24 (7), 669–678. doi:10.1080/10941665.2019.1623273
- Wright, D., and Sharpley, R. (2018). Local Community Perceptions of Disaster Tourism: the Case of L'Aquila, Italy. *Curr. Issues Tour.* 21 (14), 1569–1585. doi:10.1080/13683500.2016.1157141
- Wu, L., and Zhang, X. (2012). Psychometric Paradigm in Risk Perception Research. *J. Nanjing Univ. Sci.* 2 (3), 95. doi:10.3969/j.issn.1001-4608-B.2012.02.015
- Wut, T. M., Xu, J., Wong, S. M., Xu, J., and Wong, S.-m. (2021). Crisis Management Research (1985-2020) in the Hospitality and Tourism Industry: A Review and Research Agenda. *Tour. Manag.* 85, 104307. doi:10.1016/j.tourman.2021.104307
- Xu, Z. X., and Zhang, J. (2015). Antecedents and Consequences of Place Attachment: a Comparison of Chinese and Western Urban Tourist in Hangzhou, China. *J. destination Mark. Manag.* 5, 86–95. doi:10.1016/j.jdm.2015.11.003
- Yang, D., Qiu, H., Ma, S., Liu, Z., Du, C., Zhu, Y., et al. (2022). Slow Surface Subsidence and its Impact on Shallow Loess Landslides in a Coal Mining Area. *CATENA* 209, 105830. doi:10.1016/j.catena.2021.105830
- Yang, M., Chen, Y., Ma, J., and Liu, Z. (2018). The Relationship between Geological Disaster Risk Perception and Behavior Characteristics Based on Electroencephalogram Testing Technology. *Neuro Quantology* 16 (5), 186–192. doi:10.14704/nq.2018.16.5.1295

- Yuksel, A., Yuksel, F., and Bilim, Y. (2010). Destination Attachment: Effects on Customer Satisfaction and Cognitive, Affective and Conative Loyalty. *Tour. Manag.* 31, 274–284. doi:10.1016/j.tourman.2009.03.007
- Zhao, D. P. (2020). Design of Tourism Emergency Management and Rescue System under Sudden Natural Disasters. *J. Catastrophology* 35 (2), 171–176.
- Zheng, D., Luo, Q., and Ritchie, B. W. (2021). Afraid to Travel after COVID-19? Self-Protection, Coping and Resilience against Pandemic ‘travel Fear. *Tour. Manag.* 83, 104–261. doi:10.1016/j.tourman.2020.104261
- Zheng, Q. M., Duan, N. J., LiuChen, J. X. Q., and Zhu, A. M. (2016). A Study on the Relationship between Mountain Resort Tourists’ Motivation and Tourism Consumption Behavior -- Based on the Investigation of Vacation Tourists in Nankun Mountain, Guangdong Province. *J. Guangxi Vocat. Normal Univ.* 28 (04), 82. doi:10.3969/j.issn.1008-8806.2016.04.014
- Zhou, W. Q., Qiu, H. J., Wang, L. Y., Pei, Y. Q., Tang, B. Z., Ma, S. Y., et al. (2022). Combining Rainfall-Induced Shallow Landslides and Subsequent Debris Flows for Hazard Chain Prediction. *CATENA* 213, 106199. doi:10.1016/j.catena.2022.106199
- Zhou, Q., and Liu, D. L. (2019). Flood Risk Perception Evaluation of Residents in China Based on Knowledge, Trust and Action Model. *Yangtze River* 50 (08), 28
- Zhou, X., Xu, W., and Yuan, Y. (2012). Disaster Risk Perception and Literature Review. *J. Catastrophology* 27 (2), 114. doi:10.3969/j.issn.1000-811X.2012.02.024
- Conflict of Interest:** The authors declare that the research was conducted in the absence of any commercial or financial relationships that could be construed as a potential conflict of interest.
- Publisher’s Note:** All claims expressed in this article are solely those of the authors and do not necessarily represent those of their affiliated organizations, or those of the publisher, the editors, and the reviewers. Any product that may be evaluated in this article, or claim that may be made by its manufacturer, is not guaranteed or endorsed by the publisher.

Copyright © 2022 Hao, Tang, Hao, Ma and Jiang. This is an open-access article distributed under the terms of the Creative Commons Attribution License (CC BY). The use, distribution or reproduction in other forums is permitted, provided the original author(s) and the copyright owner(s) are credited and that the original publication in this journal is cited, in accordance with accepted academic practice. No use, distribution or reproduction is permitted which does not comply with these terms.



Multifractal Features of Particle-Size Distribution and Their Relationships With Soil Erosion Resistance Under Different Vegetation Types in Debris Flow Basin

OPEN ACCESS

Edited by:

Haijun Qiu,
Northwest University, China

Reviewed by:

Songtang He,
Institute of Mountain Hazards and
Environment CAS, China
Chao Ma,
Beijing Forestry University, China

*Correspondence:

Yongming Lin
monkey1422@163.com

[†]These authors have contributed
equally to this work and share first
authorship

Specialty section:

This article was submitted to
Geohazards and Georisks,
a section of the journal
Frontiers in Earth Science

Received: 25 April 2022

Accepted: 26 May 2022

Published: 06 July 2022

Citation:

Li S, Gao R, Huang M, Yang L, Yu H,
Yu C, Tian X, Li J and Lin Y (2022)
Multifractal Features of Particle-Size
Distribution and Their Relationships
With Soil Erosion Resistance Under
Different Vegetation Types in Debris
Flow Basin.
Front. Earth Sci. 10:927862.
doi: 10.3389/feart.2022.927862

Songyang Li^{1,2†}, Ruoyun Gao^{1,2†}, Maowei Huang¹, Liusheng Yang^{1,2}, Hang Yu^{1,2},
Chenhui Yu^{1,2}, Xue Tian^{1,2}, Jian Li^{1,2} and Yongming Lin^{1,2*}

¹College of Forestry, Fujian Agriculture and Forestry University, Fuzhou, China, ²Key Laboratory for Forest Ecosystem Process and Management of Fujian Province, Fuzhou, China

Understanding the influence of vegetation types on soil particle-size distribution (PSD) is essential to evaluate the effects of sediment control by vegetation restoration. In this work, we studied the effects of different vegetation types, including bare land, meadow, shrub and forest on soil PSD in Jiangjiagou gully, Yunnan province, China. A total of 60 soil samples were collected and analyzed for soil particle size distribution using the laser diffraction method. Fractal theory was used to calculate multifractal parameters. The volume fraction of silt particles in shrub and forest is significantly higher than that in bare land, meadow, whereas the total volume fraction of sand particles in bare land and meadow exceed that in shrub and forest. The soil particle size distribution along soil layers has no significant difference in each vegetation type. The volumetric fractal dimension is significantly higher in forest and shrub than in bare land and grassland, but there is no significant difference between forest and shrub. In addition, soil erosion resistance exhibits significant differences of forest > shrub > grassland > bare land. Multifractal parameters are highest in bare land except for multifractal spectrum values ($f(\alpha_{\max})$ and $f(\alpha_{\min})$) and the maximum value of singularity index (α_{\min}). All generalized dimensions spectra curves of the PSD are sigmoidal, whereas the singular spectrum function shows an asymmetric upward convex curve. Furthermore, soil erosion resistance has significant relationships with multifractal parameters. Our results suggest that multifractal parameters of the soil PSD can predict its anti-ability to erosion. This study also provides an important insight for the evaluation of soil structure improvement and the effects of erosion control by vegetation restoration in dry-hot valley areas.

Keywords: soil particle-size distribution, multifractal analysis, vegetation restoration, soil erosion resistance, debris flow-affected area

1 INTRODUCTION

Vegetation restoration is a key factor to control soil erosion in degraded land through both hydrological and mechanical mechanisms (Podwojewski et al., 2011; Burylo et al., 2012; Cui et al., 2019). It not only can reduce raindrop splash force, regulate surface runoff, and trap sediment (Lin et al., 2014), but also can promote soil erosion resistance (Gyssels et al., 2005; Descheemaeker et al., 2006; Ma et al., 2016; Deng et al., 2022). In general, the effect of vegetation on erosion control differs in vegetation types due to various plant coverage, species composition, and community structure (Lin et al., 2014; Dai et al., 2022). In detail, vegetation with highly complicated structure and layers has strong ability to prevent soil detachment and minimize soil movement (Lin et al., 2014), resulting in comparatively higher fine content and lower coarse particles (Burylo et al., 2012). However, many studies mainly focused on the relationship between vegetation change and the regulation and control of soil erosion (McVicar et al., 2010; Li et al., 2021a). The interaction between soil particle size distribution and vegetation types, especially in extremely degraded areas is poorly understood.

The particle-size distribution (PSD) is a typical property of soil texture and has significant effects on bulk density, porosity, organic matter, and cation exchange capacity (Bieganski et al., 2013; Wang et al., 2019). Comparing the characteristics of soil PSD is essential to understand and determine the dynamics of soil structure induced by influence factors such as vegetation succession, tillage, reforestation, and grazing (Lyu et al., 2015; Yang et al., 2022). Soil PSD has an irregular shape and self-similar hierarchical structure, indicating that it has fractal features (Guan et al., 2011; Zhang et al., 2017). Therefore,

soil PSD has been the focus of much research concerning on soil particle fractionation and physical processes (Peng et al., 2014; Lyu et al., 2015). Previous studies have focused on the effects of soil erosion on fractal dimension of soil PSD. For example, Liu et al. (2022) found that fractal dimension of soil PSD in hedgerows can reflect sediment reduction effect. Li et al. (2021a) showed that multifractal analysis captured the complexity of the PSD of suspended sediment in the Yangtze River. Although many findings with respect to fractal dimensions of soil PSD have been obtained, whether soil erosion anti-ability significantly respond to fractal dimensions of soil PSD is unknown.

In recent years, many studies have demonstrated that particle redistribution occurs in soil erosion process (Zhou et al., 2022; Liu et al., 2022; Zhang et al., 2020; Ma et al., 2021), this truth provides important clue that temporal changes in environmental conditions causing soil erosion can be identified (Schillereff et al., 2014; Wei et al., 2014). Therefore, the soil erosion resistance of different vegetation types could be reflected by their species diversity, plant density, and root characteristics (Jin and Chen, 2019; Xu et al., 2019). Several authors highlight that the size characteristics of eroded soil sediment contribute to the growing body knowledge on revised soil erosion model in the wake of erosion processes (Asadi et al., 2011; Shi et al., 2012; Liu et al., 2021). Hence, it is necessary to understand the relationship between soil erosion resistance and its PSD. However, recent works on soil PSD mostly concerned about stable or undisturbed ecosystems such as tidal flats (Lyu et al., 2015), forests (Wang et al., 2008; Xia et al., 2009), vegetation barriers (Bochet et al., 2000; Burylo et al., 2012), little is known about the relationship between soil erosion resistance of different vegetation types and fractal dimensions of soil PSD.

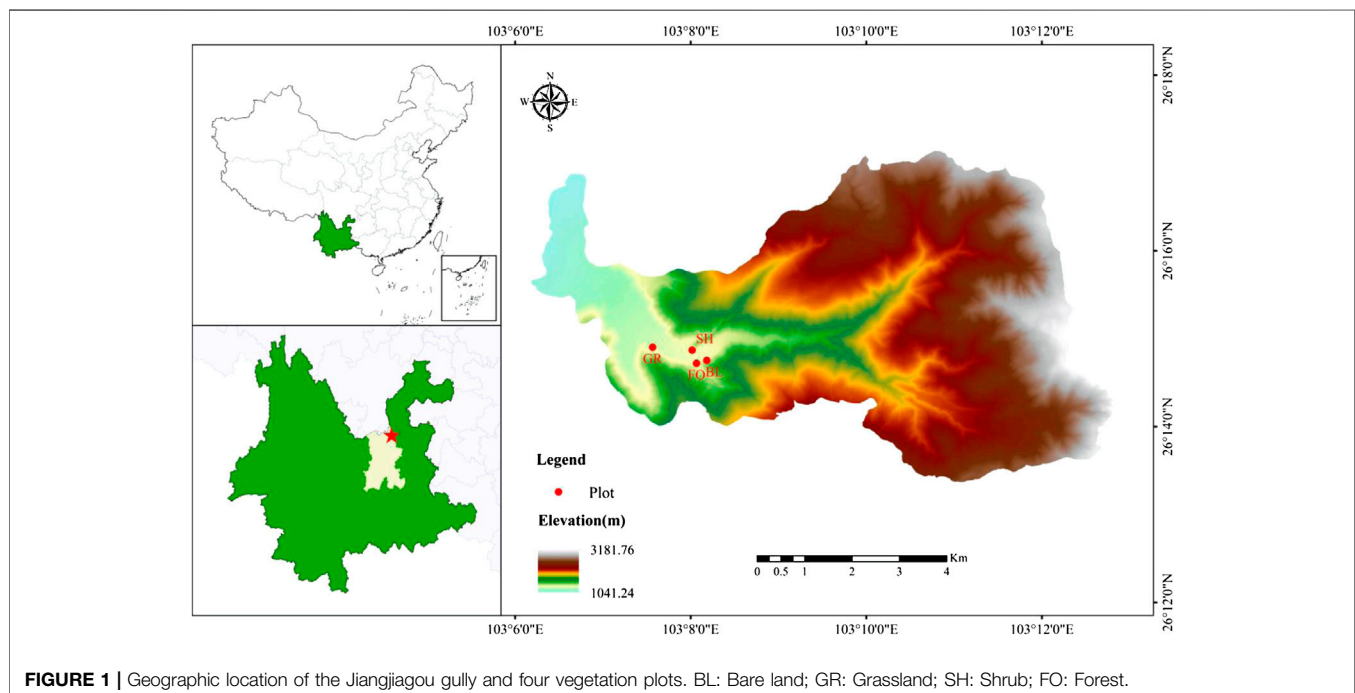


FIGURE 1 | Geographic location of the Jiangjiagou gully and four vegetation plots. BL: Bare land; GR: Grassland; SH: Shrub; FO: Forest.

TABLE 1 | Experimental conditions of four vegetation types.

Vegetation Types	Longitude/Latitude	Slope Gradient (°)	Slope-Aspect	Elevation (m)	Dominant Species	Vegetation Coverage (%)
Bare land	103°08'11"E/26°14'46"N	24	NE	1,356	—	5
Grassland	103°07'34"E/26°14'55"N	20	NE	1,288	<i>Heteropogon contortus</i>	40
Shrub	103°08'01"E/26°14'53"N	19	SW	1,337	<i>Desmodium racemosum</i>	80
Forest	103°08'04"E/26°14'44"N	20	NE	1,347	<i>Leucaena leucocephala</i>	90

**FIGURE 2** | Field views of four vegetation plots.

In extremely degraded areas, fractal dimensions of soil PSD have been used to describe the degrees of soil damage, recovery phrase, and sediment retention ability (Deng et al., 2015; Cui et al., 2019; Luo et al., 2019). Singular fractal dimension of soil PSD can vary in response to major earthquakes and can predict the effects of earthquake disturbance on soil system (Deng et al., 2015). Soil PSD-based analyses also can reflect recover phrase when natural restoration occurred in disaster-affected areas (Luo et al., 2019). Furthermore, fractal dimension of sediment PSD can reveal sediment retention ability of plants (Cui et al., 2019). In our study area—dry-hot valley of Jinsha River, there also was some research on the relationship between fractal dimensions of soil PSD and soil properties (Xie and Wei, 2011; Li et al., 2021c; Chen et al., 2016), but little research has been done to understand the effects of soil sediment sorting by different vegetation types and the relationship between soil erosion resistance and fractal dimensions of soil PSD except some qualitative analyses or overall trend analyses (Wang et al., 2004; Cui et al., 2005).

In this study, we sought to estimate the impacts of vegetation types on the soil PSD characteristics using a typical basin of dry-hot valley—Jiangjiagou gully as a case study. Our objectives are to 1) reveal the soil PSD in typical debris flow basin using both

singular and multi-fractal analysis; 2) to determine whether fractal dimensions reflect the change of vegetation types; and 3) to identify the influence of multifractal parameters on the soil erosion resistance. Our work took an integrative approach to study the effects of vegetation types on soil PSD and the relationship between soil erosion resistance and fractal dimensions of soil PSD. This study could provide theoretical support for ecological restoration and vegetation community improvement and help identify ways to rapidly evaluate the effects of soil sediment sorting and erosion control by vegetation types in dry-hot valley.

2 STUDY AREA

The study area is the Jiangjiagou watershed, Dongchuan district, Kunming, Yunnan province, China (latitude 26°13'–26°17' N, longitude 103°6'–103°13' E). It is in the altitude between 1,042 and 3269 m s L. (**Figure 1**). The study area has three vertical climate types including 1) dry-hot valley with an elevation ranging from 1,042 to 1600 m, annual precipitation of 600–700 mm year⁻¹, mean annual temperature of 20°C, and

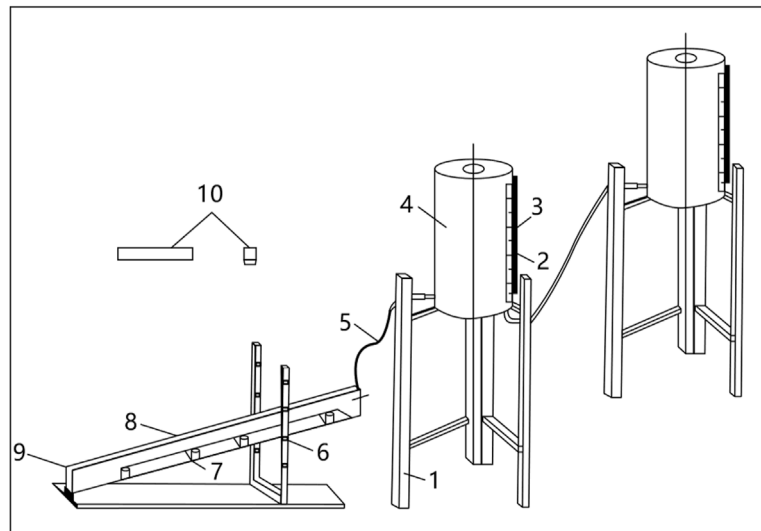


FIGURE 3 | Schematic diagram of anti-scouring test equipment (Chen et al., 2014). 1 is a bucket rack; 2 is a scale ruler; 3 is a glass tube; 4 is a bucket; 5 is a water pipe; 6 is a still water chamber; 7 is a skid; 8 is the flume for the test; 9 is the site for putting the samples; 10 is the cutting ring with 200 cm³ (10 cm length, 5 cm width, and 4 cm height).

average annual potential evapotranspiration of 3,700 mm year⁻¹; 2) subtropical and sub-humid warm temperate climate with an elevation ranging from 1,600 to 2200 m, annual precipitation of 700–850 mm year⁻¹, mean annual temperature of 13°C, and average annual potential evapotranspiration of about 1700 mm year⁻¹; 3) humid warm temperate climate with an elevation ranging from 2200 to 3269 m, annual precipitation of about 1,200 mm year⁻¹, mean annual temperature of 7°C, and average annual potential evapotranspiration of about 1,350 mm year⁻¹. The main soil types in dry-hot valley are calcic vertisols and calcic regosols according to the WRB system (Li et al., 2021b).

Due to severe soil and water loss, viscous debris flows have occurred frequently in Jiangjiagou Gully since the early Late Pleistocene. They combined with human deforestation to destroy vegetation during the period of 1950–1970, resulting in serious ecological degradation and native vegetation destruction (Lin et al., 2014). Hence, original vegetation has been replaced by man-made forests. At present, in dry-hot valley of Jiangjiagou gully, *Leucaena leucocephala* and *Eucalyptus camaldulensis* were planted as the main man-made forests; Shrubs were mainly dominated by *Coriaria sinica*, *Salix myrtilleacea*, *Desmodium racemosum*, and *Sophora davidii*; Grasslands were mainly dominated by *Heteropogon contortus*, *Eulaliopsis binata*, and *Themeda triandra*. However, vegetation coverage occupied <10% of the total area of dry-hot valley in 2004 (Cui et al., 2005). Therefore, various vegetation types enable Jiangjiagou gully to be an ideal site for studying the relationship between the soil erosion resistance of vegetation types and fractal dimensions of soil PSD.

Though the average hillslope is 43° in Jiangjiagou watershed (Lin et al., 2014), forests are mainly on slopes <25°. To avoid the discrepancy in different slope gradients, four vegetation plots

were selected, including bare land, grassland, shrub, forest in Jiangjiagou gully (Table 1). All four experimental plots developed from landslide mass (<40 years) with the soil type of calcic regosols are located in the downstream of the Jiangjiagou gully near to Dongchuan Debris Flow Observation and Research Station, Chinese Academy of Sciences (Figure 2). Among four plots, bare land developed under natural conditions with slope gradient of 24° and northeast facing slope. Grassland developed from bare land to *Heteropogon contortus* grassland with slope gradient of 20° and northeast facing slope. Shrub developed from bare land to *Desmodium racemosum* shrub with slope gradient of 19° and southwest facing slope. Forest was reforested without land leveling projects in 2004 with *Leucaena leucocephala*, slope gradient of 20° and northeast facing slope.

3 MATERIALS AND METHODS

3.1 Soil Sampling and Analysis

We set up three random quadrats (10 × 10 m in forest, 5 × 5 m in shrub, and 1 × 1 m in both grassland and bare land) each vegetation type. In selected quadrat, five soil samples were collected from the depths of 0–10 cm, 10–20 cm, 20–30 cm, 30–40 cm, and 40–50 cm. In addition, one sample was taken with a standard 200 cm³ volume (10 cm length, 5 cm width, and 4 cm height) from each soil depth for determining soil erosion resistance. A total of 60 soil samples for soil particles and soil erosion resistance were collected from the four vegetation types.

The portion to be analyzed for soil particles were taken to the lab, air-dried, disaggregated, and passed through 2 mm screen. We used the Longbench Mastersizer 2000 laser particle size analyzer to analyze the fractions particle with size <2 mm (Li et al., 2021a). The 10 ml 10% H₂O₂ was used to remove organic

matter to soak each 0.3 g soil sample for 24 h. Each sample was then treated with 5 ml of 10% HCl for 10 min to eliminate carbonate salts. Deionized water was added up to 500 ml to rinse the residual H_2O_2 and HCl for 12 h before the liquid supernatant was removed, until the pH of sample solution was adjusted to 7. We added 5 ml 0.1 ml/L sodium hexametaphosphate to separate soil particles before measurement and used the laser particle analyzer to measure the percentage volume of soil particles in the range 0.02–2000 μm after ultrasonic vibration for 10 min.

The portion to be analyzed for soil erosion resistance was stored in a plastic bag to avoid desiccation. We used the anti-scouring test equipment (Figure 3) and the method described by Chen et al. (2014) to determine soil erosion resistance:

$$k = q \times t/m \quad (1)$$

where k is the soil erosion resistance (Ls/g); q is the water volume used in flume experiment (L); t is the experiment time (s); m is the sediment weight eroded by water.

3.2 Fractal Models

The traditional approach for fractal characteristics of soil PSD is using unitedly laser diffraction method and fractal analysis (Tyler and Wheatcraft, 1992; Su et al., 2004; Peng et al., 2014; Lyu et al., 2015). Presently, two common methods including singular and multi-fractal analysis are widely used (Lyu et al., 2015). Singular fractal analysis can describe the overall or average characteristics of soil PSD and predict the change of related soil properties (Guan et al., 2011; Li et al., 2019), but seldom clearly understand the local heterogeneity of soil PSD. Therefore, multifractal analysis is used to determine the intrinsic variability of soil PSD in more detail (Lyu et al., 2015).

3.2.1 Volumetric Fractal Dimension

According to the frequency histogram obtained from the Longbench Mastersizer 2000 laser particle size analyzer, we used volumetric fractal model to establish the granularity of the soil particles as follows (Wang et al., 2005; Li et al., 2021b):

$$\frac{V_{(r < R)}}{V_T} = \left(\frac{R}{\lambda_v}\right)^{3-D_v} \quad (2)$$

where R is the soil particle size in mm; $V_{(r < R)}$ is the cumulative volume percent of particles lower than R ; V_T is the total volume of soil particles; λ_v is the maximum particle size in mm; and D_v is the volumetric fractal dimension of the soil PSD. The value of R was the arithmetic mean of the lower and upper limits of a certain class.

The following logarithmic expression was derived from Eq. 2:

$$\log\left[\frac{V_{(r < R)}}{V_T}\right] = (3 - D_v)\log\left(\frac{R}{\lambda_v}\right) \quad (3)$$

using Eq. 3, the D_v value is equal to three minus the slope of the logarithmic linear regression equation, representing the space-filling efficiency of particles (Perfect & Kay, 1995; Biswas, 2019).

3.2.2 Calculation of the Multifractal Parameters

In this study, the measurement interval $I = [0.02, 2000]$ of the laser particle size analyzer is divided into 64 smaller intervals $I_i = [\varphi_i, \varphi_{i+1}]$, $I = 1, 2, \dots, 64$, with constant $\lg(\varphi_{i+1}/\varphi_i)$. A new dimensionless interval $J = [0, 5.3]$ can then be created. A number $N(\varepsilon) = 2^k$ of cells with equal size $\varepsilon = 5.3 \times 2^{-k}$ for k is set up ranging from 1 to 5 (i.e., $\varepsilon = 2.65, 1.325, 0.6625, 0.33125$, and 0.165625). We created a certain measure μ that distributes over the interval of sizes I and each cell $\mu_i(\varepsilon)$ is contained in available data. $N(\varepsilon)$ is taken as the number of samples when the scale is ε ; and $\mu_i(\varepsilon)$ is the probability density (percentile) of the i th subinterval (J_i), namely the sum of all measurements in the sub interval J_i . The generalized fractal dimension D_q is defined as follows:

$$D_q = \lim_{\varepsilon \rightarrow 0} \frac{1}{q-1} \frac{\lg\left[\sum_{i=1}^{N(\varepsilon)} \mu_i(\varepsilon)^q\right]}{\lg \varepsilon} \quad (q \neq 1) \quad (4)$$

$$D_1 = \lim_{\varepsilon \rightarrow 0} \frac{\sum_{i=1}^{N(\varepsilon)} \mu_i(\varepsilon) \lg \mu_i(\varepsilon)}{\lg \varepsilon} \quad (q = 1) \quad (5)$$

The singularity spectrum could be computed through a parameter q by:

$$\alpha(q) = \lim_{\varepsilon \rightarrow 0} \frac{\sum_{i=1}^{N(\varepsilon)} \mu_i(q, \varepsilon) \lg \mu_i(\varepsilon)}{\lg \varepsilon} \quad (6)$$

$$f(\alpha) = \lim_{\varepsilon \rightarrow 0} \frac{\sum_{i=1}^{N(\varepsilon)} \mu_i(q, \varepsilon) \lg \mu_i(q, \varepsilon)}{\lg \varepsilon} \quad (7)$$

using Eqs 4–7, in the range of $-10 \leq q \leq 10$, the fitting calculation is carried out with 1 step size to get $D(q)$, $\alpha(q)$ and $f(\alpha)$. When $q = 0$, D_0 is the capacity dimension, reflecting the range of a continuous distribution. When $q = 1$, D_1 is the entropy dimension of the measure, providing a measure of the heterogeneity of soil particle size distribution. When $q = 2$, D_2 is the correlation dimension that can capture some of the inner details of the particle-size distributions. The parameter of D_1/D_0 can be used to quantitatively describe the dispersion degree of soil particle size distribution (Guan et al., 2011; Rodríguez-Lado & Lado, 2017).

The parameters of $\alpha(q)$ and $f(\alpha)$ can characterize local multifractal characteristics of soil particle size distribution. $\alpha(0)$ is the average value of multifractal singular spectrum. The greater $\alpha(0)$ means the smaller the local density of soil particle size distribution.

The width of multifractal singular spectrum $\Delta\alpha(q)$ representing the spatial heterogeneity of soil particle size distribution is defined as follow:

$$\Delta\alpha(q) = \alpha(q)_{\max} - \alpha(q)_{\min} \quad (8)$$

where the min and max denote the minimum and maximum values, respectively.

The shape of multifractal singular spectrum $\Delta f[\alpha(q)]$ is defined as follow:

$$\Delta f[\alpha(q)] = f[\alpha(q)_{\max}] - f[\alpha(q)_{\min}] \quad (9)$$

TABLE 2 | Soil particle size distribution and singular fractal dimension among four vegetation types and five soil layers. BL: Bare land; GR: Grassland; SH: Shrub; FO: Forest; *D*: volumetric fractal dimension; SER: Soil erosion resistance; Different letters indicate significant differences at $p < 0.05$. All data are shown using mean \pm standard error. * means median; † means mode.

Source	Very Coarse Sand (1,2 mm)	Coarse Sand (0.5–1 mm)	Medium Sand (0.25–0.5 mm)	Fine Sand (0.1–0.25 mm)	Very Fine Sand (0.05–0.1 mm)	Silt (0.002–0.05 mm)	Clay (< 0.002 mm)	<i>D</i>	SER
Vegetation types (VT)	BL ($n = 15$) 0.25 ± 0.37^a *0.06 †0	7.41 ± 4.01^a *7.78 †Null	19.04 ± 5.03^a *20.53 †Null	11.53 ± 2.12^a *11.26 †Null	12.40 ± 2.95^a *11.55 †Null	42.76 ± 7.08^b *43.39 †Null	6.51 ± 0.86^c *6.47 †Null	2.63 ± 0.02^c *2.63 †Null	21.32 ± 5.17^a *22.05 †Null
	GR ($n = 15$) 0.13 ± 0.41^a *0 †0	4.12 ± 3.66^b *3.30 †Null	16.14 ± 4.54^a *15.39 †Null	12.82 ± 3.06^a *11.80 †Null	12.70 ± 1.69^a *12.45 †Null	46.06 ± 7.37^b *45.69 †Null	7.99 ± 0.87^c *7.78 †Null	2.65 ± 0.02^b *2.65 †Null	44.02 ± 4.34^b *42.66 †Null
	SH($n = 15$) 0^a *0 †0	0.51 ± 1.10^c *0.02 †Null	4.94 ± 4.26^b *3.53 †Null	7.00 ± 2.28^b *7.39 †Null	9.49 ± 1.43^b *9.75 †Null	67.61 ± 6.28^a *68.76 †Null	10.46 ± 1.10^b *10.86 †Null	2.70 ± 0.02^a *2.71 †Null	83.71 ± 8.95^c *82.48 †Null
	FO($n = 15$) 0.00 ± 0.00^a *0 †0	0.71 ± 1.60^c *0.20 †Null	6.06 ± 8.47^b *2.13 †Null	6.26 ± 6.12^b *3.63 †Null	7.73 ± 2.44^b *7.16 †Null	66.68 ± 14.38^a *72.11 †Null	12.58 ± 2.68^a *13.83 †Null	2.72 ± 0.04^a *2.74 †Null	92.10 ± 12.17^{days} *90.72 †Null
	$p = 0.051$	$p < 0.001$	$p < 0.001$	$p < 0.001$	$p < 0.001$	$p < 0.001$	$p < 0.001$	$p < 0.001$	$p < 0.001$
Soil layers (SL)	0–10 cm ($n = 12$) 0.01 ± 0.04^a *0 †Null	2.16 ± 2.79^a *0.74 †Null	10.58 ± 7.23^a *9.28 †Null	9.03 ± 4.40^a *9.52 †Null	11.41 ± 4.51^a *11.33 †Null	57.46 ± 12.74^a *53.35 †Null	9.39 ± 2.59^a *8.43 †Null	2.68 ± 0.04^a *2.66 †Null	58.04 ± 32.65^a *61.02 †Null
	10–20 cm ($n = 12$) 0.11 ± 0.29^a *0 †Null	3.40 ± 4.05^a *1.24 †Null	10.88 ± 8.52^a *12.17 †Null	8.61 ± 4.39^a *9.28 †Null	10.21 ± 3.09^a *11.08 †Null	57.44 ± 15.10^a *51.91 †Null	9.34 ± 2.77^a *8.19 †Null	2.68 ± 0.04^a *2.65 †Null	68.94 ± 36.81^a *72.58 †Null
	20–30 cm ($n = 12$) 0.22 ± 0.51^a *0 †Null	4.51 ± 4.84^a *2.52 †Null	13.64 ± 10.12^a *15.16 †Null	9.51 ± 5.09^a *9.61 †Null	10.08 ± 2.08^a *10.88 †Null	52.87 ± 16.84^a *49.45 †Null	9.12 ± 3.29^a *7.95 †Null	2.67 ± 0.05^a *2.66 †Null	58.72 ± 26.57^a *58.31 †Null
	30–40 cm ($n = 12$) 0.02 ± 0.04^a *0 †Null	2.69 ± 3.48^a *0.57 †Null	11.40 ± 8.33^a *11.04 †Null	10.17 ± 4.61^a *10.23 †Null	10.46 ± 1.76^a *9.97 †Null	55.47 ± 14.67^a *58.06 †Null	9.65 ± 2.60^a *10.06 †Null	2.68 ± 0.05^a *2.69 †Null	62.81 ± 30.24^a *76.24 †Null
	40–50 cm ($n = 12$) 0.10 ± 0.23^a *0 †Null	2.78 ± 4.56^a *0.25 †Null	10.58 ± 8.61^a *9.66 †Null	9.57 ± 5.39^a *8.57 †Null	10.57 ± 3.00^a *11.10 †Null	56.70 ± 15.92^a *57.99 †Null	9.67 ± 3.09^a *9.15 †Null	2.68 ± 0.05^a *2.68 †Null	56.42 ± 26.38^a *62.34 †Null
	$p = 0.412$ $p = 0.783$	$p = 0.667$ $p = 0.185$	$p = 0.898$ $p = 0.784$	$p = 0.951$ $p = 0.813$	$p = 0.846$ $p = 0.644$	$p = 0.941$ $p = 0.901$	$p = 0.990$ $p = 0.858$	$p = 0.975$ $p = 0.829$	$p = 0.864$ $p = 0.025$
VT×SL									

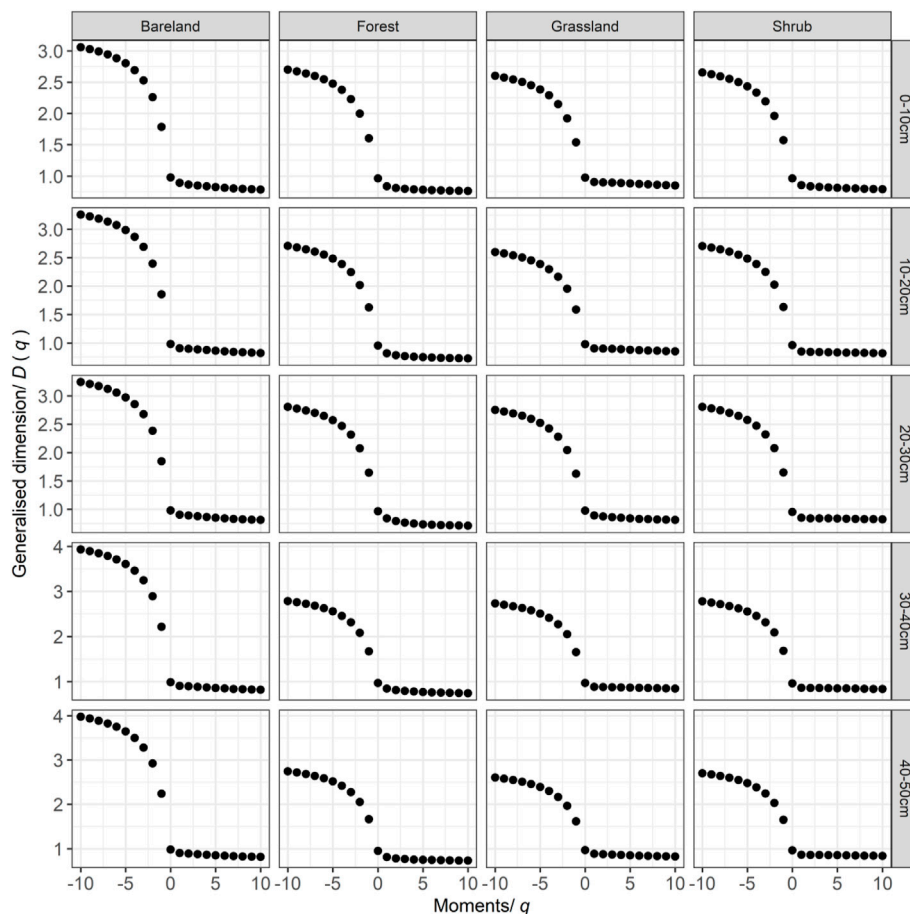


FIGURE 4 | Generalized dimension spectra $D(q)$ - q of soil particle-size distribution in different soil layers of four vegetation types in Jiangjiagou Gully.

where $\Delta f[\alpha(q)] < 0$ indicates that the high probability subsets of the soil particle size play the key role in the fractal system, showing a left hook upper convex curve (Tian et al., 2020; Li et al., 2021a).

3.3 Statistical Analysis

A one-way ANOVA in conjunction with the least significant difference (LSD) test ($\alpha = 0.05$) was used to examine sources of variation between soil particles, volumetric fractal dimensions, soil erosion resistance, and multifractal parameters among four vegetation types. Linear regression analysis was conducted to identify the relationships between soil erosion resistance and multifractal parameters. Statistical analyses were performed using R language (Version 3.4.1). All data in all tables are mean \pm standard error.

4 RESULTS

4.1 Soil Particle-Size Distribution and Soil Erosion Resistance

The volume fraction distribution of soil showed significant differences across the four vegetation types except very coarse sand, but no significant difference across soil layers (Table 2).

Among all soil particle-sizes, shrub and forest were characterized by significantly higher silt and clay and lower very fine sand, fine sand, and medium sand, compared with those in bare land and grassland. There was a significant difference in clay between shrub and forest and in coarse sand between bare land and grassland.

Table 2 also summarized the statistics of volumetric fractal dimension and soil erosion resistance across the four vegetation types. The results showed that volumetric fractal dimension was significantly higher in forest and shrub than in bare land and grassland, but there was no significant difference between forest and shrub. Soil erosion resistance showed significant differences of forest > shrub > grassland > bare land.

There was no significant difference among soil layers in volumetric fractal dimension and soil erosion resistance. The interaction between vegetation type and soil layer only markedly influenced soil erosion resistance (Table 2).

4.2 Multifractal Characteristics

Rényi dimensions spectra $D(q)$ were calculated for $-10 \leq q \leq 10$ at 1 lag increment (Figure 4). The generalized dimensional spectrum of the soil PSD under different vegetation types across five soil layers decreased monotonically and showed sigmoidal patterns (Figure 4). The multifractal parameters following the order of

TABLE 3 | Multifractal parameters among four vegetation types and five soil layers. BL: Bare land; GR: Grassland; SH: Shrub; FO: Forest; D_0 : Capacity dimension; D_1 : Entropy dimension; D_2 : Correlation dimension; $\alpha(0)$: the average value of multifractal singular spectrum; α_{\max} : the maximum value of singularity index; α_{\min} : the minimum value of singularity index; $\Delta\alpha(q)$: singularity index; $f(\alpha_{\max})$: multifractal spectrum value in α_{\max} ; $f(\alpha_{\min})$: multifractal spectrum value in α_{\min} ; $\Delta f[\alpha(q)]$: the shape of multifractal spectrum. Different letters indicate significant differences at $p < 0.05$. All data are shown using mean \pm standard error. * means median; † means mode.

Source	D_0	D_1	D_2	D_1/D_0	$\alpha(0)$	α_{\max}	α_{\min}	$\Delta\alpha(q)$	$f(\alpha_{\max})$ *1,000	$f(\alpha_{\min})$	$\Delta f[\alpha(q)]$
Vegetation types (VT)	BL ($n = 15$) 0.98 ± 0.01^a	0.90 ± 0.01^a	0.89 ± 0.02^a	0.92 ± 0.01^a	1.73 ± 0.05^a	3.81 ± 0.43^a	0.76 ± 0.03^a	3.04 ± 0.41^a	0.09 ± 0.16^b	0.37 ± 0.09^b	-0.37 ± 0.09^a
	*0.98 †Null	*0.90 †Null	*0.89 †Null	*0.92 †Null	*1.72 †Null	*3.59 †Null	*0.77 †Null	*2.82 †Null	*0.02 †Null	*0.37 †Null	*-0.37 †Null
	GR ($n = 15$) 0.97 ± 0.01^b	0.89 ± 0.01^a	0.89 ± 0.01^a	0.92 ± 0.01^a	1.57 ± 0.04^c	2.92 ± 0.09^b	0.80 ± 0.06^a	2.12 ± 0.09^b	9.16 ± 12.79^a	0.52 ± 0.20^a	-0.51 ± 0.20^b
	*0.97 †Null	*0.89 †Null	*0.88 †Null	*0.92 †Null	*1.57 †Null	*2.88 †Null	*0.79 †Null	*2.11 †Null	*2.80 †Null	*0.46 †Null	*-0.52 †Null
	SH($n = 15$) 0.96 ± 0.01^c	0.86 ± 0.01^b	0.85 ± 0.02^b	0.89 ± 0.01^b	1.62 ± 0.04^b	3.00 ± 0.08^b	0.80 ± 0.04^a	2.20 ± 0.07^b	6.13 ± 8.25^{ab}	0.58 ± 0.06^a	-0.58 ± 0.06^b
	*0.96 †Null	*0.86 †Null	*0.85 †Null	*0.89 †Null	*1.63 †Null	*2.97 †Null	*0.80 †Null	*2.18 †Null	*2.65 †Null	*0.59 †Null	*0.58 †Null
	FO($n = 15$) 0.96 ± 0.01^c	0.83 ± 0.02^c	0.80 ± 0.02^c	0.86 ± 0.01^c	1.65 ± 0.06^b	3.02 ± 0.07^b	0.71 ± 0.05^b	2.31 ± 0.09^b	0.52 ± 9.42^{ab}	0.49 ± 0.09^{ab}	-0.49 ± 0.09^{ab}
	*0.96 †Null	*0.83 †Null	*0.80 †Null	*0.87 †Null	*1.64 †Null	*3.01 †Null	*0.70 †Null	*2.34 †Null	*-2.00 †Null	*0.51 †Null	*-0.52 †Null
	$p < 0.001$	$p < 0.001$	$p < 0.001$	$p < 0.001$	$p < 0.001$	$p < 0.001$	$p < 0.001$	$p < 0.001$	$p = 0.021$	$p < 0.001$	$p < 0.001$
Soil layers (SL)	0–10 cm ($n = 12$) 0.97 ± 0.01^a	0.87 ± 0.03^a	0.85 ± 0.04^a	0.90 ± 0.03^a	1.60 ± 0.08^b	3.03 ± 0.21^a	0.76 ± 0.06^a	2.27 ± 0.23^a	-2.7 ± 5.71^b	0.45 ± 0.13^a	-0.46 ± 0.13^a
	*0.97 †Null	*0.87 †Null	*0.86 †Null	*0.90 †Null	*1.58 †Null	*2.94 †Null	*0.78 †Null	*2.19 †Null	*0.01 †Null	*0.44 †Null	*-0.46 †Null
	10–20 cm ($n = 12$) 0.97 ± 0.01^a	0.87 ± 0.04^a	0.86 ± 0.05^a	0.90 ± 0.03^a	1.62 ± 0.07^{ab}	3.10 ± 0.30^a	0.77 ± 0.06^a	2.33 ± 0.31^a	11.47 ± 13.34^a	0.47 ± 0.14^a	-0.46 ± 0.14^a
	*0.97 †Null	*0.88 †Null	*0.87 †Null	*0.90 †Null	*1.60 †Null	*2.97 †Null	*0.79 †Null	*2.20 †Null	*13.48 †Null	*0.47 †Null	*-0.46 †Null
	20–30 cm ($n = 12$) 0.97 ± 0.01^a	0.87 ± 0.03^a	0.85 ± 0.04^a	0.90 ± 0.02^a	1.62 ± 0.05^{ab}	3.19 ± 0.23^a	0.76 ± 0.06^a	2.43 ± 0.23^a	-0.26 ± 3.53^b	0.49 ± 0.12^a	0.49 ± 0.12^a
	*0.97 †Null	*0.88 †Null	*0.87 †Null	*0.91 †Null	*1.62 †Null	*3.10 †Null	*0.77 †Null	*2.34 †Null	*0.98 †Null	*0.53 †Null	*-0.54 †Null
	30–40 cm ($n = 12$) 0.97 ± 0.01^a	0.87 ± 0.02^a	0.86 ± 0.03^a	0.90 ± 0.02^a	1.67 ± 0.06^{ab}	3.27 ± 0.52^a	0.78 ± 0.06^a	2.49 ± 0.53^a	10.86 ± 9.23^a	0.52 ± 0.17^a	-0.51 ± 0.17^a
	*0.97 †Null	*0.87 †Null	*0.87 †Null	*0.90 †Null	*1.64 †Null	*3.08 †Null	*0.78 †Null	*2.27 †Null	*13.50 †Null	*0.54 †Null	*-0.54 †Null
	40–50 cm ($n = 12$) 0.97 ± 0.01^a	0.87 ± 0.04^a	0.85 ± 0.04^a	0.90 ± 0.03^a	1.69 ± 0.07^a	3.31 ± 0.65^a	0.77 ± 0.05^a	2.54 ± 0.05^a	1.41 ± 1.40^b	0.52 ± 0.16^b	-0.52 ± 0.16^b
	*0.97 †Null	*0.87 †Null	*0.87 †Null	*0.90 †Null	*1.67 †Null	*3.00 †Null	*0.77 †Null	*2.22 †Null	*1.83 †Null	*0.53 †Null	*-0.53 †Null
	$p = 0.789$	$p = 0.987$	$p = 0.993$	$p = 0.999$	$p = 0.008$	$p = 0.452$	$p = 0.941$	$p = 0.505$	$p < 0.001$	$p = 0.738$	$p = 0.760$
VT×SL	$p = 0.090$	$p = 0.007$	$p = 0.081$	$p = 0.263$	$p = 0.679$	$p < 0.001$	$p = 0.943$	$p < 0.001$	$p = 0.096$	$p = 0.970$	$p = 0.973$

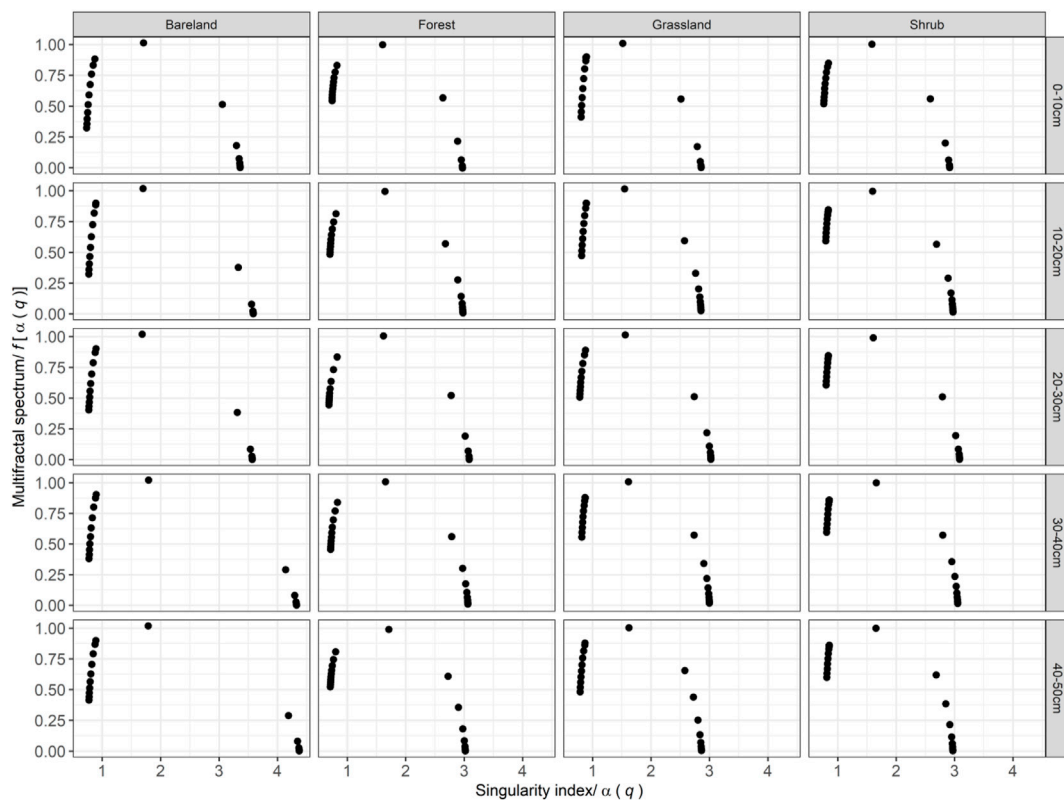


FIGURE 5 | Multifractal spectrum functions of the soil particle-size distribution in different soil layers of four vegetation types in Jiangjiagou Gully.

capacity dimension (D_0) > entropy dimension (D_1) > correlation dimension (D_2) for each vegetation type showed the non-uniformity of the soil PSD, indicating more pronounced non-uniformity in sparse areas than in dense areas (Li et al., 2021b).

Generally, multifractal parameters are higher in bare land than in the other vegetation types (Table 3) except for α_{\min} , $f(\alpha_{\max})$, and $f(\alpha_{\min})$, indicating that the soil PSD in bare land has a wider range or more homogeneous distribution in particle size and a higher heterogeneity. D_0 , D_1 , and D_2 were highest in grassland, intermediate in shrub, and lowest in forest. D_1/D_0 was highest in bare land and grassland, intermediate in shrub, and lowest in forest, whereas α_0 was higher in shrub and forest than in grassland. There were no significant differences in α_{\max} , $\Delta\alpha$, $f(\alpha_{\max})$, and $f(\alpha_{\min})$ across grassland, shrub, and forest, whereas α_{\min} was lower in forest than in the other vegetation types.

There was no significant difference among soil layers in multifractal parameters. The interaction between vegetation type and soil layer only has significant effects on D_1 , α_{\max} and $\Delta\alpha$ (Table 3).

4.3 Multifractal Singularity Spectrum

The multifractal singularity spectra named $\Delta f[\alpha(q)] - \alpha(q)$ curves of all vegetation types across five soil layers are asymmetric, left hook upper, and convex functions (Figure 5), indicating that the soil PSD has heterogeneous and multifractal characteristics. In the right part of all curves, the slope downward to the right are higher in bare land than in the other vegetation types across five soil layers, suggesting that bare land experiencing heavy soil erosion had a higher

superposition of soil particle size. Therefore, the local average singularity ($\alpha(0)$), the width of the multifractal singularity spectrum ($\Delta\alpha(q)$), and the symmetry degree of the multifractal spectrum ($\Delta f[\alpha(q)]$) were significantly higher in bare land than the other vegetation types (Table 3).

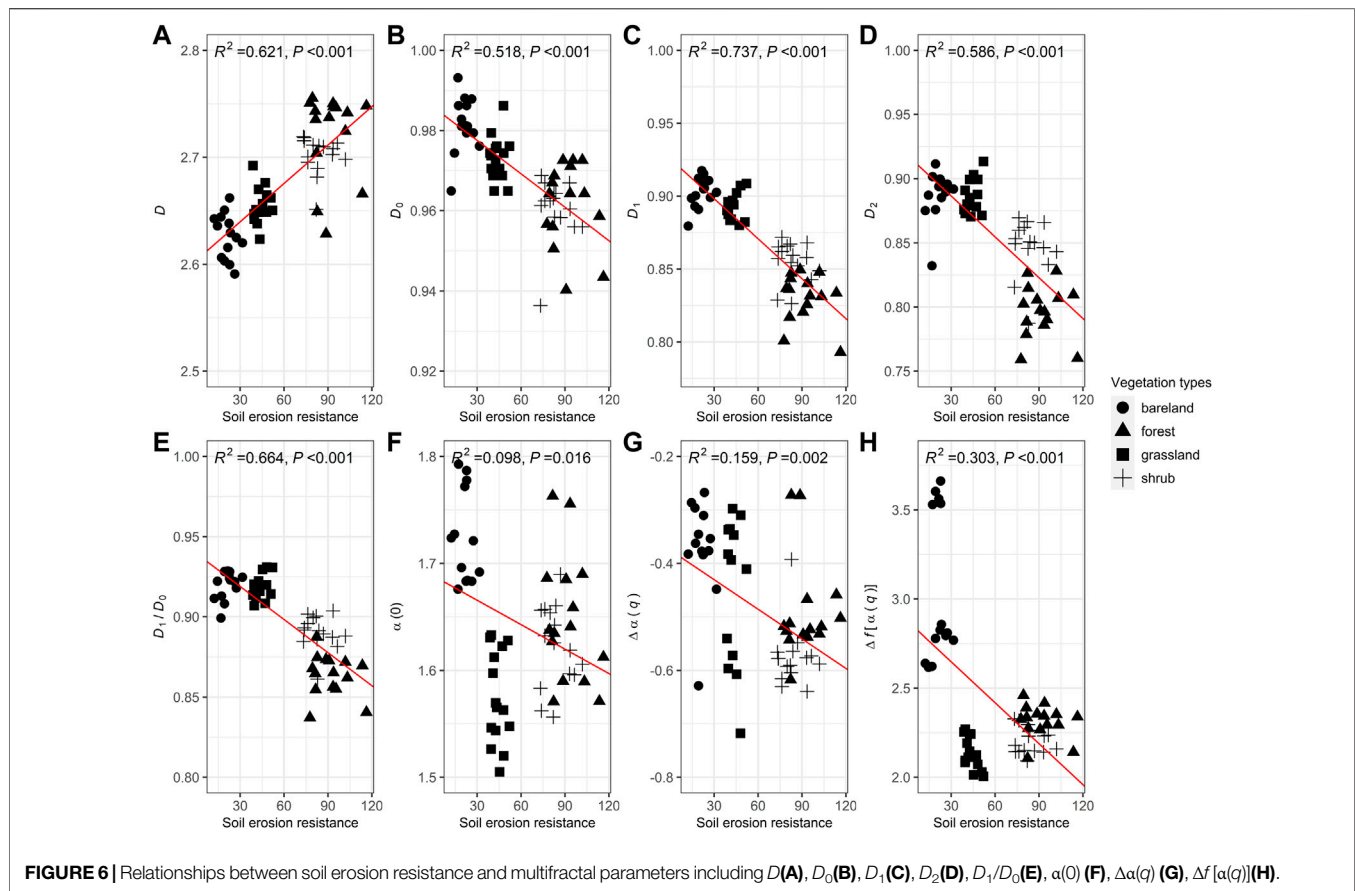
4.4 Relationships Between Multifractal Parameters and Soil Erosion Resistance

Linear regression analysis was conducted between soil erosion resistance and multifractal parameters (D , D_0 , D_1 , D_2 , D_1/D_0 , $\alpha(0)$, $\Delta\alpha(q)$, $\Delta f[\alpha(q)]$) in four vegetation types across five soil layers (Figure 6). We found that soil erosion resistance was significantly negatively correlated with D_0 , D_1 , D_2 , $\alpha(0)$, $\Delta\alpha(q)$, $\Delta f[\alpha(q)]$ but positively with D and D_1/D_0 , indicating that multifractal parameters could represent the ability of vegetation types for soil erosion control to a certain extent.

5 DISCUSSION

5.1 Soil Size Distribution, Volumetric Fractal Dimension, and Soil Erosion Resistance in Different Vegetation Types

Vegetation types can effectively control soil particle size distribution (Gui et al., 2011). Our study proved it that shrub



and forest had significantly higher volume fractions of clay and silt but lower volume fractions of very fine sand, fine sand, medium sand, and coarse sand compared with bare land and grassland, indicating that vegetation with complicated community structure, higher vegetation coverage, and greater species number could improve the soil structure (Liu et al., 2017). In other words, fine particles are easily eroded and detached from surface soil due to stronger soil erosion in younger vegetation communities, such as bare land and grassland. This result is consistent with the findings of Burylo et al. (2012), who suggest that fine particles would be preferentially detached, while coarse particles would be deposited first during water erosion. It has been well documented that soil particle size distribution can affect the structure and properties of soil (Lyu et al., 2015; Ding and Huang, 2017). Volumetric fractal dimension (D) ranging from 2.63 to 2.72 in our study sites is similar to the findings of Peng et al. (2014), who observed that the D value of forest ranged from 2.50 to 2.68. Previous studies also demonstrated that soils had good texture when D values range from 2.60 to 2.80 (Liu et al., 2009; Xu et al., 2013). However, this strategy may not be working in our case, because soils in our study developed from landslide mass (Lin et al., 2019). This may be due to discrepancies in soil formation background, parent material, and development process between our study sites and the other sites.

It is well-known that the effects of vegetation on soil erosion control can increase in accordance with positive community

succession (Lin et al., 2014; Cui et al., 2019). Although our study does not carry out long-term field observations on the process of vegetation succession, it does reveal that soil erosion resistance will fluctuate in different vegetation types. For example, we observed that the community structure, vegetation coverage, and species number increased in order of forest > shrub > grassland > bare land correspondingly; the mean soil erosion resistance is in order of forest > shrub > grassland > bare land. This result is consistent with previous investigations, which highlighted species composition and community structure as the indicators of soil and water conservation (Wang and Liu, 1999; Ma and Jiao, 2005).

However, soil layer did not significantly affect any concerned parameters, indicating that short-term (<40 years) vegetation succession could not change soil properties in soil depth (Zhou et al., 2009).

5.2 Multifractal Features in Different Vegetation Types

Multifractal analysis can capture the inner variations in the soil PSD and the inhomogeneity of its fractal structure using a distributional spectrum (Miranda et al., 2006; Cui et al., 2019; Li et al., 2021b). Capacity dimension (D_0), entropy dimension (D_1), correlation dimension (D_2), and D_1/D_0 could be used to describe the ranges of continuous distribution and particle size distribution, the homogeneity and heterogeneity among fractions, respectively

(Montero, 2005; Miranda et al., 2006). In this study, all soils in four vegetation types across 5 layers showed the trend of $D_0 > D_1 > D_2$, indicating that soils have high-dispersion particle distribution in a disordered system. This result is consistent with the findings of Cui et al. (2019), who observed that trapped sediment similar to the soil in our study displayed such laws.

Bare land and grassland had higher D_1/D_0 values than shrub and forest, suggesting that measures dispersed over the set of sizes in their soils, because D_1/D_0 value close to 1 will indicate sets with similar dimensions (Wang et al., 2008). Similarly, $\alpha(0)$, $\Delta\alpha(q)$, and $\Delta f[\alpha(q)]$ are significantly higher in bare land than in the other vegetation types, indicating that there was a wider range of variability in the heterogeneity of the samples collected from bare land. Therefore, the $\Delta f[\alpha(q)] - \alpha(q)$ curve of bare land across five soil layers is more asymmetric and has a higher slope downward to the right in its right part than the other vegetation types. Therefore, the bare land has a higher superposition of soil particle size. This result is consistent with other studies demonstrating significantly negative impacts of bare land on soil particle size distribution (Cui et al., 2005; Luo et al., 2019).

5.3 Influence of Multifractal Parameters on Soil Erosion Resistance

Soil erosion resistance in all four vegetation types across five soil layers exhibit significant linear correlations with D , D_0 , D_1 , D_2 , D_1/D_0 , $\alpha(0)$, $\Delta\alpha(q)$, and $\Delta f[\alpha(q)]$. It implies that multifractal parameters could represent the ability of soil erosion control by vegetation. However, $\alpha(0)$ and $\Delta\alpha(q)$ are less strongly related with soil erosion resistance than the other six multifractal parameters. In other words, $\alpha(0)$ and $\Delta\alpha(q)$ were not suitable for predicting soil erosion resistance, but the other six multifractal parameters can reveal erosion control effects and determine ecosystem service value of vegetation in eroded lands by considering their capacity for soil erosion resistance, because erosion control of vegetation is listed as one of the 17 major ecosystem services (Costanza et al., 1997). However, this statement should be tempered by the fact that the experiments cannot carry out on-site field observations on the whole process of vegetation succession from bare land to forest. Elucidating the relationships between soil erosion resistance and vegetation types in different soil depths would require additional research.

6 CONCLUSION

In this study, we analyzed the differences in soil particle size distribution, soil erosion resistance and multifractal parameters among four vegetation types (bare land, grassland, shrub, and

forest) across five layers (0–10 cm, 10–20 cm, 20–30 cm, 30–40 cm, and 40–50 cm). Our results suggest that vegetation types significantly affect soil particle size distribution, soil erosion resistance, and multifractal parameters. The generalized dimensions spectra curves of the PSD in four vegetation types across five soil layers are all sigmoidal, whereas the singular spectrum function shows an asymmetric upward convex curve. Despite some limitations, this study provided an important insight for the evaluation of soil structure improvement and the effects of erosion control by vegetation restoration in dry-hot valley area. Future research should extend this work by carrying out long-term on-site field observations to determine the change process of soil properties during vegetation succession.

DATA AVAILABILITY STATEMENT

The original contributions presented in the study are included in the article/Supplementary Material, further inquiries can be directed to the corresponding author.

AUTHOR CONTRIBUTIONS

SL and RG contributed equally to this work and should be considered co-first authors. SL, RG, and YL contributed to the conception and design of the study, submission preparation, and idea discussion. MH, LY, and HY carried out field work and determined soil particle size distribution. SL, RG, CY, and XT performed the statistical analysis. SL, RG, and YL wrote the first draft of the manuscript. JL, and YL contributed to manuscript revision, read, and approved the submitted version.

FUNDING

This work was supported by the joint funds of the Fujian Provincial Natural Science Foundation (Grant No. 2021J01060), the National Natural Science Foundation of China (No. 42071132 and 41790434), and the Key Laboratory of Mountain Hazards and Surface Process, Chinese Academy of Sciences (No. 2019).

ACKNOWLEDGMENTS

We thank Ying Liu, Jingwen He, Yu Cui, and Jianzhao Wu for help collecting the data.

REFERENCES

- Asadi, H., Moussavi, A., Ghadiri, H., and Rose, C. W. (2011). Flow-driven Soil Erosion Processes and the Size Selectivity of Sediment. *J. Hydrology* 406, 73–81. doi:10.1016/j.jhydrol.2011.06.010
- Bieganowski, A., Chojecki, T., Ryzak, M., Sochan, A., and Lamorski, K. (2013). Methodological Aspects of Fractal Dimension Estimation on the Basis of Particle Size Distribution. *Vadose Zone J.* 12 (1), vzj20120064–9. doi:10.2136/vzj2012.0064
- Biswas, A. (2019). Joint Multifractal Analysis for Three Variables: Characterizing the Effect of Topography and Soil Texture on Soil Water Storage. *Geoderma* 334, 15–23. doi:10.1016/j.geoderma.2018.07.035
- Bochet, E., Poesen, J., and Rubio, J. L. (2000). Mound Development as an Interaction of Individual Plants with Soil, Water Erosion and Sedimentation

- Processes on Slopes. *Earth Surf. Process. Landforms* 25, 847–867. doi:10.1002/1096-9837(200008)25:8<847::aid-esp103>3.0.co;2-q
- Burylo, M., Rey, F., Bochet, E., and Dutoit, T. (2012). Plant Functional Traits and Species Ability for Sediment Retention during Concentrated Flow Erosion. *Plant Soil* 353, 135–144. doi:10.1007/s11104-011-1017-2
- Chen, A. M., Deng, H. J., Yan, S. W., Lin, Y. M., Zhang, G. S., and Du, K. (2016). Fractal Features of Soil and Their Relation with Soil Fertility under Five Vegetation in Jiangjiagou Gully. *Mt. Res.* 34 (3), 290–296. doi:10.16089/j.cnki.1008-2786.000130
- Chen, S., Wang, D. J., Mei, Y. L., Chen, X. Y., and Zhang, S. J. (2014). The Research of Grain Composition and Sediment Generation on Landslip-Collapse Soil in Debris Flow Original Area. *Mt. Res.* 32 (1), 66–73. doi:10.16089/j.cnki.1008-2786.2014.01.009
- Costanza, R., d'Arge, R., de Groot, R., Farber, S., Grasso, M., Hannon, B., et al. (1997). The Value of the World's Ecosystem Services and Natural Capital. *Nature* 387, 253–260. doi:10.1016/S0921-8009(98)00020-210.1038/387253a0
- Cui, P., Wang, D. J., and Wei, F. Q. (2005). Model and Effect of Ecological Restoration of Dry-Hot Valley: A Case Study of the CAS Dongchuan Debris Flow Observation Station. *Sci. Soil Water Conserv.* 3, 60–64. doi:10.16843/j.sswc.2005.03.012
- Cui, Y., Li, J., Chen, A., Wu, J., Luo, Q., Rafay, L., et al. (2019). Fractal Dimensions of Trapped Sediment Particle Size Distribution Can Reveal Sediment Retention Ability of Common Plants in a Dry-Hot Valley. *Catena* 180, 252–262. doi:10.1016/j.catena.2019.04.031
- Dai, Z., Ma, C., Miao, L., Li, M., Wu, J., and Wang, X. (2022). Initiation Conditions of Shallow Landslides in Two Man-Made Forests and Back Estimation of the Possible Rainfall Threshold. *Landslides* 19, 1031–1044. doi:10.1007/s10346-021-01823-1
- De Wang, D., Fu, B., Zhao, W., Hu, H., and Wang, Y. (2008). Multifractal Characteristics of Soil Particle Size Distribution under Different Land-Use Types on the Loess Plateau, China. *Catena* 72, 29–36. doi:10.1016/j.catena.2007.03.019
- Deng, H. J., Zhang, G. S., Yu, W., Wu, C. Z., Hong, W., and Lin, Y. M. (2015). Change in Basic Characters and Fractal Dimension of Soil in Destroyed Vegetation Management Region after Earthquake and Their Correlation Analysis. *J. Plant Resour. Environ.* 24 (1), 12–18. doi:10.3969/j.issn.1674-7895.2015.01.02
- Deng, J., Ma, C., and Zhang, Y. (2022). Shallow Landslide Characteristics and its Response to Vegetation by Example of July 2013, Extreme Rainstorm, Central Loess Plateau, China. *Bull. Eng. Geol. Environ.* 81 (3), 1–18. doi:10.1007/s10064-022-02606-1
- Descheemaeker, K., Nyssen, J., Rossi, J., Poesen, J., Haile, M., Raes, D., et al. (2006). Sediment Deposition and Pedogenesis in Exclosures in the Tigray Highlands, Ethiopia. *Geoderma* 132, 291–314. doi:10.1016/j.geoderma.2005.04.027
- Ding, W., and Huang, C. (2017). Effects of Soil Surface Roughness on Interrill Erosion Processes and Sediment Particle Size Distribution. *Geomorphology* 295, 801–810. doi:10.1016/j.geomorph.2017.08.033
- Guan, X. Y., Yang, P. L., and Lv, Y. (2011). Analysis on Spatial Variability of Soil Properties Based on Multifractal Theory. *J. Basic Sci. Eng.* 19 (5), 712–720. doi:10.3969/j.issn.1005-0930.2011.05.003
- Gui, D. W., Lei, J. Q., Zeng, F. J., Mu, G. J., and Li, K. F. (2011). Characteristics of Soil Particle Size Distribution in Different Land-Use Types of Oasis Rim. *Sci. Silvae Sin.* 47 (1), 22–28. doi:10.3969/j.issn.1005-6327.2002.06.007
- Gyssels, G., Poesen, J., Bochet, E., and Li, Y. (2005). Impact of Plant Roots on the Resistance of Soils to Erosion by Water: A Review. *Prog. Phys. Geog.* 29, 189–217. doi:10.1191/0309133305pp443ra
- Jin, X., and Chen, L. H. (2019). Soil Anti-scourability and Surface Root Distribution of Different Vegetation Types in Loess Region of Western Shanxi Province. *Chin. J. Soil Water Conserv.* 33 (6), 120–126. doi:10.13870/j.cnki.stbcxb.2019.06.017
- Li, J.-L., Bao, Y.-h., Wei, J., He, X.-b., Tang, Q., and Nambajimana, J. d. D. (2019). Fractal Characterization of Sediment Particle Size Distribution in the Water-Level Fluctuation Zone of the Three Gorges Reservoir, China. *J. Mt. Sci.* 16, 2028–2038. doi:10.1007/s11629-019-5456-1
- Li, J., He, X., Wei, J., Bao, Y., Tang, Q., Nambajimana, J. d. D., et al. (2021b). Multifractal Features of the Particle-Size Distribution of Suspended Sediment in the Three Gorges Reservoir, China. *Int. J. Sediment Res.* 36, 489–500. doi:10.1016/j.ijsrc.2020.12.003
- Li, J., Liu, Y., Wu, J., He, J. W., He, J., Cui, Y., et al. (2021a). Plant Morphological and Functional Characteristics Combined with Elevation and Aspect Influence Phytogenic Mound Parameters in a Dry-Hot Valley. *J. Soil Water Conserv.* 76 (2), 142–152. doi:10.2489/jswc.2021.00031
- Li, S.-y., Lin, J.-y., Pan, J.-h., Yu, H., Gao, R.-y., and Yang, L.-s. (2021c). Multifractal Characteristics of Soil Particle-Size Distribution Under Different Land-Use Types in an Area with High Frequency Debris Flow. *Chin. J. Appl. Environ. Biol.* 27 (4), 893–900. doi:10.19675/j.cnki.1006-687x.2020.11046
- Lin, Y.-m., Cui, P., Ge, Y.-g., Chen, C., Wang, D.-j., Wu, C.-z., et al. (2014). The Succession Characteristics of Soil Erosion during Different Vegetation Succession Stages in Dry-Hot River Valley of Jinsha River, Upper Reaches of Yangtze River. *Ecol. Eng.* 62, 13–26. doi:10.1016/j.ecoleng.2013.10.020
- Lin, Y., Chen, A., Yan, S., Rafay, L., Du, K., Wang, D., et al. (2019). Available Soil Nutrients and Water Content Affect Leaf Nutrient Concentrations and Stoichiometry at Different Ages of *Leucaena Leucocephala* Forests in Dry-Hot Valley. *J. Soils Sediments* 19, 511–521. doi:10.1007/s11368-018-2029-9
- Liu, L., Liu, Y., Hui, R., and Xie, M. (2017). Recovery of Microbial Community Structure of Biological Soil Crusts in Successional Stages of Shapotou Desert Revegetation, Northwest China. *Soil Biol. Biochem.* 107, 125–128. doi:10.1016/j.soilbio.2016.12.030
- Liu, X., Zhang, G., Heathman, G. C., Wang, Y., and Huang, C.-h. (2009). Fractal Features of Soil Particle-Size Distribution as Affected by Plant Communities in the Forested Region of Mountain Yimeng, China. *Geoderma* 154, 123–130. doi:10.1016/j.geoderma.2009.10.005
- Liu, X., Zhang, G., Heathman, G. C., Wang, Y., and Huang, C.-h. (2009). Fractal Features of Soil Particle-Size Distribution as Affected by Plant Communities in the Forested Region of Mountain Yimeng, China. *Geoderma* 154, 123–130. doi:10.1016/j.geoderma.2009.10.005
- Liu, Z., Qiu, H., Ma, S., Yang, D., Pei, Y., Du, C., et al. (2021). Surface Displacement and Topographic Change Analysis of the Changhe Landslide on September 14, 2019, China. *Landslides* 18 (4), 1471–1483. doi:10.1007/s10346-021-01626-4
- Liu, Y., Qiu, H., Yang, D., Liu, Z., Ma, S., Pei, Y., et al. (2022). Deformation Responses of Landslides to Seasonal Rainfall Based on InSAR and Wavelet Analysis. *Landslides* 19, 199–210. doi:10.1007/s10346-021-01785-4
- Luo, Q. H., Wu, J. Z., Cui, Y., Sun, F., Lin, Y. M., Wang, D. J., et al. (2019). Characteristics of Soil Properties and Fractal Dimensions of Destroyed and Naturally Restored Forest Land under Flood Disaster Disturbance. *Chin. J. Appl. Environ. Biol.* 25 (1), 29–37. doi:10.19675/j.cnki.1006-687x.2018.04032
- Lyu, X., Yu, J., Zhou, M., Ma, B., Wang, G., Zhan, C., et al. (2015). Changes of Soil Particle Size Distribution in Tidal Flats in the Yellow River Delta. *PLoS One* 10 (3), e0121368. doi:10.1371/journal.pone.0121368
- Ma, C., Wang, Y.-j., Du, C., Wang, Y.-q., and Li, Y.-p. (2016). Variation in Initiation Condition of Debris Flows in the Mountain Regions Surrounding Beijing. *Geomorphology* 273, 323–334. doi:10.1016/j.geomorph.2016.08.027
- Ma, S., Qiu, H., Hu, S., Yang, D., and Liu, Z. (2021). Characteristics and Geomorphology Change Detection Analysis of the Jiangdingya Landslide on July 12, 2018, China. *Landslides* 18, 383–396. doi:10.1007/s10346-020-01530-3
- Ma, X. H., and Jiao, J. Y. (2005). Characteristics of Vegetation with Natural Restoration in Removal Lands in Loess Hilly-Gully Region and the Relationship between the Characteristics and Soil Environment. *Sci. Soil Water Conserv.* 3 (2), 15–22. doi:10.3969/j.issn.1672-3007.2005.02.004
- McVicar, T. R., Van Niel, T. G., Li, L., Wen, Z., Yang, Q., Li, R., et al. (2010). Parsimoniously Modelling Perennial Vegetation Suitability and Identifying Priority Areas to Support China's Re-vegetation Program in the Loess Plateau: Matching Model Complexity to Data Availability. *For. Ecol. Manag.* 259, 1277–1290. doi:10.1016/j.foreco.2009.05.002
- Miranda, J. G. V., Montero, E., Alves, M. C., Paz González, A., and Vidal Vázquez, E. (2006). Multifractal Characterization of Saprolite Particle-Size Distributions after Topsoil Removal. *Geoderma* 134, 373–385. doi:10.1016/j.geoderma.2006.03.014

- Montero, E. (2005). Rényi Dimensions Analysis of Soil Particle-Size Distributions. *Ecol. Model.* 182, 305–315. doi:10.1016/j.ecolmodel.2004.04.007
- Peng, G., Xiang, N., Lv, S.-q., and Zhang, G.-c. (2014). Fractal Characterization of Soil Particle-Size Distribution under Different Land-Use Patterns in the Yellow River Delta Wetland in China. *J. Soils Sediments* 14 (6), 1116–1122. doi:10.1007/s11368-014-0876-6
- Perfect, E., and Kay, B. D. (1995). Applications of Fractals in Soil and Tillage Research: A Review. *Soil Tillage Res.* 36, 1–20. doi:10.1016/0167-1987(96)81397-3
- Podwojewski, P., Janeau, J. L., Grellier, S., Valentin, C., Lorentz, S., and Chaplot, V. (2011). Influence of Grass Soil Cover on Water Runoff and Soil Detachment under Rainfall Simulation in a Sub-humid South African Degraded Rangeland. *Earth Surf. Process. Landforms* 36, 911–922. doi:10.1002/esp.2121
- Rodríguez-Lado, L., and Lado, M. (2017). Relation between Soil Forming Factors and Scaling Properties of Particle Size Distributions Derived from Multifractal Analysis in Topsoils from Galicia (NW Spain). *Geoderma* 287, 147–156. doi:10.1016/j.geoderma.2016.08.005
- Schillereff, D. N., Chiverrell, R. C., Macdonald, N., and Hooke, J. M. (2014). Flood Stratigraphies in Lake Sediments: A Review. *Earth-Science Rev.* 135, 17–37. doi:10.1016/j.earscirev.2014.03.011
- Shi, Z. H., Fang, N. F., Wu, F. Z., Wang, L., Yue, B. J., and Wu, G. L. (2012). Soil Erosion Processes and Sediment Sorting Associated with Transport Mechanisms on Steep Slopes. *J. Hydrology* 454–455, 123–130. doi:10.1016/j.jhydrol.2012.06.004
- Su, Y. Z., Zhao, H. L., Zhao, W. Z., and Zhang, T. H. (2004). Fractal Features of Soil Particle Size Distribution and the Implication for Indicating Desertification. *Geoderma* 122, 43–49. doi:10.1016/j.geoderma.2003.12.003
- Tian, X. F., Su, F. H., Guo, X. J., Liu, J. J., and Li, Y. (2020). Material Sources Supplying Debris Flows in Jiangjia Gully. *Environ. Earth Sci.* 79 (13), 1–20. doi:10.1007/s12665-020-09020-4
- Tyler, S. W., and Wheatcraft, S. W. (1992). Fractal Scaling of Soil Particle-Size Distributions: Analysis and Limitations. *Soil Sci. Soc. Am. J.* 56 (2), 362–369. doi:10.2136/sssaj1992.03615995005600020005x
- Wang, D. J., Cui, P., Zhu, B., and Wang, Y. K. (2004). Vegetation Rehabilitation Techniques and Ecological Effects in Dry-Hot Valley of Jinsha River. *J. Soil Water Conserv.* 18 (5), 95–98. doi:10.13870/j.cnki.stbcbx.2004.05.024
- Wang, G. L., Zhou, S. L., and Zhao, Q. G. (2005). Volume Fractal Dimension of Soil Particles and its Applications to Land Use. *Acta Pedol. Sin.* 42 (4), 545–550. doi:10.3321/j.issn:0564-3929.2005.04.003
- Wang, H. S., and Liu, G. S. (1999). Analyses on Vegetation Structures and Their Controlling Soil Erosion. *J. Arid. Land Resour. Environ.* 13 (2), 62–68.
- Wang, J., Zhang, J., and Feng, Y. (2019). Characterizing the Spatial Variability of Soil Particle Size Distribution in an Underground Coal Mining Area: An Approach Combining Multi-Fractal Theory and Geostatistics. *Catena* 176, 94–103. doi:10.1016/j.catena.2019.01.011
- Wei, X.-l., Chen, N.-s., Cheng, Q.-g., He, N., Deng, M.-f., and Tanoli, J. I. (2014). Long-term Activity of Earthquake-Induced Landslides: A Case Study from Qionghai Lake Basin, Southwest of China. *J. Mt. Sci.* 11, 607–624. doi:10.1007/s11629-013-2970-4
- Xie, X. J., and Wei, F. Q. (2011). Characteristics of Soil Particle Fractal Dimension under Different Coverage Grassland of the Area with High-Frequency Debris Flow. *J. Soil Water Conserv.* 25 (4), 202–206. doi:10.13870/j.cnki.stbcbx.2011.04.053
- Xu, G., Li, Z., and Li, P. (2013). Fractal Features of Soil Particle-Size Distribution and Total Soil Nitrogen Distribution in a Typical Watershed in the Source Area of the Middle Dan River, China. *Catena* 101, 17–23. doi:10.1016/j.catena.2012.09.013
- Xu, W. X., Bao, Y. H., Wei, J., Yang, L., He, X. B., and Li, J. L. (2019). Effects of Typical Herbaceous Roots on Soil Scour Resistance in Water-Level-Fluctuation Zone of Reservoir. *Chin. J. Soil Water Conserv.* 33 (4), 65–71+109. doi:10.13870/j.cnki.stbcbx.2019.04.010
- Yang, D., Qiu, H., Ma, S., Liu, Z., Du, C., Zhu, Y., et al. (2022). Slow Surface Subsidence and its Impact on Shallow Loess Landslides in a Coal Mining Area. *Catena* 209, 105830. doi:10.1016/j.catena.2021.105830
- Zhang, J. R., Wang, J. M., Zhu, Y. C., Li, B., and Wang, P. (2017). Application of Fractal Theory on Pedology: A Review. *Chin. J. Soil Sci.* 48 (1), 221–228. doi:10.19336/j.cnki.trtb.2017.01.29
- Zhang, P., Yao, W., Liu, G., Xiao, P., and Sun, W. (2020). Experimental Study of Sediment Transport Processes and Size Selectivity of Eroded Sediment on Steep Pisha Sandstone Slopes. *Geomorphology* 363, 107211. doi:10.1016/j.geomorph.2020.107211
- Zhou, X. F., Zhao, R., Li, Y. Y., and Chen, X. Y. (2009). Effects of Land Use Types on Particle Size Distribution of Reclaimed Alluvial Soils of the Yangtze Estuary. *Acta Ecol. Sin.* 29 (10), 5544–5551. doi:10.3321/j.issn:1000-0933.2009.10.044
- Zhou, W., Qiu, H., Wang, L., Pei, Y., Tang, B., Ma, S., et al. (2022). Combining Rainfall-Induced Shallow Landslides and Subsequent Debris Flows for Hazard Chain Prediction. *Catena* 213, 106199. doi:10.1016/j.catena.2022.106199

Conflict of Interest: The authors declare that the research was conducted in the absence of any commercial or financial relationships that could be construed as a potential conflict of interest.

Publisher's Note: All claims expressed in this article are solely those of the authors and do not necessarily represent those of their affiliated organizations, or those of the publisher, the editors and the reviewers. Any product that may be evaluated in this article, or claim that may be made by its manufacturer, is not guaranteed or endorsed by the publisher.

Copyright © 2022 Li, Gao, Huang, Yang, Yu, Yu, Tian, Li and Lin. This is an open-access article distributed under the terms of the Creative Commons Attribution License (CC BY). The use, distribution or reproduction in other forums is permitted, provided the original author(s) and the copyright owner(s) are credited and that the original publication in this journal is cited, in accordance with accepted academic practice. No use, distribution or reproduction is permitted which does not comply with these terms.



OPEN ACCESS

EDITED BY
Haijun Qiu,
Northwest University, China

REVIEWED BY
Wensong Wang,
Chengdu University of Technology,
China
Lei Wang,
Ludong University, China
Wei Lu,
Shandong University, China

*CORRESPONDENCE
Canming Yuan,
3187805991@qq.com

SPECIALTY SECTION
This article was submitted to
Geohazards and Georisks,
a section of the journal
Frontiers in Earth Science

RECEIVED 29 April 2022
ACCEPTED 08 July 2022
PUBLISHED 26 August 2022

CITATION
Zhou Y, Ji J, Hu X, Hu S, Wu X, Yuan C
and Zhu T (2022), Comprehensive
analysis of the stability of tailings-
geotextile composite—Iron Mine
Tailings Dam in Gushan, Anhui, China.
Front. Earth Sci. 10:931714.
doi: 10.3389/feart.2022.931714

COPYRIGHT
© 2022 Zhou, Ji, Hu, Hu, Wu, Yuan and
Zhu. This is an open-access article
distributed under the terms of the
[Creative Commons Attribution License
\(CC BY\)](https://creativecommons.org/licenses/by/4.0/). The use, distribution or
reproduction in other forums is
permitted, provided the original
author(s) and the copyright owner(s) are
credited and that the original
publication in this journal is cited, in
accordance with accepted academic
practice. No use, distribution or
reproduction is permitted which does
not comply with these terms.

Comprehensive analysis of the stability of tailings-geotextile composite—Iron Mine Tailings Dam in Gushan, Anhui, China

Yuxin Zhou^{1,2}, Jinzhi Ji³, Xuelong Hu⁴, Shengsong Hu³,
Xiaogang Wu^{1,2}, Canming Yuan^{1,2,5*} and Tianqiang Zhu⁵

¹Sinosteel Maanshan General Institute of Mining Research Co., LTD, Maanshan, China, ²State Key Laboratory of Safety and Health for Metal Mines, Maanshan, China, ³322 Geological Team of Anhui Provincial Bureau of Geology and Mineral Exploration, Maanshan, China, ⁴School of Mining Engineering, Anhui University of Science and Technology, Huainan, China, ⁵School of Resources and Environmental Engineering, Jiangxi University of Science and Technology, Ganzhou, China

The application of tailings-geotextile composites can effectively reduce tailings dam safety accidents. In this paper, the tailings dam of the Gushan Iron Mine is the research background. The construction of tailings-geotextile composites was briefly studied. Based on the existing experimental data, the permeability and physical properties of the composite material were analyzed, and the model of the composite material was generalized. The seepage characteristics of the composite were analyzed by using the numerical simulation method of the seepage field. Finally, the overall stability of the composite during the construction and storage phases was investigated. The conclusions are as follows: 1) In the early stage of stacking, the permeability coefficient of the composite body increases with the increase in filling tension; in the later stage, under the action of excess pore pressure, the composite body still exhibits strong permeability; 2) In the early stage of stacking, the height of the composite body is low, and the relative position of the saturated zone is relatively high; as the composite continues to rise or the stacking time increases, the lower part of the composite is gradually consolidated, and the position of the saturated zone is gradually raised; when the stacking is stopped, the saturated zone gradually decreases until it is close to the original position; 3) With the increase in the stacking height of the composite, the safety factor decreases rapidly; when the stacking height is 22.0 m, it decreases to the minimum; with time, the stability of the composite will gradually increase. This study helps people understand tailings-geotextile composites, and it has significant reference value for practical engineering.

KEYWORDS

tailings-geotextile composites, tailings dam, seepage characteristics, numerical simulation, stability

1 Introduction

A tailings dam, like a dam structure used for pile mine wastes in the case of dam failure, will bring immeasurable loss (Rahardjo et al., 2005; Cao et al., 2019; Yang et al., 2021). At present, tailings disposal technologies mainly include open-pit tailings discharge, wet discharge of tailings ponds, and dry stacking of tailings (Duan et al., 2013). Among them, tailings-geotextile composite heap dry backfilling materials technology can enhance the penetration of consolidation characteristics, and chambers rapidly drain the water body, effectively improve the safety and stability of tailings dam. In recent years, due to the demand for practical engineering, research on tailings-geotextile composites and their properties has developed rapidly (Wang et al., 2022; Wu et al., 2022).

Researchers mainly study the properties of the composite through direct shear and pull-out tests, but triaxial compression tests are also an effective means to study the properties of the composite. For example, Koerner (2000) performed a triaxial test and analyzed the influence of confining pressure, the influence law of the soil, and the complex shear strength index; Khedkar and Mandal (2009) compared the three kinds of pure sand under confining pressure and single complex and double complex stress-strain curves; Khaniki and Daliri (2013) analyzed the influence of confining pressure on the shear strength index of plain soil and composite through the triaxial test of composite; Chen et al. (2014) conducted consolidation drainage and consolidation undrained tests, respectively, and analyzed the shear complex microstructure in the process of change; and Nouri et al. (2016) studied the triaxial monotonous mechanical properties of the composite drainage conditions.

In terms of model testing, scholars have also conducted much work, and useful conclusions have been drawn. Pincus et al. (1993) studied a large chamber to enhance the soil confining effect for large chamber reinforced silica sand and limestone; Liu et al. (2014), Chen et al. (2015), Zhao et al. (2016), and Li et al. (2022) carried out model tests of the overtopping failure of the tailings dam. Zhao et al. revealed that the composite can effectively reduce the flood overtopping damage of the tailings dam.

Due to the complex interaction mechanism between the tailings-geotextile composite and the surrounding tailings, researchers still have an insufficient understanding of its physical structure stability. This paper takes the Gushan Iron Mine tailings dam as the research background. According to the existing test data, the permeability and physical and mechanical properties of the composite are analyzed, and the model of the composite is generalized. Second, the seepage characteristics of the composite were analyzed by a numerical simulation method. Finally, the overall stability of the composite during the construction and storage phases is investigated.

2 Construction of tailings-geotextile composites

2.1 Selection of geosynthetics

Geosynthetics are various types of geotechnical products made of synthetic polymers (such as plastics, chemical fibers, synthetic rubber, etc.) as raw materials. Because the geotechnical materials in the tailings-geotextile composite dry stack need to meet the requirements of high strength and good anti-aging properties, the geotechnical materials need to be made of polyester chemical materials. Due to the same porosity, the penetration rate of woven polyester geotextile is higher than that of nonwoven type, so in the composite dry pile of tailings-geotextile, we choose woven polyester geotextile to make geosynthetic material (Liu et al., 2002).

To increase the strength of the composite and the frictional resistance between layers, we added reinforcement materials, such as geobelt or geogrids, between the monomers. To increase the permeability of the complex, we need to add drainage strips, drain pipes, or plastic blind trenches to the complex.

2.2 Research on the stacking technology of complexes

The tailings-geotextile composite dry stacking is a process of converting tailings from suspended liquid to a solid state. The technological process is to first concentrate the tailings produced by the dressing plant into 20%–40% slurry, and then the slurry is pressed into the geoform bag by the slurry pump. Under the action of slurry pressure, self-gravity, and external force, the water in the slurry is discharged through the geotechnical bag. As the water content of the slurry gradually decreases and the slurry concentration increases, the tailings gradually consolidate, and the tailings and geotextile gradually become reinforced soil, forming a tailings-geotextile composite with higher strength (Figure 1).

From the dry stacking process of the tailings-geotextile composite, it can be seen that the whole process can be divided into the initial concentration stage of tailings slurry, the stage of tailings slurry transportation, the stage of tailings slurry filling and sedimentation dehydration and compaction consolidation and the final greening and reclamation stage. From the system point of view, it can be divided into a dense system, conveying system, natural filter press system, and auxiliary system (including greening, wastewater recovery, monitoring, and other subsystems).

2.2.1 Initial concentration process of tailings slurry

The concentration of tailings pulp produced by the dressing plant is generally low, and the original pulp needs to be concentrated to a concentration of 20%–40% by thickening equipment.

2.2.2 Tailings slurry transportation process

The tailings conveying process mainly includes conveying equipment, conveying concentration, and conveying pressure. Among them, the slurry transport concentration is an important index affecting the dry pile of tailings geotextiles. Through the experimental test, this study chose a pulp conveying concentration of 25%–35%.

2.2.3 Tailings slurry filling and sedimentation dehydration and compaction consolidation process

In this study, the following points should be noted. The size of the geotechnical bag is generally 60~600 m³; when the slurry concentration is 30%, the flow rate of the slurry is approximately 2 m/s; the better the permeability and consolidation of the tailings are, the larger the layer thickness of the composite should be.

3 Characteristics of composite and analysis of models

This study was carried out at the tailings dam of the Gushan Iron Mine in Anhui Province (Figure 2).

3.1 Research on the permeability characteristics of the composite

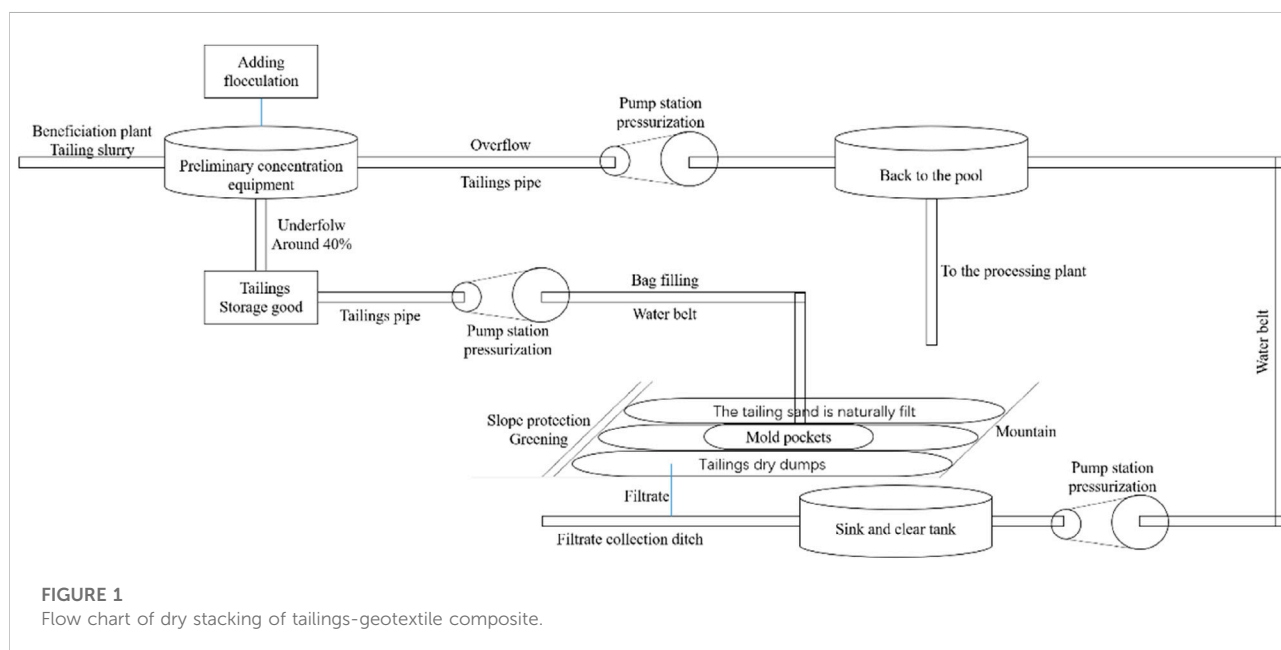
When conducting the composite permeability test on-site, we used slurry (taking tailings slag as raw material) pumps to fill 20 m × 4 m mold bags, and the seepage water was measured by a water meter. The specific test plan is as follows (Figure 3):

3.1.1 Experimental preparation

- (1) Before sampling, use the sample bucket to sample 40 samples *in situ*;
- (2) Sew the geotextile into a bucket bag with a bag length of 1,000 mm and a width of 800 mm.

3.1.2 Experimental body stacking

- (1) Level the test site, and then lay geomembrane to collect seepage water;
- (2) Divide the tailings sample into several equal parts with a bench scale, each 52.45 kg of tailings;
- (3) Pour the tailings into the mixing tank, add 11.65 kg of water to the tailings;
- (4) Pour the prepared tailings slurry into the geotextile bag; start the timer at the same time.
- (5) Seal the geotextile bag and place it horizontally;
- (6) In the process of horizontal placement, the water seepage amount of the complex per unit time is collected through the geomembrane;
- (7) Repeat steps 3–5 to bag the slurry, spread it out, and stack it in layers. There are 4 layers in total in this experiment.
- (8) After the complex is built up, it is left to stand for dehydration, and the test is carried out.



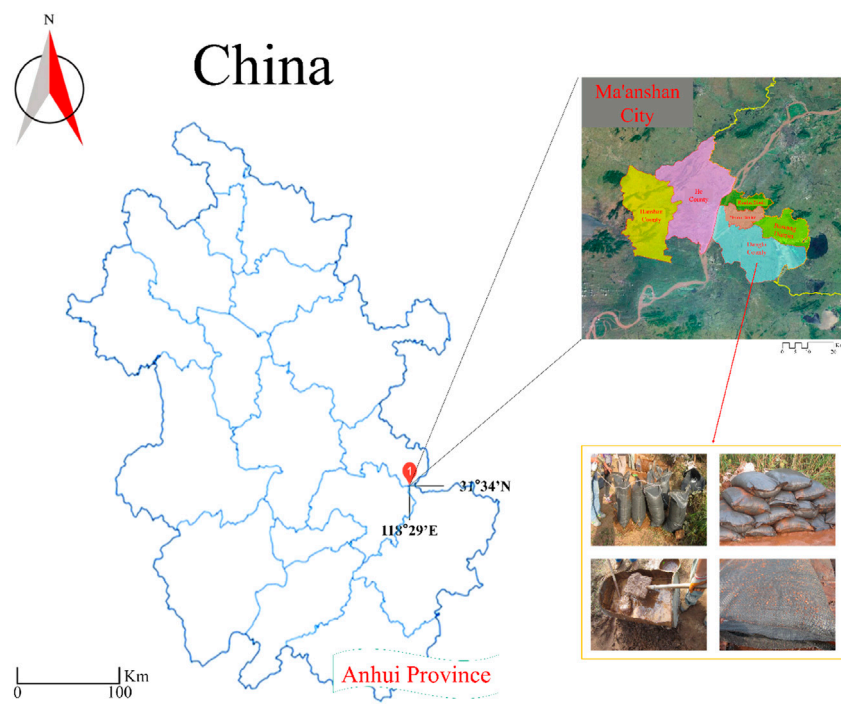


FIGURE 2
Project background picture.



FIGURE 3
Test process display diagram.

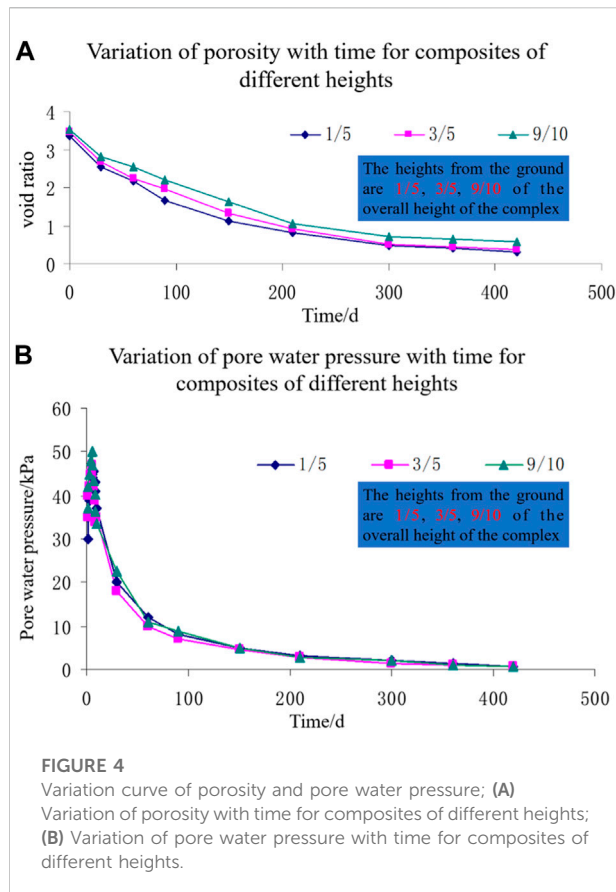


Figure 4A shows the variation in porosity with time for composites of different heights (taking the average value of multiple measurements). The rate of decrease in the void ratio of composites with different heights is not the same. Under the action of self-gravity, the void ratio of the upper part of the composite is slightly higher than that of the lower part of the composite.

Figure 4B shows the variation in pore water pressure with time for composites of different heights (taking the average value of multiple measurements). The pore water pressure at the bottom of the complex is higher than that at the top. This shows that the greater the external force applied to the complex, the faster the complex is excreted. External pressure aids in the drainage of the complex.

Based on the above analysis and experimental phenomena, we can conclude the following:

- (1) In the absence of packing pressure, the flow regime of water passing through the composite is very close to laminar flow. In the later stage, the water permeability of the composite decreases obviously with the increasing sand filling amount. However, the permeability of the composite will gradually increase under the action of filling pressure or external vibration force. When it increases to a certain value, the

permeability of the composite gradually decreases and finally tends to be stable.

- (2) In the early stage of filling, the permeability coefficient of the composite body is relatively large; as the tailings in the composite body are consolidated, the water content decreases, and the reverse filter layer is gradually formed near the geotextile. The permeability coefficient of the composite body gradually decreases (Figure 5). After the tailings are consolidated, the permeability of the composite is very weak and even becomes a relative water barrier.

3.2 Research on the physical and mechanical properties of the composite

In this study, the tailings-geotextile composite is a composite material composed of geotextile and tailings. Zhang et al. (2012) conducted a triaxial numerical simulation of the shear strength of the composite, Zhu et al. (2013) studied the interfacial friction strength characteristics of the composite woven bag, and Qin and Fu (2016) conducted a consolidation test of the composite (the above research is the source of some basic data of this paper). This leads to the following conclusions.

The physical and mechanical properties of the composite show the characteristics of the tailings-geotextile composite material. The deformation of the same composite decreases with the increasing strength of the geotextile. The strength of the composite increases gradually with increasing consolidation time. However, the geotextile has a limited effect on the increase in the internal friction angle of the composite, and it has a greater effect on the increase in cohesion. The effect of geotextiles on improving the shear strength of tailings sand is mainly reflected in increasing the “cohesion” of tailings, while the friction angle remains unchanged.

3.3 Model research

From the engineering characteristics of the tailings geotextile composite dry heap, the composite can be generalized into the following three models during stability analysis (Zhang, 2019):

3.3.1 Masonry model

The composite is layered and superimposed by tailings and geotextiles at different times. The composite has the characteristics of layering. The entire composite can be regarded as a single filling body. (Figure 6A). The model needs to know the physical and mechanical parameters, infiltration parameters, friction parameters between monomers, foundation parameters, and environmental parameters of a single dry stack during composite analysis.

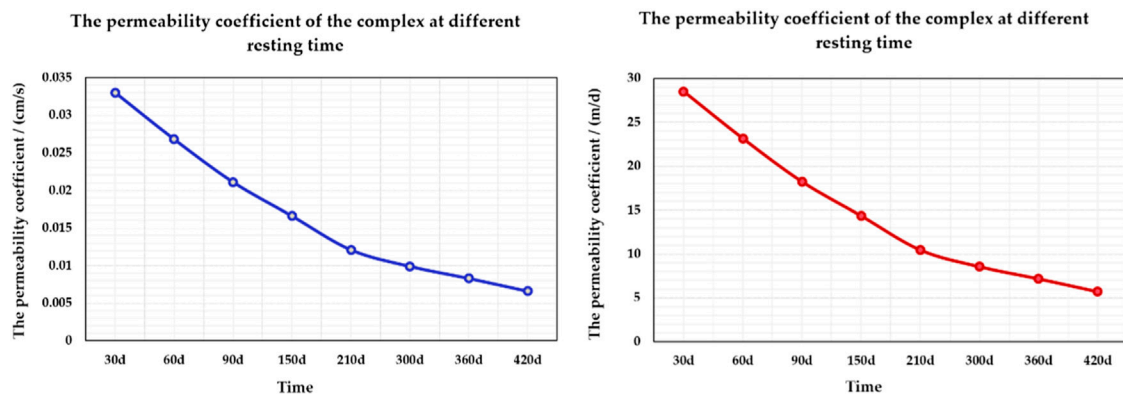


FIGURE 5

The permeability coefficient of the composite at different resting times.

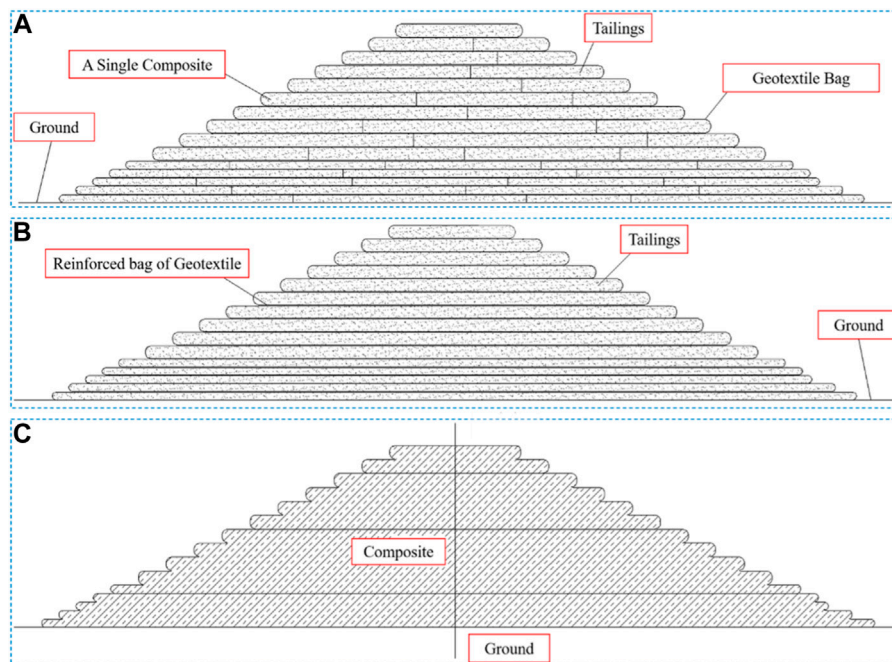


FIGURE 6

Models of the complex; (A) masonry model; (B) reinforcement model; (C) overall model.

3.3.2 Reinforcing model

The reinforcement model is to generalize the tailings in the composite into a whole (if there are areas with different physical and mechanical properties, the composite can be divided according to the properties), and the geotextile in the composite is generalized into the reinforcement of the tailings, that is, reinforcement (Figure 6B). The model needs to know the physical and mechanical parameters of tailings and

geotextiles, infiltration parameters, grip performance parameters, foundation parameters, and environmental parameters between tailings and geotextiles during composite analysis.

3.3.3 Overall model

The overall model is to generalize the composite into an enhanced “tailings body”. If the complex is homogeneous, it

can be generalized as a whole; if there are regions with different physical and mechanical properties, the complexes with the same properties can be divided into a region and then combined into a whole (Figure 6C). When analyzing the model, it is necessary to know the physical and mechanical parameters, infiltration parameters, foundation parameters, and environmental parameters of the complex.

It is theoretically feasible to analyze and compare the above three models and can be selected according to the known conditions in the specific analysis. Using the first and third models, a large number of medium-sized composite material tests need to be done before the analysis and calculation. For example, considering the time strength, the test volume is larger and more complicated. Generally, it is difficult to have the required model before design. Parameters can only be designed based on empirical data. When using the second model, only some small experiments are needed, and the analytical parameters are easier to obtain.

4 Numerical simulation analysis of composite seepage

4.1 Overview

The seepage of the tailings-geotextile composite dry heap is mainly divided into two stages: the construction stage and the storage stage. In these two phases, in addition to the same boundary conditions of groundwater source recharge and rainwater recharge, they are also recharged by the construction water source on the upper part of the complex during the construction phase.

Both rainfall and construction water supply are intermittently supplied, and a large number of experimental studies show that intermittent water supply makes the medium in a saturated-unsaturated state. Studies have shown that the stability of the slope is greatly influenced by the internal groundwater (infiltration line or saturation zone). Therefore, it is necessary to analyze and study the changes in water in the composite.

Due to the nonlinearity of the governing equations of saturated-unsaturated seepage, the complexity of the solution domain boundary, and the wide application of electronic computers, numerical methods have become the dominant method for solving saturated-unsaturated seepage fields. To ensure the solution accuracy of the numerical method, it is necessary to establish a suitable saturated-unsaturated mathematical and physical model according to the actual situation.

In porous media, the motion law of saturated water generally conforms to Darcy's law (Gray and O'Neill, 1976;

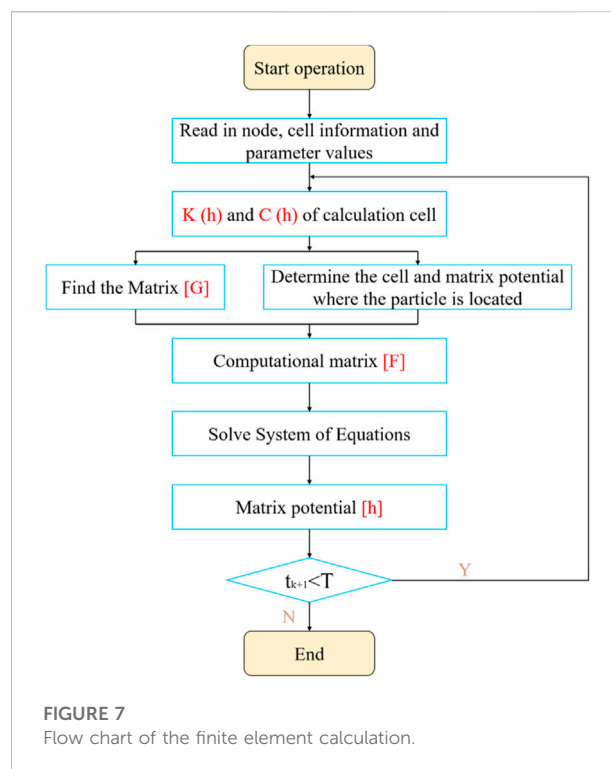


FIGURE 7
Flow chart of the finite element calculation.

Whitaker, 1986). According to Darcy's law, the basic equation of unsaturated seepage in a continuum can be extended to Eq. 1.

$$\frac{\partial \theta}{\partial t} = \frac{\partial \left[k(\theta) \frac{\partial H}{\partial x} \right]}{\partial x} + \frac{\partial \left[k(\theta) \frac{\partial H}{\partial y} \right]}{\partial y} + \frac{\partial \left[k(\theta) \frac{\partial H}{\partial z} \right]}{\partial z} \quad (1)$$

θ —the volumetric moisture content—time H —the total head, $H = h + z$ —the position head—pressure head K —the permeability coefficient x, y, z —the coordinates

This equation is a basic equation with matrix potential having the dependent variable. In the specific operation, it is solved according to the characteristic finite element principle. The block diagram of the finite element program is shown in Figure 7.

4.2 Basic parameters for the numerical simulation of composite seepage

4.2.1 Model size

The composite size is shown in Figure 8A. The height of the pile is 40 m, the slope ratio is 1:2, and the height of a single bag of the complex is 1.0 m. It takes 30 days to pile up 0~4.0, 4.0~8.0, 8.0~12.0 m, and 12~16.0 and 16.0 m, respectively. It takes 60 days for each of ~22.0 m, 90 days for 22.0~28.0 m, and 60 days for 28.0~34.0 and 34.0~40.0 m.

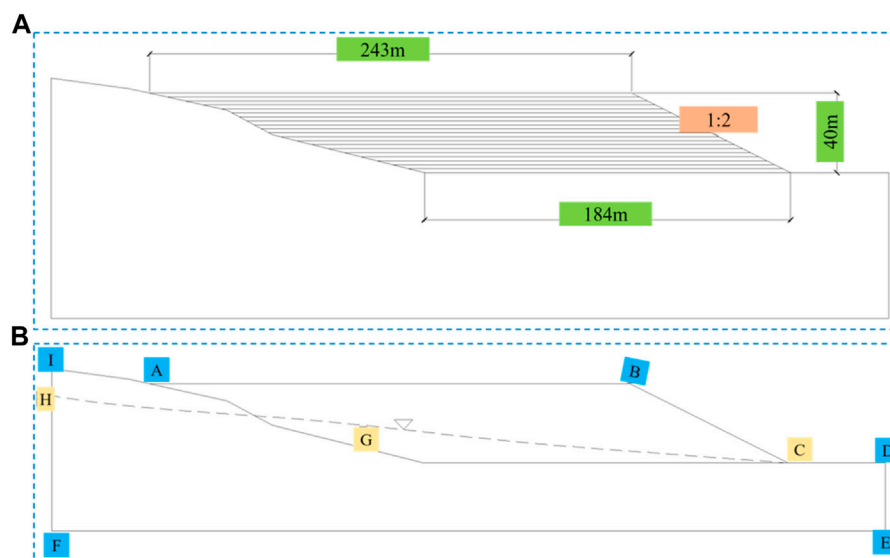


FIGURE 8

Basic parameters for numerical simulation of composite seepage; (A) Schematic diagram of the assumed composite geometry; (B) Schematic diagram of hypothetical complex hydrogeological boundary conditions.

4.2.2 Boundary conditions

The hydrogeological conditions of the complex are shown in Figure 8B. D-E-F-H-I is the flow boundary, I-A-B-C-D is the rainfall infiltration boundary, where B-C-D is the boundary of the saturated escape surface, and the dotted line H-G-C is the saturated infiltration water surface formed by groundwater, the upper part is the unsaturated area, and the lower part is the saturated area.

4.2.3 Calculation parameters

The permeability coefficients of the composite at different times are shown in Figure 5. In the analysis, the foundation permeability coefficient is assumed to be 5×10^{-7} cm/s, that is, it is assumed to be a relative water barrier. The permeability coefficient of the geotextile is taken as the permeability coefficient of sample A: 1.02×10^{-2} cm/s. In this analysis, the rain intensity is 0.22 mm/min, and the water replenishment intensity of the upper construction is $38.6 \text{ m}^3/\text{d}/\text{m}$, that is, the water replenishment intensity is 26.79 mm/min. The impact of groundwater was not considered in the study.

4.3 Numerical simulation results and analysis

The study simulated the changes in the saturation zone of the hypothetical complex at 30, 60, 90, 150, 210, 300, 360, and 420 days. The simulation results are shown in Figure 9.

According to the process of composite dry stacking, the composite is mainly supplied by slurry water and rainwater

during the construction and storage stages. When there is no direct water supply around the composite, the saturated-unsaturated theory can be used to simulate and analyze the water movement in the composite (Srivastava and Yey, 1991; Diersch and Perrochet, 1999; He et al., 2015).

From Figures 9A–H, it can be seen that under the action of only rainwater and slurry water, the following rules exist:

- (1) In the initial stage of stacking, due to the large permeability coefficient of tailings and the small height of the complex, the relative position of the saturated zone is relatively high;
- (2) With time, the composite body increases continuously, the lower composite body gradually consolidates, its permeability coefficient gradually decreases, almost becomes an impermeable layer, and the saturated zone gradually rises; when the stacking is stopped, due to the lack of a water source in the upper part Replenishment, the saturation zone gradually declines until it is close to the original position.
- (3) When rainwater or slurry water is continuously replenished, seepage water or rainwater gathers from the surface of the lower complex to the bottom of the slope. If there is no drainage channel at the bottom of the slope, it accumulates at the bottom of the slope, and the water flow at the bottom of the slope infiltrates in a near-vertical direction.

In other words, when the permeability coefficient of tailings in the complex is large, the relative position of the infiltration line is high (Kansoh et al., 2020); as the dam body continues to rise, the lower complex is gradually consolidated, and its permeability coefficient

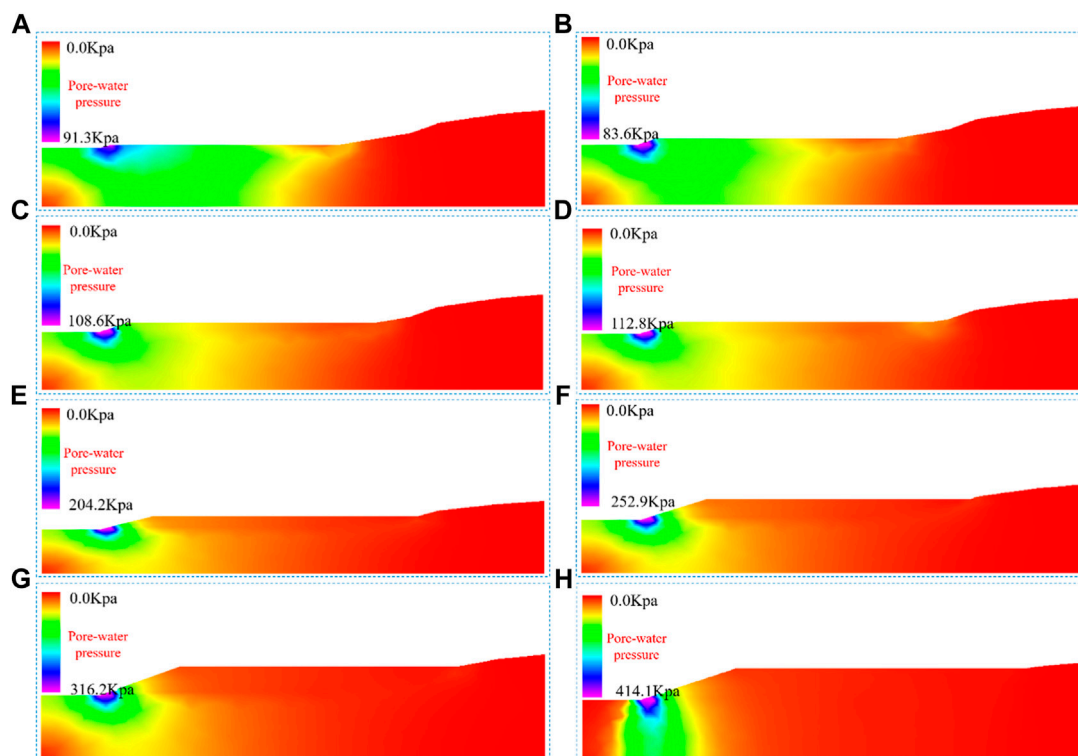


FIGURE 9

Simulation results of infiltration lines of composites at different times and heights; (A) 30 days of stacking (stacking height 4 m); (B) 60-days stacking (stacking height 8 m); (C) 90-days stacking (stacking height 12 m high); (D) 150 days (height 16 m); (E) 210 days (height 22 m); (F) 300 days (height 28 m); (G) 360 days (height 34 m); (H) 420 days of stacking (height 40 m).

gradually decreases, and the lower part is almost impermeable, the infiltration line is gradually raised; when the stacking is stopped, due to the lack of water supply in the upper part, the infiltration line gradually decreases until it is close to the original infiltration line (Shakesby and Whitlow, 1991; Chen et al., 2011). When rainwater or slurry water is continuously replenished, seepage water or rainwater gathers from the surface of the lower complex to the bottom of the slope. In the absence of a drainage channel at the bottom of the slope, it accumulates at the bottom of the slope, and the water flow at the bottom of the slope infiltrates in a near-vertical direction. According to the above research results, the influence of groundwater may not be considered in the overall stability analysis of the composite (Čarman et al., 2014).

5 Stability studies

5.1 Basic assumptions and methods of analysis

5.1.1 Basic assumption

In Section 2, composites are generalized into masonry, comprehensive and reinforced models according to their properties. Since the complex is filled with tailings and

nonrigid bodies, it is difficult to model mathematically when generalized as a masonry model. Therefore, the composite is generalized into a reinforced model and an overall model for stability analysis in this study.

For the above model, the following assumptions were made in the analysis:

- (1) The single composite is very long, and the layered height is not large, less than 3 m, which simplifies the stability as a two-dimensional plane problem;
- (2) Generalize the complex of each stage (including the final stage) into a tailings heap;
- (3) The geotextiles are generalized as reinforcement, and the tensile strength of the reinforcement is twice the tensile strength of the single-layer; the vertical spacing of the reinforcement is the layer height, and the horizontal spacing is zero;
- (4) The geotextile wraps the layered tailings. We assume that the anchoring force of the tendon is greater than the gripping force between the tailings and the geotextile and consider a single composite as a whole;
- (5) The strengthening effect of the geotextile at the end of the composite body on the tailings is used as a safety reserve, and its influence is not considered in the stability calculation;

TABLE 1 Tailings composite shear strength test value.

Consolidation time (day)	Density (g/cm ³)	Dry density (g/cm ³)	Void ratio
30	1.46	0.736	3.21
60	1.57	0.871	2.56
90	1.69	1.030	2.01
150	1.73	1.165	1.66
210	1.86	1.372	1.26
300	1.9	1.483	1.09
360	1.92	1.582	0.96
420	1.97	1.703	0.82

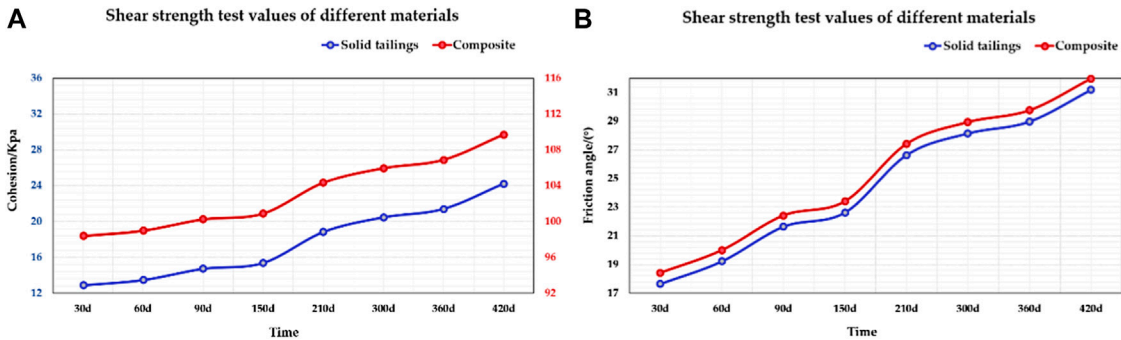


FIGURE 10 The shear strength comparison of pure tailings and tailings geotextile composites; (A) cohesion test values of different materials; (B) friction angle test value of different materials.

- (6) The influence of the foundation on the composite is not considered, that is, the foundation is considered to be free from deformation and damage;
- (7) Does not consider the effect of groundwater on the stability of the complex;
- (8) The effect of horizontal thrust on the complex is not considered;
- (9) In practical engineering, the effects of (6) and (7) should be considered. When the dry pile is used as a dam body or retaining wall, the influence of (8) should be considered, and the problem of foundation settlement should also be considered;
- (10) In this study, in addition to the above assumptions, the assumptions and applicable conditions of specific calculation methods are also met.

5.1.2 Methods of analysis

There are many methods for slope stability analysis, such as the limit equilibrium method, numerical analysis method, stochastic analysis method, and fuzzy analysis method (Hu et al., 2021; Zhang et al., 2022). However, the specification

adopts the most widely used limit equilibrium method, so this study adopts the Swedish slice method with similar assumptions to analyze the stability of the complex.

5.2 Basic parameters

5.2.1 Geometric model and parameters

The geometric model, process, and parameters are shown in Section 4.2 and Figure 8A.

5.2.2 Constraints

Constraints see basic assumptions.

5.2.2 Physical and mechanical parameters

The tailings-geotextile composite is shown in Table 1, and the tensile strength of the geotextile is 19 kN/m. The shear strength comparison of pure tailings and tailings geotextile composites is shown in Figure 10.

When calculating and analyzing, there are two ways to set the physical and mechanical parameters of the composite dry stack:

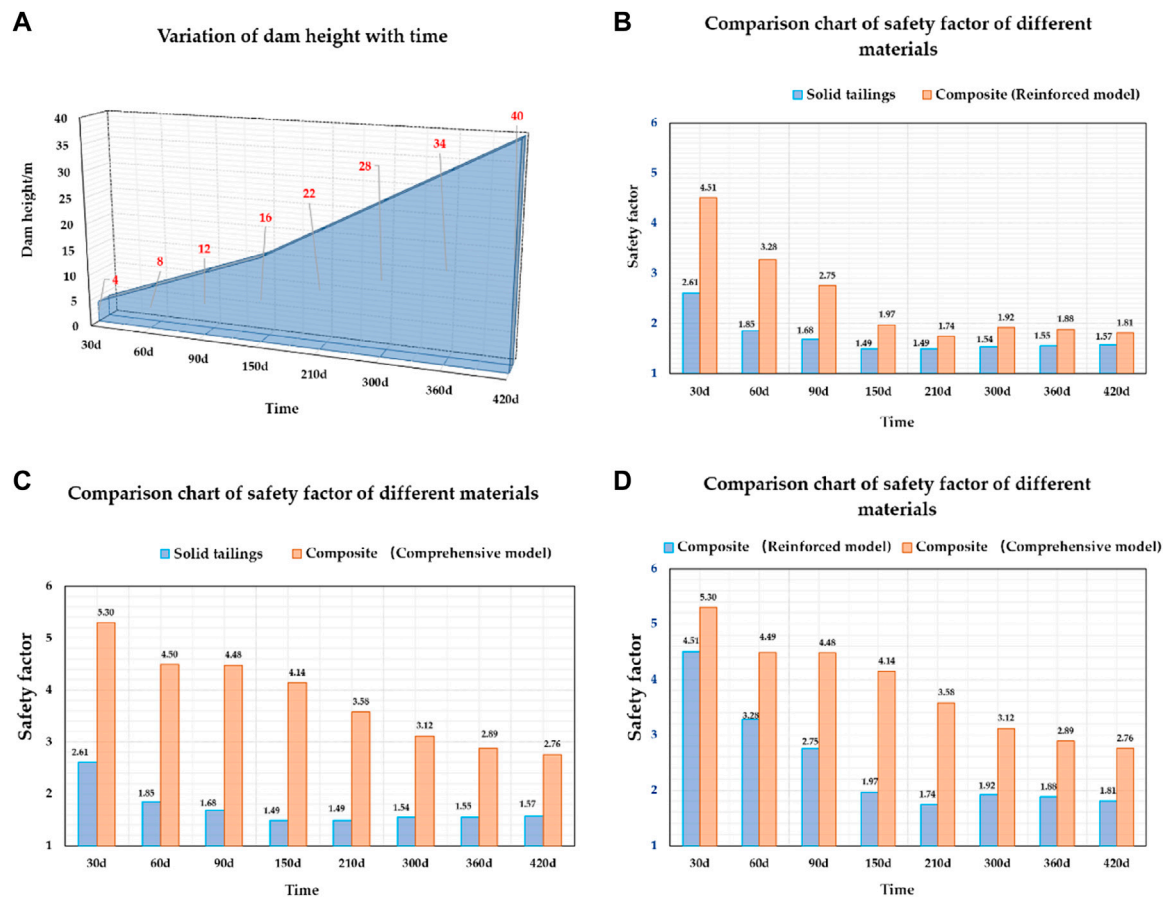


FIGURE 11

Variation in the safety factor with time and dam height; (A) Variation of dam height with time; (B) Comparison chart of safety factor for solid tailings and composite-reinforced model; (C) Comparison chart of safety factor for solid tailings and composite-comprehensive model; (D) Comparison chart of safety factor for composite-reinforced model and composite-comprehensive model.

- (1) The parameters of the tailings and the geotextile are set separately; that is, the geotextile is generalized into the reinforcement in the tailings body and then substituted into the respective physical and mechanical parameters.
- (2) Mixing settings according to the composite parameters, that is, substituting the comprehensive physical and mechanical parameters of the mixture.

5.3 Stability calculation results and analysis

According to the previous assumptions, we study and analyze the stability of the composite model at different times and heights (the overall algorithm and the reinforcement algorithm). The law of composite height and safety factor with consolidation time is shown in Figure 11.

Figure 11 shows the following:

- (1) During the stacking process of the complex, its safety and stability change with time and height; in the initial stage of stacking, with the increase in stacking height, the safety factor of the composite decreases rapidly, and the decreasing speed decreases at approximately 180 days. After 210 days (the stacking height is 22.0 m), the left and right sides are reduced to their minimum values. If the stacking is stopped at this time, the stability of the composite will gradually increase until it is stable. Therefore, the use of spaced stacking helps to enhance the stability of the composite.
- (2) Under the condition of equal consolidation, the composite body has better stability than the pure tailings dry heap.
- (3) Due to the limitation of assumptions, experimental data, and environmental conditions, the safety factor of the composite calculated by the reinforcement model is more conservative than the calculation result of the overall model. Experimental study of physical and mechanical properties.

6 Conclusion

This paper studies the overall stability of a tailings composite dry stack. It can be concluded that:

- (1) The materials (tailings, geotextiles) that make up the composite and its stacking process have a great influence on the permeability of the composite. The general rule is that in the early stage of composite stacking, the permeability coefficient of the composite body increases with increasing filling tension; in the later stage, it gradually decreases until it is stable.
- (2) The numerical simulation analysis of the seepage field of the complex shows that in the early stage of complex stacking, although the tailings permeability coefficient in the complex is large, the relative position of the saturated zone is relatively high due to the low height of the complex; with the continuous rise of the composite or the increase of the stacking time, the lower part almost becomes an impermeable layer, and the position of the saturated zone gradually increases; when the stacking is stopped, due to the lack of water supply in the upper part, the saturation zone gradually decreases until it is close to the original position.

Data availability statement

The original contributions presented in the study are included in the article/supplementary material, further inquiries can be directed to the corresponding author.

Author contributions

Drafting of manuscript: YZ and CY; planning and supervision of the research: JJ and SH; analysis and interpretation of data: XH; acquisition of data: XW; Model construction: TZ.

References

- Cao, G., Wang, W., Yin, G., and Wei, Z. (2019). Experimental study of shear wave velocity in unsaturated tailings soil with variant grain size distribution. *Constr. Build. Mater.* 228, 116744. doi:10.1016/j.conbuildmat.2019.116744
- Čarman, M., Jemec Auflič, M., and Komac, M. (2014). Landslides at a uranium mill tailing deposit site Boršt (Slovenia) detected by radar interferometry. *Landslides* 11, 527–536. doi:10.1007/s10346-013-0454-9
- Chen, R., Zhang, B. Z., Lei, W. D., and Luo, W. B. (2011). Response of soil suction to heavy rainfalls in a tailings dam. *Adv. Mat. Res.* 250–253, 1681–1685. doi:10.4028/www.scientific.net/amr.250-253.1681
- Chen, X., Zhang, J., and Li, Z. (2014). Shear behaviour of a geogrid-reinforced coarse-grained soil based on large-scale triaxial tests. *Geotext. Geomembranes* 42, 312–328. doi:10.1016/j.geotexmem.2014.05.004
- Chen, S., Zheng, Y., Wang, C., and Hsu, T. Y. (2015). A large-scale test on overtopping failure of two artificial dams in Taiwan. *Eng. Geol. Soc. Territ.* 2, 1177–1181. doi:10.1007/978-3-319-09057-3_206
- Diersch, H.-J. G., and Perrochet, P. (1999). On the primary variable switching technique for simulating unsaturated-saturated flows. *Adv. Water Resour.* 23, 271–301. doi:10.1016/S0309-1708(98)00057-8
- Duan, W., Guo, J., and Wang, B. (2013). Stacking process of metal mine tailings in China and its development trend. *Metal. Mine* 12, 118–122.
- Gray, W. G., and O'Neill, K. (1976). On the general equations for flow in porous media and their reduction to Darcy's Law. *Water Resour. Res.* 12, 148–154. doi:10.1029/WR012i002p00148
- He, W., Shao, H., Kolditz, O., Wang, W., and Kalbacher, T. (2015). Comments on "A mass-conservative switching algorithm for modeling fluid flow in variably saturated porous media, K. Sadegh Zadeh, Journal of Computational Physics, 230 (2011)". *J. Comput. Phys.* 295, 815–820. doi:10.1016/j.jcp.2015.04.019
- Hu, Q., Wu, Y., Miao, F., Zhang, L., and Li, L. (2021). Stability analysis of concave slope based on Mein-Larson infiltration model. *Chin. J. Geol. hazard control* 32, 26–35. doi:10.16031/j.cnki.issn.1003-8035.2021.06-04

Funding

The work was supported by the Major science and technology projects of Anhui Province (No.201903a07020008) and the Transportation Science and Technology Project Foundation of Fujian Provincial (No.201911).

Conflict of interest

Author YZ, XW, and CY were employed by Sinosteel Maanshan General Institute of Mining Research Co., LTD, China.

The remaining authors declare that the research was conducted in the absence of any commercial or financial relationships that could be construed as a potential conflict of interest.

Publisher's note

All claims expressed in this article are solely those of the authors and do not necessarily represent those of their affiliated organizations, or those of the publisher, the editors and the reviewers. Any product that may be evaluated in this article, or claim that may be made by its manufacturer, is not guaranteed or endorsed by the publisher.

Acknowledgments

We also thank Xiao Gu for their assistance in the test. Finally, we would like to thank the handling editor and reviewers whose valuable and constructive comments greatly improved this article.

- Kansoh, R. M., Elkholy, M., and Abo-Zaid, G. (2020). Effect of shape parameters on failure of earthen embankment due to overtopping. *KSCE J. Civ. Eng.* 24, 1476–1485. doi:10.1007/s12205-020-1107-x
- Khaniki, A. K., and Daliri, F. (2013). Analytical and experimental approaches to obtain the ultimate strength of reinforced Earth elements. *KSCE J. Civ. Eng.* 17, 1001–1007. doi:10.1007/s12205-013-0181-8
- Khedkar, M. S., and Mandal, J. N. (2009). Behaviour of cellular reinforced sand under triaxial loading conditions. *Geotech. Geol. Eng. (Dordr.)* 27, 645–658. doi:10.1007/s10706-009-9264-1
- Koerner, R. M. (2000). Emerging and future developments of selected geosynthetic applications. *J. Geotech. Geoenviron. Eng.* 126, 293–306. doi:10.1061/(asce)1090-0241(2000)126:4(293)
- Li, Q., Geng, J., Song, D., Nie, W., Saffari, P., and Liu, J. (2022). Automatic recognition of erosion area on the slope of tailings dam using region growing segmentation algorithm. *Arab. J. Geosci.* 15, 438. doi:10.1007/s12517-022-09746-4
- Liu, L., Wang, W., Chu, C., and Chi, J. (2002). Study on relation between pore size distribution and permeability of nonwoven geotextile. *J. Qingdao Univ.*, 48–52. doi:10.13306/j.1006-9798.2002.01.014
- Liu, L., Zhang, H., Zhong, D., and Miao, R. (2014). Research on tailings dam break due to overtopping. *J. Hydraulic Eng.* 45, 675–681. doi:10.13243/j.cnki.slxb.2014.06.006
- Nouri, S., Nechnech, A., Lamri, B., and Lopes, M. L. (2016). Triaxial test of drained sand reinforced with plastic layers. *Arab. J. Geosci.* 9, 53. doi:10.1007/s12517-015-2017-y
- Pincus, H., Bathurst, R., and Karpurapu, R. (1993). Large-scale triaxial compression testing of geocell-reinforced granular soils. *Geotech. Test. J.* 16, 296. doi:10.1520/GTJ10050J
- Qin, K., and Fu, K. (2016). Application of tailings geotextile composite in the treatment of a tailings pond. *Mod. Min.* 32, 214–215.
- Rahardjo, H., Lee, T. T., Leong, E. C., and Rezaur, R. B. (2005). Response of a residual soil slope to rainfall. *Can. Geotech. J.* 42, 340–351. doi:10.1139/t04-101
- Shakesby, R. A., and Whitlow, J. R. (1991). Failure of a mine waste dump in Zimbabwe: causes and consequences. *Environ. Geol. Water Sci.* 18, 143–153. doi:10.1007/BF01704668
- Srivastava, R., and Yey, T. C. J. (1991). Analytical solutions for one-dimensional, transient infiltration towards the water table in homogeneous and layered soils. *Int. J. Rock Mech. Min. Sci. Geomech. Abstr.* 28, A350. doi:10.1016/0148-9062(91)91285-Y
- Wang, W., Cao, G., Li, Y., Zhou, Y., Lu, T., Wang, Y., et al. (2022). Experimental study of dynamic characteristics of tailings with different reconsolidation degrees after liquefaction. *Front. Earth Sci. (Lausanne)* 10. doi:10.3389/feart.2022.876401
- Whitaker, S. (1986). Flow in porous media I: a theoretical derivation of Darcy's law. *Transp. Porous Media* 1, 3–25. doi:10.1007/BF01036523
- Wu, J., Li, L., and Wang, J. (2022). Dynamic shear characteristics of interface between different geosynthetics and recycled concrete aggregate. *J. Vib. Shock* 41, 279–287. doi:10.13465/j.cnki.jvs.2022.01.035
- Yang, C., Zhang, C., Li, Q., Yu, Y., Ma, C., and Duan, Z. (2021). Disaster mechanism and prevention methods of large-scale high tailings dam tailings geotextiles woven bags. *Rock Soil Mech.* 42, 1–17. doi:10.16285/j.rsm.2020.1653
- Zhang, M., Zhou, Y., Xu, C., and Cao, Z. (2012). True triaxial numerical experiment of tailing geotextile compound in an Iron mine. *Metal. Mine* 11, 132–134.
- Zhang, Z., Lin, Y., He, H., Zhang, H., and Yang, G. (2022). Instability characteristics and stability analysis of expansive soil slope. *J. Central South Univ. Sci.* 53, 104–113. doi:10.11817/j.issn.1672-7207.2022.01.006
- Zhang, L. (2019). Multi-scale Analysis of mechanical properties of textile geotextiles reinforced tailing sand. Liaoning Technical University, MA thesis. doi:10.27210/d.cnki.glnju.2019.000040
- Zhao, Y., Jing, X., Zhou, X., Cai, Z., and Liu, K. (2016). Experimental study on blocking action of bar strip on tailings dam overtopping. *China Saf. Sci. J.* 26, 94–99. doi:10.16265/j.cnki.issn1003-3033.2016.01.016
- Zhu, X., Zhang, M., Cao, Z., Li, D., Zou, Z., and Wang, J. (2013). Study on the layer interface friction strength characteristics of tailings geotextiles woven bags. *Metal. Mine* 06, 114–117.

Frontiers in Earth Science

Investigates the processes operating within the major spheres of our planet

Advances our understanding across the earth sciences, providing a theoretical background for better use of our planet's resources and equipping us to face major environmental challenges.

Discover the latest Research Topics

[See more →](#)

Frontiers

Avenue du Tribunal-Fédéral 34
1005 Lausanne, Switzerland
frontiersin.org

Contact us

+41 (0)21 510 17 00
frontiersin.org/about/contact

